Growth and characterization of in-plane solid-liquid-solid GeSn and SiSn nanowires

Edy Edward Azrak

To cite this version:

Edy Edward Azrak. Growth and characterization of in-plane solid-liquid-solid GeSn and SiSn nanowires. Materials. Normandie Université, 2018. English. NNT : 2018NORMR135 . tel-02422227

HAL Id: tel-02422227
https://theses.hal.science/tel-02422227

Submitted on 21 Dec 2019

Normandie Université

THÈSE

Pour obtenir le diplôme de doctorat

Spécialité Physique – Science des Matériaux

Préparée au sein de l'Université de Rouen Normandie

Growth and Characterization of In-Plane Solid-Liquid-Solid GeSn and SiSn Nanowires

Présentée et soutenue par
Edy Edward Azrak

Thèse soutenue publiquement le 20 Décembre 2018 devant le jury composé de		
Mme. Caroline BONAFOS	Directrice de Recherche – CEMES/ Université de Toulouse 3 - Toulouse	Rapporteur
M. Christophe DELERUE	Directeur de Recherche – IEMN/ Université de Lille 1 - Lille	Examinateur
M. Moustafa EL-KURDI	Maitre de Conférences HDR – C2N/ Université Paris Saclay - Orsay	Rapporteur
M. Pere Roca i CABARROCAS	Directeur de Recherche – LPICM/ Ecole polytechnique – Palaiseau	Examinateur
M. Sébastien DUGUAY	Maitre de conférences – GPM/ Université de Rouen Normandie	Encadrant
M. Philippe PAREIGE	Professeur – GPM/ Université de Rouen Normandie	Directeur de thèse

Thèse dirigée par Philippe PAREIGE, **laboratoire Groupe de Physique des Matériaux.**

UNIVERSITÉ DE ROUEN NORMANDIE

ED PSIME

GPM Groupe de Physique des Matériaux

ABSTRACT

Germanium-Tin alloy is a unique class semiconductor gaining a strong attention because of its significant electrical and optical properties. Sn incorporation in Ge allows straightforward band-gap engineering enabling to enhance the electron and hole mobilities, and for a sufficient Sn amount an indirect-to-direct band-gap transition occurs. Its versatility rises due the possible monolithic integration on Si-platforms making it an ideal material in domains of optoelectronics, and high speed electronic devices.

This thesis has focused on the fabrication and characterization of crystalline $Ge_{1-x}Sn_x$ nanowires with high Sn concentrations. New strategies were designed to fabricate many types of GeSn nanowires. The results have been explained as function of the existing kinetic models. A new growth mechanism was reported (i.e. Solid-Solid-Solid mechanism – SSS), it consists of growing in-plane GeSn nanowires using Sn catalysts below the melting point of Sn. Four mass transport models were proposed for the SSS growth mechanism. Various characterizations (e.g. TEM and APT) were done to investigate the physical and chemical properties of the obtained nanowires.

Keywords: Germanium-Tin (GeSn), semiconductor, band-gap, nanowires, catalyst, growth, solid-liquid-solid, solid-solid-solid, characterizations.

RÉSUMÉ

L’alliage germanium-étain est un semiconducteur qui suscite une grande attention en raison de ses propriétés électriques et optiques. L’incorporation de Sn dans le germanium permet d’ajuster la largeur de bande interdite (gap) et d’améliorer la mobilité des électrons et des trous, et pour une quantité suffisante d’étain, le matériau passe d’un gap indirect à direct. Cet alliage est versatile parce qu’il peut être intégré d’une façon monolithique sur le Si, c’est ce qui en fait un matériau idéal dans les domaines de l'optoélectronique à base de silicium.

Cette thèse est sur la fabrication et la caractérisation de nanofils cristallins $Ge_{1-x}Sn_x$ à haute concentration en Sn. Des nouvelles stratégies ont été employées pour fabriquer de nombreux types de nanofils GeSn. Les résultats ont été expliqués en fonction des modèles cinétiques existants. Un nouveau mécanisme de croissance y est décrit: le mécanisme solide-solide-solide – SSS. Il consiste à faire croître des nanofils de GeSn dans le plan du substrat à l’aide de catalyseurs d’étain à une température inférieure au point de fusion de Sn. Quatre modèles de transport de masse sont proposés pour le mécanisme de croissance du SSS. Diverses caractérisations (par exemple TEM et APT) ont été effectuées pour étudier les propriétés physiques, et chimiques des nanofils.

Mot-Clés: Germanium-Étain (GeSn), semiconducteur, bande interdite, nanofils, catalyseur, croissance, solide-liquide-solide, solide-solide-solide, caractérisation.

ACKNOWLEDGEMENT

The thesis was carried out in the laboratory Material Physics Group (GPM) UMR CNRS 6634 – University of Rouen Normandy and INSA Rouen Normandy. A part of this work was done in collaboration with Laboratory of Physics of Interfaces and Thin Films (LPICM) in École Polytechnique Palaiseau.

First I would like to thank my director Pr. Philippe Pareige and my supervisor Dr. Sébastien Duguay for their support, help, and discussions during my PhD. I am thankful to my thesis director for giving me the opportunity to work on this topic, as well as my supervisor for his indispensable guidance over the last several years. I appreciate their encouragement and knowledge which were crucial and vital to achieve the objectives of this thesis. I also enjoyed their humorous spirits, and care over the past several years.

I had a great fortune to be hosted by Pr. Pere Roca i Cabarrocas in LPICM. His invaluable guidance, high expertise and great enthusiasm were essential ingredients in the success of this PhD. I am very grateful of this fruitful collaboration.

I extend my gratitude to Dr. Wanghua Chen who was at that time in LPICM. By working closely together, I have learned a lot about catalyst preparations, thin-film depositions, and nanowires growth. I appreciate his dynamism and motivation despite many drawbacks in our work.

I would like to thank the jury who accepted to evaluate this PhD: Mr. Christophe Delerue, Research Director at IEMN from University of Lille who made me honored by accepting to be the president of the jury; Mrs. Caroline Bonafos, Research Director at CEMES from University of Toulouse and Mr. Moustafa El-Kurdi, Lecturer-Researcher at C2N from University of Paris-Saclay, who made me grateful by accepting to be the rapporteurs of my thesis, and Mr. Pere Roca i Cabarrocas, Research Director at LPICM from École Polytehnique Palaiseau, who made me very honored by accepting to be the examiner in this jury.

I thank all the GPM and LPICM people and especially my close colleagues who made this PhD an enjoyable venture.

I sent my warmest thanks to Dr. Chantal Karam for her precious contributions, unwavering support, encouragement, and patience. Without any doubt, her heart-blessings were invaluable to reach this milestone in my life.

Lastly, I am humbled to dedicate this PhD thesis to my parents, who devoted a big effort to teach me. I am very thankful for their advices, guidance, and reassurance which were very important for me.

CONTENTS

INTRODUCTION

It has been half a century that silicon is used as platforms in optoelectronics, and as main components in microelectronics, because it can be excellently passivated by SiO_2 [1], and it is largely abundant on earth [2]. Great efforts have been done to decrease the size of active Si components to integrate more of them on a single chip, and make use of their enhanced properties at nanoscales. As a consequence, the performance is further upgraded because of the miniaturization. However, nowadays the limit of Moore's law is approached [3]; micro- and optoelectronics are limited by the intrinsic properties of Si and by its insufficient light emission. Even though, the miniaturization can pursued beyond Moore's law by different designs and architectures of samples and materials (i.e. More Moore [4]), it will be limited by quantum mechanical effects [5]. For this reason, the idea of integrating other elements such as Ge or GeSn in Si-based technologies to boost their performance and increase their light emissions rises.

One of the main topics in material science today is the $Ge_{1-x}Sn_x$ (germanium-tin) alloy [6]. It has attracted a great deal of interest due to its promising properties. Incorporating Sn into Ge allows a band-structure engineering, which can expand the capabilities of the existing Si-based technologies, and open new routes towards the next generation of semiconductor devices [7]. By achieving sufficient Sn incorporation in Ge an indirect-to-direct bandgap transition occurs, which leads to a considerable advancement in the domain of optoelectronics, especially when integrated on Si platforms. GeSn with a direct band gap can be used as an active component in the near infrared region in photoemission [8], photodetection [9], or even in photovoltaics [10, 11]. Furthermore, GeSn can also upgrade the domain of nanoelectronics. Indeed, its enhanced electron and hole mobilities [12] enable the production of high speed transistors and high speed logic gates [13, 14]. Moreover, the possibility of monolithic integration is what may amplify the use of $Ge_{1-x}Sn_x$ on Si-platforms [15]. Nonetheless, there are many fundamental challenges to fabricate such an alloy: 1) the low solubility of Sn in Ge, 2) high phase separation tendency, and 3) the size difference between Ge and Sn [16]. Though, many research teams have accomplished high incorporations of Sn, the highest concentration to date is 17 at.% at the expenses of a degraded crystal quality [17]. Conversely, other researchers have fabricated a relatively better crystalline quality thin-films of GeSn, but the concentration of Sn did not exceed ~ 13 at.% [8]. In addition, there have been many studies published on $Ge_{1-x}Sn_x$ nanowires (NWs), since their high surface-to-volume ratio can bring physical and chemical properties which are not accessible in their bulk counterparts. For example, Au-catalyzed Ge NWs obtained by vapor-liquid-solid (VLS) mechanism did not attain more than ~ 10 at.% Sn [18], meanwhile the use solution-liquid-solid mechanism produced NWs with ~ 12 at.% Sn but lacking a good crystalline structure[19].

Another alloy studied but not as common as the latter one (i.e. GeSn) is $Si_{1-x}Sn_x$ [20]. The reason for the lower number of studies conducted on this alloy is the huge concentrations of Sn needed to achieve a direct bandgap; it is much higher than the ones needed for Ge. Indeed, the tight-binding based calculations within the virtual crystal approximation predict a transition at 60 at.% Sn [21], whereas the density functional theory predicts at ~ 25 at.% Sn [22]. Incorporating such concentrations of Sn is staggeringly limited as predicted by the Si-Sn phase diagram (~ 0.01 at.% Sn [23]) at the growth temperature used in this thesis. Therefore, relevant optical and electrical properties for SiSn have not been characterized so far.

In this thesis, we try to overcome the drawbacks presented above, and to achieve a high incorporation of Sn while attempting to maintain a good crystalline quality. To fabricate these nanowires, two catalyst precursors are used: SnO_2 and Sn. The fact that Sn is used as a catalyst adds more challenges to the growth of nanowires, specifically Ge NWs. Sn is known to be an unstable catalyst [24] due to its low surface tension [25], especially when it is in contact with a-Ge:H [26], a high surface energy material. In addition, Sn NPs have a higher wettability on a-Ge:H and a higher solubility in the corresponding layer [27] as compared to a-Si:H[28]. All these problems should be solved to accomplish the main objective of this study. SiSn NWs fabricated by Dr. Zhaoguo Xue (at LPICM – École Polytechnique) are characterized in this thesis.

In chapter 1, reasonable explanations will be presented to justify the use of nanowires as the layout structure of GeSn and SiSn alloys. A brief literature survey showing the state of the art growth strategies, including the top-down and the bottom-up approaches is presented. Our main focus is on the Solid-Liquid-Solid (SLS) mechanism, and the physics behind it will be carefully described. The GeSn alloy is, then introduced, along its important properties, and the challenges that could be faced during the fabrication are tackled. Two configurations of $Ge_{1-x}Sn_x$ alloy were discussed, namely: thin-films and nanowires. The part of nanowires is more extended since it is the nanostructure used in this study. Moreover, the concentration of catalyst atoms in VLS grown NWs are compared to SLS ones to highlight the importance of the SLS mechanism.

In chapter 2, the first part will describe the synthesis reactors along with the parameters of the fabrication of the catalysts and NWs. Afterwards, the characterization tools used to investigate the obtained NWs are introduced, and their functionalities are physically explained.

In chapter 3, the growth of Ge NWs using indium as a catalyst will be studied. Since it is a well-explored catalyst, the indium is implemented for the first trials of Ge NWs growth. The size of the catalyst droplets is shown to play an essential role in determining structure of Ge.

In chapter 4, the in-plane GeSn NWs growth is done using Sn catalyst by solid-liquid-solid mechanism. Although, many challenges exist, the essential factor leading to a successful growth of these NWs is presented. Specimens of different samples are characterized at atomic scales using mainly the transmission electron microscope and the atom probe tomography.

In chapter 5, an unexpected growth mechanism will be presented and compared with the SLS mechanism. Indeed, in-plane $Ge_{1-x}Sn_x$ NWs can be grown below the melting temperature of Sn NPs. Other interesting experiments about the fabrication of out-of-plane $Ge_{1-x}Sn_x$ nanowires by modifying the growth protocol, and quantification results will be discussed.

REFERENCES

1. Jana, T., Mukhopadhyay Sumita, Ray Swati, *Low temperature silicon oxide and nitride for surface passivation of silicon solar cells.* Solar energy materials and solar cells, 2002. **71**(2): p. 197-211.
2. McIntosh, K.R., Cudzinovic, Michael J, Smith, David D, Mulligan, William P, Swanson, Richard M. *The choice of silicon wafer for the production of low-cost rear-contact solar cells*. in *Photovoltaic Energy Conversion, 2003. Proceedings of 3rd World Conference on*. 2003. IEEE.
3. Kish, L.B., *End of Moore's law: thermal (noise) death of integration in micro and nano electronics.* Physics Letters A, 2002. **305**(3-4): p. 144-149.
4. Waldrop, M.M., *More than moore.* Nature, 2016. **530**(7589): p. 144-148.
5. Powell, J.R., *The quantum limit to Moore's law.* Proceedings of the IEEE, 2008. **96**(8): p. 1247-1248.
6. Zaima, S., Nakatsuka, Osamu, Taoka, Noriyuki, Kurosawa, Masashi, Takeuchi, Wakana, Sakashita, Mitsuo, *Growth and applications of GeSn-related group-IV semiconductor materials.* Science and Technology of Advanced Materials, 2015. **16**(4): p. 043502.
7. Attiaoui, A., Moutanabbir, Oussama, *Optical and Electronic Propreties of GeSn and GeSiSn Heterostructures and Nanowires.* ECS Transactions, 2014. **64**(6): p. 869-879.
8. Homewood Kevin, P., Lourenço Manon A., *The rise of the GeSn laser.* Nature Photonics, 2015. **9**: p. 78.
9. Assefa, S., Xia, Fengnian, Vlasov, Yurii A, *Reinventing germanium avalanche photodetector for nanophotonic on-chip optical interconnects.* Nature, 2010. **464**(7285): p. 80.
10. Bedell, S.W., Sadana, Devendra K, Shahrjerdi, Davood, *Spalling methods to form multi-junction photovoltaic structure*. 2015, Google Patents.
11. Xie, J., *Growth and activation of group IV semiconductors for application in infrared detectors and photovoltaics*. 2010.
12. Sau, J.D., Cohen Marvin L., *Possibility of increased mobility in Ge-Sn alloy system.* Physical Review B, 2007. **75**(4): p. 045208.
13. Yang, Y., Lu Low, Kain, Wang, Wei, Guo, Pengfei, Wang, Lanxiang, Han, Genquan, Yeo, Yee-Chia, *Germanium-tin n-channel tunneling field-effect transistor: Device physics and simulation study.* Journal of Applied Physics, 2013. **113**(19): p. 194507.
14. Gong, X., Han, Genquan, Bai, Fan, Su, Shaojian, Guo, Pengfei, Yang, Yue, Cheng, Ran, Zhang, Dongliang, Zhang, Guangze, Xue, Chunlai, *Germanium–Tin (GeSn) p-Channel MOSFETs Fabricated on (100) and (111) Surface Orientations With Sub-400°C Si2H6 Passivation.* IEEE Electron Device Letters, 2013. **34**(3): p. 339-341.
15. Soref, R.A., Friedman, Lionel, *Direct-gap germanium-tin multiple-quantum-well electro-optical devices on silicon or germanium substrates*. 1996, Google Patents.
16. Gupta, S., Chen, Robert, Huang, Yi-Chiau, Kim, Yihwan, Sanchez, Errol, Harris, James S, Saraswat, Krishna C, *Highly Selective Dry Etching of Germanium over Germanium–Tin (Ge1–x Sn x): A Novel Route for Ge1–x Sn x Nanostructure Fabrication.* Nano letters, 2013. **13**(8): p. 3783-3790.
17. Kormoš, L., Kratzer M., Kostecki K., Oehme M., Šikola T., Kasper E., Schulze J., Teichert C., *Surface analysis of epitaxially grown GeSn alloys with Sn contents between 15% and 18%.* Surface and Interface Analysis, 2017. **49**(4): p. 297-302.
18. Biswas, S., Doherty Jessica, Saladukha Dzianis, Ramasse Quentin, Majumdar Dipanwita, Upmanyu Moneesh, Singha Achintya, Ochalski Tomasz, Morris Michael A., Holmes Justin D., *Non-equilibrium induction of tin in germanium: towards direct bandgap Ge1−xSnx nanowires.* Nature Communications, 2016. **7**: p. 11405.

19. Barth, S., Seifner, Michael S., Bernardi, Johannes, *Microwave-assisted solution-liquid-solid growth of Ge1-xSnx nanowires with high tin content.* Chemical Communications, 2015. **51**(61): p. 12282-12285.
20. Masashi, K., Motohiro, Kato, Takashi, Yamaha, Noriyuki, Taoka, Osamu, Nakatsuka, Shigeaki, Zaima, *Near-infrared light absorption by polycrystalline SiSn alloys grown on insulating layers.* Applied Physics Letters, 2015. **106**(17): p. 171908.
21. Pairot, M., Zoran, Ikonić, Paul, Harrison, *Band structure calculations of Si–Ge–Sn alloys: achieving direct band gap materials.* Semiconductor Science and Technology, 2007. **22**(7): p. 742.
22. Tolle, J., A. V. G. Chizmeshya, Y.-Y. Fang, J. Kouvetakis, V. R. D'Costa, C.-W. Hu, J. Menéndez, I. S. T. Tsong, *Low temperature chemical vapor deposition of Si-based compounds via SiH3SiH2SiH3: Metastable SiSn/GeSn/Si(100) heteroepitaxial structures.* Applied Physics Letters, 2006. **89**(23): p. 231924.
23. Olesinski, R.W., Abbaschian, G. J., *The Si−Sn (Silicon−Tin) system.* Bulletin of Alloy Phase Diagrams, 1984. **5**(3): p. 273-276.
24. Misra, S., et al., *Wetting Layer: The Key Player in Plasma-Assisted Silicon Nanowire Growth Mediated by Tin.* The Journal of Physical Chemistry C, 2013. **117**(34): p. 17786-17790.
25. Nebol'sin, V.A. and A.A. Shchetinin, *Role of Surface Energy in the Vapor–Liquid–Solid Growth of Silicon.* Inorganic Materials, 2003. **39**(9): p. 899-903.
26. Chambouleyron, I., et al., *Mössbauer study of hydrogenated amorphous germanium‐tin thin‐film alloys.* Journal of Applied Physics, 1989. **66**(5): p. 2083-2090.
27. I. Chambouleyron, F.C.M., *Use of hydrogenation in the study of the properties of amorphous germanium tin alloys.* Journal of Applied Physics, 1989. **65**(4): p. 1591-1597.
28. Kulikov, G.S. and K.K. Khodzhaev, *Diffusion doping of undoped hydrogenated amorphous silicon with tin.* Semiconductors, 1998. **32**(2): p. 123-123.

I TOWARDS NANOWIRES

On the threshold of the 21th century, immense technological advances have been achieved in a wide variety of activities, such as electronics, optoelectronics, and photonics. Nowadays, these early innovations are considered to have many drawbacks such as: 1- high amount of material required for their fabrication, 2- high power consumption while performing, and 3- low efficiency. In 1959, Professor Richard Feynman has introduced for the first time the notion of nanotechnology. His lecture entitled “There is Plenty of Room at the Bottom” was about the technology and engineering at the atomic scale (10^{-9} m). The “nanoscale” is typically billionths of a meter, the difference between 1 nanometer and 1 meter is same as the difference between the diameter of the earth (12 756 200 m) and the diameter of a marble (0.012 m). Materials and functional systems built at this scale have unique capabilities due to the preponderance of surface and interface energies. However, for the benefits of the nanotechnology to be realized, scientists need to “see” atoms and learn how to manipulate them. In 1981, two professors; Bining and Rohrer from IBM laboratory, invented the scanning tunneling microscope which created an essential impact on the development of nanotechnology. Since then, nano-scale manipulations, characterizations and applications have sharply risen. By fabricating devices on the scale of a few atoms, their properties exhibit distinctive physical and chemical behavior due to quantum mechanical effects. The nanotechnology allows us to manufacture lighter, stronger, and more efficient devices that can outperform the conventional ones. Nanodevices require less amount of material to be built and less energy to perform. Different forms of miniaturized-structures can be built: 1) 0-dimension i.e. quantum dots, 2) 1-dimension i.e. nanowires, nanotubes, and nanobelts, 3) 2-dimension i.e. thin films, and quantum wells.

I.1 SEMICONDUCTOR NANOWIRES AND THEIR APPLICATIONS

Among other dimensions, 1-dimensional nanostructures; namely nanowires (NWs), have gained lots of attention due to their high surface-to-volume ratio, their susceptibility to be guided (using patterned substrate for instance), and their possible integration in electronics (e.g. NW-based FET [1] and FinFET [2] where FET denotes “Field Effect Transistor”), photonics (e.g. ZnO nanolaser [3]), mechanics (e.g. flexible-NWs [4]), electro-mechanics (e.g. NW-based resonators [5]), thermal applications (e.g. thermoelectric Si NWs [6]), biological applications (e.g. nanosensor for biological species [7]), and energy conversion applications (e.g. dye-sensitized solar-cells [8]). Three categories of NWs are available nowadays: 1) semiconductor NWs e.g. Si, Ge, GaAs, InP, 2) metallic NWs e.g. Ag, Cu, Pt, 3) insulating NWs e.g. SiO_2.

I.2 NANOWIRES FABRICATION

What is more revolutionary is the fabrication of these nanostructures for incorporation into micro- and macroscale systems. Tremendous amount of research efforts have been devoted to understand how to control precisely the dimensions, crystal structures, and compositions of such complex nanosystems. To enable their integration into useful devices, two different paths are pursued: 1) Top-down (TD) and 2) Bottom-up (BU) approaches.

I.2.1 TOP-DOWN APPROACH

From macro to nano-scale, the TD approach using lithography techniques allows to downsize bulky systems into dimensions below 100 nm, as shown in Figure.I.1. For instance, the focused ion beam lithography can reach a lateral precision of 30 nm [9]. Meanwhile, with the current optical lithography techniques, short-wavelengths such as X-ray allow to reach a sharp patterning of < 15 nm [10]. Among these lithography techniques, the most precise one is the electron beam that can reach lower than 10 nm resolution [11]. Despite that TD approaches allow to achieve small features; it becomes increasingly difficult to apply them at nanometer dimensions. In order for nanomaterials to display phenomena associated with quantized-effects, it is necessary to change the strategy of fabrication.

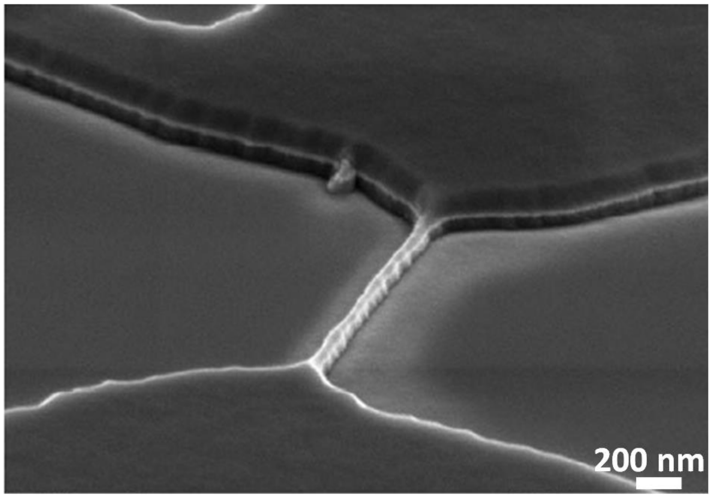

Figure.I.1- Scanning Electron Microscope (SEM) image showing a typical in-plane YBCO nanowire realized by E-Beam Lithography fabrication process. Adapted from [12].

I.2.2 BOTTOM-UP APPROACH

An ever-more-complex approach, the BU consists of building devices atom-by-atom. It is a nanofabrication process using chemical or physical forces operating at the nanoscale to assemble atomic blocks into larger structures. This atomic self-assembly occurs in nature, researchers are trying to replicate this kind of growth of specific atoms into more elaborate structures. To create extended structures at the nanoscale, it is convenient to combine the BU and TD approaches as shown in Figure.I.2. A number of BU mechanisms have been developed for producing nanowires, such as: Vapor-Liquid-Solid (VLS) [13], Vapor-Solid-Solid (VSS) [14], Solid-Liquid-Solid (SLS) [15], Vapor-Solid (VS) [16], and electro-deposition [17]. In our current study VLS, VSS, VS, and SLS will be described.

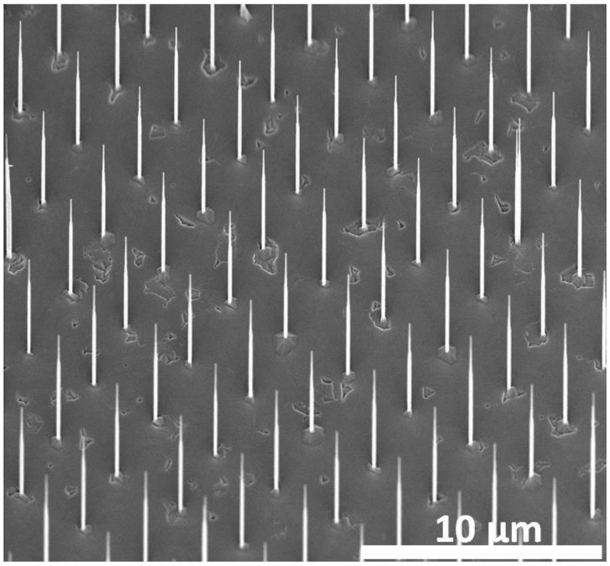

Figure.I.2- SEM image of GaAs nanowires arrays grown via VLS mechanism using Au nanodots that are defined by electron beam lithography. It is a combination of BU and TD approaches. (Courtesy of C2N – center for nanosciences and nanotechnology)

I.2.2.1 VAPOR-LIQUID-SOLID (VLS)

The VLS mechanism was discovered in 1964 by Wagner and Ellis in Bell Telephone laboratory for Silicon whiskers (nanowires) growth [18]. This new concept of crystal growth has been widely used owing to its simplicity and versatility when applied in many semiconductor systems. The key issue related to the growth of nanowires is how to induce a 1-Dimensional crystal growth, as shown in Fig.I.3, in a controlled manner.

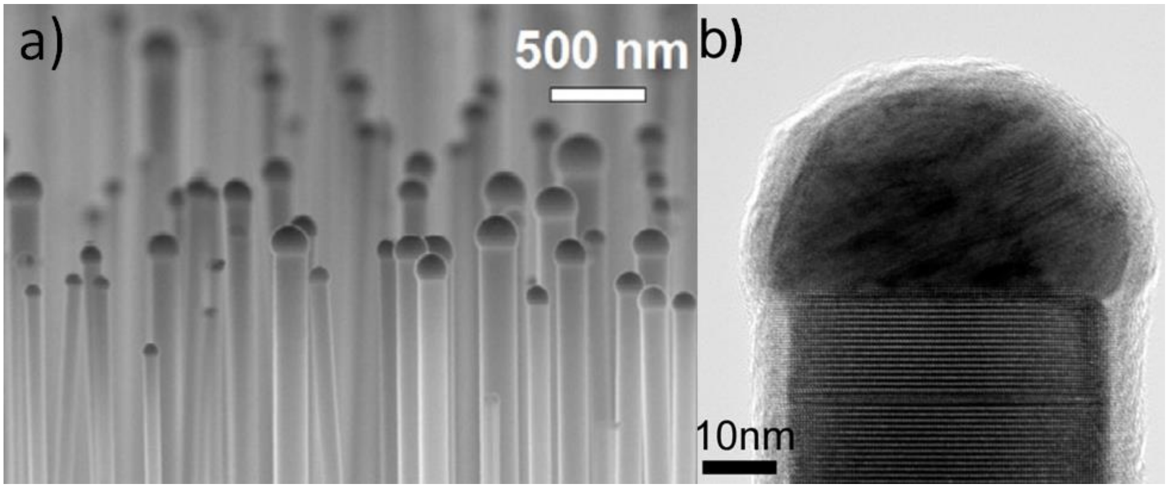

Figure.I.3- TEM and SEM micrographs showing VLS-grown NWs. a) SEM image of straight as-grown VLS GaAs NWs catalyzed by Au NPs realized by Metal-Organic Vapor-Phase Epitaxy (MOVPE) [19]. b) High-Resolution Transmission Electron Microscope (HR-TEM) image of a VLS-InAs NW catalyzed by Au NP in a Molecular-Beam-Epitaxy (MBE) reactor [20].

First, metallic droplets are deposited onto a given substrate in vacuum. Second, atomic vapors of semiconducting (SC) materials are introduced in the reactor while the system is heated at a given temperature. The role of metal droplets is to form a liquid solution for a vapor-phase absorption of the SC material (i.e. Si, Ge). The metal catalyst will form liquid alloy droplets (metal – SC alloy) by adsorbing SC vapor components [21]. In the case of Si NWs, when the temperature is above the eutectic point of Au-Si alloy which is 363℃ (Fig.I.4.a), SiH_4 molecules dissociate at the surface of the catalyst, and H_2 molecules are evacuated while Si atoms enter the liquid, as shown in Fig.I.4.b. When the actual concentration of the SC material is higher than its equilibrium concentration in the metal droplet, the alloy will be supersaturated. After an incubation time (time for crystalline-seed formation), a precipitation of a crystalline-Si (c-Si) seed occurs on the triple-phase boundary (TPB) line (vapor – solid - liquid circular line) which is located at the bottom edge of the catalyst. Subsequently, Si atoms prefer to diffuse towards the newly-formed c-Si seed because less energy will be involved (balance of chemical potentials) with the crystal growth as compared with a secondary nucleation event. Atomically, the NWs are grown layer-by-layer in a step-flow mode [22, 23]. The SC nanowire diameter is determined by the size of the catalyst [24]. The 1D crystal growth will continue as long as vapor components are supplied, and the catalyst is not consumed.

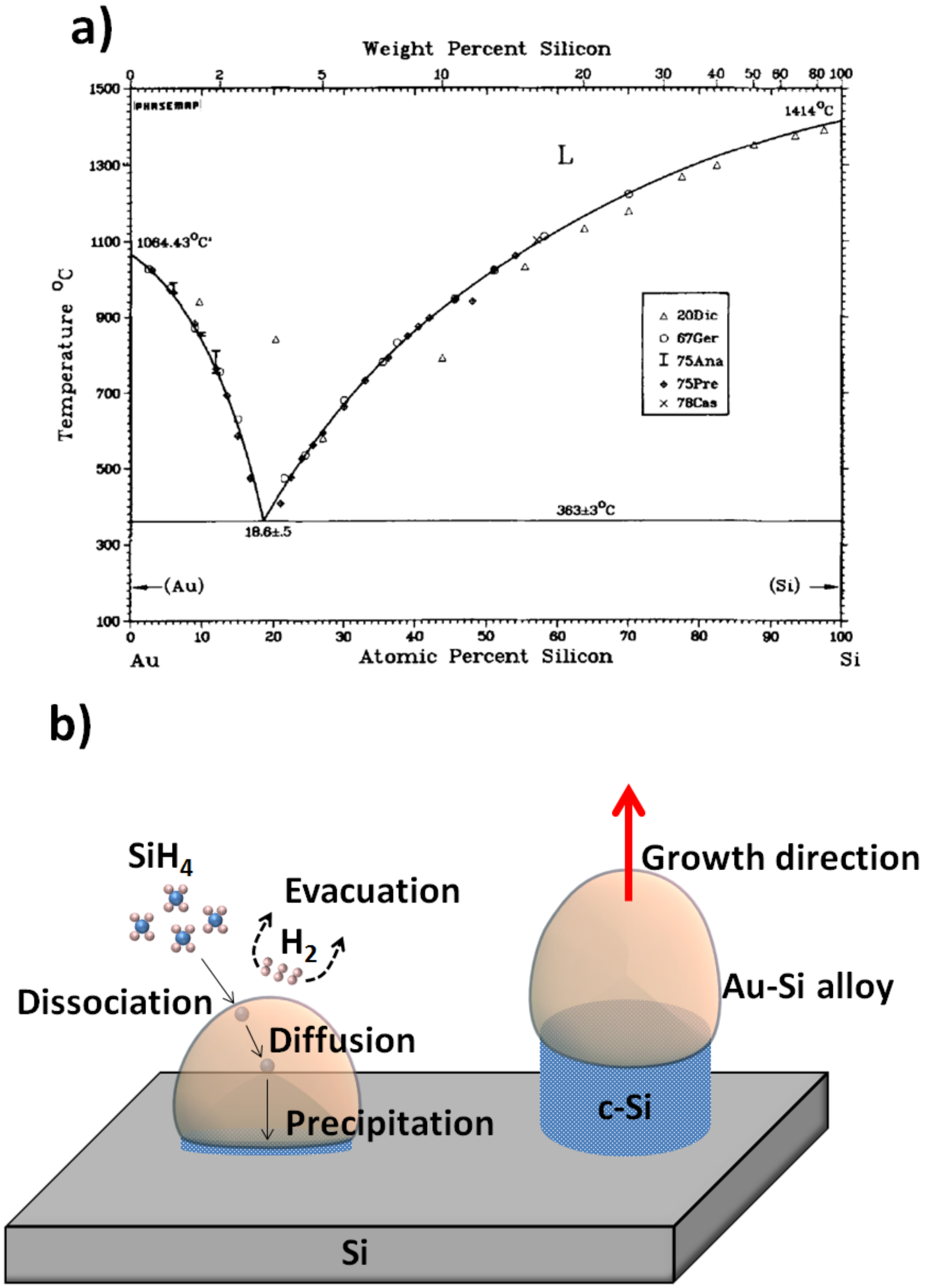

Figure.I.4- Au-catalyzed SiNWs via VLS mechanism. a) Au – Si phase diagram, the eutectic point is 363±0.3°C with a Si composition of 18.6 at.%. b) schematic illustration showing the VLS mechanism. First, Au droplets are deposited on the surface of a Si substrate. Second, the temperature of the substrate is raised sufficiently. Third, Silane (SiH_4) gas is introduced. Silane will dissociate at the surface of the molten catalyst. Since the solubility of Hydrogen is low enough inside the liquid Au, only Si atoms will penetrate the catalyst surface and proceed for diffusion. An Au-Si alloy is formed.

When the supersaturation of Si in Au is reached, precipitation of c-Si will occur at the catalyst / substrate interface. The crystalline nanowires will grow while pushing the catalyst perpendicularly further from the substrate.

I.2.2.2 VAPOR-SOLID-SOLID (VSS)

While the VLS mechanism has become routinely used for fabricating self-assembled nanowires, attention in the past two decades has been paid on the use of alternative solid catalysts [25, 26]. The VSS follows the same process as VLS, except that the temperature used for the growth is below the eutectic point of the metal – SC alloy. The limitations of VLS are: 1) the liquid catalyst can be incorporated into the nanowire affecting its properties in an unwanted way [27], 2) the formation of abrupt heterostructures along the nanowire i.e. Si/Ge/Si is fundamentally hard because of the high solubility of Ge and Si in the liquid catalyst i.e. Au [28]. This phenomenon is called “Reservoir Effect”. It creates a composition gradient along the nanowire [29], and 3) Kinking and tapering of NWs are more likely to occur in VLS growth, thus, affecting their shape and size [30]. Advantageously, for VSS mode, catalyst atoms are more bonded while at solid-state, thus, eliminating their incorporation into the NW. In addition, the growth species have lower solubility in the solid droplet which helps to create compositionally abrupt and structurally perfect heterointerfaces [31], see Fig.I.5. In this case, the catalyst is solid which makes the incubation time shorter than in the case of VLS. A tiny excess amount of SC material can raise enough the chemical potential to nucleate a c-seed, consistent with the low solubility inside the catalyst [32]. Atoms that grow the NW can follow many paths to supply the growing interface: 1- diffusion inside the solid catalyst, 2- diffusion on the surface of the catalyst, and 3- diffusion on the sidewalls of the NW [14]. The VSS mode grows NWs using the step-flow which has the same kinetics as the VLS mode [33].

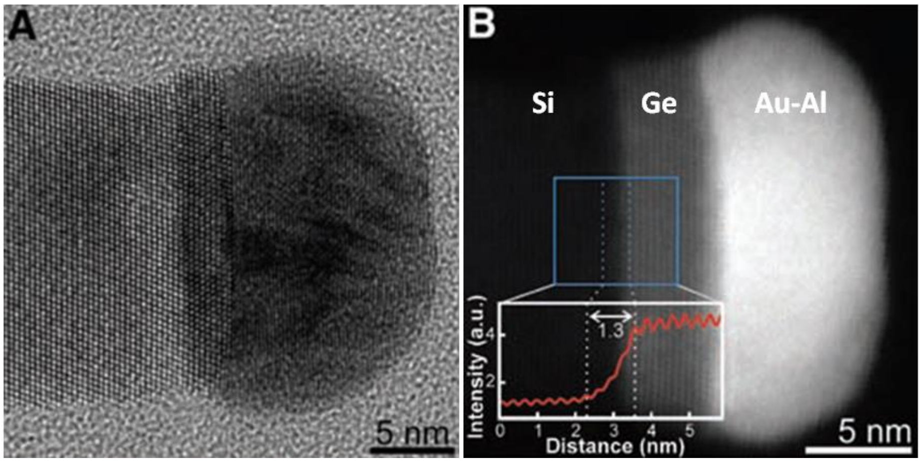

Figure.I.5- High-resolution TEM image of a Si-Ge heterojunction nanowire. a) Si NW (length 500 nm, diameter 18 nm) was grown rapidly using VLS at 510°C then cooled and grown for several minutes in the VSS mode at 360°C, followed by growth of a Ge segment at 360°C. b) HAADF-STEM image of a wire (diameter 17 nm) grown under the same conditions. The inset shows the intensity profile across the interface, averaged over a 5-nm strip along the midpoint of the wire. The width of the interface is 1.3 nm. Adapted from [32].

I.2.2.3 VAPOR-SOLID (VS)

The VS method is another approach to promote the growth of NWs while avoiding the contamination from catalyst incorporation. In the absence of the catalyst (as shown in Fig.I.6), NWs can nucleate and grow by a direct vapor-deposition on the substrate. The spontaneous catalyst-free NWs growth can be driven by screw dislocations [34], planar defects (twin boundary or stacking fault) [35, 36], anisotropic surface energy of various facets [37]. The VS-grown NWs are mainly metals and oxide-metals such as: WO_3 [38], ZnO [39], MgO [40], Fe_2O_3 [41], Sn [42].

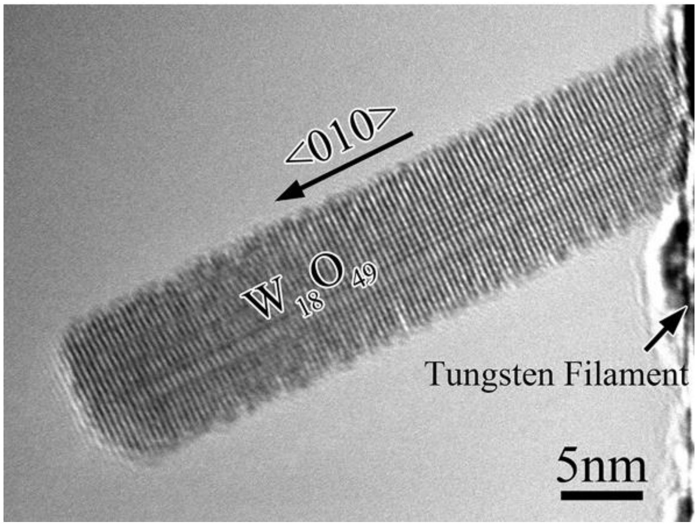

Figure.I.6- HRTEM micrograph showing the growth of a catalyst-free Tungsten-Oxide nanowire in a Vapor-Solid style from a W-filament [43].

I.2.2.4 SOLID-LIQUID-SOLID (SLS)

From an application point of view, the integration of vertical (out-of-plane) NWs grown by VLS into 2D planar devices is an essential difficulty. A formidable challenge is to manipulate and assemble vertical NWs into a 2D layout for large-scale integrations of NW-based devices. The In-Plane Solid-Liquid-Solid (IPSLS) mechanism, discovered by Cabarrocas and Yu [44], is a BU approach that could represent an ultimate solution for the fabrication of NW-based planar devices. It provides new opportunities to design and exploit novel in-plane NW-based applications. IPSLS can be perceived as a nano-liquid-phase-epitaxy [45] process or a nanoscaled metal induced crystallization [46]. The SLS is a three-step process: 1) the formation of metal nanoparticles (NPs) such as: In, Sn on an Indium-Tin-Oxide substrate for example (Fig.I.7.a). 2) An amorphous layer of SC material (i.e. Si, Ge) is deposited on top (Fig.I.7.b). 3) The temperature of the substrate is raised sufficiently to activate the lateral growth of NWs while maintaining the system in a reactive-gas-free environment (see Fig.I.7.c.d).

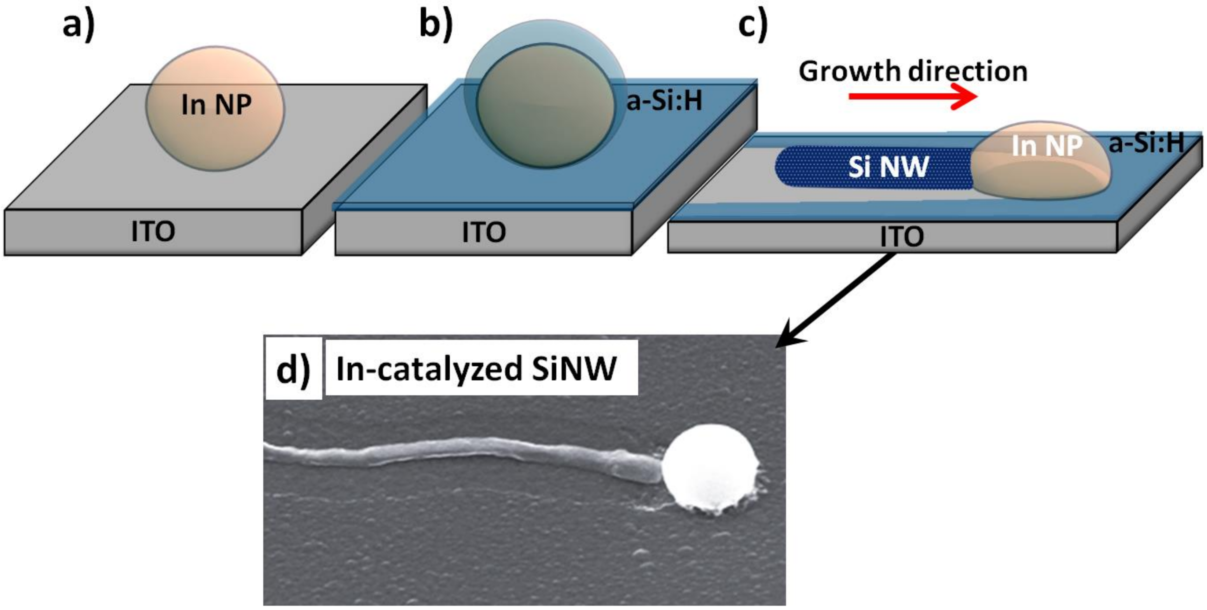

Figure.I.7- The SLS mechanism. a) In nanoparticles are formed by chemical reduction of ITO using a H_2 plasma. b) an amorphous Si layer is deposited on top of the system. c) the temperature of the substrate is raised sufficiently to activate the growth of IPSLS Si NWs. d) SEM image showing an IPSLS-SiNW catalyzed by an In droplet [47].

I.3 PRINCIPLES OF SLS: SATURATION, NUCLEATION AND DRIVING FORCE

To control the size, morphology, structure, and growth path of NWs, it is crucial to understand this nanoscale crystallization process. After the formation of catalyst NPs, a thin film of, for example, hydrogenated amorphous Silicon (a-Si:H) is deposited on top. The temperature is raised to melt the NPs which by themselves start to dissolve and absorb Si atoms from the solid-state precursor (a-Si:H). The concentration of Si in the catalyst NPs starts to increase, forming a catalyst – Si alloy NP similarly to the VLS process, leading to a supersaturation state. Thermodynamically, increasing the concentration corresponds to an increase in the chemical potential of the absorbed species in the catalyst. Therefore, a heterogeneous nucleation will occur when accommodating more Si is no longer energetically favorable. The newly-formed crystal embryo must remain stable long enough for the growth to occur. For simplification, we assimilate the crystal nucleus to a droplet shape with a given radius. The stability of this nucleus-embryo is related to its critical radius r^* [48]:

$$r^* = \frac{2\gamma}{\Delta G} \qquad (1)$$

Where γ the interfacial free energy of the nucleus in the ambient phase, ΔG is the Gibbs energy difference between Si atoms in the catalyst and Si atoms in the crystal. ΔG^* is the energy used to atomically assemble the nucleus. After exceeding the critical size, the tendency of nuclei to grow will persist (see Fig.I.8).

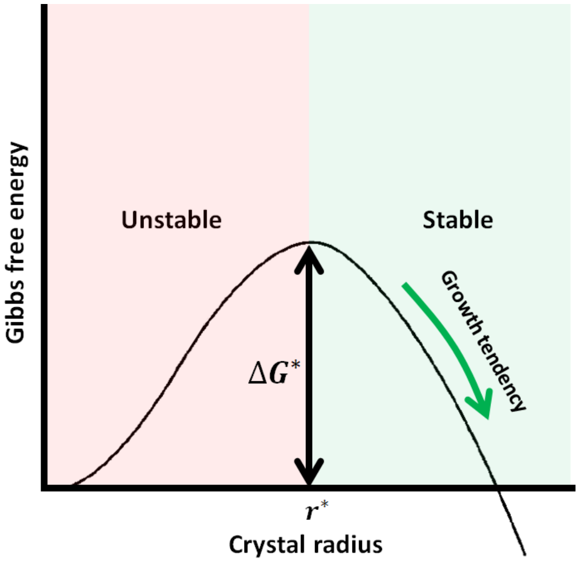

Figure.I.8- Schematic illustration showing the energetic stability of a crystal nucleus as a function of its size. In the unstable side ($r < r^*$), the nucleus risks decaying if its size remains less than the critical value r^* for a certain period of time. When $r = r^*$, the energy barrier reaches its peak ΔG^*. Beyond this value ($r > r^*$), the growth of the nucleus reduces the Gibbs energy of the system. Thermodynamically, the growth of this nucleus is allowed.

The most favorable site for the nucleation for both VLS [49] and SLS [47] mechanisms is at the TPB line, for instance in Fig.I.9, Si crystal-seeds are formed at the region where once was the TPB line during the initial stage of the growth.

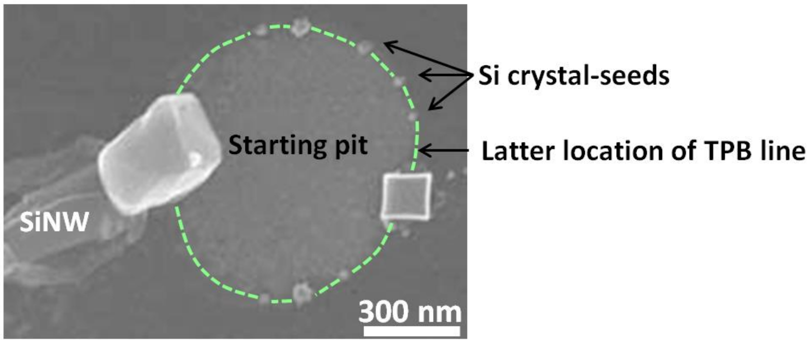

Figure.I.9- SEM image of the starting point of a nanowire (depicted by a light-green dashed line), it is the initial location of the catalyst. Si-nuclei are formed at the original TPB line during the early stage of nucleation [47].

Many nuclei can form at the bottom edge of the catalyst, but the biggest one having the lowest surface-to-volume ratio (thus, lowest Gibbs energy) is the most favorable sink for the incoming Si atoms [47]. Therefore, the biggest crystal seed grows faster than the other ones which might decay (or dissolve). Nuclei growth process can follow three types of atomic assembly [50-52]: 3-dimensional island growth (Volmer-Weber), layer-by-layer growth (Frank-van-der Merwe), and 3D islands on top of one or few epitaxial layers (Stranski-Krastanov). For the case of catalyst-assisted nanowires, in-situ observations have shown that the growth is done in a layer-by-layer fashion [53].

The initial dynamic process of the IPSLS growth is established as soon as an absorption (catalyst/a-Si:H) and deposition (c-Si/catalyst) edges appear. The Gibbs energy difference between the a-Si:H (E_a) and c-Si (E_c) is $\Delta E_{ac} = E_a - E_c \sim 0.12 - 0.15\ eV$ [54, 55]. The concentration of the dissolved Si at the absorption interface is higher than at the deposition interface. The mass transport of the dissolved Si atoms is driven by the concentration gradient across the catalyst. The absorption interface region has a higher concentration of Si atoms, which create a diffusive mass flux (J_{Si}) towards lower concentration regions inside the catalyst (near the c-Si/catalyst interface), as depicted in Fig.I.10.a. As a consequence, the absorbed-Si atoms are transported to the rear-side of the NP to grow the nanowire. The dragging of the catalyst to dissolve more a-Si:H is derived from the chemical potential difference between the front absorption edge and the back deposition edge ΔE_{ac}. Considering that the dissolution of silicon atoms from the amorphous precursor layer is a quick step, then the absorption flux rate (J_{in}) into the catalyst NP is then determined by the diffusion transport flux (J_{Si}) [47]:

$$J_{in} = J_{Si} = \frac{D_S}{L_c}(C_{eq}^{a} - C_{Si}) \qquad (2)$$

Where L_c the diameter of the catalyst NP, D_S the diffusion coefficient of Si atoms in the catalyst, $C_{eq}^{a} = C_{eq}^{c}.e^{\Delta E_{ac}/kT}$ is the equilibrium concentration of dissolved Si atoms at the absorption interface (catalyst/a-Si:H), C_{eq}^{c} is the equilibrium concentration of Si atoms near the crystalline interface, and C_{Si} is the Si concentration at the c-Si/catalyst interface. The concentration difference across the In catalyst is ΔC_{Si}. To obtain a growth rate of 10^2 nm/s, $\Delta C_{Si}/C_{eq}^{c}$ should be less than 2% (at growth temperatures between 400℃ - 500℃). For this reason, C_{Si} can be considered to be very close to C_{eq}^{a}.

The dissolved Si atoms build the NWs by forming two-dimensional nucleation centers, and then new monolayers are completed by a lateral growth of these nucleation centers. This process is repeated layer-by-layer to grow the entire NW. The atomic formation process of SiNW is described by theoretical frameworks [56, 57]. The deposition flux rate (J_{out}) can be described by the nucleation rate theory in VLS [57]:

$$J_{out} \sim G_{nc}^{-1/2} . e^{-G_{nc}/kT} \qquad (3)$$

Where G_{nc} is the nucleation barrier for the formation of 2D nucleation centers on the SiNW end, T is the temperature, and k is the Boltzmann constant.

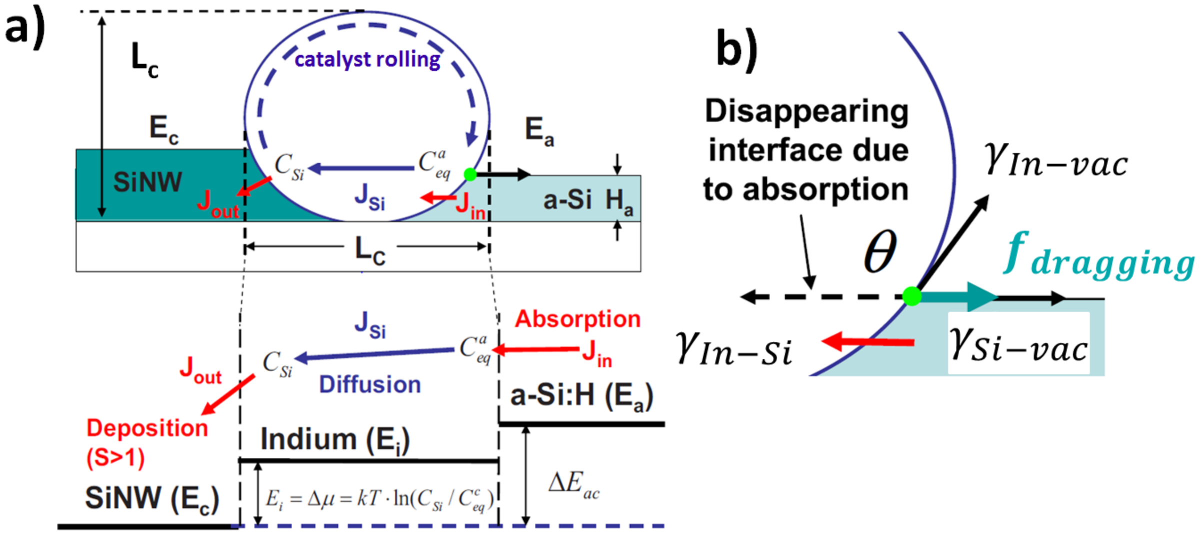

Figure.I.10- Schematic illustration for the absorption, diffusion, and deposition steps involved in the growth of lateral SiNW via IPSLS mechanism [44, 47]. a) E_a, E_c, and E_i denote the Gibbs energy of Si atoms in the amorphous, crystalline (considered as a reference), and dissolved in In catalyst drop, respectively; C_{Si} is the dissolved Si atom concentration in the catalyst drop; J_{in}, J_{out}, and J_{Si} are the absorption, deposition, and mass transport diffusion flux rates of Si atoms. The catalyst, having a diameter of L_c, is rolling (as depicted by the circular arrow inside the catalyst) towards the a-Si:H with a thickness of H_a. b) Illustration of the imbalanced TPB line due to the continuous absorption of Si atoms (depicted by a red arrow) from the a-Si:H precursor. γ_{In-Si}, γ_{In-vac}, and γ_{Si-vac} are the surface tensions of Indium catalyst/a-Si:H, Indium catalyst/ vacuum, and a-Si:H/vacuum respectively. $f_{dragging}$ is the dragging force driving the catalyst.

The dynamics of the SLS mechanism is a direct effect of the Gibbs energy difference between the two edges of the catalyst. Moments before the appearance of a dragging force, the tensions between In/vacuum (γ_{In-vac},), In/a-Si:H (γ_{In-Si}), and a-Si:H/vacuum (γ_{Si-vac}) are balanced in the horizontal direction (by projecting each component to an horizontal-axis):

$$\gamma_{In-Si} = \gamma_{Si-vac} - \gamma_{In-vac} \times cos\theta \qquad (4)$$

The catalyst/a-Si:H interface tension (γ_{In-Si}) is weakened by the dissolution and absorption of Si atoms. Consequently, the balance between the tensions is broken (as shown in Fig.I.10.b): $\gamma_{In-Si} < \gamma_{Si-vac} - \gamma_{In-vac} \times cos\theta$. The system seeks to re-establish the balance again by dragging forward the TPB line (in other terms the catalyst is dragged) and forms a new In/a-Si:H interface. Knowing that the absorption is continuous, the tensions balance will be broken again and repeatedly; thus; the dragging force will be repeatedly exerted on the TPB line. Since the catalyst is subjected to a friction at its bottom contact compared to its top, a rolling forward movement might be a possibility (as shown in Fig.I.10.a by a circular dashed arrow).

It is worth mentioning that this kind of in-plane nanowires is not only achieved using SLS mechanism. Indeed, by using different catalytic metals, such as Pb (lead), it is possible to grow in-plane VLS NWs [58]. The Pb NPs get supplied by Si atoms from a SiH_4 (Silane) plasma. At the same time and during the growth, a hydrogenated amorphous Silicon (a-Si:H) layer is deposited around and on top of the catalyst. These in-plane VLS SiNWs catalyzed by Pb NPs have no depletion (trench) of a-Si:H layer (Fig.I.11.b) compared to SLS SiNWs catalyzed by Indium (In) NPs (Fig.I.11.a). In other terms, it means that the catalyst did not consume (apparently) Si from the a-Si:H layer but from the SiH_4 plasma. This observation does not exclude the possibility that the a-Si:H is weakly thinned and used for the growth. This kind of growth might be a combination of VLS and SLS.

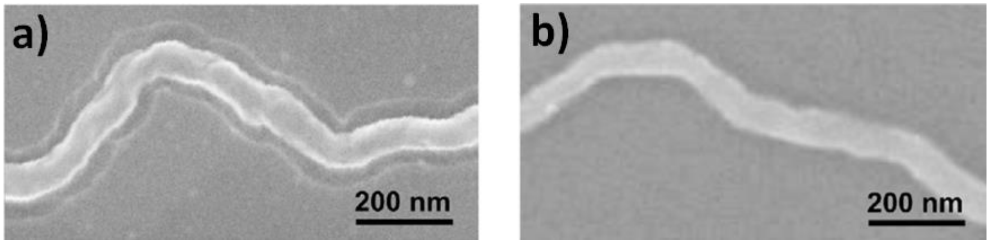

Figure.I.11- SEM micrographs of in-plane SiNWs catalyzed by a) In NP in SLS mode, and b) Pb NP in VLS mode [58].

The description of the IPSLS mechanism was done for SiNWs. The theory is well-elaborated and explained specially for SiNWs catalyzed by Indium droplets. However, this work was not extended for Ge or GeSnNWs. This will be the subject of this thesis, and it will be elaborated more in the following sections.

I.4 GERMANIUM – TIN ALLOY

It has been a few decades that Si nanoelectronics have been developed. However, the performance of Si ultra-large-scale integrated circuits (ICs) has only improved by increasing the number of elementary components (i.e. transistors, diodes) in the devices by shrinking their size. As we approach the limit of Moore’s law, with further decreasing of the components size (< 10 nm) [59], quantum tunneling and other related quantum effects will be inevitable. From this point, the necessity to develop novel materials with an increased performance rises. The crystalline Si properties such as the low carrier mobility and the indirect band-gap [60] limit further improvements in Si-based electronics and optoelectronics.

As a viable alternative to Si, the group IV compound Germanium-Tin ($Ge_{1-x}Sn_x$) is a unique class of semiconductor offering adjustable electrical and optical properties as a function of Sn concentration. The GeSn is a metastable alloy since the solubility of Sn in Ge is less than 1 at.% at the temperatures used for fabrication (Fig.I.12.a). The incorporation of Sn affects the electronic band structure of the system. For instance, in the $Ge_{1-x}Sn_x$ alloy, the direct Γ-valley decreases faster than the indirect valley (L) in the conduction band (at k = 0) with the increase of Sn incorporation. The energy difference between Γ and L valleys in c-Ge is $\Delta E = 0.14$ eV, as schematically shown Fig.I.12.b. When the Γ-valley is lower than L-valley the material becomes a direct gap [61], see for instance Fig.I.12.c. By using the non-local empirical pseudopotential method [62], it has been reported that the required Sn concentration to transform Ge into a direct gap semiconductor is above 6 %, although some contradiction regarding this value exist [63-65]. However, to achieve experimentally such concentration, several fundamental obstacles have to be solved: i) the solubility of Sn in Ge is only 1% at temperatures below 500°C [66] , ii) there is a strong Sn segregation behavior [67] and iii) the larger size of Sn compared to Ge [68] which can degrade the Ge lattice.

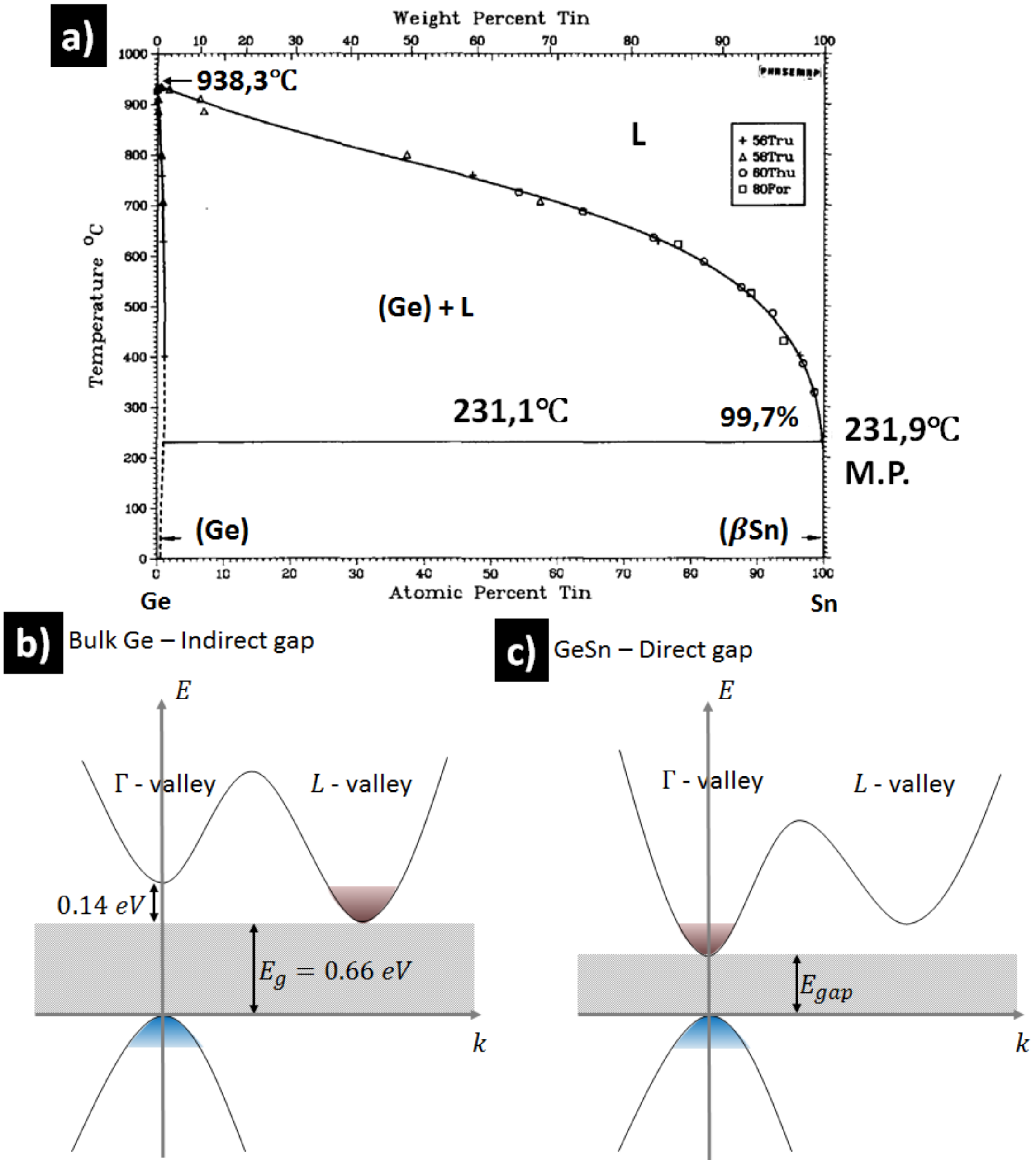

Figure.I.12. Ge and $Ge_{1-x}Sn_x$ energy band diagrams a) the Ge-Sn phase diagram (adapted from ref [69]) b) At the Brillouin zone of intrinsic Ge, the lowest conduction state is located in L-valley, whereas the highest valence state is in Γ-valley (at k = 0). An offset of 0.14 eV splits the Γ and L-valleys. In bulk-Ge, the indirect bandgap energy is $E_g = 0.66$ eV (at room temperature). c) The electronic band structure changes upon incorporation of Sn. Adding Sn, to the diamond cubic phase c-Ge nanowire, lowers the Γ-valley faster than L-valley. It is expected that a Sn content above 6% in the Ge will cause the indirect-to-direct gap transition.

This alloy presents many convenient properties such as: 1) high carrier mobility compared to Si and Ge individually [70-72], and can be further improved by increasing the Sn content, 2) tunable bandgap [73], 3) direct bandgap transition for a sufficiently high Sn content [74], 4) low thermal budget required to grow a GeSn alloy, due to its low eutectic point (231.1℃) [70], and 5) strain engineering as a stressor for strained Ge [75]. The $Ge_{1-x}Sn_x$ is very suitable as a channel material for high speed and low power consumption transistors (see Figure.I.13.), such as: Thin-Film Transistors (TFTs), Metal-Oxide-Semiconductor Field-Effect-Transistors (MOSFETs), Tunnel-FETs, FinFET [76], and Multi-Quantum-Well (MQW) LEDs [77].

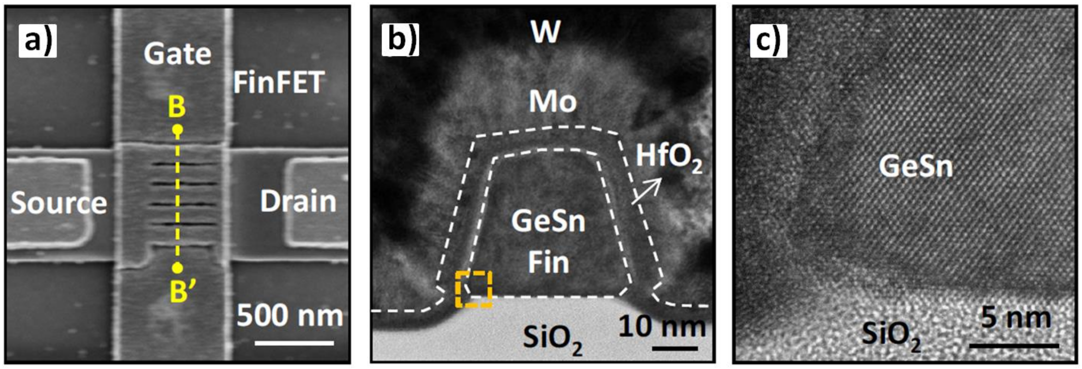

Figure.I.13- GeSn-based FinFET [76]. a) SEM tilted-view of the transistor. b) cross-section TEM image along BB' (the yellow dashed-line) showing the GeSn FinFET with fin width $W_{fin} = 30\ nm.$ c) HRTEM image showing the crystallinity of the GeSn-fin on SiO_2 with a smooth sidewall.

Moreover, this alloy has significantly increased the interest of the research and industrial communities due to its potential high performance in photonic and optoelectronic applications.

To tailor the GeSn properties, it is necessary to control the Sn concentration in the alloy. Two main bandgap engineering approaches have been developed to transform Ge into a direct bandgap semiconductor: tensile strain [78] and Sn alloying [79]. In this thesis, Sn alloying will be further developed. Two main configurations of GeSn alloys exist: i) thin-film, and ii) nanowires.

I.4.1 THIN-FILM CONFIGURATION

Extensive efforts have been done to break the barrier of the Sn equilibrium concentration without degrading the crystalline quality of GeSn alloys. The precipitation is a serious problem to achieve an effective Sn content in a homogeneous high-quality $Ge_{1-x}Sn_x$ layer. During the GeSn crystal growth and post-growth processes (such as thermal-processing), precipitation of Sn can occur. In addition, the oxidation of the GeSn alloy is shown to enhance the segregation of Sn near the surface of the structure [80]. Surface roughness has been witnessed for $Ge_{1-x}Sn_x$ epitaxy layers grown in a chemical vapor deposition (CVD) reactor [81], knowing that the temperature used for the CVD growth was between 300℃ and 350℃. Respectively, Sn precipitates are often observed at high growth temperatures (such as 400℃) that are used for Ge epitaxy. Numerous studies have proven that the substrate temperature is the key to obtain high quality GeSn layers. To avoid Sn precipitation, low-temperature growth (< 231.1℃) should be used. Recently, a successful metastable GeSn thin film has been grown with relatively high Sn content (~ 18% at. Sn) using molecular beam epitaxy (MBE) at 140°C but failed in suppressing the phase separation tendency [82], as shown in Fig.I.14. Meanwhile other groups have succeeded to maintain good crystal structure in thin films with lower Sn concentrations (~ 12% at. Sn) [83].

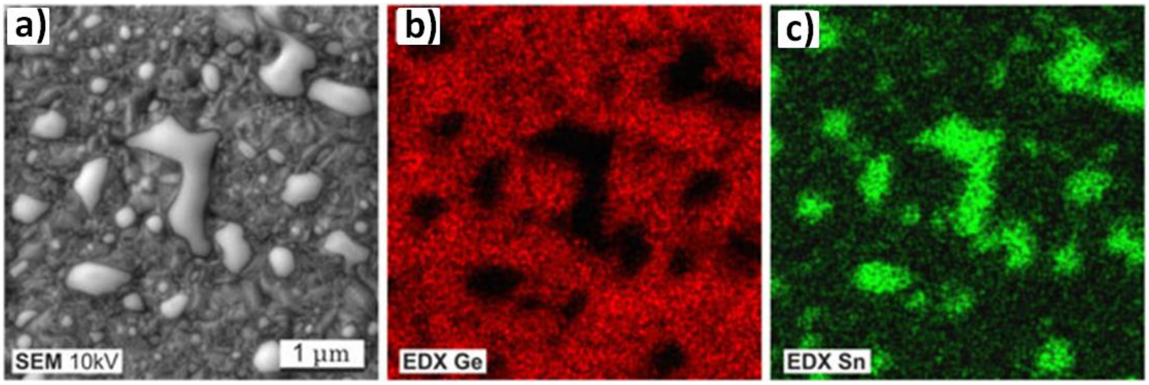

Figure.I.14. SEM and EDX results of a 200-nm thick GeSn layer with approximately 18 at.% Sn concentration. a) SEM top-view with the corresponding Energy Dispersive X-ray Spectroscopy (EDX) b) Ge, and c) Sn [82].

The abovementioned methods provide a good control of Sn incorporation, and allow creating thin-film heterostructures with sharp interfaces. Nonetheless, the elaboration of 2D films leads to a large number of misfit dislocations in the GeSn structure due to a large lattice mismatch between GeSn and the underlying Si substrate (> 4.2 %) [84]. To avoid such defects, other solutions have been developed, for example: GeSn film on insulator [85, 86], and growth of GeSn NWs using bottom-up approaches [87, 88].

I.4.2 NANOWIRE CONFIGURATION

To keep on track with miniaturization of Si-based nanoelectronics and photonics, the nanowire configuration has also been investigated. This one-dimensional (1D) nanoform has an advantageous high surface-to-volume ratio which allows a better strain-relaxation as compared to bulk and thin film approaches [89]. On one hand, the top-down techniques used for fabricating a good quality; single crystalline, straight, and uniform diameter $Ge_{1-x}Sn_x$ nanowires with no Sn clustering are rather limited due to under-developed surface and etch chemistries. On the other hand, bottom-up paradigms allow associating kinetic effects during the dynamic process of $Ge_{1-x}Sn_x$ NWs growth, which can influence the incorporation of Sn in the system. Among the most popular growth techniques [90-92] (vapor-liquid-solid that is shown in Fig.I.15.a, vapor-solid-solid, and electrodeposition), the most effective for impurity incorporation is the growth under non-equilibrium conditions [93]. For instance, Au-catalyzed

Ge NWs grown by VLS mechanism reach ~3 - 4 at.% Sn [94] with plenty of structural defects (see Fig.I.15.c), and could reach ~ 10 at.% Sn [95]. Microwave-assisted solution-liquid-solid process allowed to reach ~ 12 at.% of Sn, but the NWs lack a good quality structure [96].

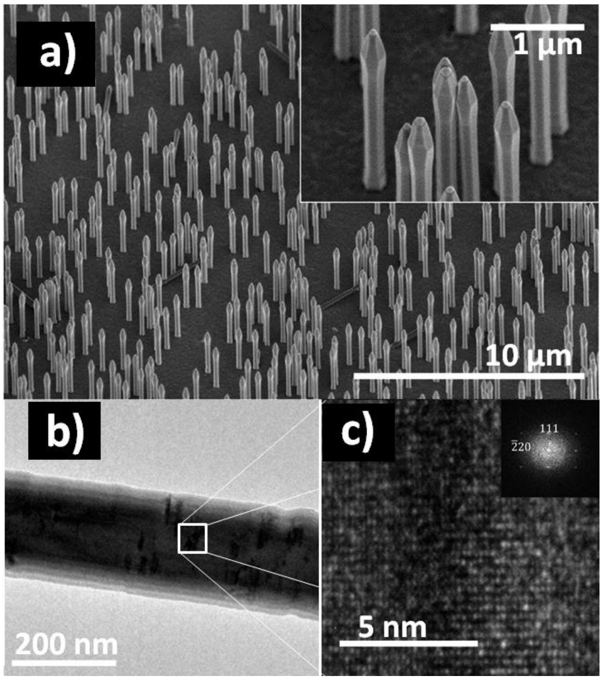

Figure.I.15. SEM and TEM micrographs of Ge-core/GeSn-shell NWs [94]. a) low magnification SEM and magnified inset of core-shell Ge/$Ge_{1-x}Sn_x$ NWs grown on Ge (111). b) low magnification TEM showing Sn-enriched coherent defect region in GeSn. c) $Ge_{1-x}Sn_x$ shell structural defects, taken from $[11\bar{2}]$ zone-axis HRTEM micrograph with Fast-Fourier Transform (FFT) inset.

I.4.3 CATALYST ATOM INCROPORATION

The immediate result of the direct contact between the liquid catalyst and the NW's growing interface is the impurity (catalyst atoms) incorporation. Formerly, it was thought that the impurity incorporation phenomenon is a deteriorating factor since it is unintentional [97] and sometimes nonuniform [98] leading to detrimental physical and chemical properties. For example, Au catalyst, which is the most commonly used material, is very deleterious to the electronic properties of c-Si [99]. It is also known that Au atoms act as recombination centers for photogenerated-carriers within SiNWs, which decrease the photovoltaic efficiency [100]. Structurally, a correlation was found between Au incorporation and the growth orientation of SiNWs [101], see Fig.I.16. Au atoms are trapped by the same types of defects more than others, depending on the interplay between surface energies. For these reasons, instead of Au, other types of catalysts have been used such as Al [102].

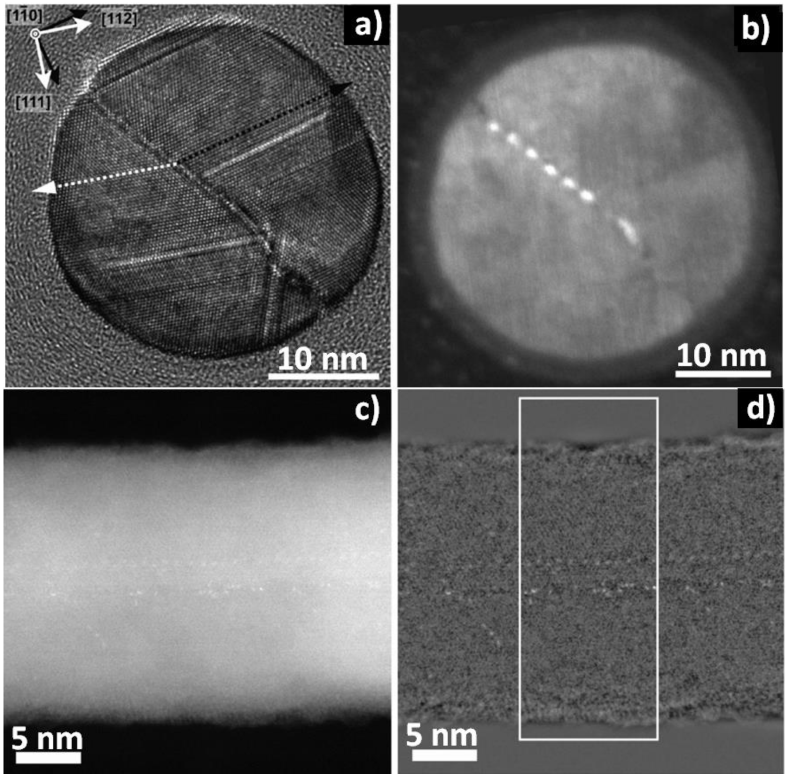

Figure.I.16. HRTEM and STEM micrographs showing the incorporation of Au in structural defects in SiNWs [27, 103]. a) radial cross-section view in HRTEM of a <110> oriented SiNW with Au-decorated grain boundary, and b) STEM view. c) STEM unprocessed image axial-view of Au atoms line in a SiNW, and d) HRTEM filtered image of the same SiNW tilted 15° about its growth axis.

An intriguing question was raised about the nature of Au incorporation [104]: what is the possible mechanism of incorporation if Au atoms can be trapped even without defects in c-SiNWs? The suggested answer was that the growth has been done under non-equilibrium conditions which lead to a kinetic impurity trapping. From this point-of-view, broad studies on this framework have been started. The essential idea was to achieve a precise control of impurities incorporation (dopants, i.e. P, B; or catalyst atoms, i.e. In, Sn) during the growth of

NWs, which will enable a novel and efficient route to functional NWs in direct technological implications. Incorporation of a suitable amount of dopant or catalyst atoms into NWs can render desirable modifications in their physical (or chemical) properties. The availability of many types of catalysts gives flexibility in fabricating NWs with different enhanced-properties. For instance, p-type doping can be achieved if the Ga catalyst gets injected into group-IV NWs [105], whereas n-type doping is achieved by using Bi catalyst [106].

I.4.3.1 FOR VERTICAL SILICON NWS

The VLS enables an in-situ impurity doping through the metal catalyst [107], and allows the formation of complex axial and radial heterostructures [108, 109]. Also, catalyst atoms were found to be homogeneously distributed throughout the NW's body rather than trapped by defects, see for instance Fig.I.17. For this reason, incorporation studies were initiated for VLS-grown NWs in 2008, namely for Au-catalyzed SiNWs [27]. An interesting finding was the incorporation of Au throughout a defect-free NW structure, so the defect-related trapping is ruled out. Here other explanations started to be developed to understand the presence of catalyst atoms in the bulk of the NW structure. One of them is that the solidus, in the Au-Si phase diagram, might shift towards higher Au concentration in the NW because of the supersaturated Au-Si liquid catalyst which makes the growth a non-equilibrium process. At this nanoscale-operation, the bulk equilibrium phase diagram cannot predict the composition neither for the catalyst nor for the NW during the non-equilibrium growth and after it. Same analogy was applied to GeNWs where a kinetic-dependent behavior was predicted to be responsible for the excessive impurity injection from the catalyst tip [95, 110]. The possibility of catalyst atoms incorporation through the NW sidewalls due to homoepitaxy by Vapor-Solid growth was also investigated, and proven to be negligible [95].

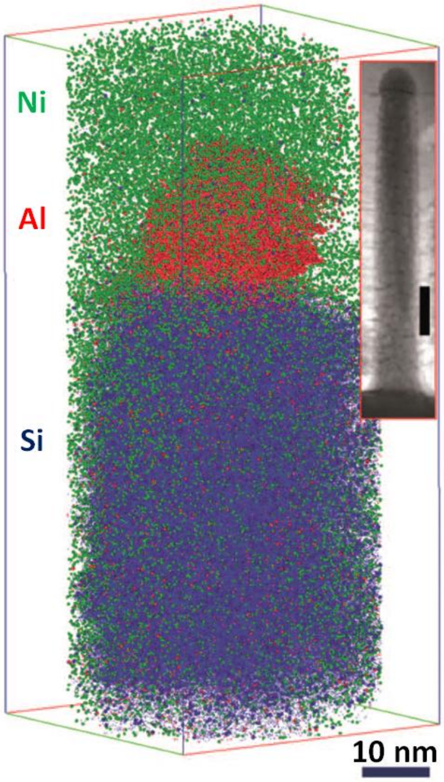

Figure.I.17. Three-dimensional APT atom-by-atom map (each point is an atom represented in the real 3-Dimensional space) showing the incorporation of Al atoms homogeneously in a SiNW grown at 410℃. The nickel serves as a protection layer from ion etching operations. Only a limited number of atoms is displayed for clarity reason (2.5×10^4 atoms of each element). Inset, a cross-sectional TEM image of an identical Si nanowire (scale bar, 40 nm), adapted from [93].

The main model used to describe the nanowires growth is based on the step flow kinetics [49, 93, 95]. In this regime, the growth is attributed to the progressive addition of atomic monolayers at the solid side of the NW/catalyst interface. The interface advances by the lateral flow of atomic steps (Fig. I.18). Consequently, the interface velocity, v_{int} (perpendicular to the interface) is proportional to the step velocity v_{step} and inversely proportional to the incubation time (which is the time for supersaturation and nucleation). Catalyst atoms adsorbed at the interface have a limited time τ_e (escape time) to diffuse back to the liquid catalyst. If the adsorbed atoms do not escape to the liquid before τ_e expires, they will be permanently incorporated at the growing solid surface.

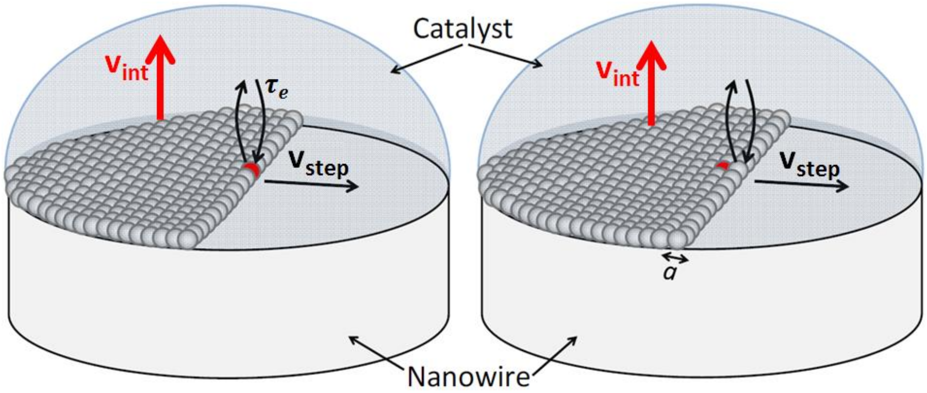

Figure.I.18. A simple schematic illustration of step growth (Supplementary information of ref. [93]). Left schema: the impurity (red atom) at the step edge can jump between the two sides of the interface during $\tau_e = a/v_{step}$ (“a” is the width of one atomic row, v_{step} is the step velocity) which is the time needed for an atomic row completion. Right schema: the impurity becomes trapped in the layer after the growth of the next row of atoms, that means when τ_e expires.

The partition coefficient, k, is commonly used to quantify the shift of solubility boundaries of the incorporated solute atoms (at the solid interface). It represents the composition ratio of the solute (catalyst atoms which are considered as impurity atoms) in the solid (NW), $C_{impurity}^{solid}$, and in the melt at the NW/catalyst interface,$C_{impurity}^{liquid}$:

$$k = C_{impurity}^{solid}/C_{impurity}^{liquid}$$

This model (step-flow) treats the case in which an atomically smooth, sharp interface advances by the periodic lateral passage of monolayer steps (as shown in Fig.I.18). The passage of a step results in the incorporation of any solute atoms into the layer. Solute diffuses back into the liquid during the period before the passage of the next step, at which point any remaining solute is assumed to be permanently trapped into the solid. The predicted velocity-dependence of k for this mechanism is [111]:

$$k(v) = k_e + (1 - k_e)\exp(-v_D/v_{int})$$

Where k_e is the equilibrium composition of the solute in the solid, $v_D = D/a$ is the diffusive velocity with D the interdiffusion coefficient across the interface and “a” is the width of one atomic row. k undergoes a strong deviation towards higher values from the classical solubility limit upon a growth rate of few m/s (as shown in Fig.I.19) [111]. The rapid progression of the NW/catalyst interface traps the solute atoms escaping from the solid side of this interface, which diffuse slower than the moving interface; this phenomenon is known as the “solute trapping” [112].

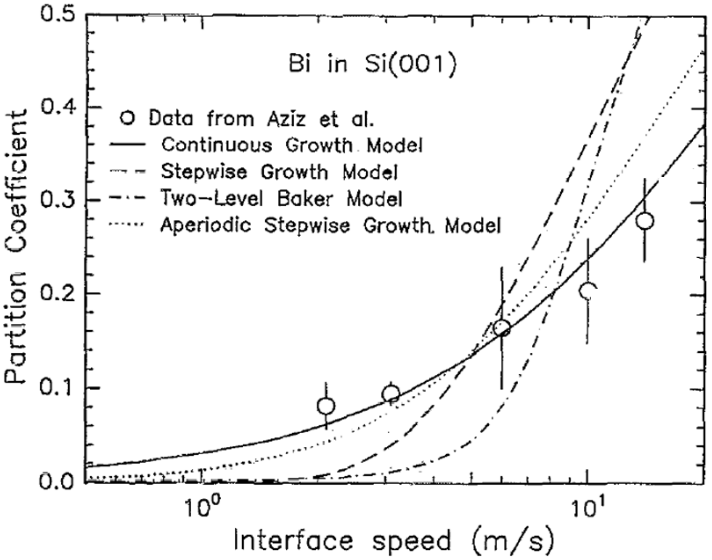

Figure.I.19. Interface velocity dependence of the partition coefficient for Bismuth in Si (001) [111]. Various models predict the increase of the partition coefficient among the increase of the growth interface velocity. The data points (Aziz et al.) are from ref. [113].

A more advanced and recent study (Moutanabbir et al. 2013 [93]) went deep into the atomistic procedure of Al-catalyzed SiNWs grown by VLS mechanism. A colossal incorporation of Al atoms into VLS-grown SiNWs has been achieved by Moutanabbir et al., with a concentration two orders of magnitude higher than their equilibrium solubility [93]. They wrote that the above-elucidated model describes the incorporation for bulk systems, and thereby cannot be used for NWs. The reason behind is the delay of formation of two successive Si-bilayers. There is an incubation time needed for nucleation which accounts for slowing down the interface velocity, and therefore minimizing the trapping-effect. Assuming that the step-growth is aperiodic, they have established an expression taking into consideration the step velocity and the bilayer formation time τ_{BL}. Despite inserting the NWs growth-characteristic parameters, they could not totally explain the reasons behind this incorporation.

However, they believed that there are two main parameters influencing the catalyst injection: i) the Gibbs free energy of the liquid at an equilibrium composition, and ii) the characteristic supersaturation. The incorporation of catalyst atoms is still an open debate, but it is clearly related to growth kinetics.

I.4.3.2 FOR IN-PLANE SILICON NWS

Discussions have also been done on the incorporation of catalyst atoms into NWs grown by the SLS mechanism [114]. In this study Chen et al. have made a comparison between the VLS and SLS growth modes using two different catalysts: In and Sn. Even though these are two distinctive mechanisms, it is interesting to validate that the incorporation process is kinetically-based. This idea can be tested by the SLS mechanism where growth rates are much higher (up to 100 nm.s^{-1} [44]) than in the VLS (1 - 10 nm.s^{-1} [115]). Therefore, one would expect a higher incorporation in SLS compared to VLS. The main reason behind these huge growth rates relies in the direct contact between the catalyst and the amorphous feeding layer (a-Si:H in this case). The growth rate effect was proved by Atom Probe Tomography (APT, for details see chap II), as shown in Fig.I.20. As predicted, the SLS mechanism does lead to a higher concentration of catalyst atoms into NWs compared to VLS, for both used catalysts In and Sn.

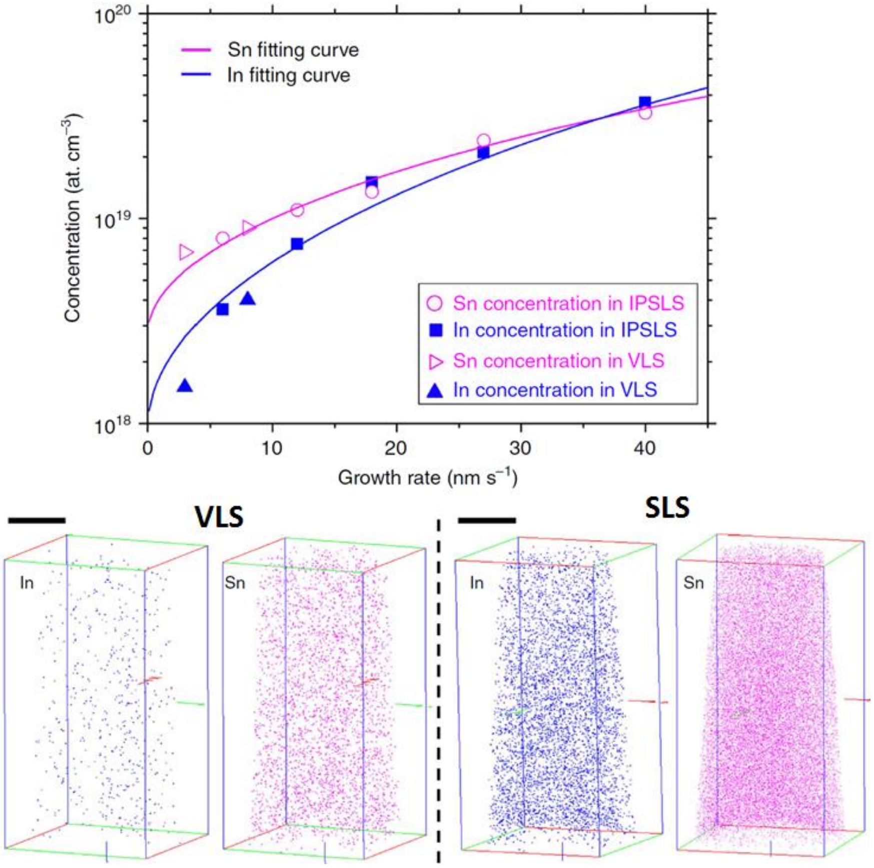

Figure.I.20. Dependence of impurity concentration on SiNW growth rate. The experimental data show an increase in impurity (In and Sn) concentration upon the increase of SiNWs growth rate. The fitting curve is derived from the dimer-insertion model developed by Chen et al. [114]. The three-dimensional APT reconstructions show the catalyst atoms distribution in SiNWs grown by VLS on the left, SLS on the right. In and Sn atoms are represented by blue and pink colors, respectively. Scale bar in the reconstruction volume, 20 nm.

Chen et al. have found, experimentally, that impurities are first incorporated in a homogeneous way into the NW and then redistributed (segregated) to nearby defects. With the introduction of impurity dimers (Si-Sn) or (Si-In) into a NW during the nucleation process, a distortion in the NW’s crystalline structure is created due to the atomic radius of the impurities (bigger than Si [116]). This distortion (stress-field) can be relaxed by the segregation of the incorporated In and Sn towards structural defects, as shown in Fig.I.21.

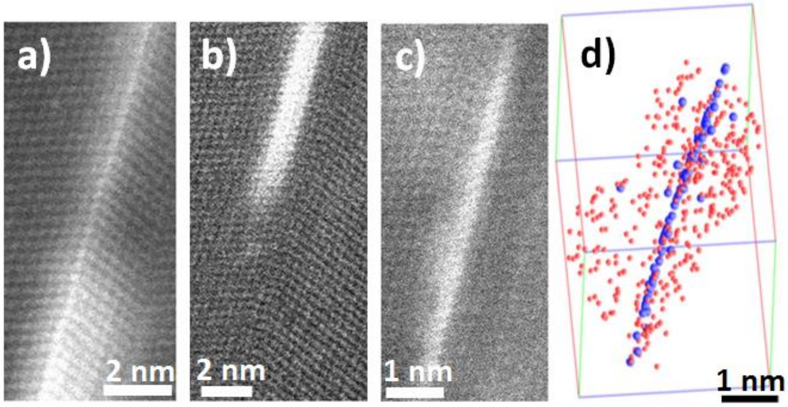

Figure.I.21. STEM images of SiNW synthesized via SLS mechanism. (a)-(b) High-magnified view of a SiNW with a twin plane decorated by In or Sn (or both) atoms. The SiNW growth direction is <211>. Correlation of (c) STEM and (d) APT results showing that the segregation at the twin plane is due to In atoms. Only 20 at.% of Si atoms are represented for clarity.

Based on this finding, they have introduced the notion of dimer-atom-insertion kinetic model to explain the high incorporation rate. The growth of SiNWs is due to a successive addition of bilayers of Si dimers (Si-Si) and impurity dimers (Si-In and Si-Sn). A dimer is an assembly of two atoms that can be identical (homodimer) or different (heterodimer). The impurity concentration C_i in SiNWs can be deduced from the ratio between incorporation rate of impurity dimers and Si dimers:

$$C_i = \frac{v_{Si-i}}{(v_{Si-Si} + v_{Si-i})}$$

Where v_{Si-i} and v_{Si-Si} are the incorporation rates of impurity dimers and Si dimers, respectively. The incorporation rate of Si dimers depends mainly on the Gibbs energy difference ($\Delta E = E_l - E_{Si-Si}$) between the dissolved state of Si atoms in droplet ($E_l = kTln[\frac{C_{Si}}{C_{eq}}]$) and the Si-Si dimer nucleation energy (E_{Si-Si}). The same analogy can be applied for the incorporation rate of impurity dimers; $\Delta E' = E_l - E_{Si-i}$. This model seemed to be consistent with experimental results, as indicated by the fitting curve in Fig.I.20.

I.5 SUMMARY

Extensive efforts have been paid to improve the performance of Si-based technologies, but this material lacks adequate physical properties for further enhancement. As a result, the new quest for researchers was finding a new material with better properties than Si, and can be integrated on Si. One of the most recent developed materials was the $Ge_{1-x}Sn_x$ alloy, which is an interesting material for microelectronics and optoelectronics. The carrier mobility is improved by the increment of Sn concentration in Ge, and an indirect-to-direct transition of the energy band-gap occurs for a sufficient amount of Sn (between 6 at.% and 11 at.%). The nanowire configuration allows decreasing more the devices size, keeping on the track of miniaturization. With the ability of controlling their properties, and guiding them to assemble a certain circuitry design, the IPSLS NWs are now the center of interest of many research laboratories. Broad and comprehensible studies have been conducted on IPSLS SiNWs, is it possible to do the same for GeSn NWs? In the next chapter (II), the machines used to grow and characterize Ge and GeSn NWs will be elaborated.

I.6 REFERENCES

1. J. Appenzeller, J.K., M. T. Bjork, H. Riel, H. Schmid, W. Riess, *Toward Nanowire Electronics.* IEEE Transactions on Electron Devices, 2008. **55**(11): p. 2827-2845.
2. Fu-Liang, Y.D.-H., Lee Hou-Yu, Chen Chang-Yun, Chang Sheng-Da, Liu Cheng-Chuan, Huang Tang-Xuan, Chung Hung-Wei, Chen Chien-Chao, Huang Yi-Hsuan, Liu Chung-Cheng, Wu Chi-Chun, Chen Shih-Chang, Chen Ying-Tsung, Chen Ying-Ho, Chen Chih-Jian, Chen Bor. *5nm-gate nanowire FinFET.* in *Digest of Technical Papers. Symposium on VLSI Technology*. 2004.
3. Pauzauskie, P.J.Y., Peidong, *Nanowire photonics.* Materials Today, 2006. **9**(10): p. 36-45.
4. Zhaoguo Xue, M.X., Xing Li, Jimmy Wang, Xiaofan Jiang, Xianlong Wei, Linwei Yu, Qing Chen, Junzhuan Wang, Jun Xu, Yi Shi, Kunji Chen, Pere Roca i Cabarrocas, *In-Plane Self-Turning and Twin Dynamics Renders Large Stretchability to Mono-Like Zigzag Silicon Nanowire Springs.* Advanced Functional Materials, 2016. **26**(29): p. 5352-5359.
5. Li Mingwei, B.R.B., Morrow Thomas J., Sioss James A., Lew Kok-Keong, Redwing Joan M., Keating Christine D., Mayer Theresa S., *Bottom-up assembly of large-area nanowire resonator arrays.* Nature Nanotechnology, 2008. **3**: p. 88.
6. Hochbaum Allon I., C.R., Delgado Raul Diaz, Liang Wenjie, Garnett Erik C., Najarian Mark, Majumdar Arun,Yang Peidong, *Enhanced thermoelectric performance of rough silicon nanowires.* Nature, 2008. **451**: p. 163.
7. Cui Yi, W.Q., Park Hongkun, Lieber Charles M., *Nanowire Nanosensors for Highly Sensitive and Selective Detection of Biological and Chemical Species.* Science, 2001. **293**(5533): p. 1289-1292.
8. Karam Chantal, G.C., Habchi Roland, Abboud Nadine, Khoury Antonio, Tingry Sophie, Miele Philippe, Utke Ivo, Bechelany Mikhael, *Urchin-inspired ZnO-TiO 2 core-shell as building blocks for dye sensitized solar cells*. Vol. 126. 2017.
9. Schröder Tim, T.M.E., Walsh Michael, Li Luozhou, Zheng Jiabao, Schukraft Marco, Sipahigil Alp, Evans Ruffin E., Sukachev Denis D., Nguyen Christian T., Pacheco Jose L., Camacho Ryan

M., Bielejec Edward S., Lukin Mikhail D., Englund Dirk, *Scalable focused ion beam creation of nearly lifetime-limited single quantum emitters in diamond nanostructures.* Nature Communications, 2017. **8**: p. 15376.

10. Maldonado Juan R., P., Martin, *X-ray lithography: Some history, current status and future prospects.* Microelectronic Engineering, 2016. **161**: p. 87-93.
11. Okazaki, S., *High resolution optical lithography or high throughput electron beam lithography: The technical struggle from the micro to the nano-fabrication evolution.* Microelectronic Engineering, 2015. **133**: p. 23-35.
12. Tafuri, F., Massarotti Davide, Galletti Luca, Stornaiuolo, Daniela Montemurro, Domenico Longobardi, Luigi Lucignano, Procolo Rotoli, Giacomo Pepe, Giovanni Piero Tagliacozzo, Arturo Lombardi, Floriana, *Recent Achievements on the Physics of High-T C Superconductor Josephson Junctions: Background, Perspectives and Inspiration.* Journal of Superconductivity and Novel Magnetism, 2013. **26**(1): p. 21-41.
13. Givargizov, E.I., *FUNDAMENTAL ASPECTS OF VLS GROWTH A2 - CULLEN, G.W*, in *Vapour Growth and Epitaxy*, E. Kaldis, R.L. Parker, and C.J.M. Rooymans, Editors. 1975, Elsevier. p. 20-30.
14. Kolasinski, K.W., *Catalytic growth of nanowires: Vapor–liquid–solid, vapor–solid–solid, solution–liquid–solid and solid–liquid–solid growth.* Current Opinion in Solid State and Materials Science, 2006. **10**(3): p. 182-191.
15. Yu Linwei, A.P.-J., Picardi, Gennaro, Roca i Cabarrocas, Pere, *An In-Plane Solid-Liquid-Solid Growth Mode for Self-Avoiding Lateral Silicon Nanowires.* Physical Review Letters, 2009. **102**(12): p. 125501.
16. Ambrosini, S., M. Fanetti, V. Grillo, A. Franciosi, S. Rubini, *Vapor-liquid-solid and vapor-solid growth of self-catalyzed GaAs nanowires.* AIP Advances, 2011. **1**(4): p. 042142.
17. Makhlouf, H., Karam Chantal, Lamouchi Amina, Tingry Sophie, Miele Philippe, Habchi Roland, Chtourou Radhouane, Bechelany Mikhael, *Analysis of ultraviolet photo-response of ZnO nanostructures prepared by electrodeposition and atomic layer deposition.* Applied Surface Science, 2018. **444**: p. 253-259.
18. R. S. Wagner, W.C.E., *VAPOR‐LIQUID‐SOLID MECHANISM OF SINGLE CRYSTAL GROWTH.* Applied Physics Letters, 1964. **4**(5): p. 89-90.
19. Brönstrup, G., C. Leiterer, N. Jahr, C. Gutsche, A. Lysov, I. Regolin, W. Prost, F. J. Tegude, W. Fritzsche, S. Christiansen, *A precise optical determination of nanoscale diameters of semiconductor nanowires.* Nanotechnology, 2011. **22**(38): p. 385201.
20. Zhang, Z., Lu Z., Chen P., Xu H., Guo Y., Liao Z., Shi S., Lu W., Zou J., *Size-dependent structural quality of InAs Nanowires Grown by Molecular Beam Epitaxy*
21. Westwater, J., Gosain D. P., Tomiya S. , Usui S. , Ruda H. , *Growth of silicon nanowires via gold/silane vapor–liquid–solid reaction.* Journal of Vacuum Science & Technology B: Microelectronics and Nanometer Structures Processing, Measurement, and Phenomena, 1997. **15**(3): p. 554-557.
22. Hofmann, S. and W.C.T. Sharma Renu, Cervantes-Sodi Felipe, Ducati Caterina, Kasama Takeshi, Dunin-Borkowski Rafal E., Drucker Jeff, Bennett Peter, Robertson John, *Ledge-flow-controlled catalyst interface dynamics during Si nanowire growth.* Nature Materials, 2008. **7**: p. 372.
23. Wu, Y., Yang Peidong, *Direct Observation of Vapor−Liquid−Solid Nanowire Growth.* Journal of the American Chemical Society, 2001. **123**(13): p. 3165-3166.
24. Yi Cui, L.J.L., Mark S. Gudiksen, Jianfang Wang, Charles M. Lieber, *Diameter-controlled synthesis of single-crystal silicon nanowires.* Applied Physics Letters, 2001. **78**(15): p. 2214-2216.
25. Kibum, K., Dong An Kim, Hyun-Seung Lee, Cheol-Joo Kim, Jee-Eun Yang, Moon-Ho Jo, *Low-Temperature Deterministic Growth of Ge Nanowires Using Cu Solid Catalysts.* Advanced Materials, 2008. **20**(24): p. 4684-4690.

26. Shruti, V.T., Ann F. Marshall, Paul C. McIntyre, *Kinetics of germanium nanowire growth by the vapor-solid-solid mechanism with a Ni-based catalyst.* APL Materials, 2013. **1**(6): p. 061101.
27. Allen, J.E., Hemesath, Eric R., Perea Daniel E., Lensch-Falk Jessica L., Li Z. Y., Yin Feng, Gass Mhairi H., Wang Peng, Bleloch Andrew L., Palmer Richard E., Lauhon Lincoln J., *High-resolution detection of Au catalyst atoms in Si nanowires.* Nature Nanotechnology, 2008. **3**: p. 168.
28. Clark Trevor E., N.P., Lew Kok-Keong, Pan Ling, Redwing Joan M., Dickey Elizabeth C., *Diameter Dependent Growth Rate and Interfacial Abruptness in Vapor–Liquid–Solid Si/Si1−xGex Heterostructure Nanowires.* Nano Letters, 2008. **8**(4): p. 1246-1252.
29. Li, N., Tan Teh Y., Gösele U., *Transition region width of nanowire hetero- and pn-junctions grown using vapor–liquid–solid processes.* Applied Physics A, 2008. **90**(4): p. 591-596.
30. Hannon, J.B., Kodambaka S., Ross F. M., Tromp R. M., *The influence of the surface migration of gold on the growth of silicon nanowires.* Nature, 2006. **440**: p. 69.
31. Samuelson, L., Thelander C., Björk M. T., Borgström M., Deppert K., Dick K. A., Hansen A. E., Mårtensson T., Panev N., Persson A. I., Seifert W., Sköld N., Larsson M. W., Wallenberg L. R., *Semiconductor nanowires for 0D and 1D physics and applications.* Physica E: Low-dimensional Systems and Nanostructures, 2004. **25**(2): p. 313-318.
32. Wen, C.-Y., Reuter M. C., Bruley J., Tersoff J., Kodambaka S., Stach E. A., Ross F. M., *Formation of Compositionally Abrupt Axial Heterojunctions in Silicon-Germanium Nanowires.* Science, 2009. **326**(5957): p. 1247-1250.
33. Wang, Y., Schmidt Volker, Senz Stephan, Gösele Ulrich, *Epitaxial growth of silicon nanowires using an aluminium catalyst.* Nature Nanotechnology, 2006. **1**: p. 186.
34. Bierman, M.J., Lau Y. K. Albert, Kvit Alexander V., Schmitt Andrew L., Jin Song, *Dislocation-Driven Nanowire Growth and Eshelby Twist.* Science, 2008. **320**(5879): p. 1060-1063.
35. Meng, F., Estruga Marc, Forticaux Audrey, Morin Stephen A., Wu Qiang, Hu Zheng, Jin Song, *Formation of Stacking Faults and the Screw Dislocation-Driven Growth: A Case Study of Aluminum Nitride Nanowires.* ACS Nano, 2013. **7**(12): p. 11369-11378.
36. Smith, A.M., Kast Matthew G., Nail Benjamin A., Aloni Shaul, Boettcher Shannon W., *A planar-defect-driven growth mechanism of oxygen deficient tungsten oxide nanowires.* Journal of Materials Chemistry A, 2014. **2**(17): p. 6121-6129.
37. Matt, L., Joshua Goldberger, Peidong Yang, *SEMICONDUCTOR NANOWIRES AND NANOTUBES.* Annual Review of Materials Research, 2004. **34**(1): p. 83-122.
38. Tokunaga, T. and T.K. Kawamoto Tadashi, Nakamura Naohiro, Hayashi Yasuhiko, Sasaki Katsuhiro, Kuroda Kotaro, Yamamoto Takahisa, *Growth and structure analysis of tungsten oxide nanorods using environmental TEM.* Nanoscale Research Letters, 2012. **7**(1): p. 85.
39. Lu, Z., Heng Xin, Chakraborty Anirban, Luo Cheng, *Growth of Ultra-Long ZnO Microtubes Using a Modified Vapor-Solid Setup.* Micromachines, 2014. **5**(4): p. 1069.
40. Yin, Y., Zhang G., Xia Y., *Synthesis and Characterization of MgO Nanowires Through a Vapor-Phase Precursor Method.* Advanced Functional Materials, 2002. **12**(4): p. 293-298.
41. Chueh, Y.L., Lai M.-W., Liang J.-Q., Chou L.-J., Wang Z. L., *Systematic Study of the Growth of Aligned Arrays of α-Fe2O3 and Fe3O4 Nanowires by a Vapor–Solid Process.* Advanced Functional Materials, 2006. **16**(17): p. 2243-2251.
42. Hsu, Y.-J., Lu Shih-Yuan, *Vapor−Solid Growth of Sn Nanowires: Growth Mechanism and Superconductivity.* The Journal of Physical Chemistry B, 2005. **109**(10): p. 4398-4403.
43. Chen, C.L., H. Mori, *In situ TEM observation of the growth and decomposition of monoclinic W 18 O 49 nanowires.* Nanotechnology, 2009. **20**(28): p. 285604.
44. Yu, L., Alet Pierre-Jean, Picardi Gennaro, Roca i Cabarrocas Pere, *An In-Plane Solid-Liquid-Solid Growth Mode for Self-Avoiding Lateral Silicon Nanowires.* Physical Review Letters, 2009. **102**(12): p. 125501.

45. Umit Cosckun, A., Yaman Yener, Faruk Arinc, *Simulation of dissolution of silicon in an indium solution by spectral methods.* Modelling and Simulation in Materials Science and Engineering, 2002. **10**(5): p. 539.
46. Pereira, L., Barquinha P., Fortunato E., Martins R., *Influence of metal induced crystallization parameters on the performance of polycrystalline silicon thin film transistors.* Thin Solid Films, 2005. **487**(1): p. 102-106.
47. Yu, L., i Cabarrocas Pere Roca, *Growth mechanism and dynamics of in-plane solid-liquid-solid silicon nanowires.* Physical Review B, 2010. **81**(8): p. 085323.
48. Porter, D.A., Easterling K.E., *Phase Transformations in Metals and Alloys, Third Edition (Revised Reprint).* 1992: Taylor & Francis.
49. Wacaser Brent, A., Dick Kimberly A., Johansson Jonas, Borgström Magnus T., Deppert Knut, Samuelson Lars, *Preferential Interface Nucleation: An Expansion of the VLS Growth Mechanism for Nanowires.* Advanced Materials, 2009. **21**(2): p. 153-165.
50. Evans, M.M.R., Glueckstein, J. C., Nogami, J., *Epitaxial growth of manganese on silicon: Volmer-Weber growth on the Si(111) surface.* Physical Review B, 1996. **53**(7): p. 4000-4004.
51. Jiang, X., K. Schiffmann, A. Westphal, C.-P. Klages, *Atomic‐force‐microscopic study of heteroepitaxial diamond nucleation on (100) silicon.* Applied Physics Letters, 1993. **63**(9): p. 1203-1205.
52. Osten, H.J., Klatt, J., Lippert, G., Dietrich, B., Bugiel, E., *Surfactant-controlled solid phase epitaxy of germanium on silicon.* Physical Review Letters, 1992. **69**(3): p. 450-453.
53. Oh, S.H. and K.Y. Chisholm Matthew F., Kaplan Wayne D., Luo Weidong, Rühle Manfred, Scheu Christina, *Oscillatory Mass Transport in Vapor-Liquid-Solid Growth of Sapphire Nanowires.* Science, 2010. **330**(6003): p. 489-493.
54. Štich, I., Car R., Parrinello M., *Amorphous silicon studied by ab initio molecular dynamics: Preparation, structure, and properties.* Physical Review B, 1991. **44**(20): p. 11092-11104.
55. Roorda, S., Doorn S., Sinke W. C., Scholte P. M. L. O., van Loenen E., *Calorimetric evidence for structural relaxation in amorphous silicon.* Physical Review Letters, 1989. **62**(16): p. 1880-1883.
56. Dubrovskii, V.G., Sibirev N. V., Cirlin G. E., Harmand J. C., Ustinov V. M., *Theoretical analysis of the vapor-liquid-solid mechanism of nanowire growth during molecular beam epitaxy.* Physical Review E, 2006. **73**(2): p. 021603.
57. Dubrovskii, V.G., Sibirev Nickolai V., *Growth rate of a crystal facet of arbitrary size and growth kinetics of vertical nanowires.* Physical Review E, 2004. **70**(3): p. 031604.
58. Kočka, J., Müller Martin, Stuchlík Jiří, Stuchlíková Ha, Červenka Jiří, Fejfar Antonín, *Role of a‐Si:H in lateral growth of crystalline silicon nanowires using Pb and In catalysts.* physica status solidi (a), 2016. **213**(7): p. 1821-1825.
59. Waldrop, M.M., *The chips are down for Moore's law.* Nature, 2016. **530**(7589): p. 144-147.
60. Jacobsen, R.S., et al., *Strained silicon as a new electro-optic material.* Nature, 2006. **441**(7090): p. 199-202.
61. Zhang, P., et al., *Computational design of direct-bandgap semiconductors that lattice-match silicon.* Nature, 2001. **409**(6816): p. 69-71.
62. Gupta, S., et al., *Achieving direct band gap in germanium through integration of Sn alloying and external strain.* Journal of Applied Physics, 2013. **113**(7): p. 073707.
63. Moontragoon, P., R. A. Soref, Z. Ikonic, *The direct and indirect bandgaps of unstrained SixGe1−x−ySny and their photonic device applications.* Journal of Applied Physics, 2012. **112**(7): p. 073106.
64. Pairot, M., Zoran Ikonić, Paul Harrison, *Band structure calculations of Si–Ge–Sn alloys: achieving direct band gap materials.* Semiconductor Science and Technology, 2007. **22**(7): p. 742.
65. Gupta, S., Blanka Magyari-Köpe, Yoshio Nishi, Krishna C. Saraswat, *Achieving direct band gap in germanium through integration of Sn alloying and external strain.* Journal of Applied Physics, 2013. **113**(7): p. 073707.

66. Trumbore, F.A., *Solid Solubilities and Electrical Properties of Tin in Germanium Single Crystals.* Journal of the Electromchemical Society, 1956. **103**(11): p. 3.
67. Li, H., et al., *Characteristics of Sn segregation in Ge/GeSn heterostructures.* Applied Physics Letters, 2014. **105**(15): p. 151906.
68. Gencarelli, F., Vincent, B., Demeulemeester, J., Vantomme, A., Moussa, A., Franquet, A., Kumar, Arul, Bender, Hugo, Meersschaut, J., Vandervorst, Wilfried, Loo, R.,Caymax, Matty, Temst, K., Heyns, M., *Crystalline Properties and Strain Relaxation Mechanism of CVD Grown GeSn*. Vol. 50. 2013. 875-883.
69. Olesinski, R., Abbaschian GJ, *The Ge− Sn (Germanium− Tin) system.* Bulletin of Alloy Phase Diagrams, 1984. **5**(3): p. 265-271.
70. Noriyuki, U., Tatsuro Maeda, Ruben R. Lieten, Shingo Okajima, Yuji Ohishi, Ryohei Takase, Manabu Ishimaru, Jean-Pierre Locquet, *Carrier and heat transport properties of polycrystalline GeSn films on SiO2.* Applied Physics Letters, 2015. **107**(23): p. 232105.
71. Sau, J.D., Cohen Marvin L., *Possibility of increased mobility in Ge-Sn alloy system.* Physical Review B, 2007. **75**(4): p. 045208.
72. Ruben, R.L., Tatsuro Maeda, Wipakorn Jevasuwan, Hiroyuki Hattori, Noriyuki Uchida, Shu Miura, Masatoshi Tanaka, Jean-Pierre Locquet, *Tensile-Strained GeSn Metal–Oxide–Semiconductor Field-Effect Transistor Devices on Si(111) Using Solid Phase Epitaxy.* Applied Physics Express, 2013. **6**(10): p. 101301.
73. Cong, H., Yang Fan, Xue Chunlai, Yu Kai, Zhou Lin, Wang Nan, Cheng Buwen, Wang Qiming, *Multilayer Graphene–GeSn Quantum Well Heterostructure SWIR Light Source.* Small, 2018. **14**(17): p. 1704414.
74. Homewood Kevin, P., Lourenço Manon A., *The rise of the GeSn laser.* Nature Photonics, 2015. **9**: p. 78.
75. Zaima, S. and T.N. Nakatsuka Osamu, Kurosawa Masashi, Takeuchi Wakana, Sakashita Mitsuo, *Growth and applications of GeSn-related group-IV semiconductor materials.* Science and Technology of Advanced Materials, 2015. **16**(4): p. 043502.
76. Wang, W., Lei Dian, Huang Yi-Chiau, Lee Kwang Hong, Loke Wan-Khai, Dong Yuan, Xu Shengqiang, Tan Chuan Seng, Wang Hong, Yoon Soon-Fatt, Gong Xiao, Yeo Yee-Chia, *High-performance GeSn photodetector and fin field-effect transistor (FinFET) on an advanced GeSn-on-insulator platform.* Optics Express, 2018. **26**(8): p. 10305-10314.
77. Stange, D. and v.d.D.N. Wirths S., Mussler G., Stoica T., Ikonic Z., Hartmann J. M., Mantl S., Grützmacher D., Buca D., *Optical Transitions in Direct-Bandgap Ge1–xSnx Alloys.* ACS Photonics, 2015. **2**(11): p. 1539-1545.
78. Yasuhiko, I., Kazumi Wada, Douglas D. Cannon, Jifeng Liu, Hsin-Chiao Luan, Lionel C. Kimerling, *Strain-induced band gap shrinkage in Ge grown on Si substrate.* Applied Physics Letters, 2003. **82**(13): p. 2044-2046.
79. Mathews J., R.T.B., J. Tolle, C. Xu, R. Roucka, J. Kouvetakis, J. Menéndez, *Direct-gap photoluminescence with tunable emission wavelength in Ge1−ySny alloys on silicon.* Applied Physics Letters, 2010. **97**(22): p. 221912.
80. Kimihiko Kato, T.A., Noriyuki Taoka, Mitsuo Sakashita, Wakana Takeuchi, Osamu Nakatsuka, Shigeaki Zaima, *Robustness of Sn precipitation during thermal oxidation of Ge 1− x Sn x on Ge(001).* Japanese Journal of Applied Physics, 2014. **53**(8S1): p. 08LD04.
81. Gencarellia, F., B. Vincenta, J. Demeulemeesterc, A. Vantommec, A. Moussaa, A. Franqueta, A. Kumara, H. Bendera, J. Meersschauta, W. Vandervorsta, R. Looa, M. Caymaxa, K. Temstc, M. Heynsa *Crystalline Properties and Strain Relaxation Mechanism of CVD Grown GeSn.* ECS J. Solid State Sci. Technol., 2013. **2**(4): p. 134-137.
82. Kormoš, L., Kratzer M., Kostecki K., Oehme M., Šikola T., Kasper E., Schulze J., Teichert C., *Surface analysis of epitaxially grown GeSn alloys with Sn contents between 15% and 18%.* Surface and Interface Analysis, 2017. **49**(4): p. 297-302.

83. WirthsS, et al., *Lasing in direct-bandgap GeSn alloy grown on Si.* Nat Photon, 2015. **9**(2): p. 88-92.
84. Mączko, H.S., Kudrawiec R., Gladysiewicz M., *Material gain engineering in GeSn/Ge quantum wells integrated with an Si platform.* Scientific Reports, 2016. **6**: p. 34082.
85. Dian, L., Kwang Hong Lee, Shuyu Bao, Wei Wang, Bing Wang, Xiao Gong, Chuan Seng Tan, Yee-Chia Yeo, *GeSn-on-insulator substrate formed by direct wafer bonding.* Applied Physics Letters, 2016. **109**(2): p. 022106.
86. Toko, K., N. Oya, N. Saitoh, N. Yoshizawa, T. Suemasu, *70 °C synthesis of high-Sn content (25%) GeSn on insulator by Sn-induced crystallization of amorphous Ge.* Applied Physics Letters, 2015. **106**(8): p. 082109.
87. Zhu, Z., Y. Song, Y. Han, Y. Li, Z. Zhang, L. Zhang, S. Wang. *GeSn/Ge dual-nanowire heterostructure*. in *2017 IEEE Photonics Society Summer Topical Meeting Series (SUM)*. 2017.
88. Assali, S. and L.A. Dijkstra A., Koelling S., Verheijen M. A., Gagliano L., von den Driesch N., Buca D., Koenraad P. M., Haverkort J. E. M., Bakkers E. P. A. M., *Growth and Optical Properties of Direct Band Gap Ge/Ge0.87Sn0.13 Core/Shell Nanowire Arrays.* Nano Letters, 2017. **17**(3): p. 1538-1544.
89. Xiang, H.J., Wei, Su-Huai, Da Silva, Juarez L. F., Li, Jingbo, *Strain relaxation and band-gap tunability in ternary InxGa1-xN nanowires.* Physical Review B, 2008. **78**(19): p. 193301.
90. Karam, C., et al., *Urchin-inspired ZnO-TiO 2 core-shell as building blocks for dye sensitized solar cells*. Vol. 126. 2017.
91. Greytak, A.B., et al., *Growth and transport properties of complementary germanium nanowire field-effect transistors.* Applied Physics Letters, 2004. **84**(21): p. 4176-4178.
92. Kodambaka, S., et al., *Germanium Nanowire Growth Below the Eutectic Temperature.* Science, 2007. **316**(5825): p. 729-732.
93. Moutanabbir, O., Isheim Dieter, Blumtritt Horst, Senz Stephan, Pippel Eckhard, Seidman David N., *Colossal injection of catalyst atoms into silicon nanowires.* Nature, 2013. **496**(7443): p. 78-82.
94. Meng, A.C., Fenrich Colleen S., Braun Michael R., McVittie James P., Marshall Ann F., Harris James S., McIntyre Paul C., *Core-Shell Germanium/Germanium–Tin Nanowires Exhibiting Room-Temperature Direct- and Indirect-Gap Photoluminescence.* Nano Letters, 2016. **16**(12): p. 7521-7529.
95. Biswas, S., Doherty Jessica, Saladukha Dzianis, Ramasse Quentin, Majumdar Dipanwita, Upmanyu Moneesh, Singha Achintya, Ochalski Tomasz, Morris Michael A., Holmes Justin D., *Non-equilibrium induction of tin in germanium: towards direct bandgap Ge1−xSnx nanowires.* 2016. **7**: p. 11405.
96. Barth, S., M.S. Seifner, and J. Bernardi, *Microwave-assisted solution-liquid-solid growth of Ge1-xSnx nanowires with high tin content.* Chemical Communications, 2015. **51**(61): p. 12282-12285.
97. Bullis, W.M., *Properties of gold in silicon.* Solid-State Electronics, 1966. **9**(2): p. 143-168.
98. Thompson, K., Flaitz Philip L., Ronsheim Paul, Larson David J., Kelly Thomas F., *Imaging of Arsenic Cottrell Atmospheres Around Silicon Defects by Three-Dimensional Atom Probe Tomography.* Science, 2007. **317**(5843): p. 1370-1374.
99. Sprokel, G.J., Fairfield J. M., *Diffusion of Gold into Silicon Crystals.* Journal of The Electrochemical Society, 1965. **112**(2): p. 200-203.
100. Gunawan, O., Guha Supratik, *Characteristics of vapor–liquid–solid grown silicon nanowire solar cells.* Solar Energy Materials and Solar Cells, 2009. **93**(8): p. 1388-1393.
101. Bar-Sadan, M., Barthel Juri, Shtrikman Hadas, Houben Lothar, *Direct Imaging of Single Au Atoms Within GaAs Nanowires.* Nano Letters, 2012. **12**(5): p. 2352-2356.
102. Ke, Y., Weng Xiaojun, Redwing Joan M., Eichfeld Chad M., Swisher Thomas R., Mohney Suzanne E., Habib Youssef M., *Fabrication and Electrical Properties of Si Nanowires Synthesized by Al Catalyzed Vapor−Liquid−Solid Growth.* Nano Letters, 2009. **9**(12): p. 4494-4499.

103. Hemesath, E.R., Schreiber Daniel K., Gulsoy Emine B., Kisielowski Christian F., Petford-Long Amanda K., Voorhees Peter W., Lauhon Lincoln J., *Catalyst Incorporation at Defects during Nanowire Growth.* Nano Letters, 2012. **12**(1): p. 167-171.
104. Allen Jonathan, E., Hemesath Eric R., Perea Daniel E., Lensch-Falk Jessica L., Li Z. Y., Yin Feng, Gass Mhairi H., Wang Peng, Bleloch Andrew L., Palmer Richard E., Lauhon Lincoln J., *High-resolution detection of Au catalyst atoms in Si nanowires.* Nature Nanotechnology, 2008. **3**: p. 168.
105. Givargizov, E.I., Sheftal N. N., *Morphology of silicon whiskers grown by the VLS-technique.* Journal of Crystal Growth, 1971. **9**: p. 326-329.
106. Kumar, R.R., Rao K. Narasimha, Phani A. R., *Bismuth catalyzed growth of silicon nanowires by electron beam evaporation.* Materials Letters, 2012. **82**: p. 163-166.
107. Cui, Y., Lieber, Charles M., *Functional Nanoscale Electronic Devices Assembled Using Silicon Nanowire Building Blocks.* Science, 2001. **291**(5505): p. 851-853.
108. Gudiksen, M.S., Lauhon Lincoln J., Wang Jianfang, Smith David C., Lieber Charles M., *Growth of nanowire superlattice structures for nanoscale photonics and electronics.* Nature, 2002. **415**: p. 617.
109. Lauhon, L.J., Gudiksen Mark S., Wang Deli, Lieber Charles M., *Epitaxial core–shell and core–multishell nanowire heterostructures.* Nature, 2002. **420**: p. 57.
110. Kodambaka, S., Tersoff J., Reuter M. C., Ross F. M., *Germanium Nanowire Growth Below the Eutectic Temperature.* Science, 2007. **316**(5825): p. 729-732.
111. Reitano, R., Patrick M. Smith, Michael J. Aziz, *Solute trapping of group III, IV, and V elements in silicon by an aperiodic stepwise growth mechanism.* Journal of Applied Physics, 1994. **76**(3): p. 1518-1529.
112. Aziz, M.J., White C. W., *Solute Trapping in Silicon by Lateral Motion of {111} Ledges.* Physical Review Letters, 1986. **57**(21): p. 2675-2678.
113. Aziz, M.J., Tsao J. Y., Thompson M. O., Peercy P. S., White C. W., *Solute Trapping: Comparison of Theory with Experiment.* Physical Review Letters, 1986. **56**(23): p. 2489-2492.
114. Chen, W., Yu Linwei, Misra Soumyadeep, Fan Zheng, Pareige Philippe, Patriarche Gilles, Bouchoule Sophie, Cabarrocas Pere Roca i, *Incorporation and redistribution of impurities into silicon nanowires during metal-particle-assisted growth.* Nature Communications, 2014. **5**: p. 4134.
115. Linwei, Y., Pierre-Jean Alet, Gennaro Picardi, Isabelle Maurin, Pere Roca i Cabarrocas, *Synthesis, morphology and compositional evolution of silicon nanowires directly grown on SnO 2 substrates.* Nanotechnology, 2008. **19**(48): p. 485605.
116. Jones, S.W., *Diffusion in Silicon (ICKnowledge LCC, 2006).*

II FABRICATION & CHARACTERIZATION TECHNIQUES

In this chapter, the elaboration and characterization techniques used in this PhD thesis will be presented. First, the catalyst preparation is detailed, two physical vapor deposition (PVD) methods are used: i) magnetron sputtering, and ii) thermal evaporation. Second, the NWs growth reactor will be presented. It is a reactor where the bottom-up assembly is done, namely, the plasma-enhanced chemical vapor deposition reactor (PECVD). Third, basic principles of SEM, FIB (focused ion beam), TEM (and STEM), and APT characterization will be presented. Moreover, the FIB preparation methods (coarse milling, fine milling, lift-out, welding and cleaning) for TEM and APT will be discussed.

II.1 CATALYST PREPARATION

The first step for the growth of NWs is the catalyst deposition. The catalyst plays an essential role in the production of nanowires. Many catalyst-related parameters (such as: size, composition and density) can strongly affect the shape, morphology, size and composition of the NWs. Therefore, it is important to control these parameters to tune the growth of NWs. The first type of catalyst used is Indium since its fabrication is well optimized for NWs growth. In order to fabricate the catalyst, an ITO (Sn-doped In_2O_3) thin-film is deposited using the magnetron sputtering machine, then, it is transformed by chemical reduction to In NPs in the PECVD reactor. Since our work consists of fabricating GeSn NWs using Sn catalysts, the second type of catalyst is Sn. These NPs are fabricated using the thermal evaporation of a Sn powder.

II.1.1 MAGNETRON SPUTTERING

Magnetron sputtering is a physical type of deposition technique (PVD), where a plasma reactor is involved Fig.II.1. In our system an inert gas, Argon, is utilized as a sputter particle. A glow discharge plasma is ignited and confined within a close distance to the target material, ITO (Sn-doped In_2O_3) in our case, which is to be deposited [1]. The surface of the target material is eroded (bombarded) by highly energetic ions (Ar^+ in our case) created by the plasma. The ejected atoms, coming from the targeted specimen, travel through the vacuum environment and deposit onto a Si substrate to form a thin film, as shown in Fig.II.2. To ignite the plasma, two-parallel electrodes are used: a negatively charged electrode, namely cathode, which is placed behind the carrier of the target material, and an anode which is commonly connected to the chamber as an electrical ground [2]. When an electric potential is applied (ranging from few hundreds to few thousands electron-volts), Ar atoms will be ionized. As soon as Ar^+ ions are formed, they will be accelerated towards the specimen and, therefore, strike the target material with enough energy to dislodge and eject atoms. In order to increase the deposition rate, the number of high energy collisions should be increased and high molecular weight gases should be used, such as: Ar and Xe [3]. If a reactive sputtering is desired, gases such as Oxygen and Nitrogen can be introduced during the film formation. In this thesis, ITO thin-films are deposited using the sputter reactor.

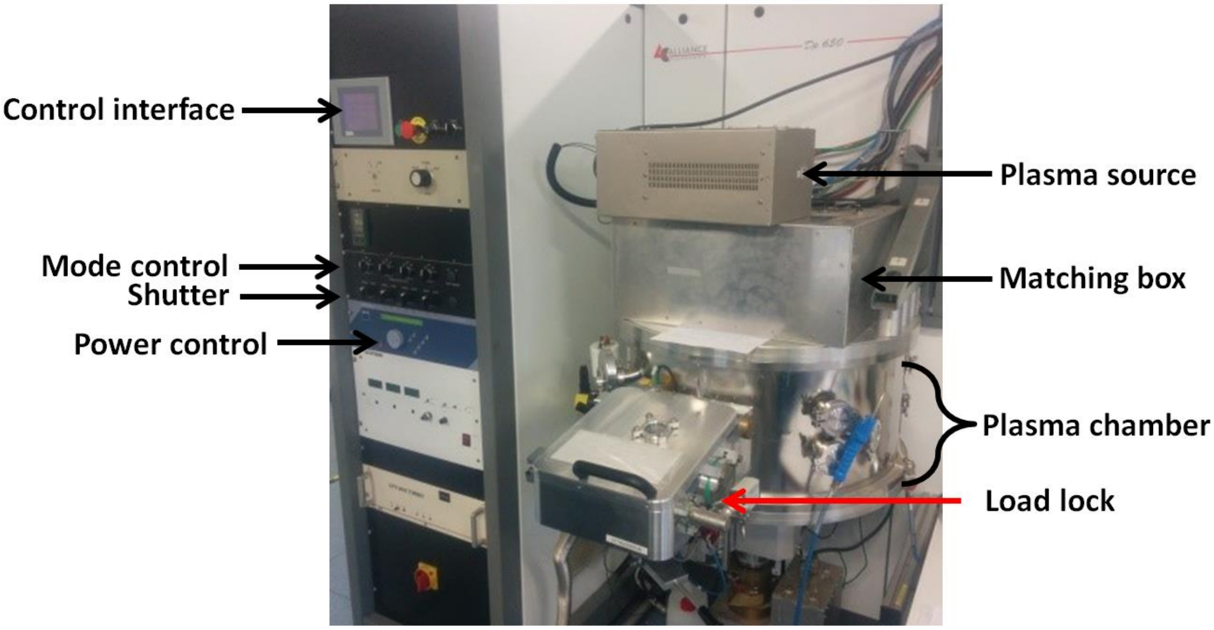

Figure.II.1.Photograph of the sputtering machine used in this study (at LPICM).

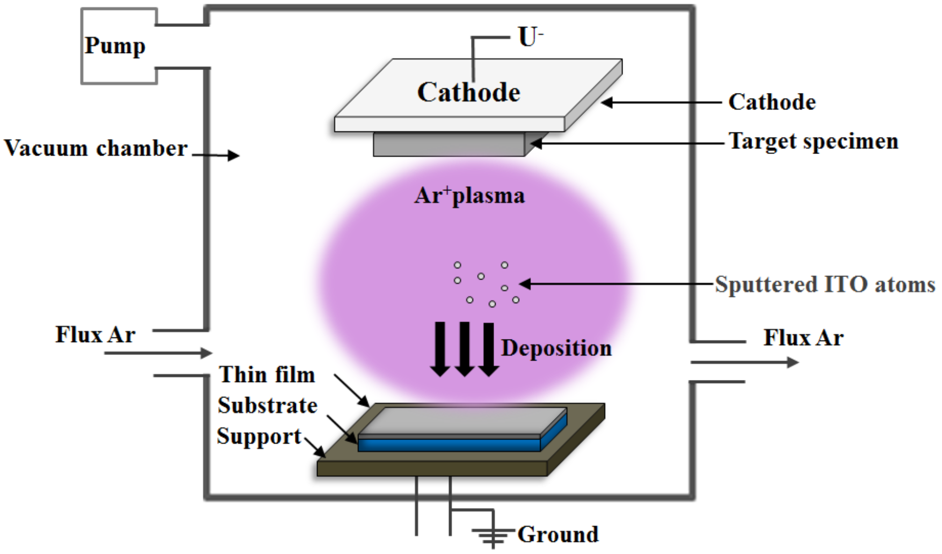

Figure.II.2.Schematic illustration of a magnetron sputtering coater.

II.1.2 THERMAL EVAPORATION

Another common, yet, simple method of PVD is thermal evaporation in which the “Joule-effect” is used. Maintained in high-vacuum, a crucible (i.e. Tungsten, Molybdenum) contains the source material to be deposited in a form of powder or pellets. The evaporation starts when the temperature is significantly increased (i.e. > 800℃ for Sn). When source atoms have enough energy, they will eventually leave the surface of the source and travel through the vacuum environment to reach the substrate which is positioned above the crucible (see Fig.II.3).

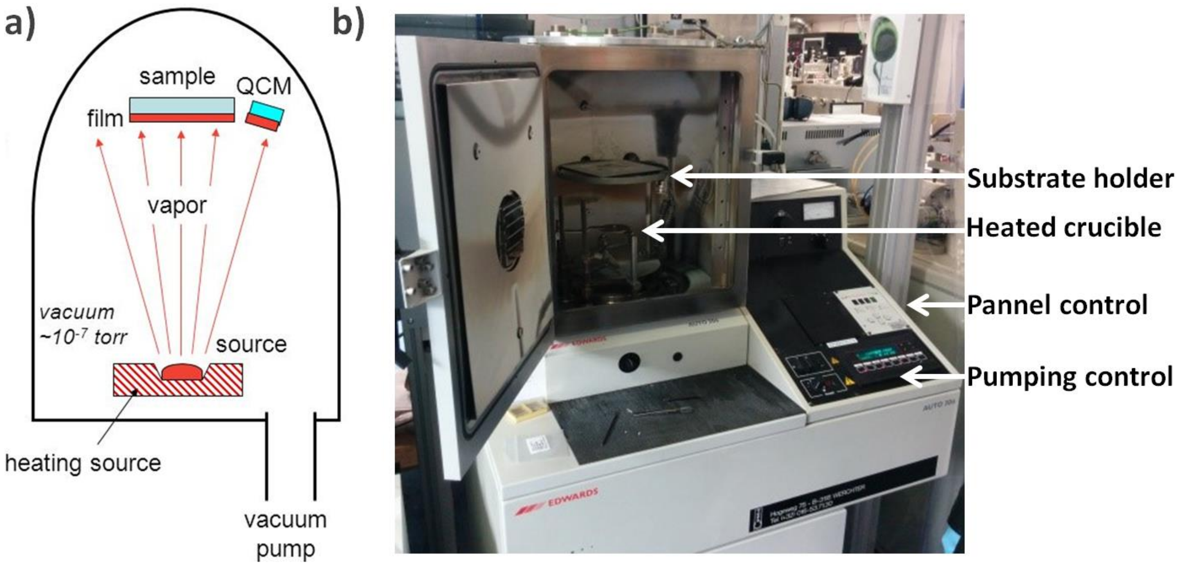

Figure.II.3. a) Schematic illustration of a thermal evaporator, QCM denotes: quartz crystal monitor which is a tool used to control the rate and thickness of the deposited material (the deposition control in (b) is possible with the aid of a QCM). The source material is located in resistive crucible that is heated enough to evaporate source atoms [4]. b) a photograph of the thermal evaporator used in this study (at LPICM).

The deposition rate can be controlled by the intensity of the flowing current through the resistive crucible, increasing the current will results in increasing the temperature and therefore the deposition rate. The pressure is held low to decrease contamination, and to maintain a long mean free path for the evaporated atoms to reach the substrate. In this thesis, the thermal evaporator (shown in Fig.II.3.b) is used for the deposition of pure Sn catalyst NPs, since a target specimen of Sn is not provided for the deposition in the magnetron coater (shown in the previous section).

II.2 NANOWIRES ELABORATION: PLASMA ENHANCED CHEMICAL VAPOR DEPOSITION (PECVD)

PECVD is one of the most used technologies for the fabrication of thin films and nanowires. Not only used in research laboratories, the PECVD has been scaled up for industrial applications [5]. The PECVD reactor, used in this study [6], satisfies the requirements for production of high-performance thin film- and nanowire-based devices. For instance, one can control precisely the process parameters such as: gas flow rates, gas pressure, RF (radio-frequency) power, and the temperatures of the reactor wall, the substrate holder, and electrodes. It is a versatile reactor where surface treatments, deposition, and etching using different types of plasma in a one pump-down process are possible. The numerous reactive gases, such as: Silane (SiH_4), Germane (GeH_4), Methane (CH_4), Phosphine (PH_3), Diborane (B_2H_6), Tetrafluorosilane (SiF_4), Dihydrogen (H_2), and Ammonia (NH_3), give a huge flexibility in the fabrication process. Unlike the conventional CVD using only thermal energy to dissociate molecules, this technique is plasma-assisted where energetic electrons collide with gas molecules and ionize them (Fig.II.4). Therefore, the processes can be operated at low temperatures (down to room temperature). In this system, two electrodes are placed in parallel to create a capacitive configuration; the substrate is connected to the ground electrode while the other electrode is powered by a DC or a RF (in our case), or a Very-High Frequency (VHF) source. The dissociation of the reactive gases in this kind of systems is achieved through their excitation in a 13.56 MHz capacitively couple RF discharge where the power is provided by an RF generator. Electrons acquire enough energy, by the electric field created between the two parallel plate electrodes, to dissociate the molecules in the reactor (Fig.II.4). Numerous reactive species can be created in the plasma depending on the energy of the electrons, thus, electric field. Let us take the dissociation of Germane (GeH_4) for instance, for different electron impact energies i.e. 8.2 eV, 8.7 eV, 8.9 eV, and 9.4 eV; different radicals are produced correspondingly: GeH_3^-, GeH_2^-, GeH^-, and Ge respectively [7].

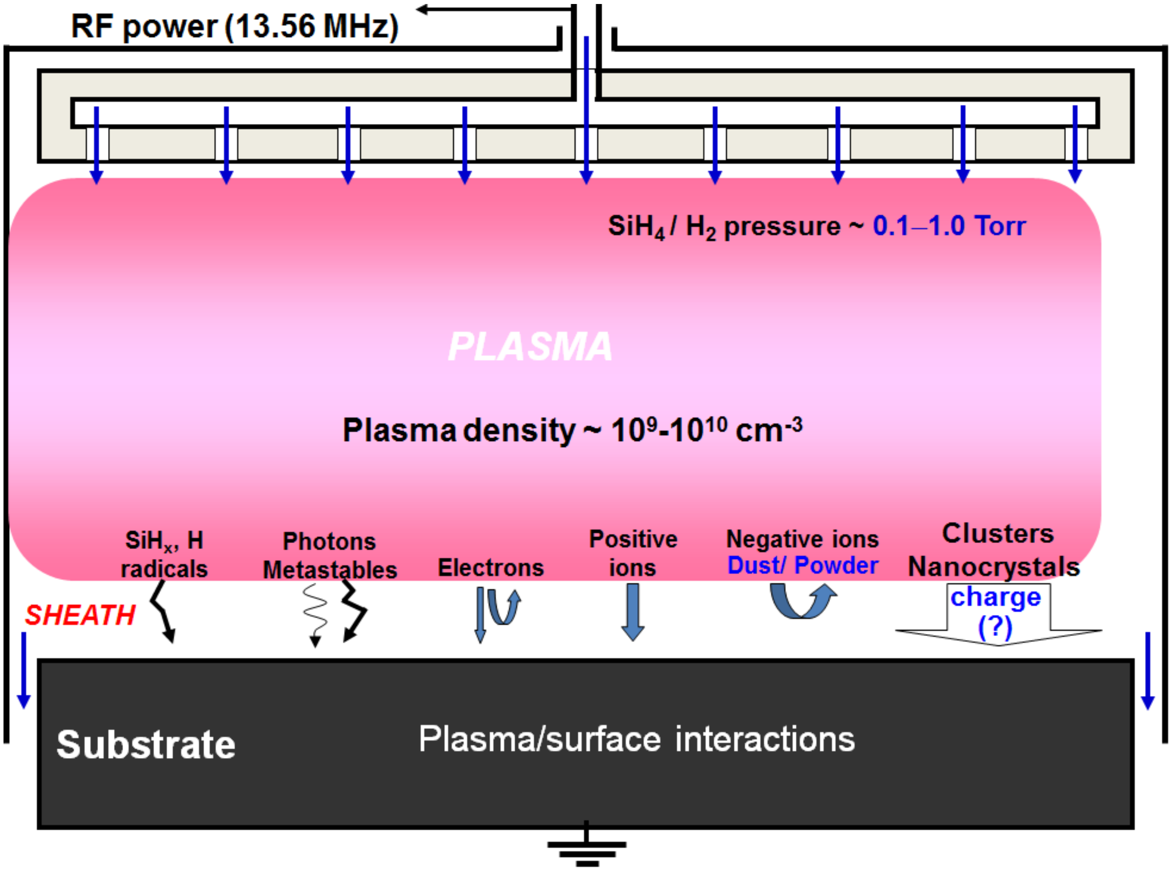

Figure.II.4. a) Schematic illustration of a capacitively coupled RF glow discharge reactor. The plasma provides the reactive species which their interaction with the substrate depends on their charge due to the presence of a space charge region (dark region between the plasma and the substrate). The species contributing to deposition are shown at the space charge region. SiH_x are the main radicals for the deposition. They diffuse through the dark region to reach the substrate (this diffusion depends on their mean free path, hence, the pressure in the plasma chamber). Photons and metastable species interact with the growing films, but fewer studies have been conducted to know their impact on films properties. Electrons and negative ions are mostly confined in the plasma due to its higher potential compared to the substrate. On the contrary, positive ions will be accelerated towards the substrate as soon as they arrive to the space charge region. Clusters and nanocrystals formed in the plasma may or may not diffuse towards the substrate depending on their charge [8].

As shown in Fig.II.4, a wide variety of species are present in the plasma: Si radicals (SiH_3, SiH_2, SiH, and Si), electrons, positive ions, photons and metastable species, negative ions, clusters, and nanocrystals [9]. These species will react on the substrate in different amounts depending on the process conditions.

The dark region plays an important role in filtering the diffusing charged particles depending on their charges. One can observe that this region surrounds the bulk plasma and it is called plasma "sheath", see for instance Fig.II.5.a. In fact, since electrons are much lighter than ions, they can escape from the plasma much faster as there is no confining potential barrier. The electrons will accumulate on the chamber walls, thus, building up a negative field repelling all incoming negatively-charged particles (mainly electrons), as shown in Fig.II.5.b. This dark region with a low electron density results in the decrease of electron-molecule collisions and therefore a decrease of gas excitation leading to this dark-region.

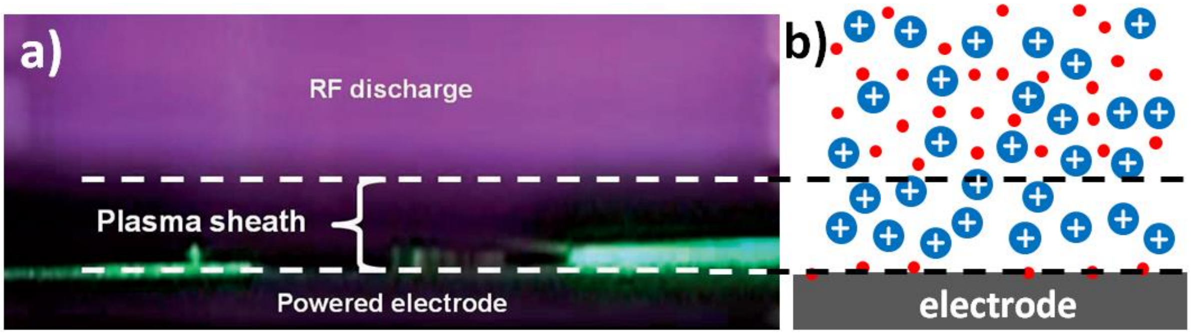

Figure.II.5. Plasma sheath region, a) photography showing the dark region between the bulk plasma and the powered electrode [10]. b) schematic illustration showing the lack of electrons near the electrode, due to a repelling field created by their accumulation on the surface. Since the collision between electrons and molecules is reduced, no light is emitted in the sheath.

When radicals reach the substrate, mainly they will get physisorbed and diffuse along the growing layer. These radicals experience a variety of reactions: i) they can desorb back to the sheath depending on their sticking coefficient, ii) recombine with another radical to form new ones (e.g. $GeH_3 + GeH_3 = Ge_2H_6$), iii) recombine to a hydrogen atom from the surface of the substrate (e.g. $GeH_3 + H = GeH_4$), leaving a dangling bond on the surface which might form a chemical bond with another radical (e.g. GeH_3), iv) radicals can get chemically bonded with dangling bonds at the surface of substrate (Si dangling bond in the case of a Si substrate) which leads to the deposition.

In this thesis, two PECVD reactors were used: PLASFIL and ARCAM. Each has its own advantages; on one hand, PLASFIL can be heated to a temperature of 650 ℃ for the substrate holder and 450℃ for the RF electrode. It is a monochamber reactor where the substrate holder is located below the RF electrode. The typical conditions for chemical reduction of SnO_2 are: temperature of the substrate is 250℃, pressure is set to 0.6 Torr, hydrogen flow is 100 sccm (standard cubic centimeter), the optimal plasma power is 30 W, and the duration depends on whether the SnO_2 is a native oxide layer or a NP (for the case of NP; t = 10 min, and for the latter case t = 2 min). Moreover the deposition conditions used in this thesis are: i) substrate's temperature is between 120℃ and 350℃, pressure stabilized at 0.3 Torr, Germane, hydrogen flows are 50 sccm and 40 sccm respectively, plasma power should be 2 W, and the duration depends on the desired thickness (10 min deposition corresponds to ~15 nm). The annealing step, where the growth is activated, is normally done under flow of 100 sccm hydrogen at temperatures between 230℃ and 350℃.

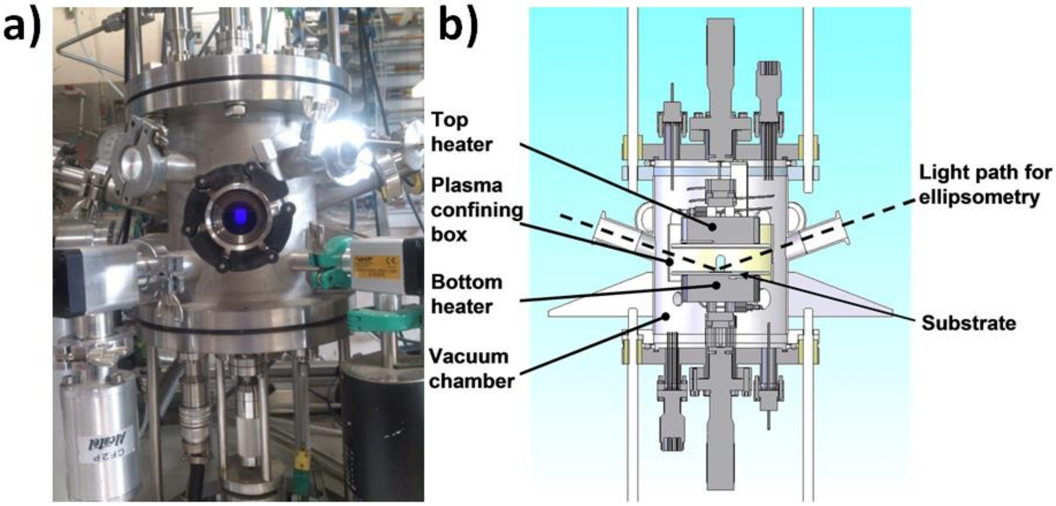

Figure.II.6. PLASFIL reactor a) photography, b) schematic illustration of the reactor's design

On the other hand, ARCAM reactor has three independent plasma boxes (15 cm in diameter) grouped in a big single vessel. This multiplasma-monochamber reactor allows the fabrication of various kinds of samples in a one pump-down. For example, three samples can be produced successively: intrinsic, n-type, and p-type NWs (or thin-films) each grown in a separate plasma chamber, which helps enormously to reduce the processing time and therefore the fabrication cost. However, the temperature cannot exceed 350℃. Here it is noteworthy that the same fabrication conditions are used as in PLASFIL, except that the temperature should not exceed the 300℃.

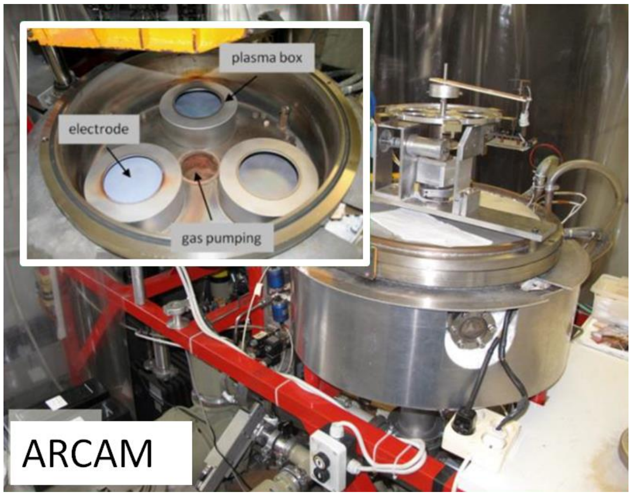

Figure.II.7. Photography of ARCAM reactor, the inset shows the three-plasma chambers located inside the reactor's main vessel.

II.3 CHARACTERIZATION TECHNIQUES

The process of fabrication may not be as difficult as the characterization one. Investigations of chemical and physical properties of nanowires (nanoscale) require appropriate and sophisticated techniques. In the following parts, we will describe the characterization techniques used in this thesis: Scanning Electron Microscope (SEM), Focused Ion Beam (FIB), Raman spectroscopy, Transmission Electron Microscope (TEM), and Atom Probe Tomography (APT).

II.3.1 DUAL BEAM ELECTRON – ION MICROSCOPE

The fastest way for feedback concerning all aspects of the NWs growth, is provided by the SEM observations [11]. In this study, a Zeiss NVision 40 FIB-SEM composed of ionic and electronic columns (which are shown in Fig.II.8), has been employed for feedback, and nanoscale preparations for TEM and APT analyses. NVision 40 combines a high resolution

SEM with the precision milling and nanofabrication abilities of a high resolution FIB. All characterization and processing can be controlled using a computer interface with a dedicated software (SmartSEM).

II.3.1.1 SCANNING ELECTRON MICROSCOPE

SEM is a highly versatile electron beam instrument that can provide images over 100 times more magnified than commercial optical microscopes, and permits the observation and characterization of heterogeneous organic and inorganic materials on a nanometer scale [12]. The electron column consists of an electron gun which is in our case a Schottky field emission Gemini column that operates between 100 V to 30 kV. The resolving capabilities of the featured SEM are 1.1 nm at 20 kV and 2.5 nm at 1 kV. The electron path is controlled by two or more electromagnetic lenses located inside the column. A high vacuum is achieved, i.e. in our case 10^{-10} mbar in the gun column and between 10^{-6} – 10^{-7} mbar in the system (analysis chamber where the specimen is located). These ultra-low pressures are mandatory in order to: i) minimize the electron-particle collisions which make the electrons deviate from their initial trajectory, and ii) avoid contamination.

The scanned image is formed point-by-point. Usually two pairs of electromagnetic deflection coils, dubbed “scanning coils”, are used to sweep the beam across the specimen. In fact, the scanning coils cause the beam to move and to scan a series of discrete locations along a line, then along another line below the first. This process is repeated until an electronic rectangular image of the specimen is generated [13]. Upon electron-specimen interactions, many types of signals can be generated, such as: Secondary Electrons (SE), BackScattered Electrons (BSE), Auger Electrons (AE), X-ray, visible light (cathodoluminescence), and electron-hole pairs, as shown in Fig.II.9.a. The BSE and SE are the most used signals to construct images. For instance, the SE signal provides a detailed inspection of the topography of the sample’s surface, Fig.II.9.b. Meanwhile, BSE provide beneficial information on the material composition, crystallography and magnetic field, Fig.II.9.c.

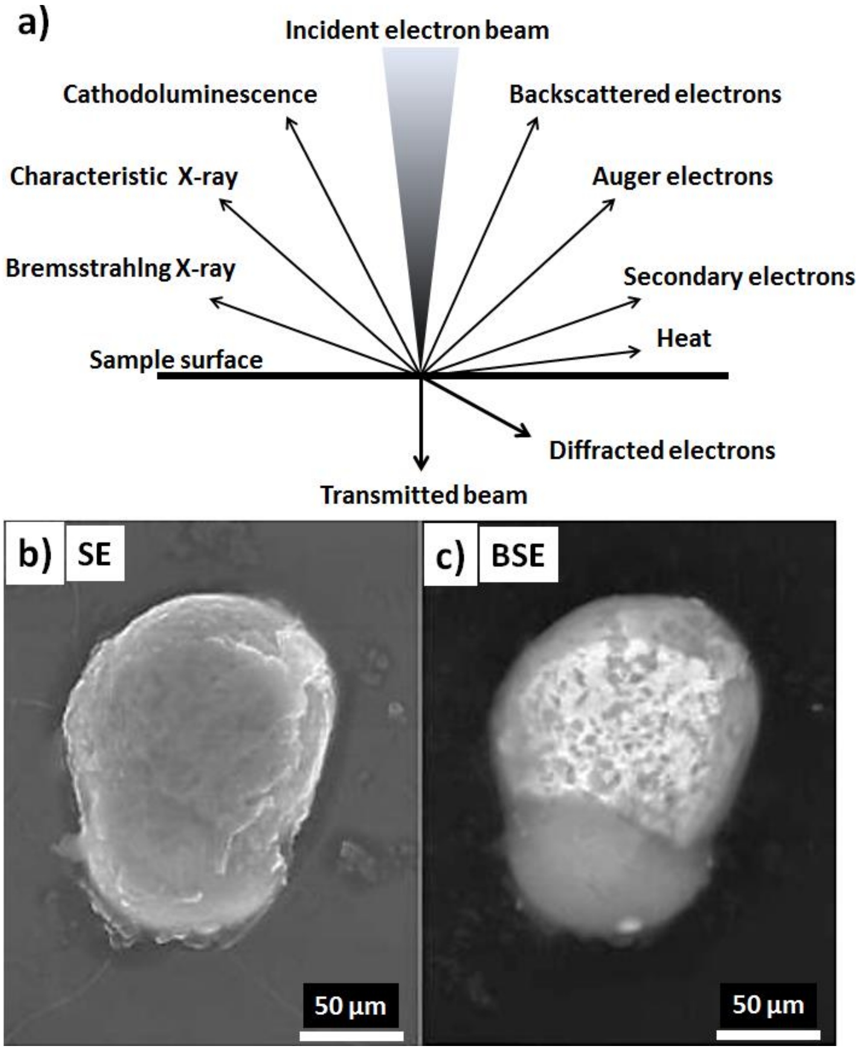

Figure.II.9. Different signals obtained upon electrons collision in SEM. a) Schematic illustration of different types of signals produced consequent to the electron-specimen interactions. b) electronic image constructed using SE in SEM at an accelerating voltage of 20 kV of a particle made of Pb and Ba. The SE image shows the detailed topological features of the particle, however it shows no contrast difference related to the atomic number Z. c) image of the same particle constructed using BSE, the contrast difference is Z-related and helps differentiate the location of different elements in the particle. The whiter elements are Pb (SEM image courtesy of LKA Bayern, Karl Lüftl)

II.3.1.2 FOCUSED ION BEAM

Similar to SEM, the FIB consists of a vacuum column, electromagnetic coils, and a Liquid-Metal Ion Source (LMIS, typically a reservoir of liquid Ga) responsible for creating a finely focused ion beam. In our study, the ion gun (inclined 54° with respect to the SEM column) featured in the FIB is SIINT Zeta Ga^+ ion which can be operated between 1 kV and 30 kV with ion currents between 0.1 pA and 45 nA. The resolution of the ion beam is 4 nm at 1 pA, which is lower than SEM because ions cannot be as finely-focused as electrons.

The FIB has capabilities that are not available in any other milling technique, such as: an accurate target – area selection which enables the selectivity of a ROI, and milling both sides of a chunk (parallel milling) [14]. These capabilities are very important for high quality TEM and Atom-probe specimen fabrications. Despite these advantages, the ion milling causes extensive damages to the ROI, such as structural defects (amorphization), and ion implantation [15]. These artifacts are related to the ion-beam incident angle and accelerating voltage. In fact, Ga ions that are accelerated by 30 kV helps to coarsely mill the chunk, for this reason it is considered to be a time efficient process. However, at this accelerating voltage lots of damages are created by the incident ions. It was shown that by reducing the accelerating voltage, less damage is produced, i.e. 5kV produces less damage to the surface (and sub-surface) than 30 kV, as shown in Fig.II.10.

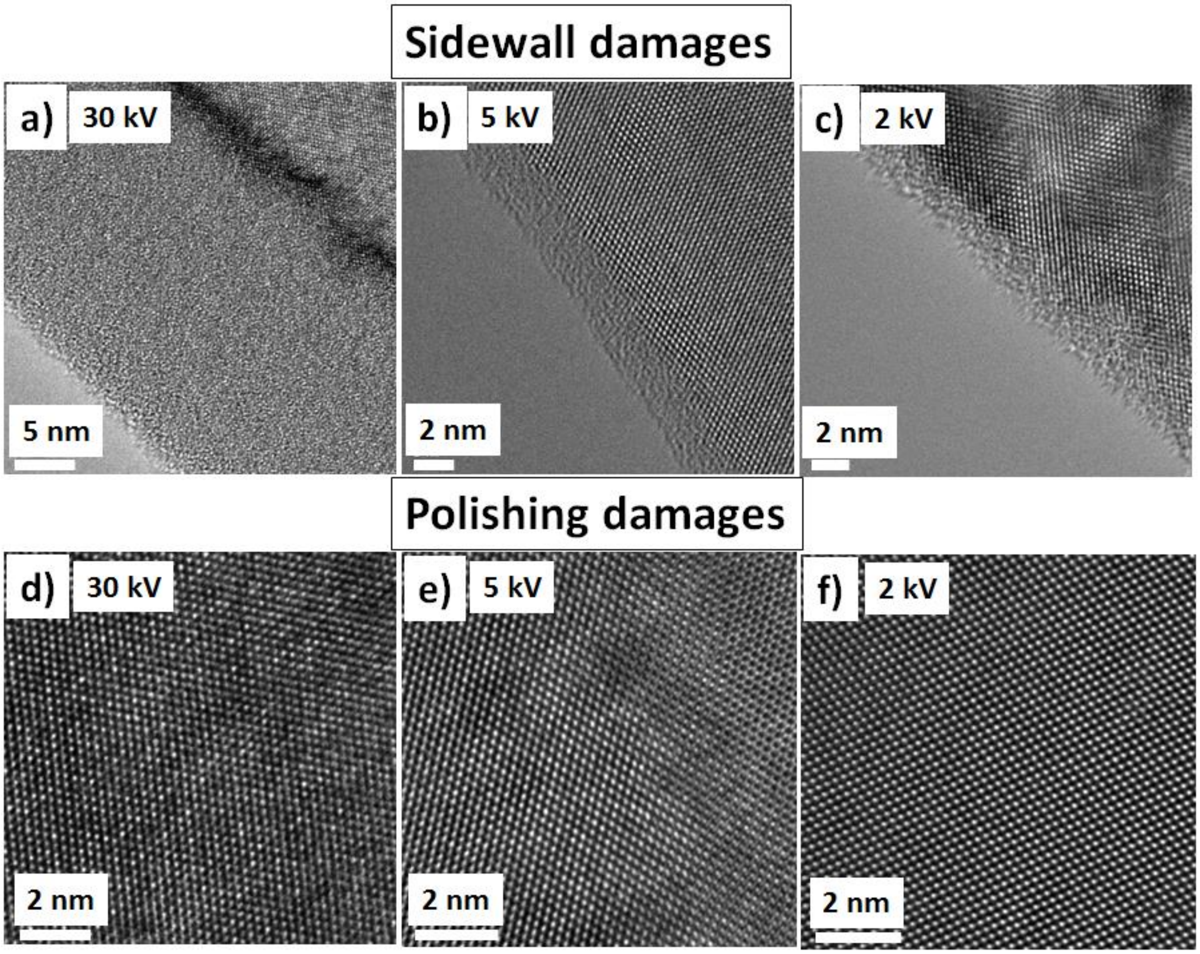

Figure.II.10. HR-TEM images for Si lamellas [110] prepared using three accelerating voltage: 30 kV, 5 kV, and 2 kV. The sidewall amorphization size induced by a) 30 kV, the amorphous thickness is ~ 20 nm, b) 5kV, the thickness is ~ 2 nm, c) 2kV, the thickness range between 0.5 and 1.5 nm. d) the polishing damage induced by a 30 kV accelerating voltage, e) 5 kV, and f) 2 kV. (Image adapted from ref [16]).

Moreover, it was shown that increasing the incident angle while using 50kV will increase the damages and implantation. To avoid these drawbacks, the incident angle should be lowered while coarse milling. Nevertheless, it was shown that even at 1° incident angle the sample will get damaged [17]. It is impossible to avoid the damages completely during a coarse mill, but a cleaning process can repair the damaged surface. The optimal accelerating voltage for a cleaning procedure is 2 kV [16] (Fig.II.10.f). At this voltage, Ga ions will not be able to penetrate the surface, but only have the energy to clean the defected surface. This type of cleaning requires increasing the incident angle (typically, ± 4°) knowing that at low kV exposing the surface to the beam will not induce further damaging.

The NVision 40 is equipped with a Gas Injection System (GIS). The gas supply consists of $(CH_3)_3CH_3C_5H_9Pt$ precursor reservoir that is heated up to 40℃ resulting in a gas flux of 10^{18} molecules/cm^{2}s. The gas is introduced into the chamber using a nozzle of 0.5 mm diameter. The open-end of the nozzle is brought into close proximity to the substrate surface. The SE is mainly produced by the collisions of the incident ions or electrons with the substrate surface [18]. The SE possesses low energy < 50 eV which corresponds to the precursor molecules bonding energy. Therefore, SE is responsible for cracking the gas molecules as well as the formation of bonds between the created species and the substrate surface atoms. Ion and electron beams can be used to deposit material at a specific region [19]. The CVD can be achieved in two ways: i) Ion Beam-Induced Deposition (IBID) [20], and ii) Electron Beam Induced Deposition (EBID) [21, 22]. However, the ion beam is much more efficient (faster) for the deposition than the electron beam, because the ion beam creates an important number of secondary electrons upon the collision with the sample compared to an electron beam. The usual conditions for IBID are: 30 kV accelerating voltage, 40 pA (for 4 μm × 4 μm surface area), dwell time of 0.4 μs, and a pixel fill factor of 55%. Note that increasing the deposition surface area requires increasing the ion current for a more efficient deposition. For the EBID the typical conditions are: 5 kV accelerating voltage, slow scan speed, and a current of few nA (high current mode – 60 μm aperture). Chemical analysis has shown that IBID – Pt contains a large amount of carbon incorporated into it from the broken down precursor gas 30–50 at.%, meanwhile EBID – Pt contains up to 70 at.% [23].

II.3.1.2.1 SAMPLE PREPARATION FOR TEM AND APT

The dual-beam is equipped with a micro-manipulator (Kleindiek, Nanotechnik, Germany) which is used for lift-outs during this study. As a first step, in the lift out process, Pt is deposited in SEM via EBID on the Region-Of-Interest (ROI), as shown in Fig.II.11.a,b. This preliminary coating serves as a protection from the ion beam imaging; the thickness should be between 100 to 150 nm. The ion imaging is done at an ion current of 40 pA and an accelerating voltage of 30 kV. The second layer of Pt, with a thickness ranging from 300 to 400 nm deposited via IBID, serves as a protection from coarse milling operations. High ion currents (1.5 nA to 3 nA) are then controlled to be focused perpendicularly towards the surrounding of the ROI, in a sputtering process called milling process, Fig.II.11.c. Therefore, the newly-formed chunk is only attached to the substrate from one side that is underneath the ROI, see Fig.II.11.c. At this point, the Kleindiek micromanipulator is introduced, and then its tip is welded on the chunk using IBID of Pt, Fig.II.11.d. Then, a milling step is necessary to detach the chunk from the main specimen and lift it out using the micromanipulator, Fig.II.11.e. Now the following preparation procedure depends on the type of the fine-characterization that will be done after FIB-SEM operations (TEM or APT).

In the case of TEM, the chunk welded on the tip of the micromanipulator is also welded on the TEM copper lamella using Pt IBID, and the contact point between the micromanipulator and the chunk is milled using Ga^+ to achieve their detachment, Fig.II.11.f. For TEM observations, the chunk is thinned to thicknesses less than 100 nm using low ion currents (40 pA to 80 pA), Fig.II.11.g. As a final step, a cleaning process (at a low accelerating voltage: 2 kV) is necessary to remove most of the ion-damaged regions from the ROI cross-section, thus, leaving the crystalline structured material ready for TEM analysis, Fig.II.11.h, i.

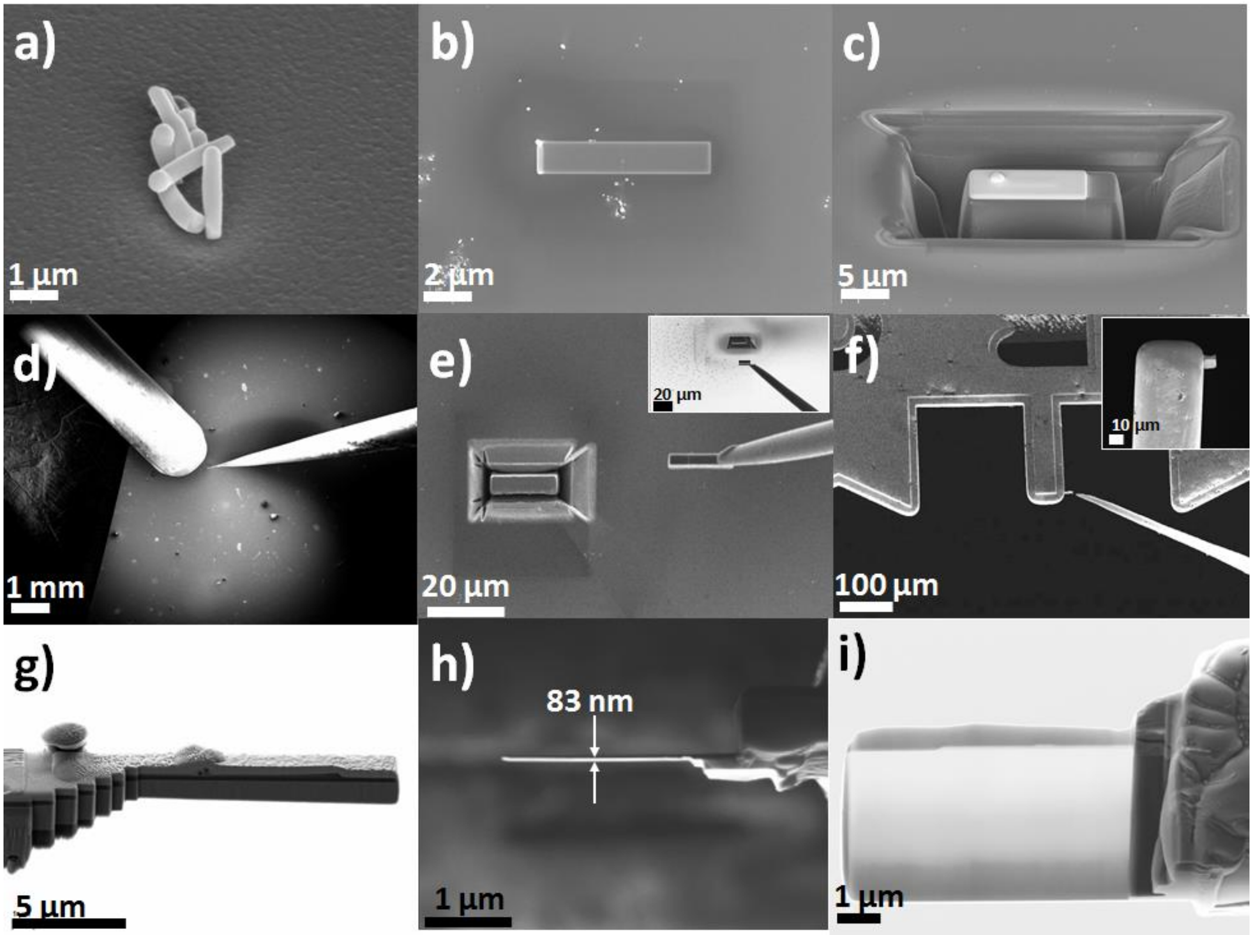

Figure.II.11. SEM images of TEM-lamella preparation using FIB. a) SEM image showing the ROI (NWs), b) deposition of Pt protective layer using EBID, c) coarse milling around the chunk leaving only the downside part attached to the substrate, d) The GIS nozzle and the micromanipulator are inserted nearby the chunk. Pt is used to weld the micromanipulator with the chunk, e) SEM image of the lifted-out chunk, after the welding, ions are controlled to mill the downside part of the chunk in order to detach it from the main sample. Insert: simultaneous FIB view, f) the chunk is welded on the copper TEM-lamella and then detached from the micromanipulator, g) coarse milling process in order to reduce the chunk size for proper TEM observations, h) top-view of the chunk after fine milling, i) side-view of the chunk after cleaning at 2 kV accelerating voltage and 30 pA ion current.

In the case of APT, the chunk is welded on a W-tip by Pt welding. Afterwards, an annular milling is achieved using the FIB. In fact, the mask shown in Fig.II.12.a is to protect the ROI while milling the other parts. The accelerating voltage used in this process is 30 kV and the ion current is between 40 pA to 80 pA. The latter process is repeated while decreasing the mask size. As a final step, a cleaning process is required to remove the FIB-damaged region using an accelerating voltage of 2 kV with 30 pA as an ion current. Fig.II.12.b is an SEM image showing a p-i-n junction SiNW milled and cleaned using FIB and ready for APT analysis.

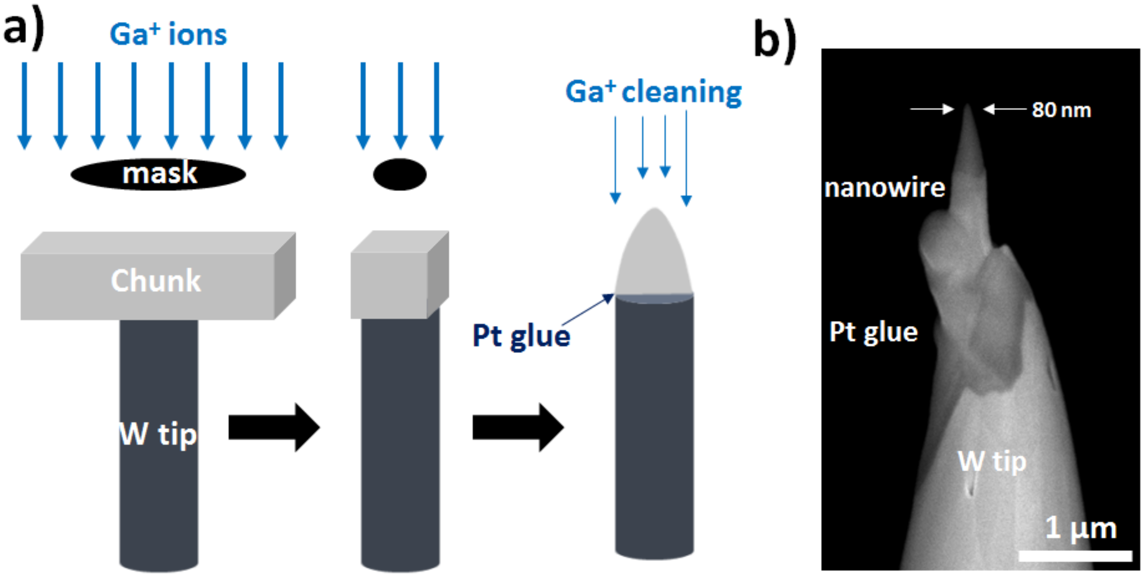

Figure.II.12. APT tip preparation a) schematic illustration showing the preparation process of an APT tip, first the chunk is welded using Pt on a W tip support, then it is coarsely milled by 30 kV accelerated-Ga$^+$ ions, while a mask is protecting the ROI. When the apex radius is less than 50 nm, a cleaning process is required to remove the damages induced by the FIB. In this process, the Ga ions accelerating voltage is reduced to 2 kV. b) SEM image showing a p-i-n junction SiNW milled, cleaned, and ready for APT analysis.

II.3.2 RAMAN SPECTROSCOPY

Raman spectroscopy is a non-invasive, practical, and quick tool for composition identifications and quantifications [24, 25]. When light is scattered from a molecule or crystal, most photons are elastically scattered with the same energy (wavelength) as the incident photons. However, only a small fraction of light (roughly 1 part in 10 million) is scattered at frequencies different from the incident photons. The Raman effect, which is the process of inelastic scattering, is too weak to be seen by the naked eye; for this reason a highly sensitive spectrometer is used. The shift in wavelength of the inelastically scattered radiation provides chemical and structural information. Raman shifted photons can be of either lower (Stokes scattering) [26] or higher (anti-Stokes scattering) energy [27], depending upon the vibrational state of the molecule under study, whereas the Raleigh scattering is when the photons have equal amount of energy as the incident ones (Fig.II.13). It was demonstrated that the Raman spectroscopy can be used to quantify the composition of a given material, and the strain-state in a certain structure by tracking the pic shift (Stokes, or anti-Stokes) [28, 29].

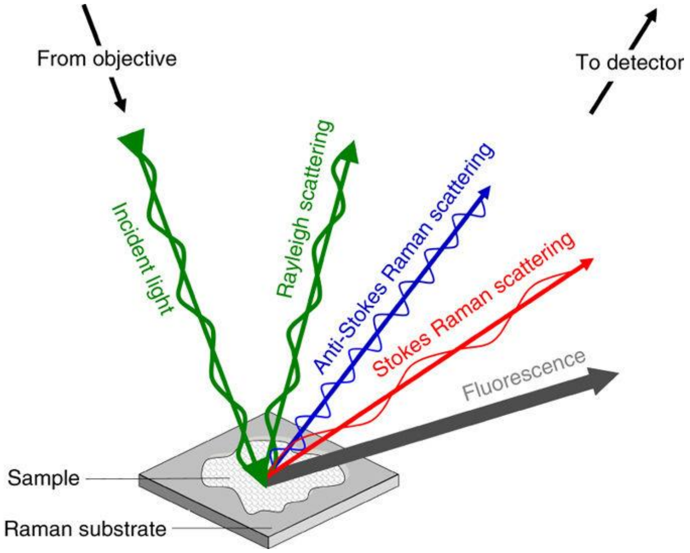

Figure.II.13. Schematic identifying light scattering after laser exposure on a sample [30].

Raman scattering experiments show that the frequency of the Ge peak (corresponding to the bulk w_{Ge} = 301 cm^{-1}) decreases with the increasing Sn concentration in the alloy, as shown in Fig.II.14.

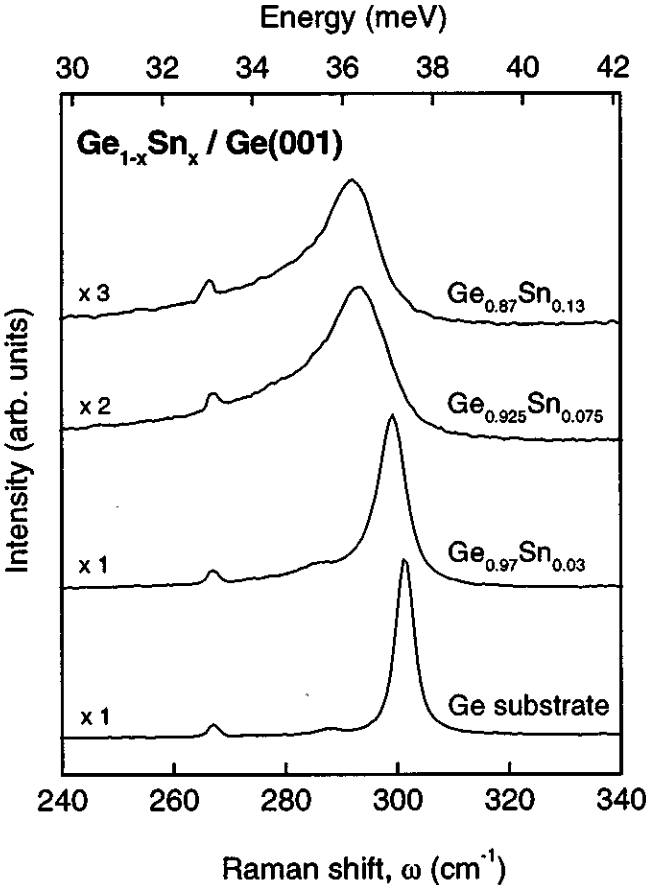

Figure.II.14. Raman spectra from a bulk Ge substrate and fully strained $Ge_{1-x}Sn_x$ layers grown on Ge (001). Films compositions x and thicknesses from bottom to top are: x = 0.03, t = 62 nm; x = 0.075, t = 40 nm; and x = 0.13, t = 31 nm.

The shift is linearly related to x in $Ge_{1-x}Sn_x$ and is given by $\Delta w_{GeSn} = - k. x$, where k is the prefactor depending on the strain state of the structure and x is the atomic fraction of Sn. In fact, accommodating Sn in Ge will create a compressive strain (due the Sn-induced bond stretching) causing a shift in the frequency. In this thesis, the micro-Raman used is Horiba LabSpec 5 (at LPICM), equipped with Helium-Neon (HeNe) laser with an excitation wavelength of λ_{laser} = 633 nm and CCD detector.

II.3.3 TRANSMISSION ELECTRON MICROSCOPE (TEM)

As highlighted previously, the nanometer resolutions attained in a SEM are highly compatible with the actual developments of the nanotechnology [31]. Since the nanoscience is an nanometer-scale material engineering (ranging from 1 nm to 100 nm), a more advanced microscopy is required for atomic characterization. An in-depth analysis of individual nano-objects requires the use of the Transmission Electron Microscopy (TEM). The main advantage of TEM relies on the volumetric information acquired, as in this case the electrons with superior energies as against the SEM transverse the specimen. For instance, the typical electron energies used in a SEM range from 1 to 30kV, whilst the accelerated voltage in a commercial TEM ranges from 60 to 300kV, but less or higher for specific configurations. The principles of a TEM rely on the wave-particle duality, which was first theorized by Louis de Broglie [32] in 1925. This theory stands at the bases of the relationship between the energy of an electron and its characteristic wavelength:

$$\lambda = \frac{h}{[2m_0eV(1+\frac{eV}{2m_0c^2})]^{1/2}}$$

Where h is Plank's constant, m_0 and e are the mass and charge of an electron respectively, V is the accelerating voltage (eV is the energy of an electron), and c the speed of light in vacuum. This equation stipulates that an electron accelerated by acceleration voltages of 200 kV or 300 kV have a wavelength of 3 or 2 pm respectively. Therefore, increasing the electron velocity will eventually decrease its wavelength; and thereby the resolution of an electron micrograph will increase. In 1932, the idea of an electron microscope first came to the mind of Ernst Ruska who, afterwards, received the prestigious Nobel prize (1986) [33]. Only 4-years after his breakthrough, commercial TEMs started to be built. In TEM, the electron beam kinetic energy can range from 100 keV to 400 keV, and recently an ultra-high voltage TEM was built that can reach a superior value of 1.25 MeV for enhanced resolutions [34, 35]. Very fast, this TEM showed its limitations in terms of materials to investigate, since the high acceleration voltages induce important changes in the materials structure, e.g. the beam-induced damages.

The schematic representation of a TEM setup is displayed in Figure II.15, with the highlight on the main constitutive segments, which were progressively improved in time in an effort to achieve the ultimate resolutions. From a technological point of view, huge advances were achieved with the development of the correctors for the aberrations encountered in the condenser and objective lenses. Such correctors installed on commercial TEMs allow to rich point to point resolutions down to 70 pm in TEM parallel mode. In the same time, the development of new cameras and detectors allows one to gather different types of signals and to build up more and more complex approaches. As function of the information researched and the material investigated, several modes can be developed in a TEM. Only the working modes employed during the current investigations are further described.

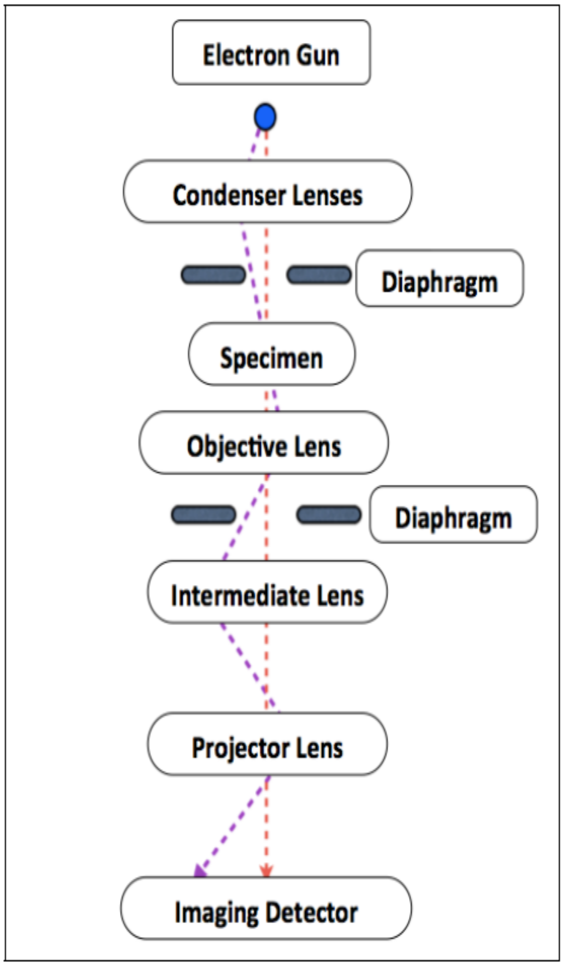

Figure.II.15. Schematic image representing the TEM basic setup.

II.3.3.1 HIGH RESOLUTION – TEM

In a TEM, an incident coherent parallel beam can be used to achieve high resolution enabling to visualize even atomic columns, e.g. High Resolution TEM. Different types of contrasts can be generated in TEM, for example diffraction contrast and mass-thickness contrast [36]. Upon electron-specimen interactions, the waves of the electrons that have interacted with the sample will undergo a phase shift as compared to electrons that have not interacted with the sample. This phase shift is the main component of the contrast when high resolution images are acquired, and this is the reason why the HRTEM imaging is named phase contrast imaging.

In the case of crystalline materials, their orientation in the zone axis as against the electrons beam is obligatory for HRTEM imaging. It can be achieved by specimen tilting in the microscope to the desired zone axis under diffraction mode. The diffraction mode is usually employed by selecting an area of interest from the sample to explore the material's crystal orientation and/or crystal structure within the very specific area [37]. The electronic diffraction is mainly described by Bragg's law [38].

II.3.3.2 SCANNING – TEM (STEM)

In STEM mode, a small energetic probe (highly-focused electron beam) scans the sample and with a well-defined speed [39]. The directly transmitted beam (elastically scattered and part of the diffracted electrons) is registered by a circular detector i.e. Bright-Field STEM imaging mode, whereas the electrons scattered at large angles are acquired by annular detectors under Dark Field STEM mode, as shown in Fig.II.16.a [40]. The transmitted beam can be detected on the BF detector, Fig.II.16.b. Electrons that are deviated over small angles with respect to the transmitted beam can be detected on the annular DF (ADF) detector (angles between 10 and 40 mrad). Electrons impinging on the ADF detector can be diffracted electrons; therefore the image is sensitive to diffraction contrast [41]. Whilst, electrons deviated at higher angles can be detected on the HAADF detector (angles > 40 mrad), Fig.II.16.c. The electrons collected by the HAADF detector are incoherently scattered [42], and the contrast in HAADF STEM depends on the atomic number Z, hence $I \propto Z^2$. Meaning that heavy elements (i.e. Sn) can be easily distinguished by a higher intensity area from lighter ones (i.e. Ge), which appears darker.

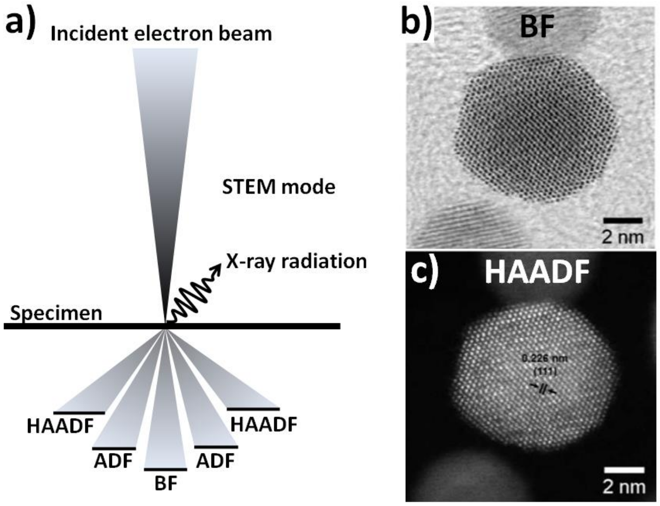

Fig.II.16. a) The STEM principle and the associated detectors located beneath the specimen; high-angle-annular dark-field (HAADF) annular dark-field (ADF), and bright-field (BF). The X-ray detector is located above the specimen surface. b) aberration-corrected STEM BF mode image of a PtCo NP, and c) HAADF mode of the same particle

Apart from the imaging contrast, the STEM methodology can be employed to probe the exact location of specific chemical events and/or to build up maps of the constitutive elements or of the chemical imprint (hybridization states for example) within the sample. To this end, additional spectroscopy devices are associated to the imaging mode, as described in the next section.

Similar with the TEM mode, the spatial resolution in the STEM mode can be improved by the addition of corrections for the spherical and/or chromatic aberrations. Such, sub nanometer resolutions are commonly attained in Cs probe corrected microscopes under STEM mode.

II.3.3.3 ENERGY DISPERSIVE X-RAY SPECTROSCOPY

The abovementioned TEM modes are mainly used for structural and crystallographic investigations, but chemical analysis can be performed as well by using the Energy Dispersive X-rays Spectroscopy (EDS) or Electron Energy Loss Spectroscopy (EELS). The principle behind the electron spectroscopy techniques within the TEM are schematized in Fig II.17. Such, an electron located in a core-state of an atom can be ejected by the energetic incident electron to an unfilled state or vacuum. Afterwards, a shell-electron fills the empty core-state resulting in a characteristic X-ray emission captured by the EDX detector, whereas the incident electrons which lost part of their energy will be collimated and detected on the EELS spectrometer. Each element in the periodic table has its own characteristic energy signature under EDS or EELS, which are further employed for the materials characterization.

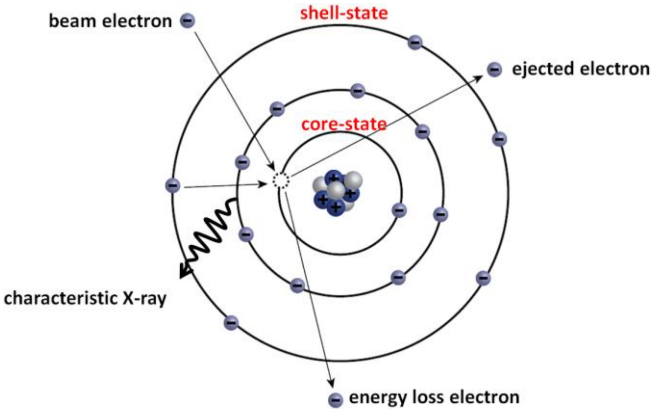

Figure.II.17. Schema of the fundamental emission processes of the characteristic x-rays, and the energy loss electrons, which are acquired afterwards by a dedicated EDX and EELS detectors.

In this study, the TEM experiments were carried out on a Cs probe corrected JEOL ARM200 TEM and a double corrected TEM, both analytical TEMs operated at 200kV. The double corrected TEM is equipped with a 100mm Centurio EDX detector and a Quantum GIF for the energy electron loss spectroscopy EELS. This configuration allows to attain spatial point resolutions down to 78 pm under TEM. A probe of 0.1 nm was used to scan the specimen in STEM mode. A camera length of 8 cm and high speed scanning protocol (5µsec/px) was employed for the STEM-HAADF images. 256x256px chemical maps were recorded for every element of interest by continuous scanning with exposures times of 20µseconds/px and for mean recording durations of 45 minutes. Cross-correlations algorithms were applied every 30 seconds along the experiment to avoid the maps misalignments due to specimen spatial drifts.

II.3.5 ATOM PROBE TOMOGRAPHY

The atom probe tomography (APT) is one of the most advanced forms of microscopy for atomic-scale characterizations. It is a high-resolution tri-dimensional analytical microscope. It is worth noting that APT is derived from the field ion microscope (FIM), and both were invented by Prof. Erwin Müller [43-45] and, more widely, is part of the field emission microscope family. The principle of APT relies on the atom evaporation and further ionization from a sample surface using a high electric field. In order to achieve such high field, a needle-like sample, with an apex radius less than 50 nm, which preparation by FIB, usually used for semiconductors, is subjected to a high positive voltage (typically between 2 to 15kV). The sharpness of the tip allows the electric field to be very intense at the apex (few tens of V/nm). The electric field F is given by:

$$F = \frac{V}{kR}$$

Where V is the standing voltage, R the curvature radius of the tip, and k is a geometrical factor taking into account the shape of the tip. By assuming k = 1, for a standing voltage of 2 kV and a tip radius of 50 nm, then the electric field on the apex of the tip is F = 40 V/nm. The sample is then evaporated atoms by atoms, atomic layer by atomic layer. The evaporation atom by atom is controlled by applying a voltage inferior to its evaporation field and then applying short electric pulses (for metals or alloys) or laser pulses (semiconductors) [Ref. Baptiste Gault, Atom Probe Microscopy]. The mass-to-charge ratio is, then, calculated using the ToF and the value of the applied voltage on the tip. Assuming that the evaporated atoms leaving the tip have no initial velocity, they acquire their speed from the electrostatic field in the chamber. In other words, the acquired kinetic energy (E_c) by an evaporated atom is equal to the potential energy (E_p) of the electrostatic field. Consequently, the energy conservation is written as $E_c = ½\, mv^2 = n\, e^- V = E_p$, where m and v are respectively the mass and speed of the atom, ne^- is the charge of the ion (n is the charge state 1+, 2+…), and V is the applied voltage. The maximum speed is attained by the ions just before they hit the detector, then, v = L/ToF (L is the distance between the tip and the detector). As a result, the mass-to-charge ratio can be calculated by:

$$\frac{m}{n} = 2eV[\frac{ToF}{L}]^2$$

The identification of the detected atoms is done by determining their mass-to-charge ratios which is derived from a direct measurement of ToF, L, and V for each single atom. It is worth noting that the APT experiment is carried out in an analysis chamber with an ultra-high vacuum (10^{-10} mbar) to avoid gases ionization at the tip surface. The tip is also cooled down to temperatures usually between 10 K and 80 K. This cryogenic temperature is important to reduce the thermal agitation at the surface of the tip and reduce the diffusion of atoms from the specimen across its surface.

In this study, Laser-Assisted Wide Angle Tomographic Atom Probe (LAWATAP, CAMECA shown in Fig.II.18) and Flexible-TAP (FlexTAP, CAMECA) are used for the analysis of semiconducting NWs. The FlexTAP enables the user to change distance between the sample and the detector, while this distance is fixed in LAWATAP. In these APTs, femtosecond lasers are implemented for an extremely short laser-pulse (400 fs) which is necessary to obtain a highly-resolved mass spectrum. In this work, a wavelength of λ = 515 nm (green), and a temperature of 80 K were chosen for the analysis of nanowires.

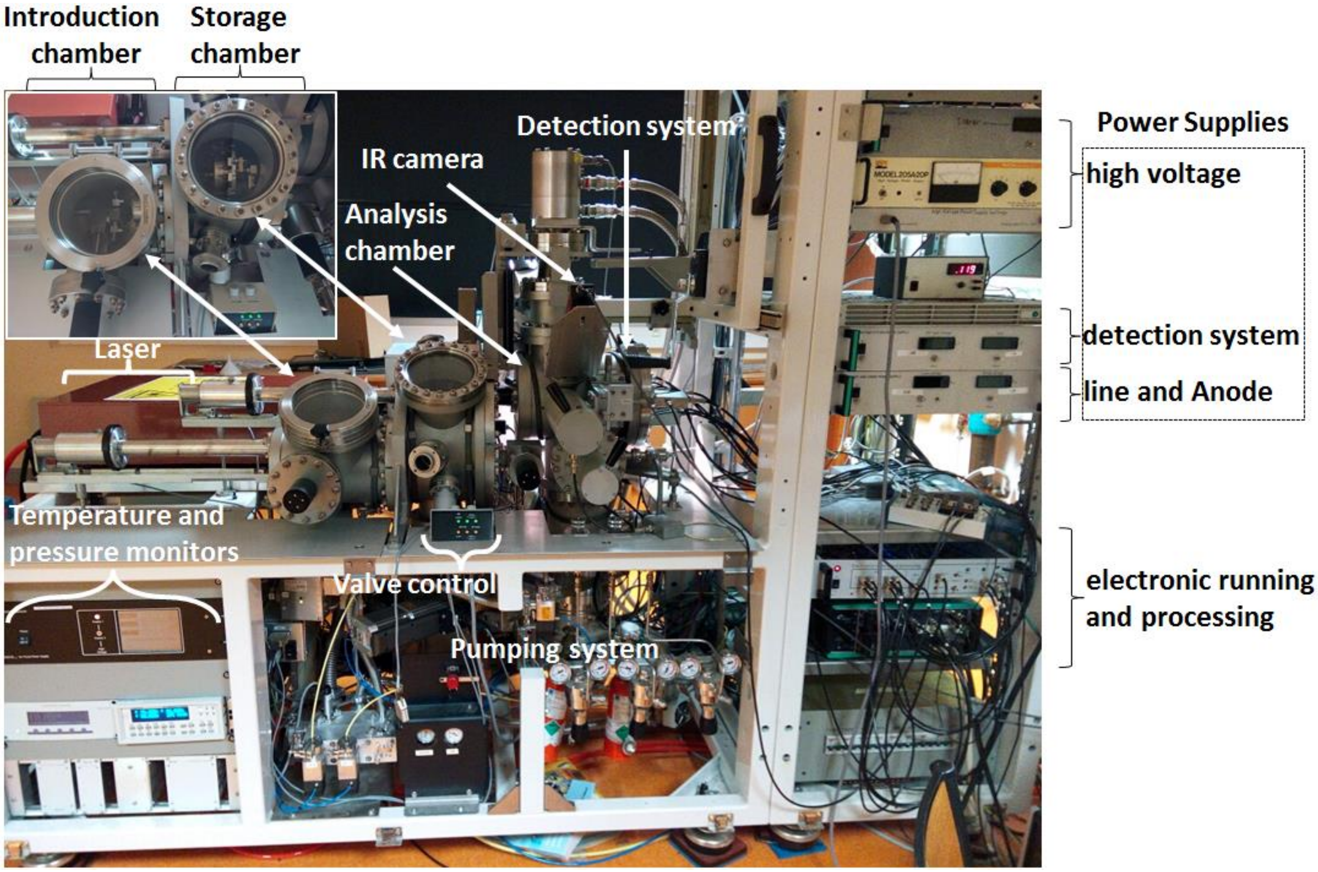

Figure.II.18. Photograph showing the LAWATAP used in this study.

II.3.5.1 3D VOLUME RECONSTRUCTION

The used ion detector is not only time-resolved (measures ToFs), but also sensitive to impact positions of ions (recording the X,Y coordinates of each ion) [46]. In modern APTs, the ion detector is enhanced by micro-channel plates (MCPs) to convert the impact of a single ion into a cascade of up to millions of electrons [47].

In the case of LAWATAP and FlexTAP, an advanced delay-line detector (aDLD) capable of resolving multi-ion hits simultaneously is placed behind the MCPs [48]. The aDLD consists of parallel conductive lines closely-assembled to form a conductive plate, Fig.II.19. Two conductive plates are used to determine the X,Y coordinates of the impact, knowing that each one of the conductive plates gives information about only one dimension (either X, or Y). The electron cloud formed by the MCPs upon the ion impact travels in the vicinity of the analysis chamber to reach the aDLD. The electronic system of the APT digitize the position of the atoms laterally (in X,Y dimensions).

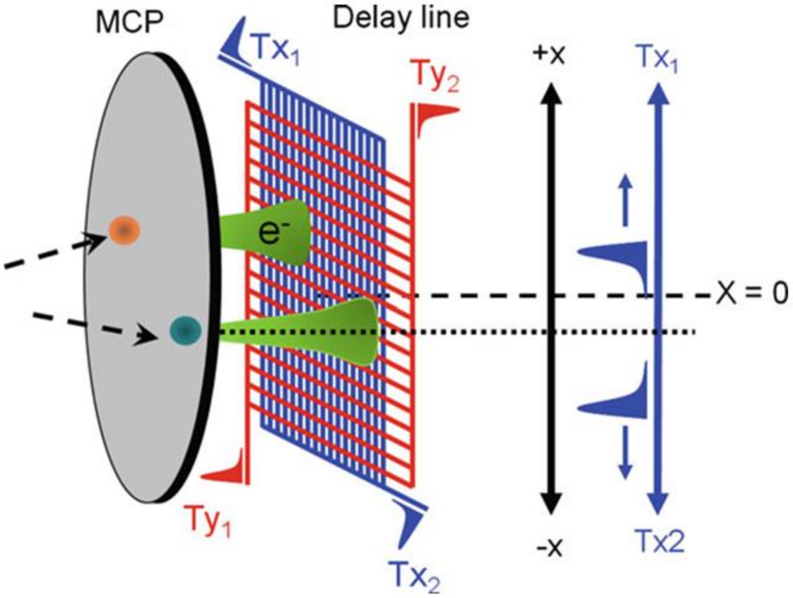

Figure.II.19. schematic illustration showing the concept of a delay-line detector [49]. Two ions hit the MCP which result in two electron clouds that travel towards the X,Y plates. Then the system measure the propagation time in X and Y plates in order to calculate the impact coordinates.

Two electrical signals are created when the electron cloud hits the two-plates of the aDLD. Afterwards, these signals travel through the conductive lines to reach the collectors of the X,Y plates. The propagation time to reach both ends of each plate can be measured which enables the determination of the lateral impact coordinates (X_D,Y_D) on the detector:

$$X_D = L_x \frac{T_{x2} - T_{x1}}{2T_{P_x}}$$

Where L_x is the length of the detector line, T_{x1} and T_{x2} are the times needed to reach both ends of the conductive line (for X-dimension), and Tp_x is the total propagation time for a signal travelling between both ends (along the entire line). Same analogy can be done for Y_D.

Using the coordination and sequence of arrival dataset recorded by the APT electronic system, all detected atoms can be traced back to their initial position on the tip. The reconstruction is then made atom by atom. Many models have been proposed in the past years concerning the 3-dimensional reconstruction [50-52]. Under the hypothesis that the reconstruction is performed by a point projection model, the general expression to determine the original atomic position on the surface of the tip is given by [53]:

$$x = \frac{X_D \ \xi \ V}{L \ k \ F}$$

Where x is the real x-dimension of the atom on the tip, X_D is the ion-MCP impact coordinate, ξ is the compression factor that takes into account the modification of the field lines due the constant change in the shape of the tip, and L is the flight length. The same analogy is used for y-dimension. From this simple expression which was established initially, a more complex and advanced algorithm was developed by Bas et al. [52] taking into consideration several parameters influencing the reconstruction such as: the tip curvature, and the tilt angle between the tip axis and the detector. In order to get a 3D reconstruction, a z position (depth coordinate) is calculated for each atom using the APT analysis data and several assumptions. [52] The reconstruction and data treatment (mass spectrum, composition, cluster, etc..; analyses) is made in the home-made GPM 3D software. It is worth noting that the reconstruction protocol works quite well for homogeneous materials. However, as far as several phases or layers are presents in the APT analysis, some limitations related to the trajectory aberrations of ions, known as local magnification effects, will distort the reconstruction, limit the spatial resolution and its capacity to investigate to probe the local composition [53, 54].

II.4 SUMMARY

In this chapter, a description of fabrication and characterization machines used in this thesis is given. Two catalyst elaboration techniques were used: magnetron sputtering coater, and thermal evaporator. Each was used to elaborate a different type of catalysts; the first is used to deposit a thin-film of ITO that will be transformed to InNPs using the PECVD reactor (as it will be discussed in Chapter III), the second is for evaporating Sn to form the NPs. The PECVD reactor is used for surface treatments, depositions, and growth of NWs.

Moreover, different characterization techniques are used for speculations and investigations of the obtained NWs. The FIB/SEM dual beam was used to fabricate specimens that are specially designed for TEM (lamella) and APT (tip). Furthermore, the SEM is used for feedback on the shape and size of the NWs, as well as the growth success rate after the fabrication process. The TEM allows having a deep insight on the NWs atomic structure, and the EDX allows the quantification of the components constituting the NWs. The APT is considered the ultra-fine characterization tool, with abilities to reconstruct in 3D real-space the atom-by-atom evaporated NWs. The mass-spectrometry, equipped in the atom probe, gives the ability of identifying the detected evaporated atoms with single atom precision. In the next chapter, the synthesis and characterization of the Ge and GeSn NWs catalyzed by In and Sn NPs will be detailed.

II.5 REFERENCES

1. Vossen, J., Kern, W., *"Thin film processes II" Academic Press (1991): 179. London.*
2. Vossen, J., Kern, W., *"Thin film processes II". Academic Press (1991): 184. London.*
3. Kelly, P.J., Arnell, R. D., *Magnetron sputtering: a review of recent developments and applications.* Vacuum, 2000. **56**(3): p. 159-172.
4. *http://slideplayer.com/slide/7404434/*.
5. Treutler, C.P., *Industrial use of plasma-deposited coatings for components of automotive fuel injection systems.* Surface and Coatings Technology, 2005. **200**(5-6): p. 1969-1975.
6. Cabarrocas, P., J. B. Chévrier, J. Huc, A. Lloret, J. Y. Parey, J. P. M. Schmitt, *A fully automated hot‐wall multiplasma‐monochamber reactor for thin film deposition.* Journal of Vacuum Science & Technology A, 1991. **9**(4): p. 2331-2341.
7. Hoshino, M., Matejčík Š, Nunes Y., Ferreira da Silva F., Limão-Vieira P., Tanaka H., *Negative ion formation through dissociative electron attachment to GeH4: Comparative studies with CH4 and SiH4.* International Journal of Mass Spectrometry, 2011. **306**(1): p. 51-56.
8. P Roca i Cabarrocas , K.K.-H., Cariou Romain, Labrune Martin, Johnson EV, Moreno M, Rios A Torres, Abolmasov Sergey, Kasouit Samir, *Low temperature plasma synthesis of nanocrystals and their application to the growth of crystalline silicon and germanium thin films.* MRS Online Proceedings Library Archive, 2012. **1426**: p. 319-329.

9. Wilfried van Sark , L.K., Francesco Roca, *Physics and technology of amorphous-crystalline heterostructure silicon solar cells*. 2012: Springer.
10. Kroesen, G.M.W., Beckers J., Trienekens D., Schrader A., van Heerebeek J., de Kluijver R. , *Particle charge and electrical field studied in the pre-sheath of an RF discharge.*
11. Adams, F., Barbante Carlo, *Chapter 7 - Electron-Based Imaging Techniques*, in *Comprehensive Analytical Chemistry*, F. Adams and C. Barbante, Editors. 2015, Elsevier. p. 269-313.
12. *Scanning Electron Microscopy*, in *Materials Science and Technology*.
13. Unakar, N.J., Tsui J. Y., Harding C. V., *Scanning Electron Microscopy.* Ophthalmic Research, 1981. **13**(1): p. 20-35.
14. Mayer Joachim, G.L.A., Kamino Takeo, Michael Joseph, *TEM Sample Preparation and FIB-Induced Damage.* MRS Bulletin, 2011. **32**(5): p. 400-407.
15. Thompson K., G.B., Larson D., Leer B. van, Hong L., *Minimization of Ga Induced FIB Damage Using Low Energy Clean-up.* Microscopy and Microanalysis, 2006. **12**(S02): p. 1736-1737.
16. Giannuzzi L. A., G.R., Ringnalda J., *2 keV Ga+ FIB Milling for Reducing Amorphous Damage in Silicon.* Microscopy and Microanalysis, 2005. **11**(S02): p. 828-829.
17. McCaffrey J. P., P.M.W., Madsen L. D., *Surface damage formation during ion-beam thinning of samples for transmission electron microscopy.* Ultramicroscopy, 2001. **87**(3): p. 97-104.
18. Park YK, N.T., Takai M, Lehrer C, Frey L, Ryssel H, *Comparison of beam-induced deposition using ion microprobe.* Nuclear Instruments and Methods in Physics Research Section B: Beam Interactions with Materials and Atoms, 1999. **148**(1-4): p. 25-31.
19. Saxey, D.W., Cairney J. M., McGrouther D., Honma T., Ringer S. P., *Atom probe specimen fabrication methods using a dual FIB/SEM.* Ultramicroscopy, 2007. **107**(9): p. 756-760.
20. Sadki, E.S., S. Ooi, and K. Hirata, *Focused-ion-beam-induced deposition of superconducting nanowires.* Applied Physics Letters, 2004. **85**(25): p. 6206-6208.
21. van Kouwen, L., Botman Aurelien, Hagen Cornelis W., *Focused Electron-Beam-Induced Deposition of 3 nm Dots in a Scanning Electron Microscope.* Nano Letters, 2009. **9**(5): p. 2149-2152.
22. Donev, E.U., Hastings J. Todd, *Electron-Beam-Induced Deposition of Platinum from a Liquid Precursor.* Nano Letters, 2009. **9**(7): p. 2715-2718.
23. Puretz J, S.L., *Focused ion beam deposition of Pt containing films.* Journal of Vacuum Science & Technology B: Microelectronics and Nanometer Structures Processing, Measurement, and Phenomena, 1992. **10**(6): p. 2695-2698.
24. Ferrari, A.C., Basko Denis M., *Raman spectroscopy as a versatile tool for studying the properties of graphene.* Nature Nanotechnology, 2013. **8**: p. 235.
25. Dresselhaus, M.S., Dresselhaus G., Saito R., Jorio A., *Raman spectroscopy of carbon nanotubes.* Physics Reports, 2005. **409**(2): p. 47-99.
26. Kneipp Katrin, K.H., Itzkan Irving, Dasari Ramachandra R., Feld Michael S., *Ultrasensitive Chemical Analysis by Raman Spectroscopy.* Chemical Reviews, 1999. **99**(10): p. 2957-2976.
27. Zumbusch, A., Holtom Gary R., Xie X. Sunney, *Three-Dimensional Vibrational Imaging by Coherent Anti-Stokes Raman Scattering.* Physical Review Letters, 1999. **82**(20): p. 4142-4145.
28. Rojas-López, M., H. Navarro-Contreras, P. Desjardins, O. Gurdal, N. Taylor, J. R. A. Carlsson, J. E. Greene, *Raman scattering from fully strained Ge1−xSnx (x⩽0.22) alloys grown on Ge(001)2×1 by low-temperature molecular beam epitaxy.* Journal of Applied Physics, 1998. **84**(4): p. 2219-2223.
29. Hai, L., Robert Chen, Yijie Huo, Theodore I. Kamins, James S. Harris, *Raman study of strained Ge1−xSnx alloys.* Applied Physics Letters, 2011. **98**(26): p. 261917.
30. Butler Holly J., A.L., Bird Benjamin, Cinque Gianfelice, Curtis Kelly, Dorney Jennifer, Esmonde-White Karen, Fullwood Nigel J., Gardner Benjamin, Martin-Hirsch Pierre L., Walsh Michael J., McAinsh Martin R., Stone Nicholas, Martin Francis L., *Using Raman spectroscopy to characterize biological materials.* Nature Protocols, 2016. **11**: p. 664.
31. Joy, D.C., *Limits of SEM Resolution.* Microscopy Today, 2018. **4**(5): p. 10-11.

32. de Broglie, L., *L'Oeuvre d'Einstein et la Dualit\'e des Ondes et des Corpuscules.* Reviews of Modern Physics, 1949. **21**(3): p. 345-347.
33. Ernst, R., *Electron microscope*. 1941, Google Patents.
34. Zhang, X.W., Boyen H. G., Deyneka N., Ziemann P., Banhart F., Schreck M., *Epitaxy of cubic boron nitride on (001)-oriented diamond.* Nature Materials, 2003. **2**: p. 312.
35. Hyung Seok, K., , Suh Ju Hyung, Park Chan Gyung, Lee Sang Jun, Noh Sam Kyu, Song Jin Dong, Park Yong Ju, Choi Won Jun, Lee Jung Il, *Structure and thermal stability of InAs/GaAs quantum dots grown by atomic layer epitaxy and molecular beam epitaxy.* Journal of Crystal Growth, 2005. **285**(1): p. 137-145.
36. Petroff, P.M., *Transmission electron microscopy of interfaces in III–V compound semiconductors.* Journal of Vacuum Science and Technology, 1977. **14**(4): p. 973-978.
37. L., R., *Electron diffraction methods in TEM, STEM and SEM.* Scanning, 1979. **2**(1): p. 3-19.
38. Bragg, W.L., Darbyshire J. A., *The structure of thin films of certain metallic oxides.* Transactions of the Faraday Society, 1932. **28**(0): p. 522-529.
39. Okunishi, E., Ishikawa Isamu, Sawada Hidetaka, Hosokawa Fumio, Hori Madoka, Kondo Yukihito, *Visualization of light elements at ultrahigh resolution by STEM annular bright field microscopy.* Microscopy and Microanalysis, 2009. **15**(S2): p. 164.
40. Friedrich, H., McCartney M. R., Buseck P. R., *Comparison of intensity distributions in tomograms from BF TEM, ADF STEM, HAADF STEM, and calculated tilt series.* Ultramicroscopy, 2005. **106**(1): p. 18-27.
41. Nellist, P., Pennycook SJ, *The principles and interpretation of annular dark-field Z-contrast imaging*, in *Advances in imaging and electron physics*. 2000, Elsevier. p. 147-203.
42. McBride, J.R., Kippeny Tadd C., Pennycook Stephen J., Rosenthal Sandra J., *Aberration-Corrected Z-Contrast Scanning Transmission Electron Microscopy of CdSe Nanocrystals.* Nano Letters, 2004. **4**(7): p. 1279-1283.
43. Müller, E.W., Bahadur Kanwar, *Field Ionization of Gases at a Metal Surface and the Resolution of the Field Ion Microscope.* Physical Review, 1956. **102**(3): p. 624-631.
44. Müller, E.W., *Resolution of the Atomic Structure of a Metal Surface by the Field Ion Microscope.* Journal of Applied Physics, 1956. **27**(5): p. 474-476.
45. Erwin, W.M., John A. Panitz, S. Brooks McLane, *The Atom‐Probe Field Ion Microscope.* Review of Scientific Instruments, 1968. **39**(1): p. 83-86.
46. *A. Cerezo, T.J. Godfrey, G.D.W. Smith, Rev. Sci. Instrum. 59, 862–866 (1988).*
47. Blavette, D., Deconihout B., Bostel A., Sarrau J. M., Bouet M., Menand A., *The tomographic atom probe: A quantitative three‐dimensional nanoanalytical instrument on an atomic scale.* Review of Scientific Instruments, 1993. **64**(10): p. 2911-2919.
48. G. Da Costa, H.W., S. Duguay, A. Bostel, D. Blavette, B. Deconihout, *Advance in multi-hit detection and quantization in atom probe tomography.* Review of Scientific Instruments, 2012. **83**(12): p. 123709.
49. Gault, B., Michael P, Cairney Julie M, Ringer Simon P, *Atom probe microscopy*. Vol. 160. 2012: Springer Science & Business Media.
50. *D. Blavette, A. Bostel, J.M. Sarrau and J. Gallot, Proc. 29th IFES (1982) p. 497.*
51. Blavette, D., Sarrau JM, Bostel A, Gallot J, *Direction et distance d'analyse a la sonde atomique.* Revue De Physique Appliquee, 1982. **17**(7): p. 435-440.
52. Bas, P., Bostel A., Deconihout B., Blavette D., *A general protocol for the reconstruction of 3D atom probe data.* Applied Surface Science, 1995. **87-88**: p. 298-304.
53. Gault, B., De Geuser Frederic, Stephenson Leigh T, Moody Michael P, Muddle Barrington C, Ringer Simon P, *Estimation of the reconstruction parameters for atom probe tomography.* Microscopy and Microanalysis, 2008. **14**(4): p. 296-305.
54. Melkonyan Davit, F.C., Arnoldi Laurent, Demeulemeester Jelle, Kumar Arul, Bogdanowicz Janusz, Vurpillot Francois, Vandervorst Wilfried, *Atom probe tomography analysis of SiGe fins embedded in SiO2: Facts and artefacts.* Ultramicroscopy, 2017. **179**: p. 100-107.

III IN-PLANE SOLID-LIQUID-SOLID GERMANIUM NANOWIRES

Germanium is a good candidate to integrate in Si-based technologies in order to develop new applications ranging from integrated circuit interconnects to new generations of electronics [1, 2]. Fabricating Ge in a 1-dimensional nanowire configuration allows the downsizing of Ge-based electronic nanocomponents. Therefore, growing in-plane GeNWs for convenient 2D planar integrations is a crucial and important aspect to achieve for further development in the domain of electronics. However, the growth of these building blocks (GeNWs) is not well explored as for SiNWs. It has been demonstrated that lateral SiNWs can be grown using wide variety of catalyst, and implemented into many technologies. One of the most used mechanisms of growth for SiNWs is the SLS mechanism. It is an important mode of fabrication since it allows obtaining SiNWs that are in-plane. These SiNWs have been implemented in a wide variety of functional technologies, such as: SiNW-based FET [3, 4], sensors [5], and solar-cells [6]. In this chapter, we will investigate the possibility of growing Indium-catalyzed GeNWs using the SLS mechanism. It is important to understand the influence of certain growth parameters on the GeNWs, which allows to fully control and master the GeNWs growth. Moreover, SEM, FIB, and TEM were used as characterization techniques to provide structural and compositional information, which enables comprehending the effect of growth parameters.

III.1 GROWTH USING INDIUM-TIN NANOPARTICLES

The first step in the growth procedure is the formation catalyst NPs, namely, InSn NPs. A Si (111) was used as a substrate for the deposition of an ITO thin film. The PVD of ITO was done in the magnetron sputtering reactor where an ITO target was sputtered by a 200 W Ar^+ plasma for 10 min at 180°C under 6×10^{-3} mbar, Fig.III.1.a.c. The thickness of the deposited ITO thin film is ~ 400 nm. It is noteworthy, that it is also possible to deposit ITO films at room temperature [7]. Then the Si substrate containing the ITO film is introduced in the PECVD reactor. A Hydrogen plasma is ignited in the chamber under the conditions: 5 W, 0.38 Torr, H_2 flow 100 sccm “standard cubic centimeter”, 1 min and T = 400°C (which is above the melting point of In 156.6°C). The surface of the ITO film is chemically reduced by hydrogen atoms and transformed into a Sn-doped In layer. This superficial metal layer de-wets and agglomerates to form catalyst NPs [8]. As shown in Fig.III.1.d, the ITO surface has been roughened compared to the untreated ITO which means that the H_2 plasma has reduced the surface creating reactively the InSn NPs. It has been shown that the diameter of InSn NPs is proportional to the temperature (i.e. InSn diameter increases with the increasing temperature) [9]. The EDX measurement shows that under these fabrication conditions, the NPs are made of 90 % In and 10 % Sn, hence, we consider referring to these In-rich droplets as In NPs [10].

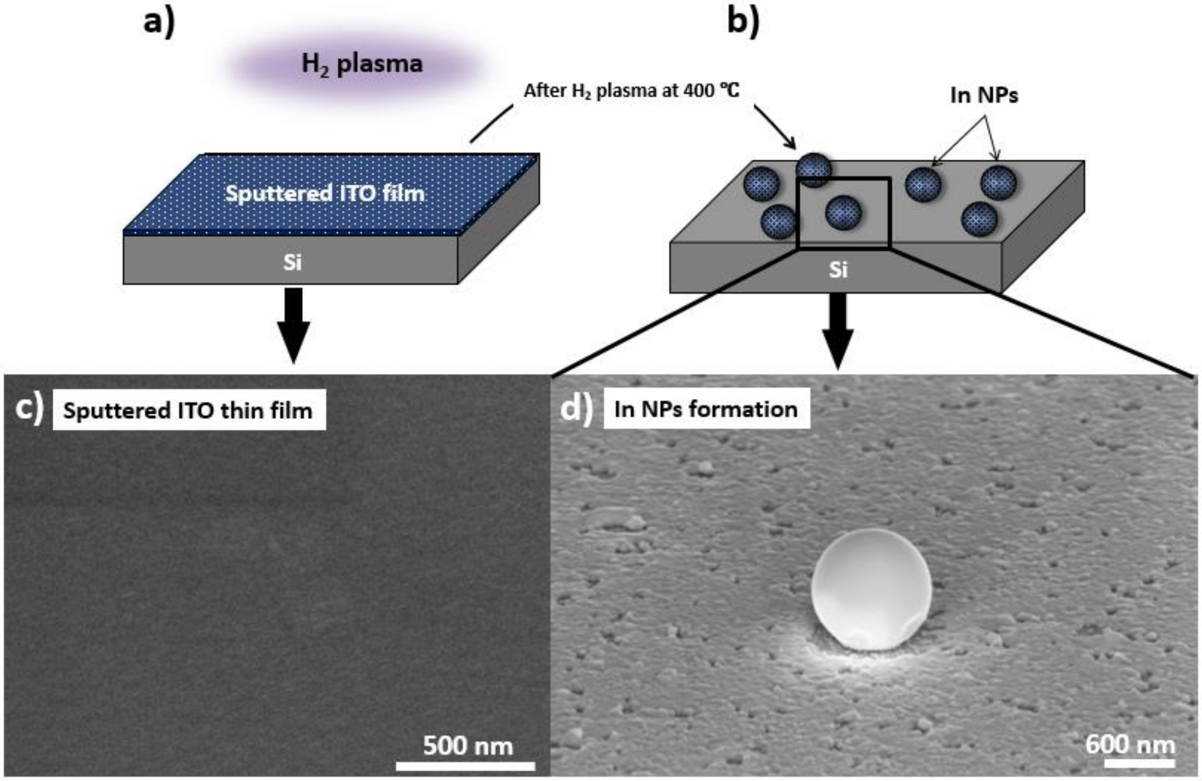

Figure.III.1.Schematic representation of the In NPs formation process: a) the thin film of ITO deposited using the RF sputter reactor, is exposed to a hydrogen plasma at 400℃. b) after the chemical reduction of ITO, In NPs are formed. c) SEM image top-view of as-deposited ITO film. d) SEM image tilted view (50°) showing the In NP formation after the H_2 plasma treatment.

III.1.1 GERMANIUM CRYSTALS

Before initiating the Ge NW growth, an amorphous Ge layer should be deposited on top of the catalyst NPs. The thickness of the amorphous layer is a very important factor for NW growth. The objective is to supersaturate the NPs in order to precipitate crystalline Ge seeds and for this reason the thickness of the a-Ge:H must be adapted to the size of the catalyst. In the case of Si, its solubility in In is lower than 0.01 at.% at 300℃ and less than 0.1 at.% at 600℃, therefore, In NPs are easily saturated by Si at the annealing temperature used. Meanwhile, in the case of Ge, its solubility in In is ~ 1 at.% at 300℃, and more than 10 at.% at 600℃ [11]. In other words, Ge is 100 times more soluble in In NPs than Si at the temperatures used in this study. As a result, the a-Ge:H layer should be thicker than the a-Si:H layer to achieve the supersaturation in the In NPs. As a preliminary measurement of the a-Ge:H thickness, a spectroscopic ellipsometry is used. Fig.III.2.a shows the real and the imaginary parts of the pseudo-dielectric function of an a-Ge:H film deposited on a corning glass under the conditions indicated in table in FigIII.2.b. The modelling (based on Tauc-Lorentz model [12]) of the spectra indicates that the film thickness is ~ 14 nm. The deposition rate of a-Ge:H is 2 × 10^{-2} nm/s for the conditions shown in Fig.III.2.b.

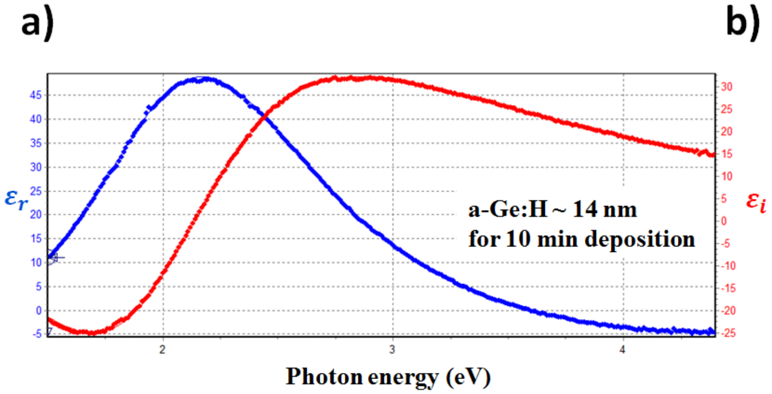

b)

Parameters	Conditions
Temperature	120°C
Pressure	0.3 Torr
H_2 flow	40 sccm
GeH_4 flow	50 sccm
Plasma power	2 W
Duration	10 min

Figure.III.2. Deposition rate measurement of a-Ge:H. a) measurements and the fitting results of a-Ge:H deposited on a corning glass by a phase-modulated ellipsometry from 1.5 to 4.5 eV with incident angle of 70°. b) the deposition conditions used to obtain a deposition rate of 2 × 10^{-2} nm/s.

Our first attempt to grow GeNWs using In NPs as a catalyst was not successful, as shown in Fig.III.3.a. From the SEM observations, it can be inferred that there is no sign of Ge seed formation. In fact, the a-Ge:H deposition is done in 5 min, that means the estimated thickness is ~ 7 nm. The amount of Ge is not enough to supersaturate the catalyst droplets, specially that the annealing process is done at ~ 440℃ which means that the solubility of Ge in In is between 3 at.% and 5 at.% [11]. Purposely to investigate if the deposited Ge quantity is sufficient for supersaturation, we calculated the amount of Ge consumed in this case, and estimated its atomic percentage in the In droplet. The concentration of Ge is estimated to be ~ 0.05 at.% which is far lower than the amount needed for supersaturation. In a second trial shown in Fig.III.3.b, the thickness of a-Ge:H is increased to ~ 28 nm. In this case, Ge seeds nucleate on the bottom edges of In droplets, which means that the supersaturation is reached. Normally the catalyst should travel a longer distance to produce a c-NW, but in this case the distance travelled is short with respect to the catalyst size, for this reason we call these structures Ge nanocrystals (GeNCs). Here, it is important to cite few potential applications for the Ge crystals; for example: detectors for Gamma ray spectroscopy because of the low band-gap energy (0.7 eV) of Ge resulting in the creation of a large number of electron-hole pairs (which means an enhanced sensitivity) [13, 14]. Moreover, In-doped Ge crystals (p-type) have a great potential in the field of nanoelectronics [15-17]. The fact that the Ge NWs in Fig.III.3.b are short might be related to the annealing temperature. It has been demonstrated that amorphous Ge starts to crystallize at temperatures above 350℃ [18, 19]. The amorphous-to-crystalline transition affects the system in a way that stops the growth earlier. Indeed, the driving force for NW growth is the difference in Gibbs energy between the a-Ge and c-Ge. The thermodynamic force derived from the Gibbs energy difference between the front absorption edge and the back deposition edge of the catalyst is insignificant if the growth temperature is above 350℃, because all the bottom edges of the catalyst are in contact with a crystalline Ge structure.

To solve this problem, the same conditions have been used for the growth, except that the annealing temperature was reduced from 440℃ to 220℃ to prevent the a-Ge:H crystallization. Even though the catalysts shown in Fig.III.3 (b) and (c) are fabricated using the same parameters, there is a large size distribution in both samples. Therefore, here, we show two different sizes to compare the growth trials using different catalyst sizes. Attempts have shown that even if the temperature is reduced below the crystallization temperature of a-Ge:H, only Ge seeds are formed with no further growth (no NWs), Fig.III.3.c. By comparing Fig.III.3. (b) and (c), smaller catalysts (diameter = 1 µm ± 100 nm) can grow larger Ge-seed (with respect to their diameter) compared to catalysts from (b) (diameter = 2 µm ± 300 nm). It should be noted that in section III.1.3, long Ge NWs are produced with the same conditions but with different catalyst size.

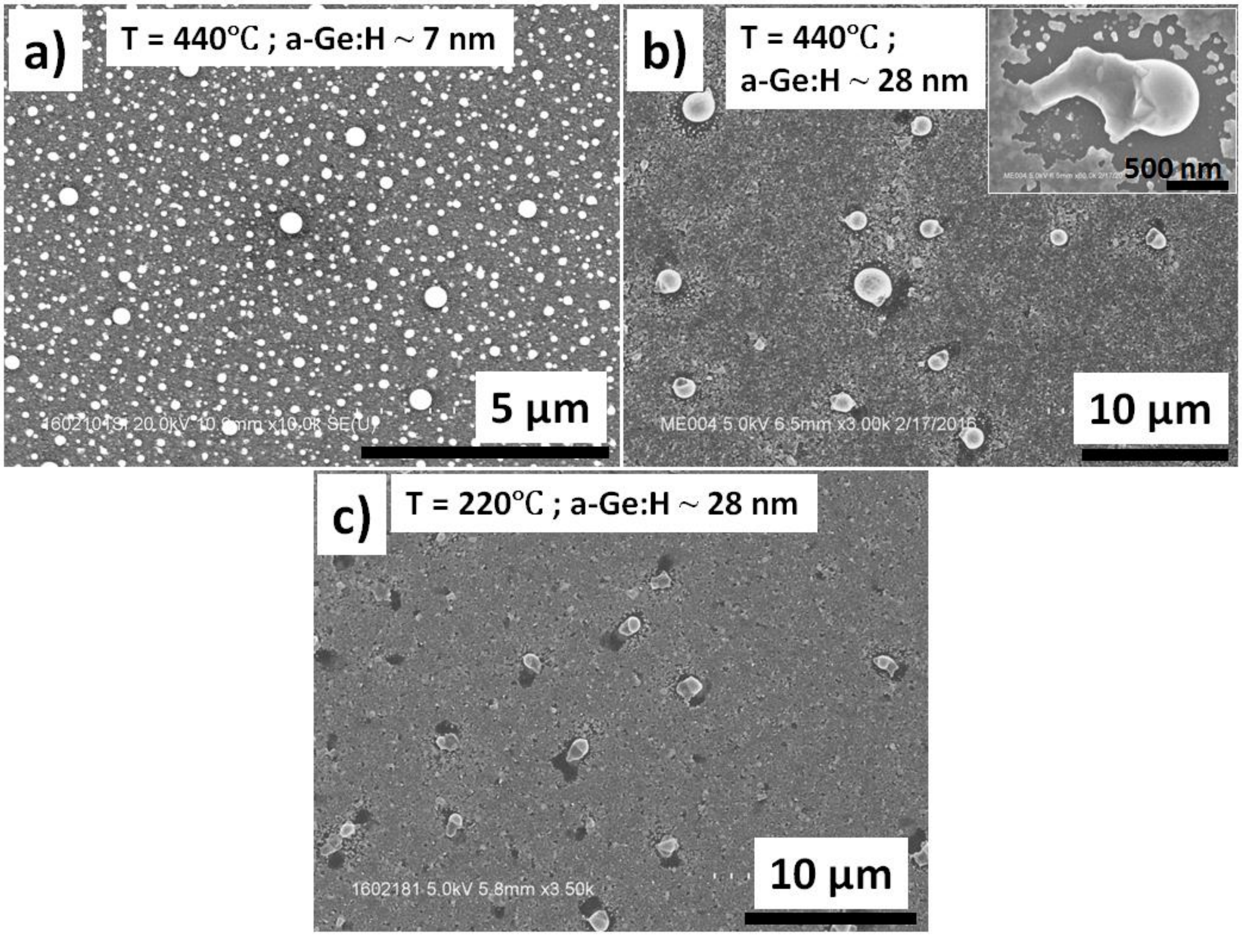

Figure.III.3. SEM observations of In-catalyzed GeNWs growth trials. a) no GeNWs observed due to inactive In NPs. The deposited a-Ge:H thickness on top of the system is estimated to be ~ 7 nm. b) Same conditions as in (a) but with a thicker a-Ge:H layer ~ 28 nm. Ge crystals have been formed on the bottom edges of In NPs. c) Bigger Ge crystals are formed with respect to the size of the catalysts, which is clear by comparing (b) and (c).

The TEM is used to investigate their structure, and composition, as well as the interface SiO_x/GeNCs (SiO_x denotes “native silicon oxide”). The crystalline nature of GeNCs is proven by TEM micrographs shown in Fig.III.4. The interface Ge/Si is separated by a native silicon oxide with a thickness ranging between 2 nm to 3 nm. The SiO_x is considered to have a rougher surface compared to the crystalline Si substrate which affect the GeNCs crystallinity inducing structural defects, see Fig.III.4.b,c,d in the Ge region. The depicted white dashed-line in Fig.III.4.c is a Ge grain at the interface with a different orientation than its surrounding. The STEM-HAADF micrograph of the same grain (Fig.III.4.d) shows no contrast difference related to Z (atomic number) meaning that it is indeed a Ge grain.

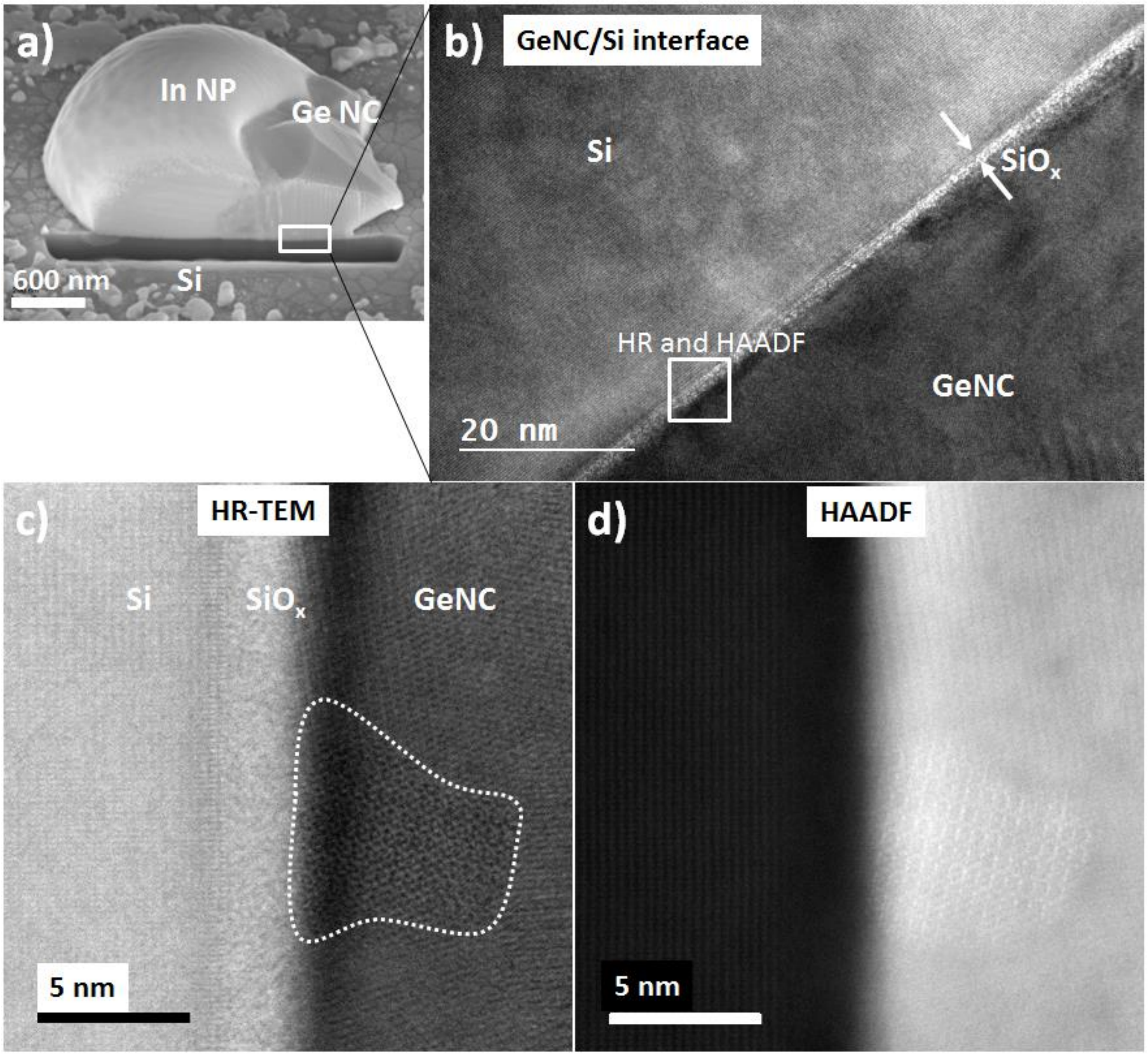

Figure.III.4. Structural analysis of the interface GeNC/Si. a) SEM tilted view (54°) during FIB milling, b) TEM micrograph shows a part of the GeNC/Si interface, c) HR-TEM micrograph showing a highly magnified part of the interface. The dashed white line depicts a Ge grain with a different orientation than its surroundings, and d) HAADF STEM micrograph of the same grain, the dark region is the Si substrate and the bright region is the GeNC. No contrast difference between the grain and the surrounding NC, which means that they are both Ge.

The linear concentration profiles, obtained by EDX measurements, prove that In exists at the interface. The quantifications, done in Fig.III.5, indicates a maximum value of 4 at.% ± 1 at.% of In. As a possible explanation, In atoms get bonded on the SiO_x because of the existing dangling bonds on the oxide surface. Here it is worth mentioning that despite approximately 2 nm SiO_x exist according to the TEM micrographs in Fig.III.4, the EDX concentration profile in Fig,III.5.b only shows ~ 30 at.% oxygen at the interface, which is due to the EDX resolution.

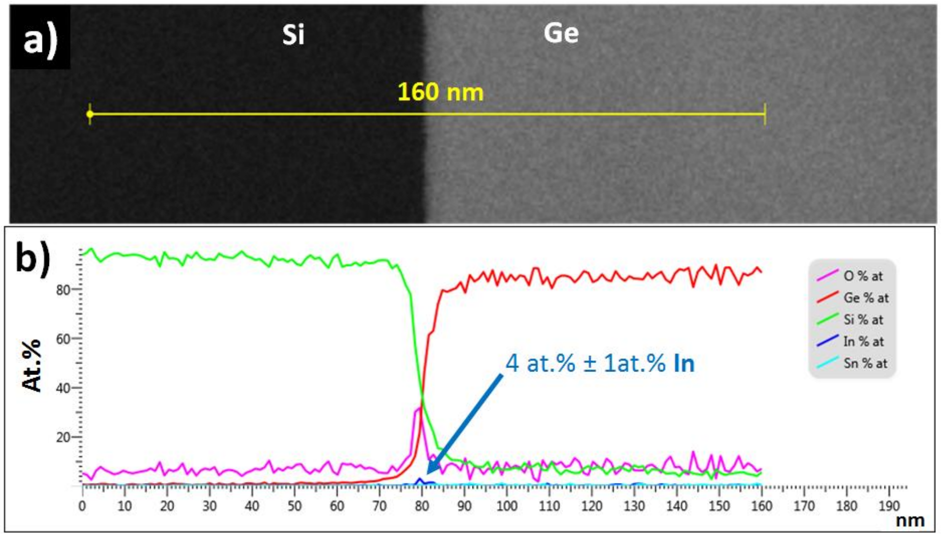

Figure.III.5. Compositional analysis of the GeNC/Si interface, a) TEM image of the investigated area along the 160 nm line, b) atomic concentration profile of Ge/Si along the interface. Oxygen (up to 30 at.%) exist on the interface due to SiO_x. In is present with an atomic percentage of up to 4%. Note that the complement to 100% is due to presence of the Cu grid nearby the analyzed area, plus the Ga and Pt atoms that are incorporated at the surface of the sample during the ion beam preparation process.

Not only Ge grains can exist at the Si/GeNC interface, HAADF-STEM shows a bright contrast indicating the presence of heavier elements (Fig.III.6.a). The EDX cartography, in Fig.III.6.b, shows the existence of In and Sn elements at the interface. The EDX quantifications of the InSn-rich region show that the compositions are: 68 at.% Ge; 19 at.% O; 11 at.% In; and 1 at.% Sn. Two hypotheses may explain the presence of such region: i) the sputtered ITO layer may not be completely converted to InSn droplets during the H_2 plasma reduction, thus, leaving a residual untreated region behind, and ii) The location of the scanned area is close to the GeNC/catalyst interface. By looking at Fig.III.6.b, the oxygen atoms seem to be more located at the native oxide region, but not preferentially located in the metal-rich region. As a consequence, the possibility (i) of an untreated residual ITO layer is ruled out leading the analysis to the second possibility.

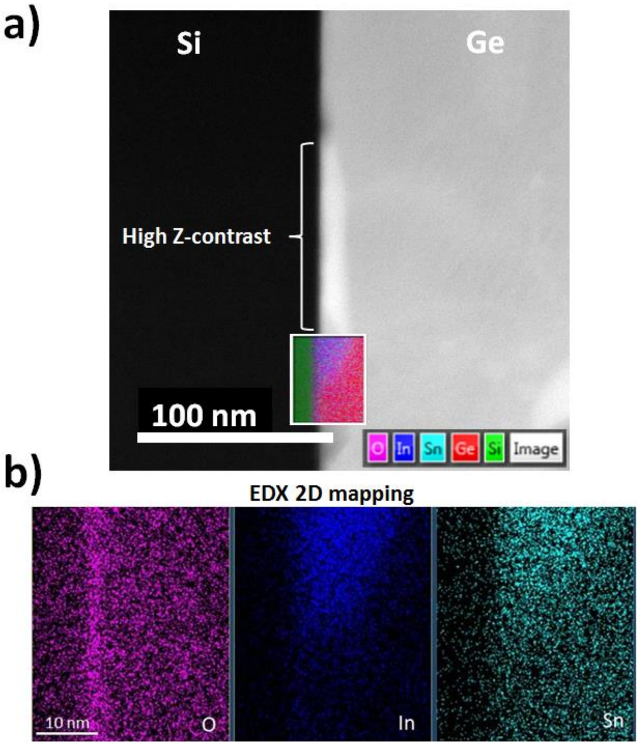

Figure.III.6. InSn exists at the interface between Ge and Si. a) STEM-HAADF shows a Z-contrast difference at the interface, a 2D EDX cartography is also shown on the same micrograph revealing the existence of InSn, b) explicit EDX cartography shows O, In, and Sn distribution in this region.

In general, no heteroepitaxy is found between the GeNC and the Si substrate. As an exception, on one local part along the scanned interface we did find a region without native oxide, where the GeNC is in direct contact with the c-Si underlying substrate as shown in Fig.III.7.a (white circle). The crystalline Si surface seems to influence the Ge structure by inducing a certain crystalline orientation in the GeNC. In this particular Ge region, fewer defects are observed compared to when it is in contact with the SiO_x. To prove the better crystallinity, a selected area electron diffraction pattern (SAEDP) was done for the GeNC nearby the "heteroepitaxy" region, Fig.III.7.b. The zone axis in the SAEDP is evaluated to be [$\bar{2}33$]. This kind of epitaxial growth phenomenon was demonstrated for in-plane SiNWs on Si (100) wafers where the crystallographic orientations of the Si (100) help aligning (or guiding) the SiNWs. Moreover, the crystalline structure of the Si substrate was reflected epitaxially along the entire SiNWs [20]. Indeed, the in-plane nanostructures are heavily influenced by the underlying substrate. Therefore, one of the possibilities to improve the crystalline structure of the NC (and NWs) is to make a direct contact with a crystal surface.

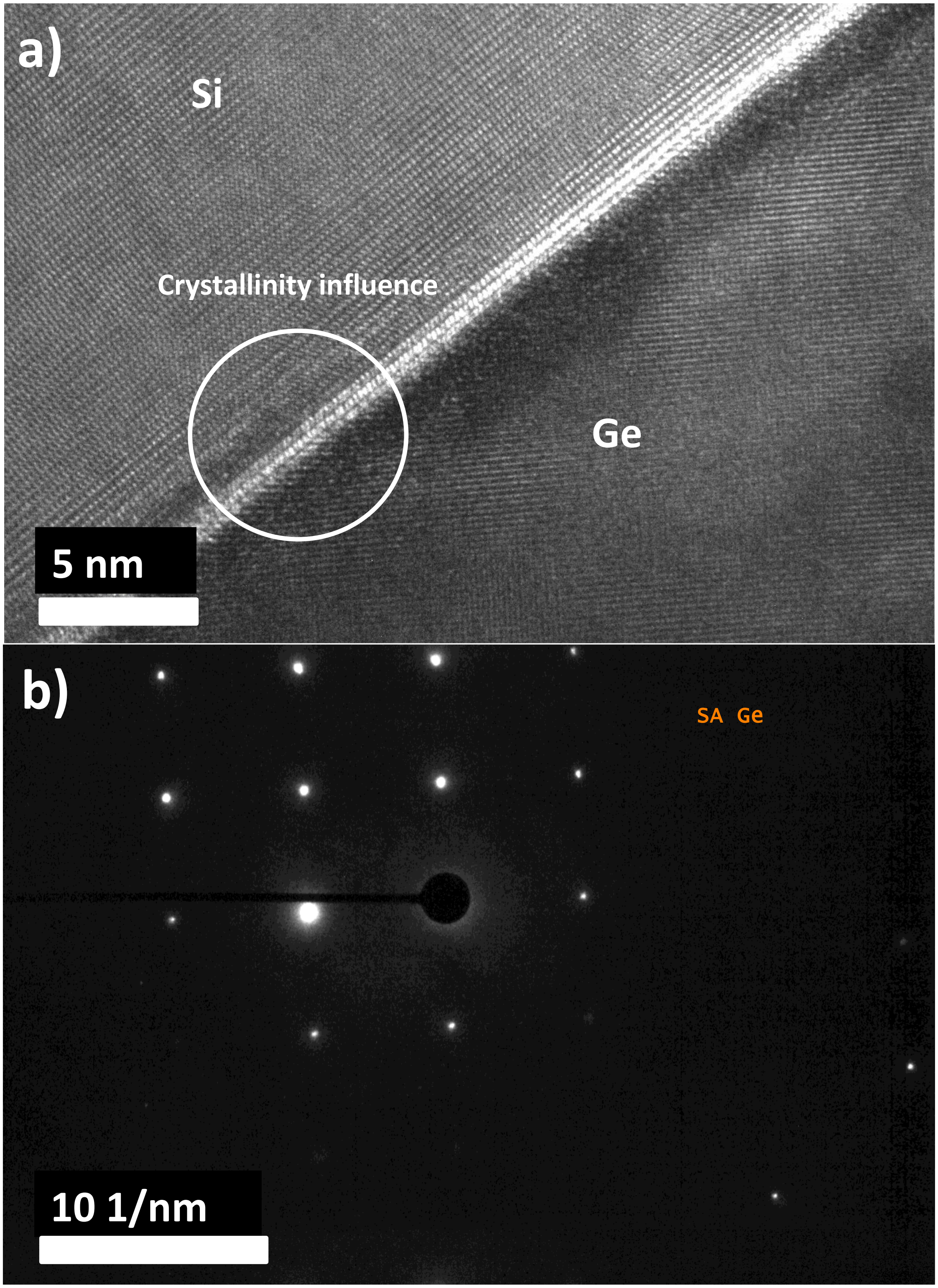

Figure.III.7. Region of heteroepitaxy between GeNC/Si. a) HR-TEM micrograph shows the depicted region of heteroepitaxy. The crystallinity of Ge is highly improved upon this crystal contact, b) SAEDP of the GeNC nearby the heteroepitaxy region; the zone axis is $[\bar{2}33]$.

III.1.2 EUTECTIC CATALYST

During the FIB operations, eutectic structures were observed in catalyst NPs such as these in Fig.III.8.a. Many catalysts have shown to be nanostructured on the inside (see inset of Fig.III.8.a, which is a magnified image of the catalyst cross-section). The difference in contrast is firmly related to Z, this means two kinds of lamellas (or rods) are built inside the catalyst (possibly Ge and In). However, the interesting point is that the Ge-In binary phase diagram (Fig.III.8.b) shows an eutectic point at 99.9927 at.% for In, hence, 0.0073 at.% for Ge at a temperature 156 ℃, which is not enough for the Ge to build such structures.

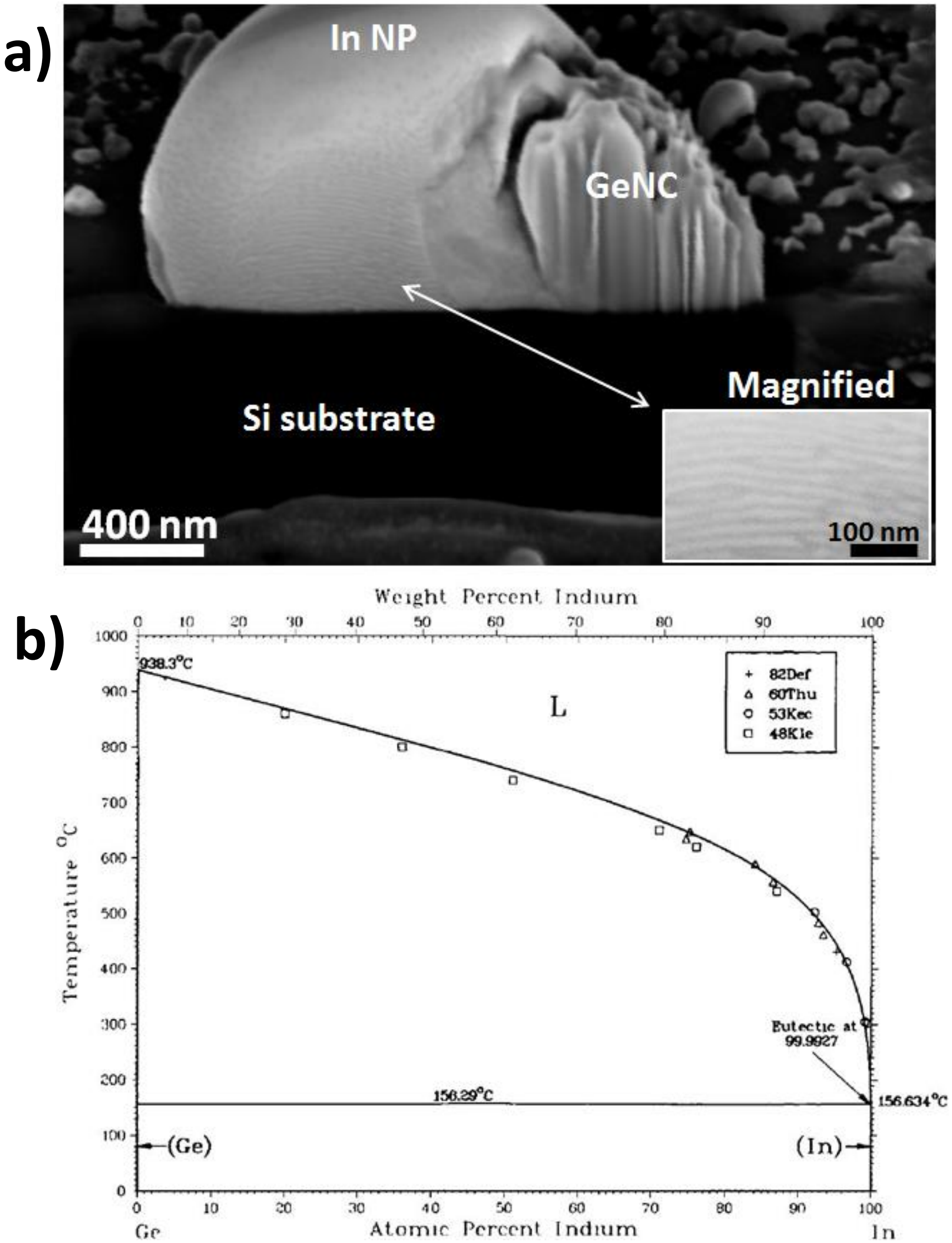

Figure.III.8. Eutectic structure in In catalyst, a) SEM micrographs showing nanostructured In catalyst. The brighter lamellas (or rods) have a width of 17 nm ± 2 nm and the darker have 15 nm ± 2 nm. It is noteworthy that these milling operations are done using the FIB ZEISS XB 540.

b) Ge-In phase diagram

To investigate the composition, TEM-EDX measurements are needed. Unfortunately, the FIB seemed to affect the eutectic structure of the catalysts during the preparation of TEM lamellas, as shown in Fig.III.9. Small In NPs form around the bigger In droplets when milling using FIB in nearby regions, as depicted by the black arrows in Fig.III.9a. Up to 12 catalysts have been milled using FIB, all of them showing eutectic structures during the first part of milling. Then, these structures are completely lost during the advancement of the preparation which means that no nanostructuring is observed by SEM at the end. In Fig.III.9.b, it can be noticed that the catalyst under the ion-operation have a shape of a molten liquid, even though it is protected by a Pt layer. Possibly the FIB is raising locally the temperature, and the In has a relatively low melting temperature of In (156.6℃) could lead to this behavior.

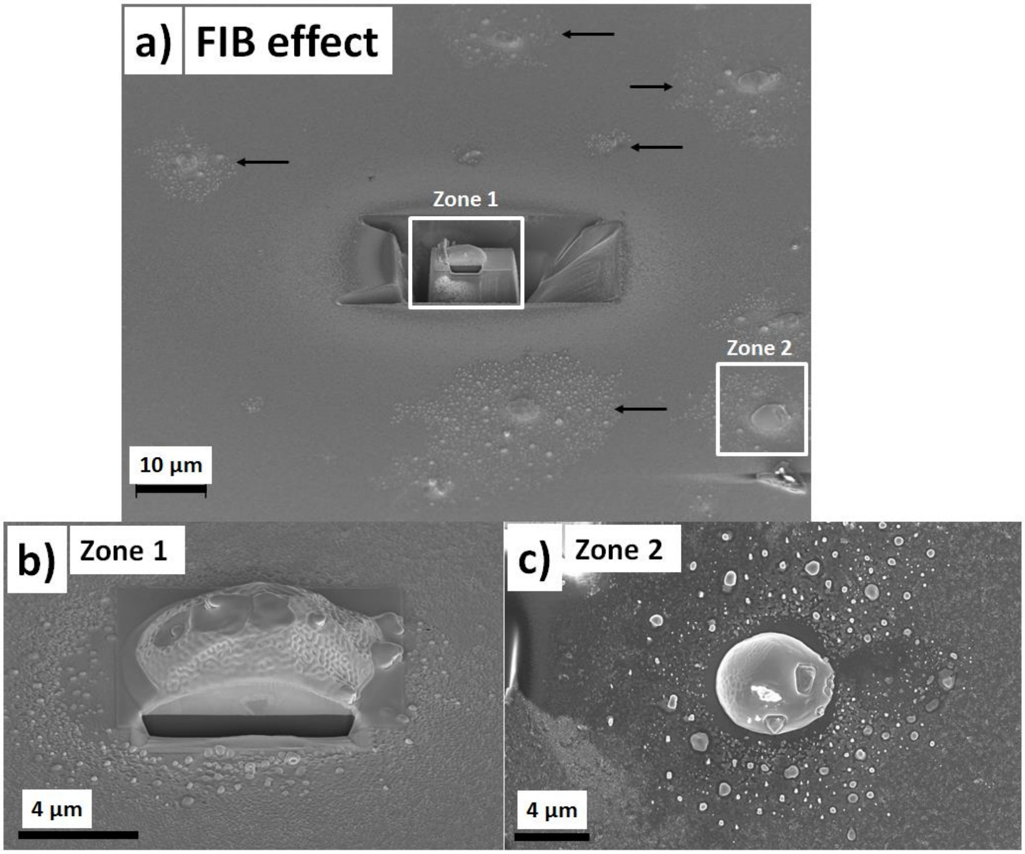

Figure.III.9. SEM micrographs showing that FIB is affecting the catalyst. a) A general view around the milling region, where the black arrows indicate the affected catalysts. Small NPs start to appear around In droplets, b) a magnified image of zone 1 shows that the catalyst appear as a "melt" with NPs around, despite that the catalyst is protected by a Pt layer. c) A magnified image of zone 2 shows an unprotected catalyst by Pt, NPs start to grow in the surrounding upon FIB milling in nearby region. The milling process was done in FIB NVISION 40.

Despite this deteriorating effect, a TEM lamella was made for fine structural and compositional investigations. No eutectic structure was observed in the catalyst using TEM due to FIB processing, Fig.III.10.a,b. Moreover, it was found that the high energy electron beam induces a recrystallization in the catalyst, Fig.III.10.c. The recrystallized region of In increases in size for an increased exposure under the 200 keV beam, Fig.III.10.d. The quantification measurements using EDX showed that the In NP is made of almost 100 at.% In. Meanwhile, Fig.III.10.(e) and (f) show that Ge grains exist on the surface of the catalyst. These grains are located between the Pt layer and the catalyst surface, and their sizes vary between 10 nm and 40 nm. How did the Ge grains form on the surface of the catalyst? To answer this question we need to analyze the growth procedures of the GeNCs. In the beginning of the process, In NPs are in their liquid state dissolving Ge atoms from the amorphous layer. After the formation of Ge crystal seeds at the bottom edges of the catalyst, the dissolved Ge atoms will diffuse towards the most favorable c-Ge seed. When the temperature is decreased, the thermodynamic process starts to slow down. The Ge atoms remaining inside the catalyst will be either deposited on a c-Ge seed, or diffuse outside the catalyst to reach the surface (because the solubility of Ge in In decreases with the decreasing temperature), or they will stay inside the catalyst (forming the eutectic structure). Yet, another explanation can be proposed for the formation of these grains. It is shown that FIB affects the structure of the catalyst by heating it locally; maybe the eutectic structure inside the catalyst which is possibly made of Ge/In lamellas (or rods) disappears due to the diffusion of Ge atoms towards the outer surface of the catalyst and forming these Ge grains. Since experimentally it is hard to investigate due the previously mentioned limiting factors, a calculation based on SEM observation is made. It is important to know if the Ge quantity inside the catalyst is enough to build these lamellas (inside the In) or grains (on the In surface). In Fig.III.11, the region around the catalyst (depicted by a white line) corresponds to the consumed a-Ge:H layer. By measuring the surface, and knowing the thickness of a-Ge:H layer, the number of Ge atoms that are consumed by the In NP having a diameter D = 1.3 μm can be estimated. Using the same analogy, the number of Ge atoms needed to build the GeNC can be estimated by measuring its volume (knowing that GeNCs are stable under the FIB). The same calculation is done for 12 catalysts of the same sample. By comparing these two values, we find that there is an excess of 30 at.% to 40 at.% of Ge inside the catalyst which is more than enough to build the GeNC and Ge lamellas.

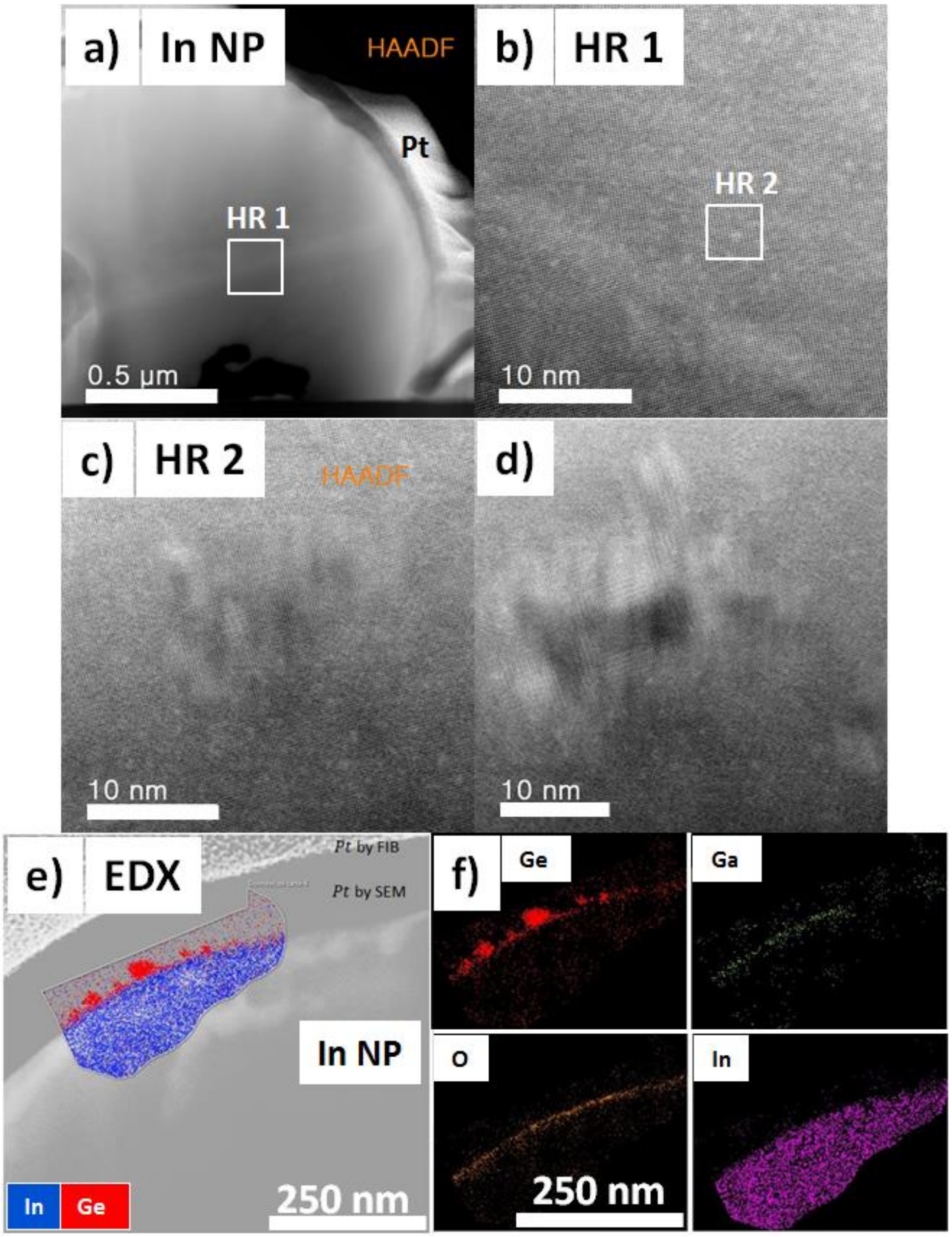

Figure.III.10. In NP TEM investigations, a) STEM-HAADF micrograph of an In catalyst protected by a Pt layer, no eutectic structure is found. b) HRTEM micrograph of zone HR1 in (a), showing a grain boundary and white dots around it. c) HRTEM micrograph showing a recrystallization process of In due to the high energy electron beam. d) HR of the same region showing the increase in size of the defect created by the beam with the increase of exposure time. e) 2D EDX cartography showing grains of Ge on the surface of the catalyst. f) an explicit elemental view and their distribution of the same region shown in (e). The Ge grains are penetrated by Ga ions due during the IBID process. The Oxygen is coming from the native oxide formed by In upon the contact with atmosphere.

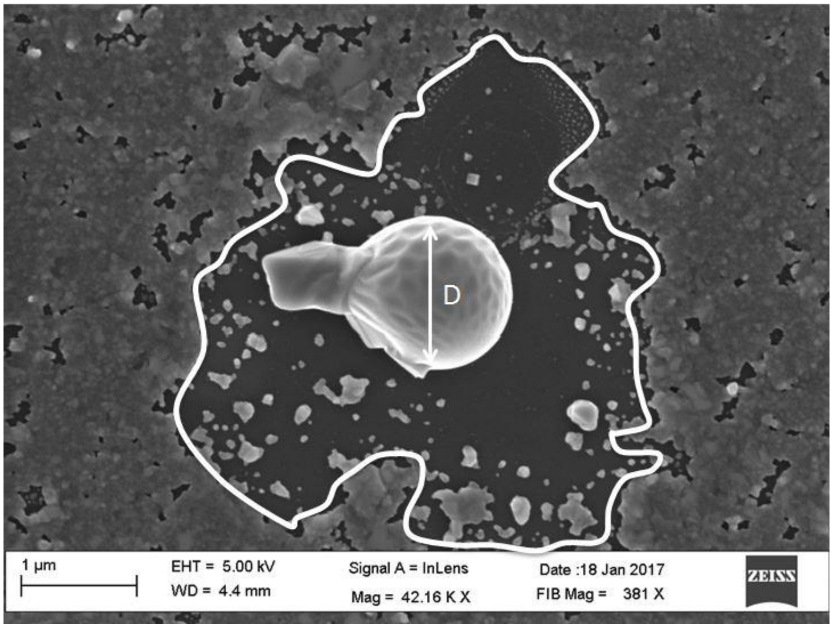

Figure.III.11. A SEM micrograph of GeNC grown by In NP. The depicted region is the consumed a-Ge:H, and D is the catalyst diameter.

III.1.3 GERMANIUM NANOWIRES

The inability to grow long GeNWs seemed to be related to the catalyst size, as can be inferred from Fig.III.12. Bigger catalyst sizes (diameter ~ 1 µm), like the one shown in Fig.III.12.a, travel a short distance compared to InNPs that have catalyzed the NWs in Fig.III.12.b. Moreover, the small catalysts seem to be totally consumed by the NWs; therefore the direct measurement of their diameters cannot be performed. Nonetheless, the trench size indicates approximatively the diameter of the catalyst which is in this case (Fig.III.12.b) close to 60 nm.

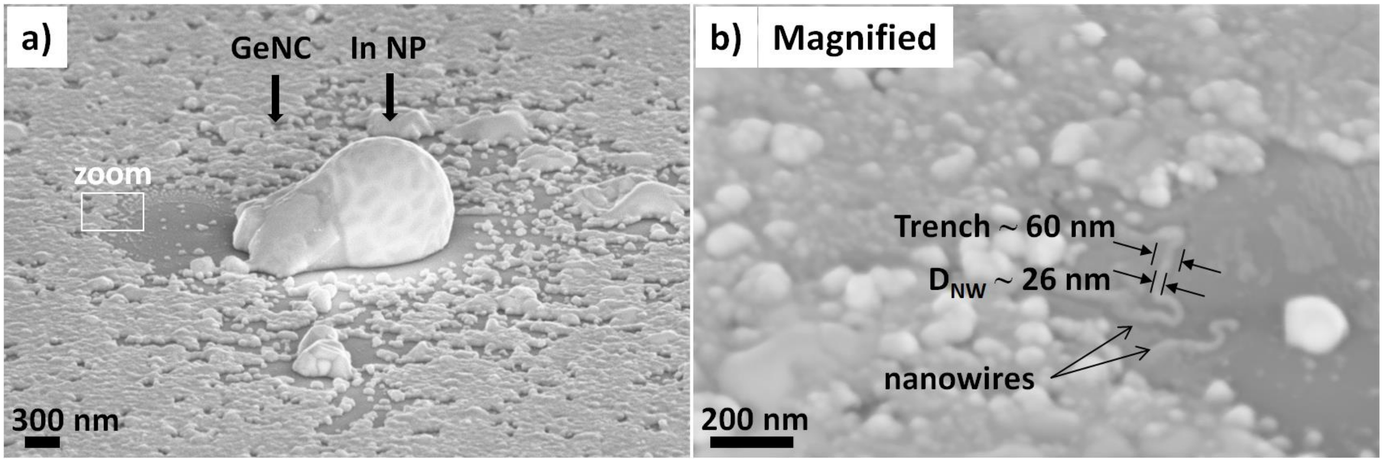

Figure.III.12. SEM images tilted (54°) showing the effect of In NP size on the growth of GeNWs. a) GeNC grown by a 1 μm diameter In droplet. b) Magnified image of the depicted trench region in (a) showing the growth NWs with a diameter D_{NW} ~ 26 nm. The trench is 60 nm wide, which is indicates approximatively the In NP diameter.

The size effect has already been explained by the discoverers of the SLS mechanism Linwei Yu and Pere Roca i Cabarrocas [21]. The absorption flux rate J_{in} is considered to be dependent on the Ge diffusion flux inside the catalyst, Fig.III.13.a (see section I.3 in Chap.I). This diffusion is imposed by the Ge concentration gradient (inside the catalyst) between the front absorption edge and the back deposition edge. A Ge mass transport inside the catalyst is created due to this gradient. Moreover, the deposition flux rate J_{out} is considered to be dependent on the nucleation barrier of Ge onto the NW, Fig.III.13.a (see section I.3 in Chap.I). Linwei Yu et al. (ref. [21]) have fitted these flux rates as a function of Si concentration in In NPs, Fig.III.13.b. As a function of Si concentration inside the InNP, the red line represents the deposition flux rate and the blue lines represent the absorption flux rates for different catalyst sizes (L_{Ci} with i = 1,2,3). The L_c denotes the length of the catalyst. It is noteworthy to mention that the catalyst shape is fluctuating during the growth, therefore the catalyst diameter is not constant, and may be elliptical in some cases. A closer look on Fig.III.13.b shows that when the catalyst size decreases from L_{C1} to L_{C3} the absorption and deposition flux rates increase, which means that catalysts having small L_{Cs} travel faster on the surface of the substrate. The dissolution of the amorphous layer is faster as well as the deposition process for small sized catalysts.

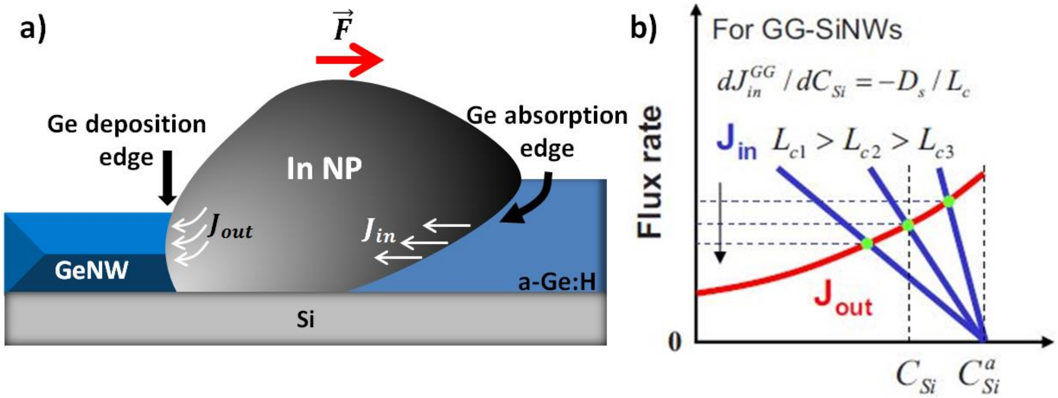

Figure.III.13. Theoretical explanation of the catalyst size effect on the growth of GeNWs. a) Schematic illustration showing the absorption (J_{in}) and deposition (J_{out}) edges on the bottom part of the catalyst. b) Depicts the variation in the balanced condition in the catalyst drops with different sizes of $L_{C1} > L_{C2} > L_{C3}$ [21].

Interestingly, the samples having large In droplets (700 nm to 1.5 µm) also have smaller ones (i.e. 60 nm to 200 nm) due to the large size distribution during the formation of InNPs by H_2 plasma. Fig.III.14 shows that long GeNWs are successfully grown with lengths up to 15 µm.

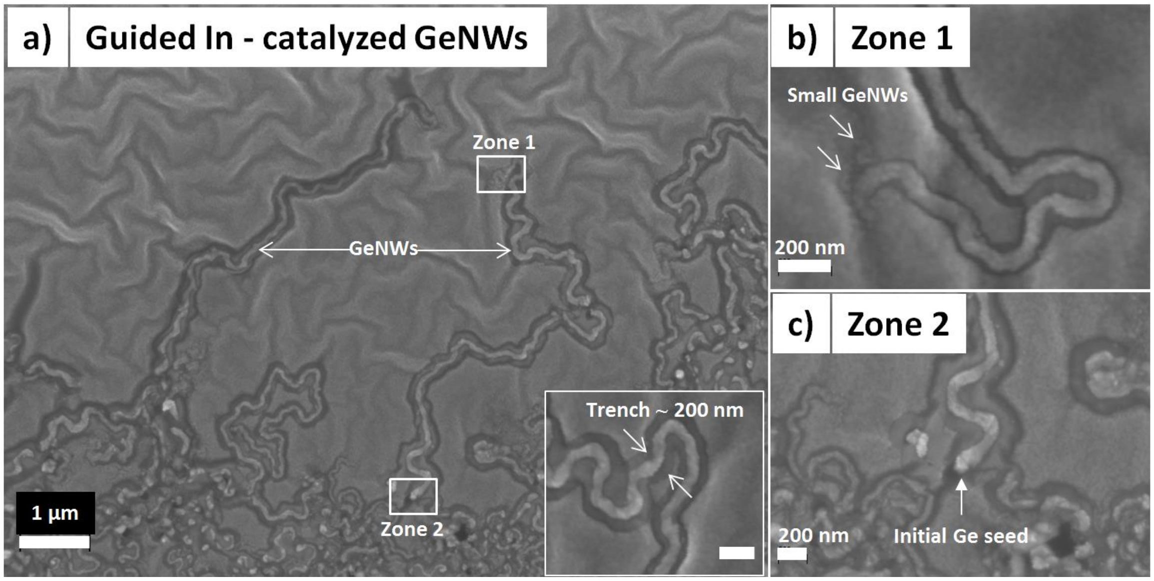

Fig.III.14. SEM images showing In-catalyzed GeNWs guided by surface patterns. a) the length of these NWs can reach up to 15 µm. The sample features surface defects that guides the NWs growth. The inset shows the trench size ~ 220 nm (scale bar 200 nm). b) A magnified image of zone 1 which corresponds to the end region of the NW's growth. Small NWs are produced (indexed by white arrows) due to the splitting of the In NP into smaller ones. c) A magnified image of zone 2 showing the initial Ge crystal seed precipitated at the beginning of the growth process.

The important point is that the long GeNWs are obtained under the same growth conditions of GeNCs (in other words both NCs and NWs were obtained on the same sample). The only difference is the catalyst size. These NWs seem to be guided by patterns (which are basically substrate defects) featured on the surface. This implies that GeNWs catalyzed by In NPs can be intentionally guided by a patterned substrate (using lithography for instance).

III.2 SUMMARY

In this chapter, the study covered the fabrication of In-catalyzed Ge NCs and NWs. The objective was to fabricate GeNWs using the catalyst and mechanism as used for SiNWs. In droplets were implemented for this SLS growth. It was shown that the a-Ge:H layer should have enough thickness to supersaturate the catalyst, and then to precipitate the crystalline Ge. Using these Indium droplets, GeNCs were obtained. Their crystallinity is shown to be affected tremendously by the substrate structure. Therefore for improving the crystalline quality of GeNCs, they should grow directly on a crystalline interface. After the FIB cross-sectional milling, the SEM shows that In droplets are nanostructured. Most probably, a eutectic structure was formed by alternation of Ge and In phases inside the droplet. However, it was not possible t achieve TEM or APT characterizations due to ion-induced damages during the preparation process in FIB.

Moreover, it was shown that in-plane SLS GeNWs can be fabricated using In NPs. In fact, decreasing the size of the catalyst can increase the length of NWs. This can be explained by the increased deposition rate for small sized NPs (i.e. ≤ 200 nm) compared to bigger sizes. Therefore long In-catalyzed IPSLS GeNWs were produced, and were intrinsically guided by the defects on the surface of the substrate. It means that GeNWs can be equally guided using simple surface features (such as step-edges, or substrate crystallinity influence) just like SiNWs.

III.3 REFERENCES

1. Yu, B., Sun, XH, Calebotta, GA, Dholakia, GR, Meyyappan, M, *One-dimensional germanium nanowires for future electronics.* Journal of Cluster Science, 2006. **17**(4): p. 579-597.

2. Higashi, H., Kasahara, K, Kudo, K, Okamoto, H, Moto, K, Park, J-H, Yamada, S, Kanashima, T, Miyao, M, Tsunoda, I, *A pseudo-single-crystalline germanium film for flexible electronics.* Applied Physics Letters, 2015. **106**(4): p. 041902.
3. Cui, Y., Zhong, Zhaohui, Wang, Deli, Wang, Wayne U, Lieber, Charles M, *High performance silicon nanowire field effect transistors.* Nano letters, 2003. **3**(2): p. 149-152.
4. Yu, L., Chen, Wanghua, O'Donnell, Benedict, Patriarche, Gilles, Bouchoule, Sophie, Pareige, Philippe, Rogel, Regis, Claire Salaun, Anne, Pichon, Laurent, Roca i Cabarrocas, Pere, *Growth-in-place deployment of in-plane silicon nanowires.* Applied Physics Letters, 2011. **99**(20): p. 203104.
5. Rurali, R., *Colloquium: Structural, electronic, and transport properties of silicon nanowires.* Reviews of Modern Physics, 2010. **82**(1): p. 427.
6. Yu, L., Misra, Soumyadeep, Wang, Junzhuan, Qian, Shengyi, Foldyna, Martin, Xu, Jun, Shi, Yi, Johnson, Erik, Cabarrocas, Pere Roca, *Understanding light harvesting in radial junction amorphous silicon thin film solar cells.* Scientific reports, 2014. **4**: p. 4357.
7. Mikio, M., Hiroaki Kakinuma, Masaaki Sakamoto, Hideo Sawai, *Plasma Etching of ITO Thin Films Using a CH 4 /H 2 Gas Mixture.* Japanese Journal of Applied Physics, 1990. **29**(10A): p. L1932.
8. Alet, P.-J., Yu Linwei, Patriarche Gilles, Palacin Serge, Roca i Cabarrocas Pere, *In situ generation of indium catalysts to grow crystalline silicon nanowires at low temperature on ITO.* Journal of Materials Chemistry, 2008. **18**(43): p. 5187-5189.
9. Linwei, Y., Benedict O'Donnell, Martin Foldyna, Pere Roca i Cabarrocas, *Radial junction amorphous silicon solar cells on PECVD-grown silicon nanowires.* Nanotechnology, 2012. **23**(19): p. 194011.
10. Fan, Z., Maurice Jean-Luc, Chen Wanghua, Guilet Stéphane, Cambril Edmond, Lafosse Xavier, Couraud Laurent, Merghem Kamel, Yu Linwei, Bouchoule Sophie, Roca i Cabarrocas Pere, *On the Mechanism of In Nanoparticle Formation by Exposing ITO Thin Films to Hydrogen Plasmas.* Langmuir, 2017. **33**(43): p. 12114-12119.
11. Keck, P.H., Broder Jacob, *The Solubility of Silicon and Germanium in Gallium and Indium.* Physical Review, 1953. **90**(4): p. 521-522.
12. Kildemo, M., Ossikovski R, Stchakovsky M, *Measurement of the absorption edge of thick transparent substrates using the incoherent reflection model and spectroscopic UV–visible–near IR ellipsometry.* Thin Solid Films, 1998. **313**: p. 108-113.
13. Scovell, P., Meehan E, Araújo HM, Dobson J, Ghag C, Kraus H, Kudryavtsev VA, Majewski P, Paling SM, Preece RM, *Low-background gamma spectroscopy at the boulby underground laboratory.* Astroparticle Physics, 2018. **97**: p. 160-173.
14. Simpson, J., *The euroball spectrometer.* Zeitschrift für Physik A Hadrons and Nuclei, 1997. **358**(2): p. 139-143.
15. Chroneos, A., H. Bracht, R. W. Grimes, B. P. Uberuaga, *Vacancy-mediated dopant diffusion activation enthalpies for germanium.* Applied Physics Letters, 2008. **92**(17): p. 172103.
16. Kube, R., H. Bracht, A. Chroneos, M. Posselt, B. Schmidt, *Intrinsic and extrinsic diffusion of indium in germanium.* Journal of Applied Physics, 2009. **106**(6): p. 063534.
17. Feng, R., F. Kremer, D. J. Sprouster, S. Mirzaei, S. Decoster, C. J. Glover, S. A. Medling, J. L. Hansen, A. Nylandsted-Larsen, S. P. Russo, M. C. Ridgway, *Electrical and structural properties of In-implanted Si1−xGex alloys.* Journal of Applied Physics, 2016. **119**(2): p. 025709.
18. P. Germain, K.Z., S. Squelard, J. C. Bourgoin, A. Gheorghiu, *Crystallization in amorphous germanium.* Journal of Applied Physics, 1979. **50**(11): p. 6986-6994.
19. Fumiya, O., Yoshio, Ogawa, Yoshibumi, Fujiki, *Effect of Deposited Metals on the Crystallization Temperature of Amorphous Germanium Film.* Japanese Journal of Applied Physics, 1969. **8**(8): p. 1056.
20. Yu, L., Xu Mingkun, Xu Jie, Xue Zhaoguo, Fan Zheng, Picardi Gennaro, Fortuna Franck, Wang Junzhuan, Xu Jun, Shi Yi, Chen Kunji, Roca i Cabarrocas Pere, *In-Plane Epitaxial Growth of*

Silicon Nanowires and Junction Formation on Si(100) Substrates. Nano Letters, 2014. **14**(11): p. 6469-6474.

21. Yu, L., i Cabarrocas Pere Roca, *Growth mechanism and dynamics of in-plane solid-liquid-solid silicon nanowires.* Physical Review B, 2010. **81**(8): p. 085323.

IV IN-PLANE SOLID-LIQUID-SOLID GERMANIUM-TIN NANOWIRES

The objective of this thesis is the fabrication of a GeSn alloy in a NW configuration. GeSn alloy has already started grabbing the attention of many researchers, due its huge potential properties. It can be used many functional applications such as: Laser emission in mid-infrared region [1], Li-ion batteries [2], photodiodes [3], FinFET [4], and MOSFET [5]. The SLS mechanism is very interesting since it can lead to a faster growth rates compared to the classical VLS. Therefore, it can be used as a strategy to increase the incorporation of catalyst atoms in Ge NWs as it was demonstrated for SiNWs [6]. Here, the SLS method is implemented to grow GeSn NWs.

In the first part of this chapter, the growth of Sn-catalyzed IPSLS SiNWs (fabricated by Dr. Xue Zhaoguo at LPICM) will be discussed.

In the second part, the same mechanism used for SiSn NWs (i.e. SLS) will be used for the GeSn NWs. Growth attempts were done using two Sn-based precursors are used: i) pure Sn NPs, and ii) SnO_2 NPs. Compositional and structural characterizations are done for GeSn NWs.

In the third part, Sn concentrations are also measured for SiNWs to compare with the results of GeSn NWs. The quantifications are done using the APT.

IV.1 IN-PLANE SOLID-LIQUID-SOLID SILICON-TIN NANOWIRES

Si nanowires (SiNWs) are one important type among a wide variety of nanomaterials. What is boosting the interest in these NWs is the ability to engineer their properties and shapes for different kinds of applications. For instance, the growth path of IPSLS SiNWs can be controlled by guiding the catalysts using step-edges (or by the influence of the Si substrate crystallinity) to design functional networks or circuits [7, 8]. Moreover, SiNWs can be doped and prepared for nanoelectronic [9] or photovoltaic [10] applications. However, alloying Si with Sn is fundamentally a hard task to achieve. The phase diagram of Si-Sn shows that Sn cannot be incorporated in Si at the growth temperatures used in our processes (300℃ to 400℃), the solubility of Sn in Si is ~ 0.01 at.% at these temperatures [11]. Nevertheless, it is crucial to achieve such an alloy regarding to the major improvement in its properties, which are very useful in the domain of nanoelectronics [12] and has a great potential for photovoltaics [13].

These SiNWs have been fabricated using the IPSLS mechanism, which is the same one used for the growth of GeSn NWs. The growth includes five steps to synthesize these NWs: i) deposition of Sn NPs via thermal evaporation, ii) creation of Sn strips using standard lithography (Fig.V.1.a), iii) Sn native oxide removal by H_2 plasma reduction iv) deposition of an a-Si:H layer on top of these strips, and v) annealing the sample at temperatures above the eutectic point of Sn (Fig.V.1.b-e). The fabrication of these samples was done by Mr. Zhaoguo Xue at LPICM – École Polytechnique Palaiseau.

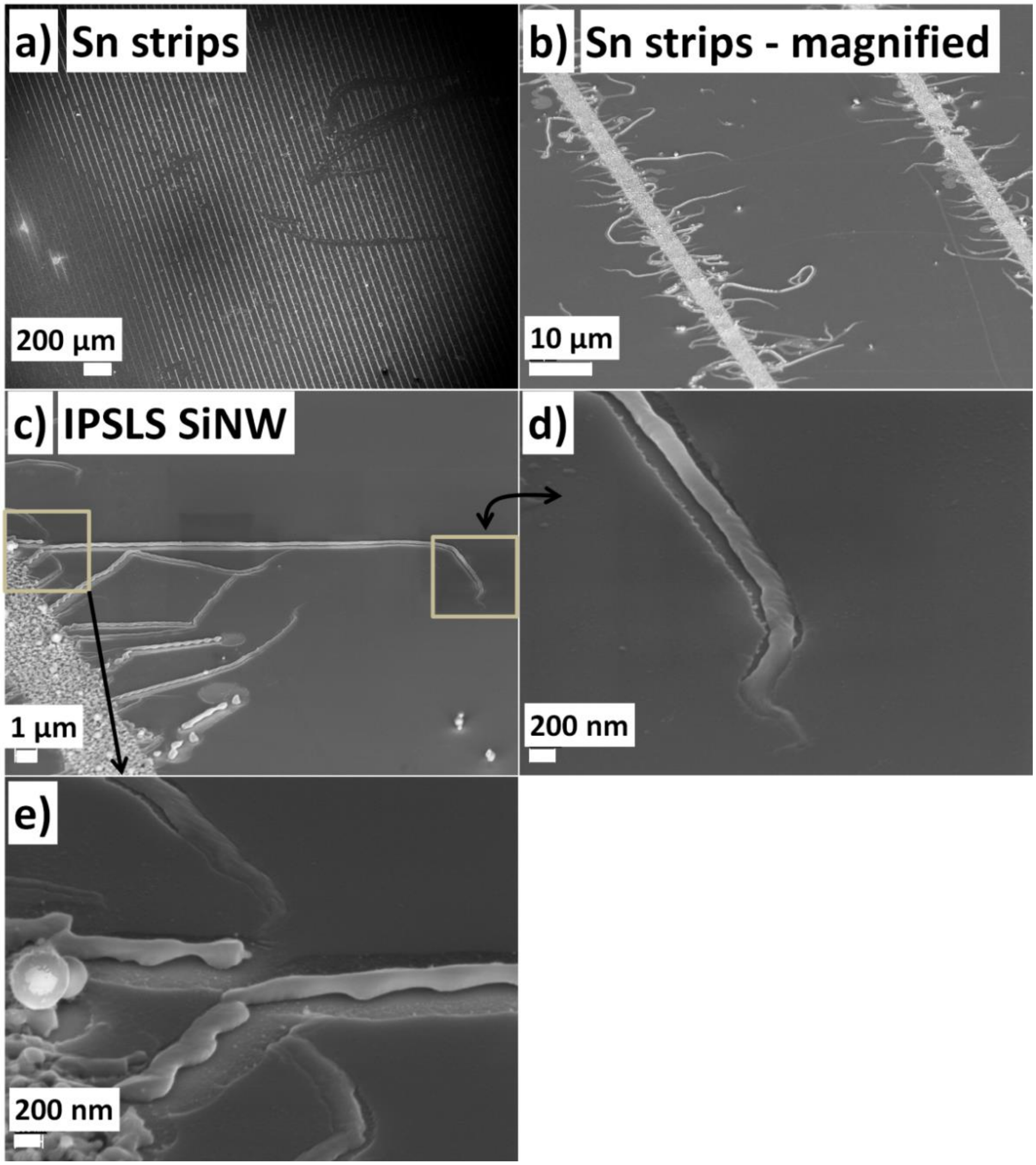

Fig.IV.1 SEM images of IPSLS SiNWs. a) Sn strips as etched by lithography, b) magnified image of (a) showing the growth of Sn-catalyzed SiNWs along the strips, c) SiNW of ~ 23 µm long grown at 400℃ during, d) the end region of the growth, and e) the starting region of the SiNW growth.

The length of IPSLS SiNWs obtained using Sn catalyst can reach ~ 23 µm, as the one shown in Fig.IV.1.c. This is due to the low solubility of Sn in Si. For the fabrication of SiNWs, pure metallic Sn was used, and there is no complete wetting behavior of Sn NP at the region where the SiNW ends, see Fig. IV.1.d. Therefore, the Sn NPs seem to be stable during the growth process of SiNWs. Since the objective is to fabricate GeSn NWs, growth attempts using the same mechanism and methodology will be made in the next section.

IV.2 GROWTH USING TIN PRECURSOR CATALYSTS

The main objective of this study is to create crystalline GeSn NWs. The incorporation of Sn into Ge (forming a diamond cubic phase αGeSn) improves the mobility of charge carriers and changes the bandgap from indirect to direct for a sufficient amount of Sn. The controllable incorporation of Sn in Ge allows straightforward band-gap engineering, providing an efficient route towards a full GeSn integration in a novel range of Si-based optoelectronics and nanoelectronics. However, exploiting GeSn potentials requires a non-equilibrium growth mechanism. In this work, we present the catalytic growth of in-plane GeSn nanowires using two Sn-based catalysts: 1) metallic Sn nanoparticles (NPs), and 2) SnO_2 colloids. The in-plane solid-liquid-solid (IPSLS) method is used for the growth of Ge_xSn_{1-x} NWs, by employing a thin film of hydrogenated amorphous Ge (a-Ge:H) as the source of Ge atoms.

IV.2.1 EVAPORATED TIN NANOPARTICLES

The first set of growth experiments is carried out using pure Sn NPs as catalysts. High purity Sn powder is evaporated and deposited onto the surface of a Si substrate with an average diameter of 16 nm, Fig.IV.2.a,d. Afterwards, the sample is introduced in a PECVD reactor. A H_2 plasma is ignited at a substrate temperature of 400℃ in order to remove the native oxide from the Sn droplets. To deposit the a-Ge:H layer, the temperature is decreased to 120℃ and the substrate with Sn NPs on top is exposed to a Germane and Hydrogen plasma with a flow of 50 sccm and 20 sccm respectively and a RF power of 2 W during 10 min, Fig.IV.2.b. Under these conditions, an a-Ge:H layer ~ 14 nm thick is deposited on top of the catalyst NPs. Finally, the temperature is raised above the eutectic point of Sn (231℃, for instance 270℃) to activate the NW growth.

Growth attempts using this strategy have been unsuccessful as shown in Fig.IV.2.c,e; possibly due to the high density of Sn NPs (1.9×10^{11}/cm^2), Fig.IV.2.d. Sn NPs should be distant from each other, since the growth of NWs requires a space where NPs can travel to achieve the growth.

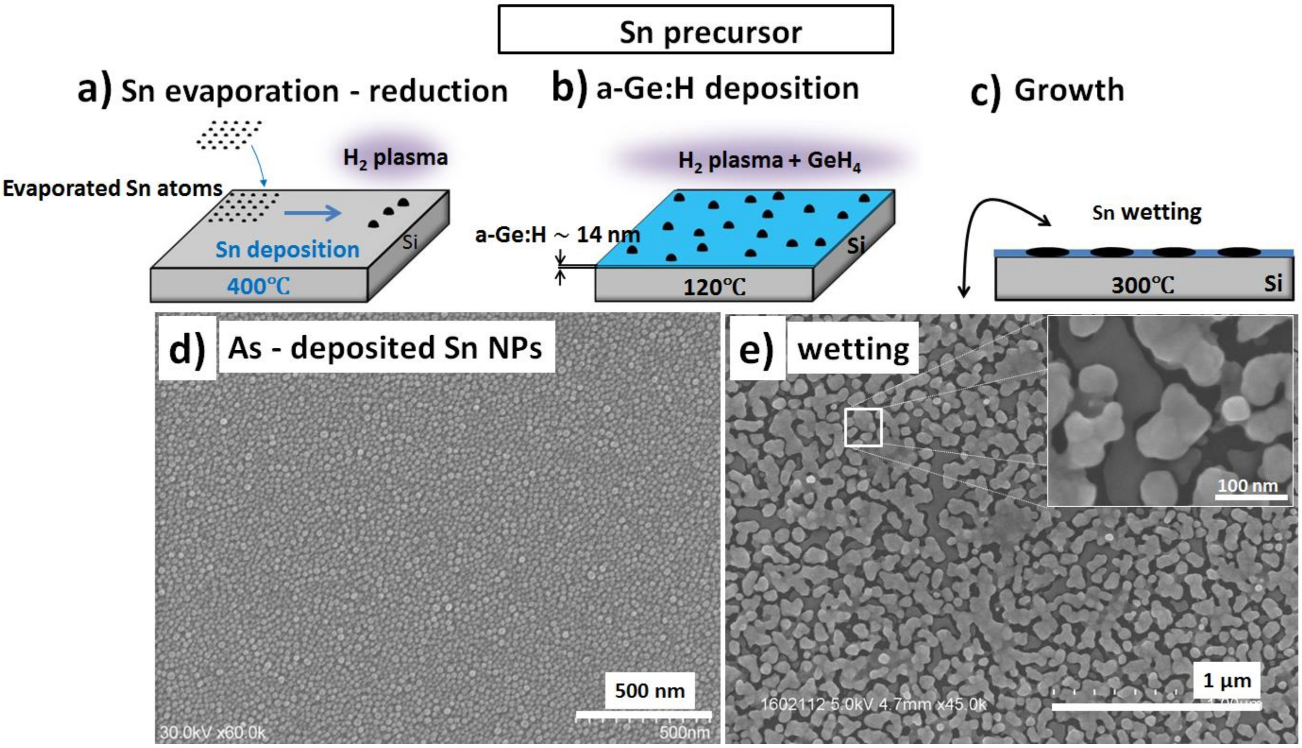

Fig.IV.2. Growth trials using evaporated Sn. a) Thermal evaporation of a Sn thin film onto a crystalline Si substrate. Sn NPs (~16 nm) are formed after annealing at 400°C in a hydrogen plasma. b) Deposition of the hydrogenated amorphous Ge layer (~14 nm) on the Si substrate containing the Sn NPs. c) Sn wetting behavior upon annealing at 300°C. d) SEM image of as-deposited Sn NPs by evaporation, the density is estimated to be ~ 1.9×10^{11}/cm^2. e) SEM image showing the result of the annealing process of Sn NPs topped with an a-Ge:H layer. The inset shows a magnified image.

In order to make room for the NPs to do their trip, Sn strips are used. The Sn strips are also evaporated and deposited onto a Si substrate. The average diameter of the NPs is 200 nm. The space between Sn strips is obtained using standard lithography. (The Sn strips are prepared by Zhaoguo Xue in the school of electronics science and engineering – Nanjing University – China). Even though the Sn strips have enough regions with only a-Ge:H on top of the Si substrate, no growth occurs as shown in Fig.IV.3.

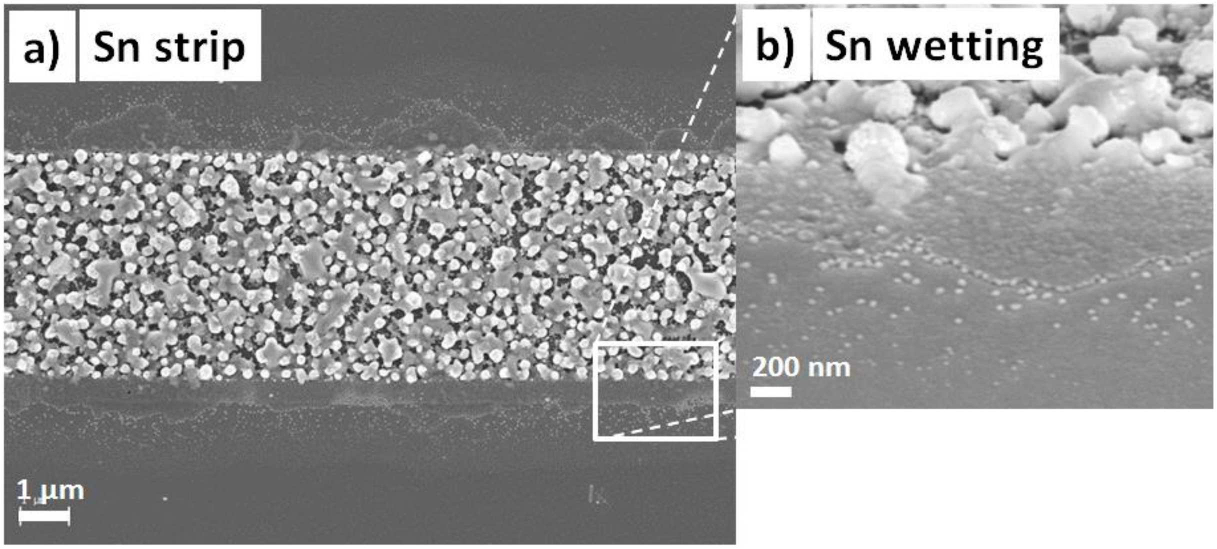

Fig.IV.3. Growth trials using Sn strips. a) SEM image top-view showing the unsuccessful growth attempt. b) Magnified tilted view (54°) showing the Sn wetting and no NWs are formed.

After careful analysis, it can be concluded that the strong wetting of Sn on a-Ge:H surface is the main factor preventing the growth of GeSn NWs, Fig.IV.3.b. Indeed, Sn is known to be an unstable catalyst [14] due to its low surface tension [15] especially when it is in contact with a-Ge:H [16], a high surface energy material. In addition, Sn NPs have a higher wettability on a-Ge:H and a higher solubility in the corresponding layer [17] as compared to a-Si:H [18]. For this reason, the growth of in-plane GeSn NWs using Sn is certainly more challenging than the growth of Si NWs.

IV.2.2 TIN DIOXIDE COLLOIDS

A second set of growth experiments was designed using SnO_2 NPs as a catalyst precursor. The reason for using this type of Sn is to prevent the wetting. For instance, simple surface features, such as step-edges, help pinning and directing the catalysts, thereby guiding the growth of NWs [19]. The liquid catalyst is energetically more stable when located on a step-edge rather than on a flat substrate. This pinning effect may be used in our case to prevent the Sn from wetting when in contact with a-Ge:H above the melting point. The objective is to partially reduce the SnO_2 to pure Sn, leaving a SnO_2 NP that pins the liquid Sn (reduces the wetting behavior), and therefore favoring the growth of NWs.

To prepare the NPs, 8 grams of commercial SnO_2 powder are added to 25 ml of Diethylene glycol (DEG). The mixture is grinded in a milling machine to reduce the size of SnO_2 particles and disperse them. By centrifugation, the supernatant which is mostly DEG is separated from heavy SnO_2 particles. After pouring out the DEG from the main solution, a 0.01 mol/L of Tetramethylamonium Hydroxide (TMAOH) is used as a solvent to prevent precipitation. Then, the TMAOH/SnO_2 mixture undergoes another round of centrifugation to separate the smaller particles from the bigger aggregated particles. Ultra-sonic treatment is applied to better disperse the NPs in the colloidal solution (Fig.IV.4.a). Further aging of the SnO_2 colloidal solution leads to SnO_2 aggregates (dubbed SnO_2 clusters), as shown in Fig.IV.4.b.

The Si substrate, onto which the corresponding SnO_2 colloids will be deposited, should be cleaned and prepared. The substrate is soaked for 1 hour in TFD (a surface cleaning detergent). To further clean the organic residue off the substrate's surface, two methods are employed: 1- Piranha solution (based on sulfuric acid H_2SO_4 and hydrogen peroxide H_2O_2), 2- UV-Ozone treatment. To render the surface hydrophilic and provide a cationic character for the surface that allows attracting negatively charged species (the SnO_2 NPs are surface charged by the TMAOH) a PDDA Poly(diallyldimethylammonium chloride) layer is deposited. As a last step, the Si substrate is covered by a few drops of the colloidal SnO_2 NPs for 5 min. Afterwards, the sample is rinsed with distilled water and blown dried. The SnO_2 colloids was prepared by Shiwen Gao (internship student from LPICM) in "Laboratoire de Physique de la Matière condensée" (PMC) in École Polytechnique – Palaiseau.

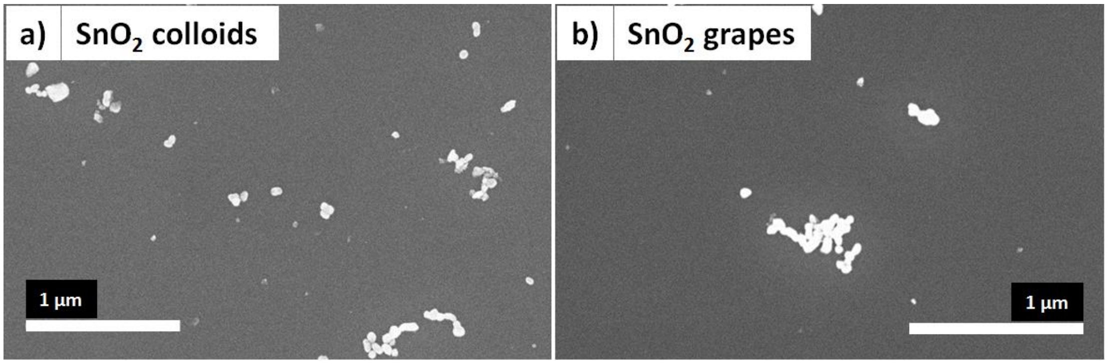

Fig.IV.4. SEM images of colloidal SnO_2 NPs deposited on a substrate that is cleaned by TFD and UV-ozone. a) Centrifuged at 1000 g (g is the unit of the effective gravitational force) and diluted 5 times. b) After aging the solution (a) for 2 weeks.

For further surface treatments and growth processing the sample is loaded in the PECVD reactor. The oxide catalyst is partially reduced to pure Sn using H_2 plasma for 10 min at 250℃ and a power density of 22 mW/cm^2. For the a-Ge:H deposition and annealing procedure we used the same parameters as in the case of Sn evaporation (section III.2.1).

IV.2.2.1 GERMANIUM-TIN NANOWIRES

The SnO_2 NPs are partially reduced to pure Sn using H_2 plasma. In order for the Sn NPs to form and coalesce, the substrate temperature should be above the melting point of Sn (231.1°C) namely 250°C during the H_2 plasma reduction (Fig.IV.5.a). To deposit the a-Ge:H layer, the temperature is set to 120°C and a 2 W plasma is ignited for 10 min under a flow of 50 sccm Germane (the gas composition is 1 at.% of GeH_4 in H_2) and 40 sccm of H_2 (Fig.IV.5.b). The GeSn NW growth takes place during annealing at temperatures ranging between 250°C to 300°C under 100 sccm of H_2 flow (Fig.IV.5.c). The SnO_2 NP standstill in its initial site during the growth because it remains solid due to its high melting point (> 1600°C) as shown by the SEM images of Fig.IV.5.d. Indeed, the pinning effect created by SnO_2 NPs seems to play an essential role in the growth of GeSn NWs.

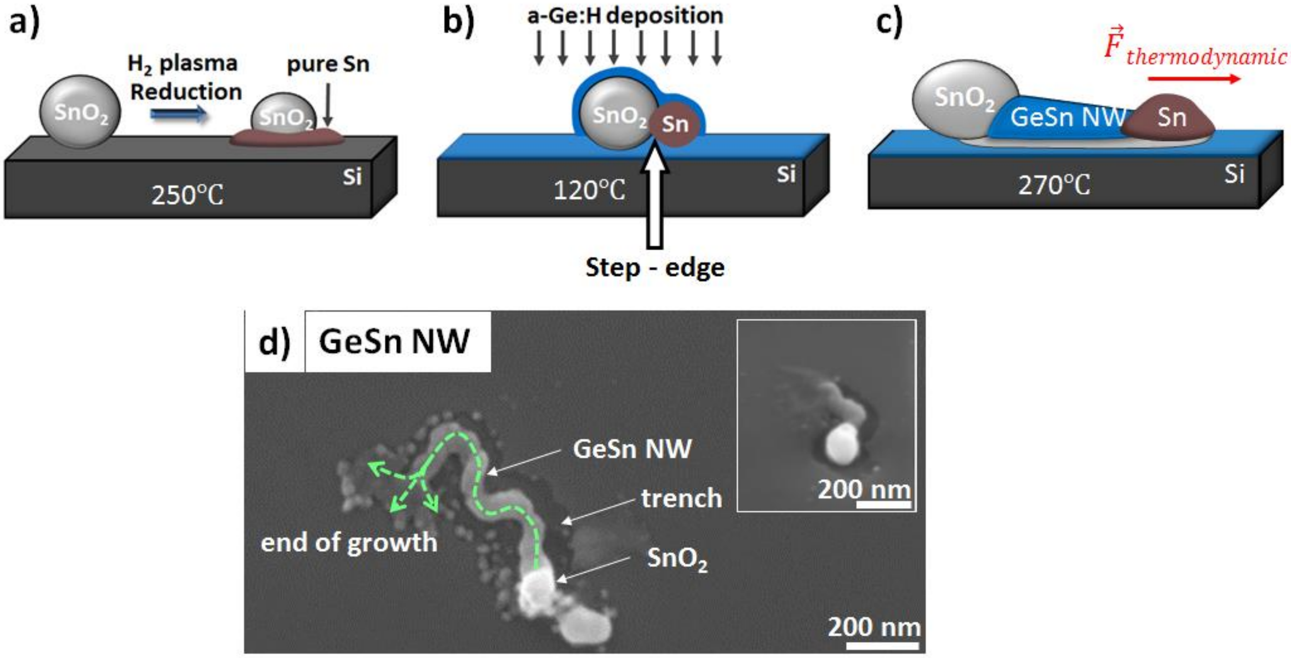

Fig.IV.5. GeSn NWs growth process. a) Schematic illustration showing the reduction step of SnO_2 NP partially into pure Sn using a H_2 plasma at 250°C. b) A 15 nm a-Ge:H layer is deposited on top of the system at 120°C. c) Growth of GeSn NWs at 270°C, the thermodynamic force drags the Sn NPs to catalyze the growth. d) SEM top view of a GeSn NW grown by the SLS mechanism. The SnO_2 NP remains at the initial position. The trench is an empty region or extremely thinned a-Ge:H, which it is produced by movement of the catalyst. The end of the growth is characterized by a wetting behavior of the catalyst.

At the initial stage of growth, the Ge concentration in the Sn NP starts to increase and the SnO_2 NP plays the role of a ledge that prevents liquid Sn from wetting until supersaturation of Ge in the Sn NP is attained. Energetically favorable sites for crystalline nanowire nucleation are located at the Sn – SnO_2 interface. Many crystal seeds can form, but the one having the lowest surface-to-volume ratio, thus, the lowest Gibbs energy, will preferentially attract the dissolved Ge atoms. Once a catalyst-seed interface is built, an absorption and deposition edge will appear. Amorphous Ge has a higher Gibbs energy than its crystalline form; this energy difference, between the back side (catalyst-crystalline interface) and the front side (catalyst-amorphous interface) of Sn NPs, creates a thermodynamic driving force that drags the catalysts toward the amorphous layer as shown in Fig.IV.5.c. Sn NPs dissolve the a-Ge:H at their front absorption side while digging a trench in the corresponding layer. As a consequence, the total system energy is reduced upon the transformation of a-Ge:H into a c-Ge NW.

IV.2.2.1.1 RAMAN SPECTRA

As a first approach to characterize the composition of GeSn NWs, Horiba LabSpec 5 micro-Raman spectroscopy was used. A Helium-Neon (HeNe) laser with a wavelength of λ = 633 nm is used for the excitation; the signal is detected using CCD detector. Fig.IV.6 shows the micro-Raman spectra measured on an a-Ge:H layer and on a region containing GeSn NWs. Bulk Ge has a strong Ge-Ge longitudinal optical (LO) phonon peak at $w_{Ge} = 301 \pm 0.5\ cm^{-1}$ [20], which progressively shifts to lower frequencies with an increasing Sn concentration. The wavenumber shift can be described by the linear equation: $\Delta w_{GeSn} = -k.x\ cm^{-1}$ where x is Sn atomic fraction and k is a prefactor depending on the strain state of the nanowires [21]. Accordingly, for strained and relaxed nanowires, the prefactors are respectively $k_s = 30.3$ and $k_r = 76.8$. In Fig.IV.6, the Ge-Ge longitudinal optical (LO) phonon peak is located at $293\ cm^{-1}$ due to the spectral feature of the compressive strain and the substitution-Sn-induced bond stretching in GeSn NWs. Using the linear shift equation, the Sn atomic percentage in GeSn NWs is estimated to be ~ 10 % for a completely relaxed structure and ~ 26% for a strained structure.

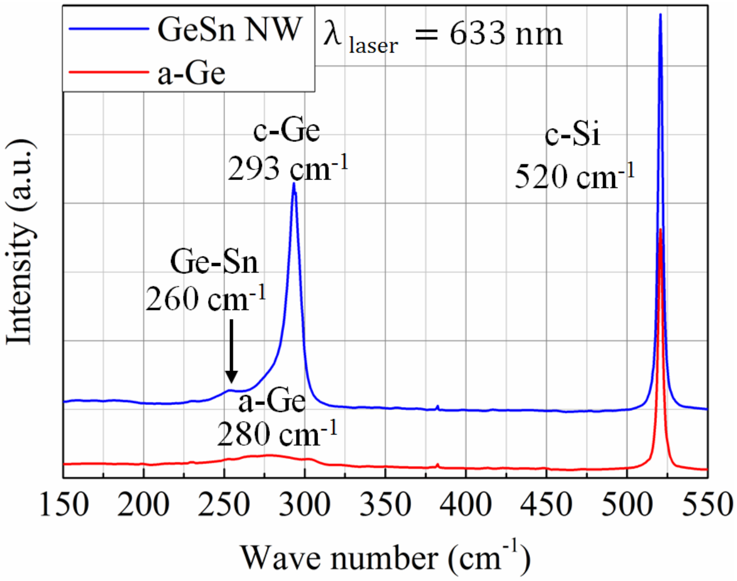

Fig.IV.6. Micro-Raman spectra (λ = 633 nm excitation) of a sample containing GeSn NWs (blue) and a region containing only a-Ge:H (red).

IV.2.2.1.2 TEM-EDX MEASUREMENTS

In Scanning TEM (STEM) mode, and by using High Angular Annular Dark Field (HAADF), the intensity scales with the atomic number of the constitutive elements. This allows complementary analysis with Energy Dispersive X-ray spectroscopy (EDX) to map the chemical composition. The complete STEM-HAADF and STEM-EDS investigation of a GeSn NW cross-section prepared by FIB is displayed in Fig.IV.7. According to the linear concentration profile of the 55 nm diameter NW shown in Fig.IV.7.b, the Ge and Sn have a spatial distribution complementarity. The Ge varies from 20 at.% which marks the edge of the NW to reach 70 at.% inside, whereas, in Fig.IV.7.d, the EDX cartography shows that Ge and Sn are homogeneously distributed at the nanometer scale without visible precipitations. Since a 1.5 nm spatial resolution has been employed for the STEM-EDS mapping experiments, the presence of atomically ordered GeSn alloy cannot be ascertained. For a more accurate quantification, a well-defined rectangular area was selected for an EDX count, the average Sn composition is 22 ± 3 at.% Sn. These measurements have been repeated for other GeSn NWs produced under the same growth conditions, therefore leading to an average concentration of 21.3 at.% Sn.

By correlating the STEM-EDS analysis and the micro-Raman of the Sn concentration, we can infer that GeSn NW is strained (the prefactor is k = 36.4) due to the accommodation of ~ 22 % of Sn atoms in the Ge lattice.

The high resolution HAADF micrograph (Fig.IV.7.c) identifies the crystalline nature of the NW. To identify the orientation of the NW cross-section, the interatomic distance is measured, d_{atomic} = 0.2 nm, using the HR micrograph (Fig.IV.7.c). The miller indices (h,k,l) are deduced using the cubic crystal system:

$$d_{atomic} = \frac{a}{\sqrt{h^2 + k^2 + l^2}}$$

Where “a” is the lattice constant. In fact, it is not accurate to use the lattice constant of Ge (a_{Ge}) or Sn (a_{Sn}) since it is an alloy. Both elements in this structure (78 at.% Ge and 22 at.% Sn) affect the lattice constant, for this reason Vegard’s law is used to obtain a more accurate value:

$$a_{GeSn} = 0.78 \times a_{Ge} + 0.22 \times a_{Sn}$$

Knowing that a_{Ge} = 0.56579 nm and a_{Sn} = 0.64892 nm (diamond structure of Sn), therefore a_{GeSn} = 0.58407 nm, and $\sqrt{h^2 + k^2 + l^2}$ = 2.92. In the case of diamond structure, the summation $N = h^2 + k^2 + l^2$ is restricted to 2,8,11,16,19. In this particular case, N = 8. Thereby, the most probable orientation is [220] according to the diffraction database [22].

Another axial cross-section is prepared using the GeSn NW shown by Fig.IV.8.a.b. The NW is crystalline but with structural defects, as shown in the GeSn region of Fig.IV.8.c. These structural defects might be due to two possible reasons, 1) the accommodation of a high concentration of Sn in Ge and 2) the FIB damage during the TEM lamella preparation. On the one hand, Sn and Ge have different atom sizes which results in a poor crystalline structure. On the other hand, during FIB operation; atoms are displaced (i.e. point defects) upon Ga^+ collisions which make the structure lose its long-range ordering (for sufficient point defects) in localized regions of GeSn. To get rid of these FIB-related structural defects, a cleaning process is conducted. The cleaning process consists of accelerating the Ga^+ at 2 kV to gently dismantle the defected regions leaving, thus, a less damaged surface [23]. Here, it is noteworthy that the accelerating voltage used for FIB coarse milling is 30 kV. As a consequence, most of the defects seen in Fig.IV.8.c are related to the accommodation of Sn in Ge.

The TEM lamella shows that the NW has 21 at.% Sn and 79 at.% Ge. The elements are quite homogeneously distributed inside the NW, Fig.IV.8.d. In this case, these NWs have been grown at 300℃, unlike the latter case (270℃).

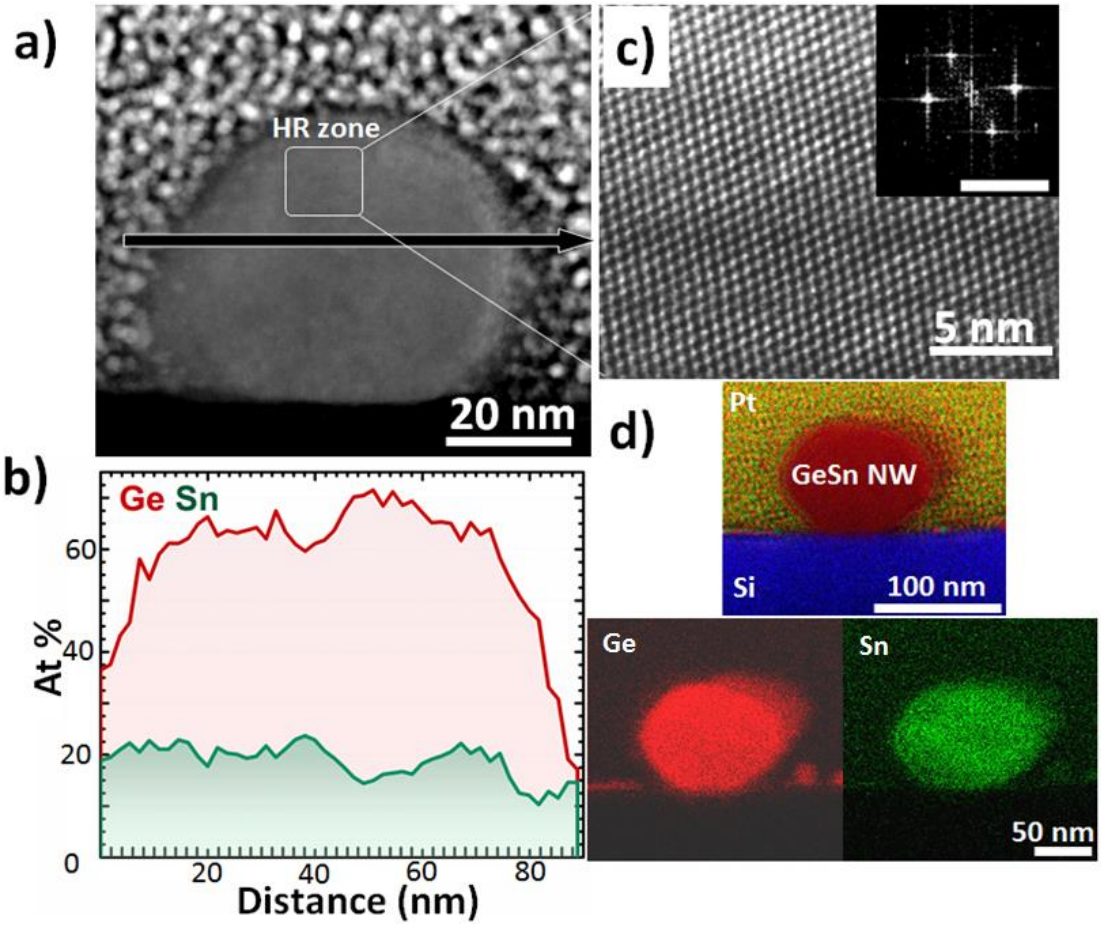

Fig.IV.7 High-resolution two-dimensional Energy Dispersive X-ray (EDX) map and structure of a Sn catalyzed Ge nanowire. a) HAADF micrograph showing a radial cross-section of a GeSn NW grown on a Si substrate at 270°C, and protected by a Pt layer. b) The composition profile along the black arrow zone (along the diameter of the nanowire) indicates the atomic percentage of Ge and Sn (the complement to 100% is due to presence of Si, Ga, O, and Pt atoms incorporated at the surface of the sample during the ion beam preparation process. c) A high-resolution image, depicted as HR Zone (white square), shows a defect free crystalline material. d) A cross-sectional HRTEM – EDX, 30 min count, displays the elemental spatial distributions of Ge in red, Sn in green, Si in blue, and Pt in yellow.

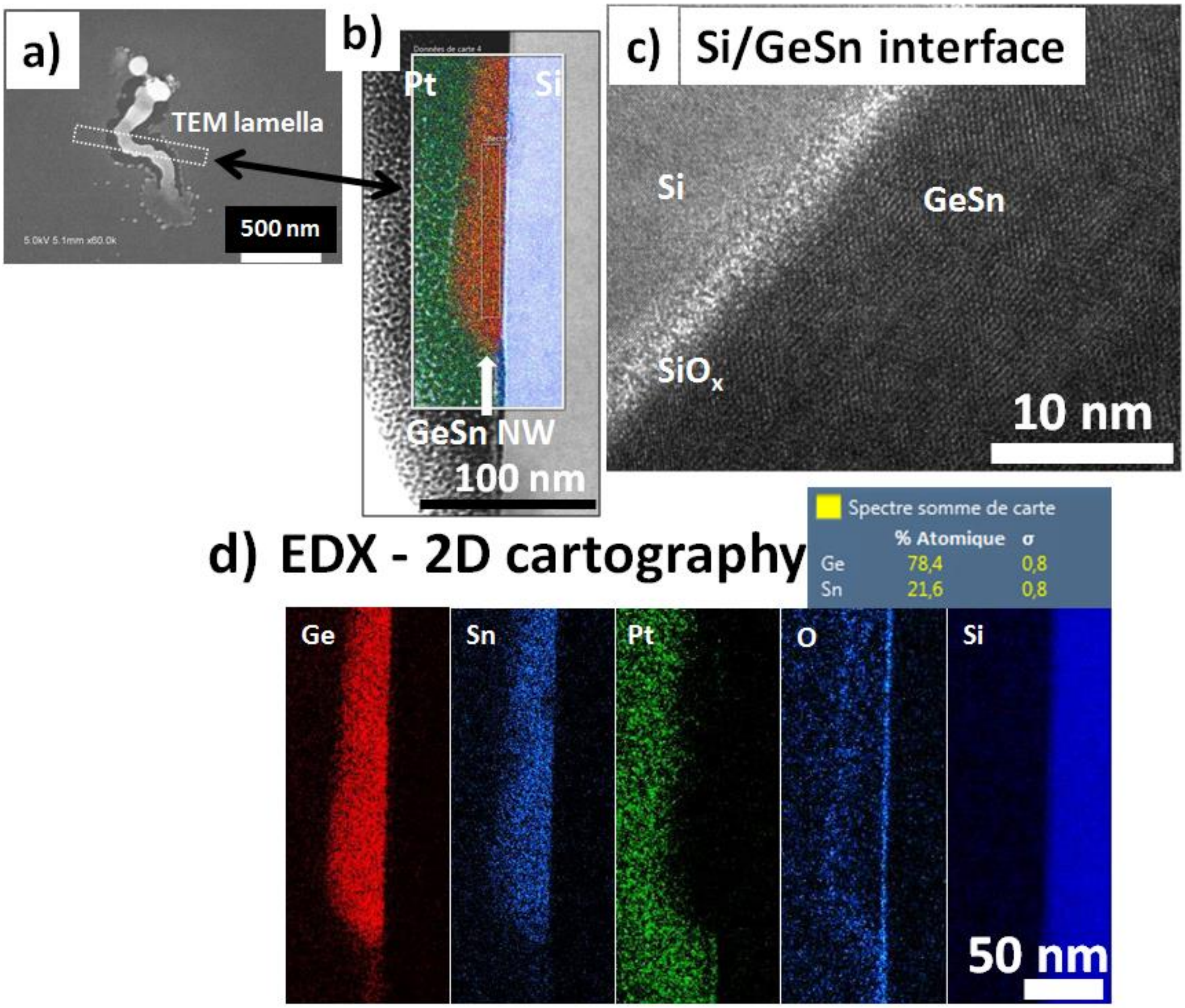

Spectre somme de carte

	% Atomique	σ
Ge	78,4	0,8
Sn	21,6	0,8

Fig.IV.8 Axial cross-section of an in-plane SLS GeSn NW grown on a Si substrate at 300℃. a) SEM image showing a GeSn NW, the indexed region is the axial TEM lamella analyzed in TEM. b) bright-field micrograph superposed with EDX measurements. The Ge-Sn presents the nanowire, Pt is the protective layer, O is present due to native oxide and Si is the substrate. c) HRTEM micrograph showing the interface region between the GeSn NW and the Si substrate. d) 2D cartography showing the homogeneous distribution of Ge and Sn along the nanowire. The inset shows the concentration of Sn in Ge > 21 at.% (The quantification has been done in the white rectangle inside the NW shown by the bright-field image (b)).

Since the growth is a thermally activated process, increasing the temperature will eventually increase the growth rate of NWs. As demonstrated by Chen et al.[6], the catalyst incorporation in the NWs depends on the growth rate. In our case, increasing the temperature from 270℃ to 300℃ should increase the growth rate and therefore the incorporation of Sn. However, the TEM results show that there is no meaningful variation in terms of Sn concentration in both samples annealed at 270℃ and 300℃. Two possibilities are presented, either the incorporation of Sn is not related to the temperature but to another parameter, or it is indeed related to the temperature. Here, it is important to discuss the IPSLS growth process technically. After the deposition of a-Ge:H at 120℃, the temperature should be raised above the melting point of Sn (231.1℃ which is also the Ge-Sn eutectic point), namely 300℃, to activate the growth. While raising the temperature to reach the desired value, the NWs start to grow as soon as the supersaturation is reached in the liquid catalyst. When reaching the nominal temperature of 300℃, many GeSn NWs have already grown and some of them have grown around 270℃. This means that the exact temperature at which a NW is grown is difficult to be deduced.

As a perspective, a hint can be used to extract the NW’s growth temperature. The hint is related to the size of the catalyst. It will be demonstrated in section – III. 2.2.1.3.2, that by increasing the temperature; bigger catalyst will be activated. For example, a catalyst of 250 nm diameter cannot be activated using a temperature below 300℃. In brief, increasing the growth temperature will increase the size of the activated catalysts. A relationship between the temperature and the catalyst size should be established to deduce the growth temperature.

IV.2.2.1.3 HIGH TIN-INCORPORATION EXPLANATION

In order to explain the high incorporation of Sn in GeSn NWs, one imperatively needs to address the problem of the atomic motion within the system at the NW/catalyst interface. Understanding the kinetic behavior of the newly obtained material with enhanced solubility is essential for tailoring the NW properties..

IV.2.2.1.3.1 COMPLEMANTARITY OF GE AND SN

In the concentration profile of the IPSLS GeSn NW obtained by STEM-EDX shown in Fig.IV.7.b, a complementary distribution of Ge and Sn is witnessed. This observation raises the possibility that there are not enough Ge atoms in the Sn NP to build an atomic layer, which implies that Sn atoms are completing the deficiencies. To clarify if there is a shortage from the Ge part, a comparison is made between the Ge amount needed to build an atomic monolayer and the amount of Ge in the liquid Sn catalyst. Therefore, if the concentration of Ge is not enough in the liquid catalyst, then Sn atoms might be completing the layer.

As a first step to approach the calculation, we consider that the NW's radial cross-section has a squared surface; with W_{NW} is the size of a square side, and the diameter of the catalyst, D_{NP}, is estimated by the trench size (Fig.IV.9.a). In Fig.IV.9.b, one atomic layer is considered to have a thickness of a_{GeSn}.

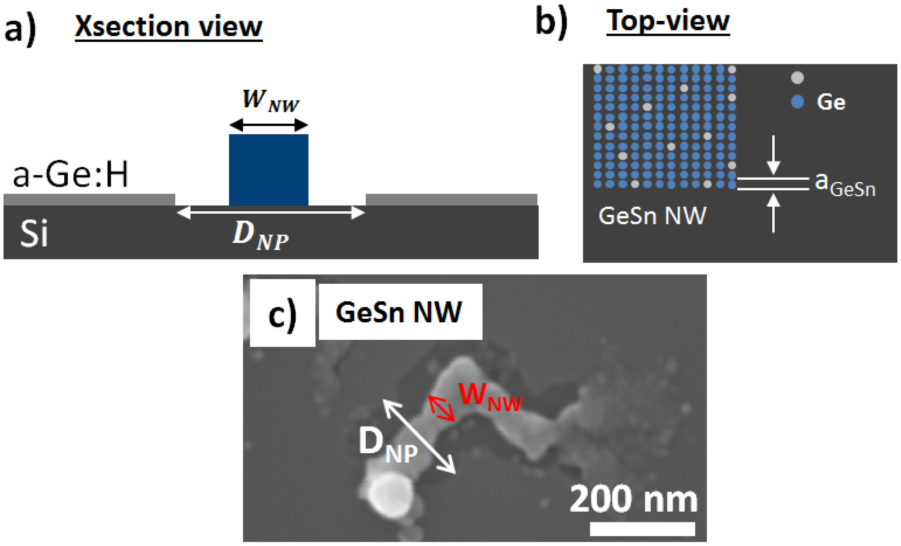

Fig.IV.9 Cross-section schematic illustrations showing the model proposed for the complementarity calculations. a) A radial cross-section view considering that the NW's surface is a square with a width of W_{NW} and D_{NP} is the diameter of the Sn NP. b) top view of the NW considering that an atomic monolayer width is a_{GeSn}. c) SEM top-view image of the GeSn NW used to estimate the Ge amounts.

The atomic radiuses of Ge and Sn are r_{Ge} = 125 pm and r_{Sn} = 142 pm. The W_{NW} is made up by the summation of Ge and Sn atoms, therefore:

$$W_{NW} = N\times[0.21 \times (2.r_{Sn}) + 0.79 \times (2.r_{Ge})]$$

N is the total number of atoms making up the atomic line having a length of W_{NW}. As shown in Fig.IV.9.c, the NW has an average width of 57 nm and the average D_{NP} = 150 nm is deduced from the trench size. These parameters lead to N = 221 atoms. Since the NW's radial cross-section is considered to be a square, therefore $N^2 = (221)^2 = 48841$ atoms is the number of Ge and Sn constituting an atomic layer at the crystalline interface of the NW. This monolayer is formed by 79 at.% Ge, therefore, the number of Ge atoms in this monolayer is $N_{Ge} = 0.79 \times N = 38584$ atom. However, since our objective is to determine if the Ge atoms present in liquid Sn are enough to build an entire Ge layer at the NW's surface, the number of Ge atoms in that monolayer is considered to be equal to N^2.

The number of Ge atoms in the liquid catalyst is estimated using the Ge-Sn phase diagram. To do so, the number of Sn atoms in the catalyst should be estimated first. The volume of the Sn NP is considered to be a half-sphere:

$$V_{NP} = \frac{2\pi}{3}\left(\frac{D_{NP}}{2}\right)^3 = 8.8\ \times 10^{-22}\ m^3$$

The Sn density is given by $\rho_{Sn}(T) = 7.375 - 6.765\ \times 10^{-4} \times T(K)$ [24]. The growth temperature is 270℃ which makes $\rho_{Sn} = 7.015\ g/cm^3$. The mass of Sn catalyst is $m_{Sn} = 6.18 \times 10^{-15}$ g and knowing the molar mass of Sn (118.71 g/mol), the molar quantity is $n = 5.2 \times 10^{-17}$ mol. Therefore the number of Sn atoms constituting the NP is $N_{Sn} \sim 31\times10^6$ atoms. The phase diagram of Ge-Sn indicates that 0.5 at.% of these atoms are Ge (at 270℃ and under equilibrium conditions), therefore the number of Ge atoms in the liquid catalyst is $N_{Ge/SnNP} = 1.5\times10^6$ atoms. As a result, there are enough Ge atoms in the Sn NP to build ~ 30 crystalline layers of Ge at the NW's crystalline interface. This means another atomistic mechanism is underlying the high incorporation of Sn. Other models based on the kinetic theory will be considered (in sections III.2.2.1.3.(2), (3), and (4)) to overcome the limitation of the latter one.

IV.2.2.1.3.2 STEP-FLOW KINETIC MODEL

The step flow kinetics is the commonly used model to described the growth of nanowires with a non-equilibrium catalyst atom incorporation (see Chapter I - section I.4.3.1 for more details) [25, 26]. From a mechanistic perspective, the out-of-equilibrium Sn incorporation in our case is most probably caused by a kinetics-related factor, controlled by the growth rate. The previous findings reported by Chen et al. [1] show that high growth rates lead to high Sn and In incorporation into SiNWs grown by the IPSLS method (which is faster than the VLS method). This is the result of the direct contact of Sn NPs with the a-Ge:H feeding layer, this contact creates a powerful force dragging the catalyst, and thus leads to higher growth rates compared with VLS.

Amazingly, in our case, for a partition coefficient k = 0.21 (see Chapter I - section I.4.3.1 for more details) the growth rate is of few tens of nm/s, which is much lower than the capability of kinetic trapping as predicted by the existing model [27]. The kinetic model states that the catalyst/NW interface velocities should be of the order of a few m/s to obtain such high partition coefficient. Biswas et al. [26] suggested that the time required for Sn atoms to escape from the solid interface towards the liquid catalyst corresponds to the time needed to complete a step, rather than completing an interface layer as suggested by the main step-flow model. In other words, the V_{step} is responsible for solute trapping and should be considered in the calculation of "k" instead of V_{int}. However, at the atomic level, the process consists of embedding Sn atoms at the step-edges (at the solid part of the NW/catalyst interface) right after the construction of the next row of atoms. Therefore, the velocity of atomic line formation V_{al} should be accounted for this non-classical incorporation of Sn rather than the step velocity V_{step} (Fig.IV.10).

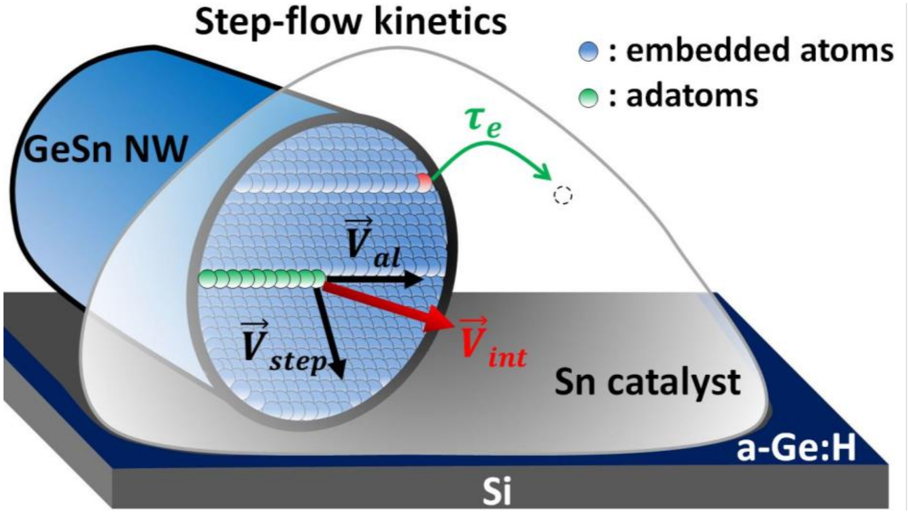

Fig.IV.10. Schematic illustration showing the stepwise growth regime at the NW/catalyst interface, where V_{int}, V_{step}, V_{al}, τ_e are the interface velocity, step velocity, atomic line velocity (that is the velocity of atomic line formation) and the escape time of adsorbed atoms, respectively. The blue atoms are frozen at the nanowire's solid surface; the green atoms are the newly adsorbed atoms on the solid interface. Atoms at the step-edges can jump back to the liquid (as indicated by the red atom) as long as the newly adsorbed atoms did not form a row.

To calculate the partition coefficient "k", the velocities should be calculated. Typically, these velocities are deduced from the growth rate (GR). As mentioned in section III.2.2.1.2; each time the temperature increases by 1℃ to reach the desired value (i.e. 300℃), a group of catalysts having a certain size are activated. As a consequence, the GR is difficult to determine since the temperature at which the NWs start to grow is not known. Therefore, dividing the length of a NW by the annealing duration (which should be the growth duration) will probably give an incorrect GR value. After this reasoning, the best approach is to consider an interval of GRs. To determine a feasible range within our framework, we consider that the growth is done between 1 min and 3 min (see Chapter IV section – IV.1.4 for a detailed explanation about the growth duration) and the average IPSLS GeSn NWs length is 1 μm based on SEM observations. Therefore, the estimated GR interval is [5 nm/s – 16 nm/s].

One crystalline layer has the thickness of a_{GeSn} = 0.58407 nm which is the estimated lattice constant of the alloy. The number of layers, N_L, built per second is equal to the GR divided by a_{GeSn}:

- In the case of GR = 5 nm/s → 8.5 layers / s
- In the case of GR = 16 nm/s → 27 layers / s

The time required for one atomic layer, τ_{1L}, to be built is equal to $1/N_L$ for both cases (5 nm/s and 16 nm/s):

- $\tau_{1L}^{5\ nm/s}$ = 0.117 s
- $\tau_{1L}^{16\ nm/s}$ = 0.037 s

By considering a typical NW's width, W_{NW} = 57 nm, the step velocity at which the step flows V_{step} across the NW's width is equal to $W_{NW}/\ \tau_{1L}$:

- $V_{step}^{10\ nm/s}$ = W_{NW} / 0.117 = 487 nm /s
- $V_{step}^{30\ nm/s}$ = W_{NW} / 0.037 = 1540 nm /s

The fundamental component of the flowing step is the velocity of atomic line formation V_{al}. The time required to build one atomic line, t_{al}, at the step-edge is:

- $t_{al}^{5\ nm/s}$ = (a_{GeSn} × $\tau_{1L}^{5\ nm/s}$) / W_{NW} = (0.58407 × 0.117) / 57 = 1.19 ms
- $t_{al}^{16\ nm/s}$ = (a_{GeSn} × $\tau_{1L}^{16\ nm/s}$) / W_{NW} = (0.58407 × 0.037) / 57 = 0.37 ms

Therefore the velocity of an atomic line formation V_{al} (to complete a line of 57 nm during t_{al}) is:

- $V_{al}^{5\ nm/s}$ = W_{NW} / $t_{al}^{5\ nm/s}$ = 48 µm / s
- $V_{al}^{16\ nm/s}$ = W_{NW} / $t_{al}^{16\ nm/s}$ = 150 µm / s

The velocity of atomic line formation V_{al} (see Fig.IV.10, in our case V_{al} is between 48 µm/s and 150 µm/s) should be accounted for this non-classical incorporation of Sn rather than the step velocity V_{step} = [0.48 µm/s – 1.5 µm/s]. The solute atoms (Sn for instance) would have a shorter escape time if the trapping process depended on the atomic line formation τ_e = [1.2 ms – 0.38 ms] instead of [0.117 s – 0.037 s] in the case of the step completion.

The main formula of "k" for a step-wise growth regime is given in Chap I section I.4.3.1. The K_e can be neglected since it is less than 0.01 (because the equilibrium solubility of Sn in Ge is < 1 at.%). Therefore, a more simplified formula is obtained:

$$k(v) \sim \exp(-v_D / V_{int})$$

V_{int} is the interface velocity, and v_D is the diffusive velocity given by :

$$v_D = D / \lambda$$

where D is the diffusion coefficient of the solute atom (i.e. Sn) in the liquid (Sn catalyst) at the interface (NW/catalyst) and λ is the atomic jump height. We consider that λ is equal to a_{GeSn} = 0.584 nm. The interdiffusion coefficient at 300℃ is $D = 0.29 \times 10^{-8}$ m^2/s according to ref.[28]. This implies that the diffusive speed at 300℃ is v_D = 4.8 m/s. As a result, Sn atoms have plenty of time to leave the growing layer before being trapped. Therefore, despite considering the atomic line formation V_{al} for the calculations using the velocity dependent partition coefficient, the step flow model predicts an insignificant Sn incorporation in the NWs.

IV.2.2.1.3.3 CONTINUOUS GROWTH MODEL

The CGM is another conventional kinetic model that might accounts for the incorporation of Sn beyond the equilibrium limit [29]. This model operates in the case of a high driving force (conversely to step-flow kinetics) where the solid part of the interface (NW/catalyst) will advance continuously [30]. This model treats the case where the interface is atomically rough. At steady-state, the growth occurs by direct impingement of atoms on high energy sites of the interface [31]. However, the detailed atomistic description of the solute incorporation process is not provided. The partition coefficient for CGM given by this model is:

$$k(v) = \frac{v_{int}/v_D + k_e}{v_{int}/v_D + 1}$$

By inserting V_{int} (that is the growth rate) into the equation, the values of k are very small. In fact, the solute atoms (Sn) have a diffusive velocity; $v_D \sim 5$ m/s which is fast enough compared to V_{int} to be trapped at the interface. The V_{al} cannot be used in this model since it is a direct impingement mechanism. Even if the maximum V_{al} is used in the equation the partition coefficient is ~ 10^{-5}. Therefore, these models only fit the rapid cooling process where growth rates are few m/s, which are necessary to trap the diffusive solute atoms.

IV.2.2.1.3.4 DIMER-INSERTION MODEL

For the case of Sn incorporation into Si NWs using the IPSLS growth mechanism, Chen et al. proposed a model based on the insertion of dimers [1] where the nucleation of Si is realized via Si pairs or dimers (Si-Si) and the incorporation of Sn atoms is realized via Si-Sn dimers. At low growth temperature (e.g. < 400 °C), the dimers are likely to be stable without breaking into two atoms. By analogy, the same dimer-based nucleation mechanism can be proposed for our GeSn NWs. Once Ge-based dimers are formed, other adatoms or dimers can join and constitute the nuclei of a growing terrace. Such kind of nucleation around the Ge-based dimers occurs on the whole growing interface with multi sites. As a consequence, growing terraces can coalesce with each other and then form a complete layer. Based on the dimer nucleation with multi sites, a very high interface velocity (NW growth rate) is expected. Two types of dimers can be found in our NW growth system including Ge-Ge and Ge-Sn. With the increase of NW growth rate (higher supersaturation), more Ge adatoms in the Ge/Sn alloy droplet are available allowing more Ge-Sn dimers to be formed. Therefore, the concentration C_{Sn} will increase with the increase of NW growth rate:

$$C_{Sn} = \frac{\nu_{Ge-Sn}}{\nu_{Ge-Ge} + \nu_{Ge-Sn}} \qquad (1)$$

Where ν_{Ge-Ge} and ν_{Ge-Sn} are the incorporation rates of Ge-Ge and Ge-Sn dimers respectively, which are obtained by analogy to ν_{Si-Si} and ν_{Si-Sn} [1]. The ν_{Ge-Ge} is given by:

$$\nu_{Ge-Ge} \approx \nu_0 [\frac{C_{Ge}}{2} e^{\Delta E/kT} + (1 - \frac{C_{Ge}}{2}) e^{-\Delta E/kT}] \qquad (2)$$

Where C_{Ge} is the concentration of Ge in the Sn NP, ν_0 is the vibrational frequency, k is Boltzmann’s constant, T is the growth temperature, ΔE is the Gibbs energy difference between the dissolved Ge atoms in droplet and the Ge-Ge dimer nucleation energy (which is considered to be zero), and C_{eq} is the equilibrium concentration of Ge in Sn which is ~ 0.5 at.% at 270℃.

The ν_{Ge-Sn} is given by:

$$\nu_{Ge-Sn} \approx \nu_0 [C_{Ge} e^{\Delta E'/kT} + (1 - C_{Ge}) e^{\Delta E'/kT}] \qquad (3)$$

Where $\Delta E'$ is the Gibbs energy difference between the dissolved state of Ge in the Sn NP, and the Ge-Sn dimer nucleation energy which is reasonably considered to be zero. After inserting equations (2) and (3) into (1) and rearranging, the dimer-insertion formula can be written as:

$$C_{Sn} = \frac{(\alpha\eta C_{eq})^2 + C_{eq}\exp(\sqrt{V/b})(\exp\left(2\sqrt{V/b}\right) - (\alpha\eta C_{eq})^2)}{2\alpha\eta C_{eq}(1+\alpha\eta C_{eq}) + C_{eq}\exp(\sqrt{V/b})(\exp\left(2\sqrt{V/b}\right)(2+\alpha\eta C_{eq}) - \alpha\eta C_{eq} - 2(\alpha\eta C_{eq})^2)} \quad (4)$$

Where α is the insertion coefficient and is considered as a fitting parameter, in our case $\alpha_{Sn} = 1.3$, which corresponds to the growth of GeSn NWs using Sn catalyst (the insertion coefficient of impurity atoms used in literature for Si NWs catalyzed by In and Sn: $\alpha_{Sn} = 27$ and $\alpha_{In} = 2.95$ are given for comparison), $\eta = \exp(\Delta G/kT)$ where ΔG is the Sn segregation energy barrier. Actually, the segregation starts between 320℃ and 350℃, therefore the thermal energy is equal to 78 ± 2 meV, thus, $\eta = 4.48 \pm 0.34$, thereby the main curve giving the Sn concentration prediction versus the growth rate (GR) will have a certain error margin, $C_{eq} = 0.5\ at.\%\ Sn$ is the equilibrium solubility of Sn in Ge at the growth temperature 270℃, V is the GR, and "b" is the maximum growth rate measured using Sn catalyst for SiNWs and it is equal to 50 nm/s. The dimer-insertion model developed for Sn incorporation in GeSn NWs function of the growth rate is represented by the black line in Fig.IV.11. Since there is an uncertainty of segregation temperature (2 meV), the curve has a certain error margin that is represented by two red curves.

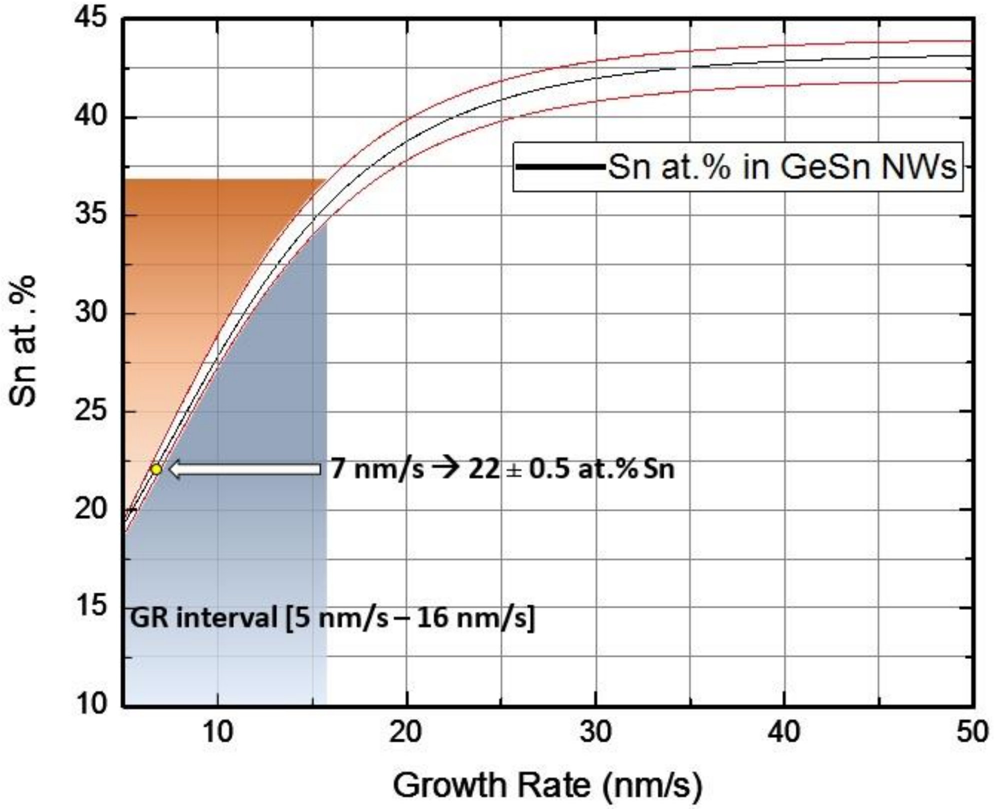

Fig.IV.11. Dependence of Sn concentration on GeSn NWs growth rate (black curve) based on the dimer insertion model. The Sn atomic percentage values (red region) correspond to the GR interval [5 nm/s – 16 nm/s] (blue region) estimated for the growth of IPSLS GeSn NWs at 270℃. The yellow point on the curve shows that for a 22 at.% Sn incorporation the GR should be equal to 7 nm/s. The error caused by the uncertainty of the temperature at which the segregation starts is represented by the two red curves.

The GR corresponding to 22 ± 0.5 at.% Sn is 7 nm/s according to the curve which relies in the previously determined interval of GRs [5 nm/s and 16 nm/s] for IPSLS GeSn NWs grown at 270℃. As a conclusion, among the kinetic models used in the literature for describing the high incorporation of solute atoms (such as Sn) in a crystalline host (such as a Ge NW), the DIM is the best to predict the Sn concentration for a given growth rate. By insertion of Ge-Sn and Sn-Sn dimers into the NW crystalline interface, high Sn incorporation is achieved.

IV.2.2.1.4 EFFECT OF TIN-INCORPORATION ON NANOWIRES LENGTH

The length of a nanowire (L_{NW}) is strongly correlated with the solubility of catalyst atoms in its structure, such that Sn-catalyzed Silicon NWs are tens of micrometers long [32] due to the low solubility of Sn in solid Si (< 0.01% at. Sn) at temperatures between 400℃ and 500℃

[33]. In the case of Ge, the relatively short NWs provide an indirect evidence for an important incorporation of Sn into the GeSn NWs. The assumption that L_{NW} is correlated with the catalyst size is correct as long as the limiting factor for the growth is the availability of the catalyst. By inserting into the model the catalyst diameter (D_{NP} = 300 ± 10 nm) at the starting region, we find that ~ 22 at.% Sn should be incorporated to obtain the observed NW length (~ 886 nm).

For the IPSLS nanowires, the catalyst is in their liquid state during growth. The shape of the liquid NP is hard to determine, as it is changing constantly during growth [34]. However, the volume of the droplet can be approximated by a 1/4 sphere (Fig.IV.12.a):

$$V_{Sn\ NP} = V_{\frac{1}{4}spherical} \qquad (5)$$

In this measurement the initial diameter of the catalyst is assumed to be $D_{NP} = 305 \pm 10\ nm$ and the length of the nanowire is $L_{NW-exp} = 886 \pm 89nm$. Due to the wetting, the exact length of the NW is hard to determine. For this reason, the error (± 89 nm), which is the end of the NW is considered to extend from the beginning of the wetting region till its end as shown in Fig.IV.12.b.

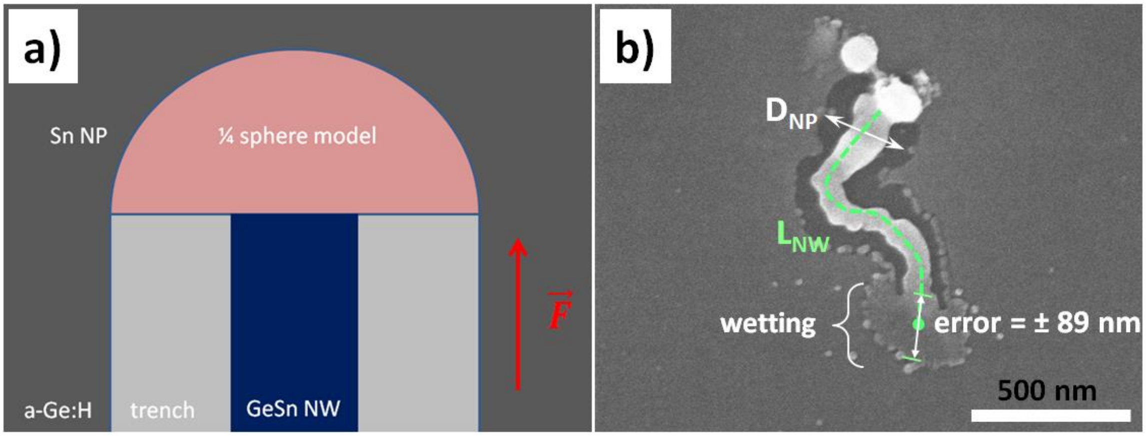

Fig.IV.12 a) Schematic illustration showing the supposed catalyst shape during growth. b) SEM image of an IPSLS GeSn NW used as an example in this calculation. D_{NP} denotes the diameter of the Sn NP (305 ± 10 nm) which is assumed to be equal to the trench size, L_{NW} is length of the NW shown by the green dashed line that starts at the edge of the SnO_2 NP and ends at the green point. The error is considered to be 89 nm, therefore L_{NW-exp} = 886 ± 89 nm.

Let N_{Layer} be the number of atomic layers making up the nanowire. We assume that the NW is monocrystalline. Sn atoms from the catalyst are incorporated in each monolayer in a certain percentage (i.e. 21 at.% Sn). Therefore, dividing the number of Sn atoms of the catalyst (N_{Sn}^{NP}) by the number of consumed Sn in each layer (N_{Sn}^{layer}) will give the total number of layers forming the NW N_{layer}:

$$N_{layer} = \frac{N_{Sn}^{NP}}{N_{Sn}^{layer}} \qquad (6)$$

By measuring the trench, we can calculate the total number of Sn atoms in the NP:

$$N_{Sn}^{NP} = \underbrace{\frac{1}{4}\frac{4\pi}{3}\left(\frac{D_{NP}}{2}\right)^3}_{\text{Quarter-sphere volume}} . \underbrace{\frac{N_A}{M_{Sn}}.D}_{\text{Amount of matter}} \qquad (7)$$

Where D_{NP} is diameter of the catalyst, $N_A$is the Avogadro number and M_{Sn} is the Sn Molar mass (118.71 g/mol), and D is the density of Sn. The measured diameter of the hemisphere (molten Sn drop) is $\sim 305\ nm$, which corresponds to 137 × 10^6 Sn atoms.

The diameter of the NW is continuously decreasing during growth. The linear decrease in size can be written as a mathematical equation. If at the beginning of the nanowire $D_0 = 128\ nm$ and at the end $D_{end} = 83\ nm$, therefore we have a decrease of $\Delta D = 45\ nm$. The length of this nanowire is $L_{NW-exp} = 886\ nm$. If we divide ΔD by the total length of the nanowire we obtain the shrinking rate:

$$\frac{\Delta D = 45\ nm}{L_{NW-exp} = 886\ nm} = 0.05 \qquad (8)$$

Thus, every 1 nm traveled by the Sn NP the diameter of the NW shrinks by 0.05 nm. Statistically, the average shrinking rate of GeSn NWs from the same sample is:

$$\frac{\Delta D_{average}}{L_{NW\ average}} = 0.047 \qquad (9)$$

The mathematical expression describing the fact that the diameter of the NW is a decreasing function of the growth distance by a certain shrinking rate is:

$$Diameter\ of\ nanowire = -0.047 \times growth\ distance + initial\ diameter$$

$$D_{NW} = -0.047 \times d + D_0 \qquad (10)$$

The diameter of the nanowire is a function of the distance travelled by the catalyst (or function of the growth distance). The shrinking rate is negative which describes the decrease of the nanowire's diameter.

Even though the Sn percentage is constant along the entire NW, the number of consumed Sn atoms in each monolayer is a function of the growth distance. In fact, not all the layers are incorporating the same amount of Sn atoms. The first layer incorporates the most, and thereafter the number starts to decrease in a constant rate in the following layers due to the decreasing D_{NW}. The cross-sectional surface of the NW is considered to be a disk. The expression that gives the number of consumed Sn atoms as a function of the growth distance is:

$$N_{sn} = \left[\frac{\pi(-0{,}028.d+D_0)^2}{S_{cube}}\right] \times 8 \times Sn\ at.fraction \qquad (11)$$

Where $\mathrm{S_{cube}}$ is the surface of one diamond cube, which is equal to $(\mathrm{a_{GeSn}})^2$, the term $\pi(-0.028 \times \mathrm{d} + \mathrm{D_0})^2$ is the surface of one atomic layer constituting the NW interface which is considered as a surface of a disk ($\pi \times D_{NW}^2$), "d" is the growth distance, which maximum value is equal to the nanowire's length and the minimum is equal to one atomic layer ($\mathrm{a_{GeSn}}$), and "D_0" is the initial diameter of the nanowire.

When $\pi(D_{NW})^2$ is divided by S_{cube}; one would obtain the number of cubes constituting the layer for a certain "d". For each value of "d", a certain number of cubes are calculated. Note that Microsoft excel was used to do the loop calculations. By multiplying the number of cubes by 8, one would obtain the number of atoms in the layer. The multiplication by the atomic fraction (i.e. 0,21) gives the number of Sn atoms incorporated in that layer. Therefore, the main formula is:

$$N_{layers} = \frac{N_{Sn}^{catalyst}}{N_{Sn}^{NW\ layers}} = \frac{\frac{14\pi}{4\ 3}\left(\frac{D_{NP}}{2}\right)^3 . \frac{Density \times N_A}{M_{Sn}}}{\left[\frac{\pi\times(-0{,}047.d+D_0)^2}{S_{cube}}\right] \times N_{at.\ per\ diamond\ cube} \times Sn\ at.fraction} \qquad (12)$$

By multiplying $a_{GeSn} \times N_{layers}$ the NW's length can be obtained. To compute equation (12), the GeSn NW shown in Fig.IV.12.b is taken as an example. In fact, the trench is the trace of the catalyst, in this case, we assume that the diameter of the catalyst is equal to the trench size: D_{NP} = 305 nm, and $L_{NW\text{-}exp}$ = 886 nm. The dependence of D_{NP} on L_{NW} for different Sn incorporation fractions is shown in Fig.IV.13. To resume, two variables are present in this formula (eq.12): D_{NP}

and Sn atomic fraction. Therefore, to obtain the atomic percentage of Sn inside the NW, D_{NP} is inserted into eq.(12), and the Sn atomic fraction should be fitted so that the theoretical length of the NW, L_{NW}, matches the experimental length of the NW (i.e. $L_{NW\text{-}exp}$ = 886 nm). Therefore, the Sn at.% corresponding to the measured $L_{NW\text{-}exp}$ is 22 at.%, as shown by the "black curve" in Fig.IV.13.

Furthermore, if the incorporation of Sn increases the L_{NW} decreases and vice-versa as shown in Fig.IV.13.

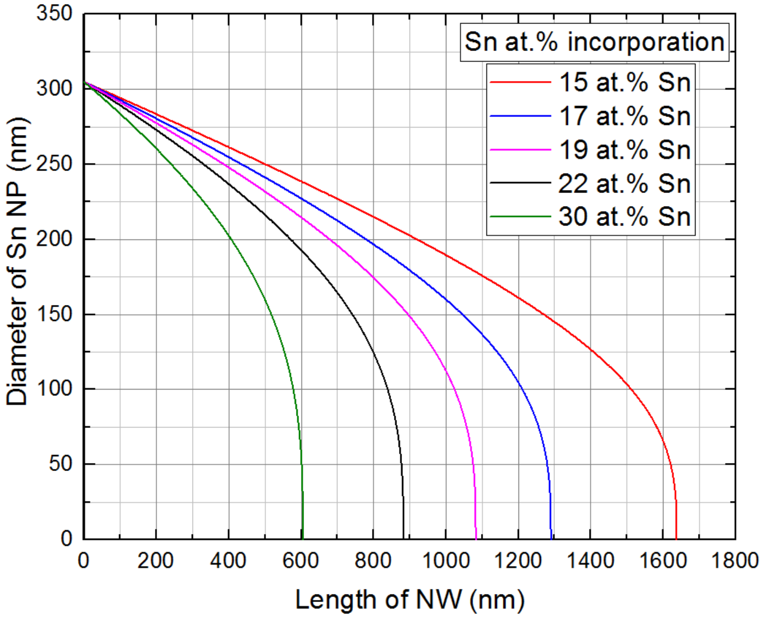

Fig.IV.13. The developed model showing the variation of D_{NP} as a function of $L_{NW\text{-}theoretical}$ for different incorporation percentages of Sn. The initial D_{NP} is 305 nm and it starts to decrease as function of L_{NW}. A higher incorporation percentage results in steeper decrease in D_{NP}. The theoretical length $L_{NW\text{-}theoretical}$ is extracted at D_{NP} = 0 nm). Under the condition of 22 at.% Sn incorporation, $L_{NW\text{-}theoretical}$ is equal to 883 nm (black curve) which is the closest to the experimental value of L_{NW} (886 ± 89 nm).

Fig.IV.14 shows the difference of L_{NW} with and without considering the shrinking rate in the calculation. The formula without the shrinking rate (the modified part is highlighted in red) is:

$$N_{layers} = \frac{\frac{\pi}{3}\left(\frac{D_{NP}}{2}\right)^{3} \cdot \frac{Density \times N_A}{M_{Sn}}}{\left[\frac{\pi \times (D_0)^2}{S_{cube}}\right] \times 8 \times Sn\ at.fraction} \qquad (13)$$

An error of 220 nm is committed on L_{NW} if the decrease in the size of catalyst (hence the diameter of the NW) is not considered.

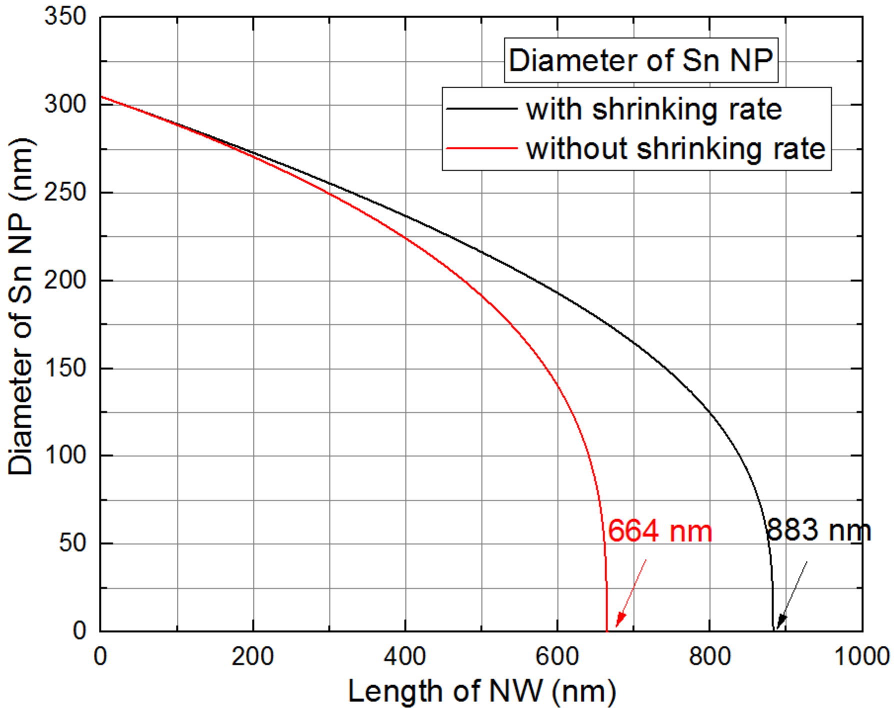

Fig.IV.14. The dependence of D_{NP} on L_{NW} with and without considering the shrinking rate in modelling. The red curve shows the L_{NW} (that is 664 nm) without considering the shrinking rate of the catalyst diameter, meanwhile it is considered for the black curve. An error of more than 200 nm is committed in L_{NW} if the shrinking rate is not considered.

More accurate results can be obtained by considering a more realistic shape of the catalyst, and taking account the Sn NPs pinned on the trench sides. Furthermore, the statistics used to average the shrinking rate can be more elaborated to approach the real values. This model can be extended for other types of NWs with high incorporation of catalyst atoms (e.g. SiNWs catalyzed by Sn).

IV.2.2.1.5 EFFECT OF ANNEALING

The technology steps to process GeSn NWs into electronic or optoelectronic devices will involve annealing steps (for instance for contact optimization). It is therefore important to determine a thermal window in which GeSn NWs are stable. Under thermal constraints, Ge-Sn systems are known to phase-separate. Annealing such a system might induce changes on its microstructural and physical properties. In the case of an epitaxially grown GeSn thin-film, strain relaxation starts by the formation of misfit dislocations at temperatures between 450℃ - 540℃, whilst higher temperatures lead to a steeper segregation and precipitation [35].

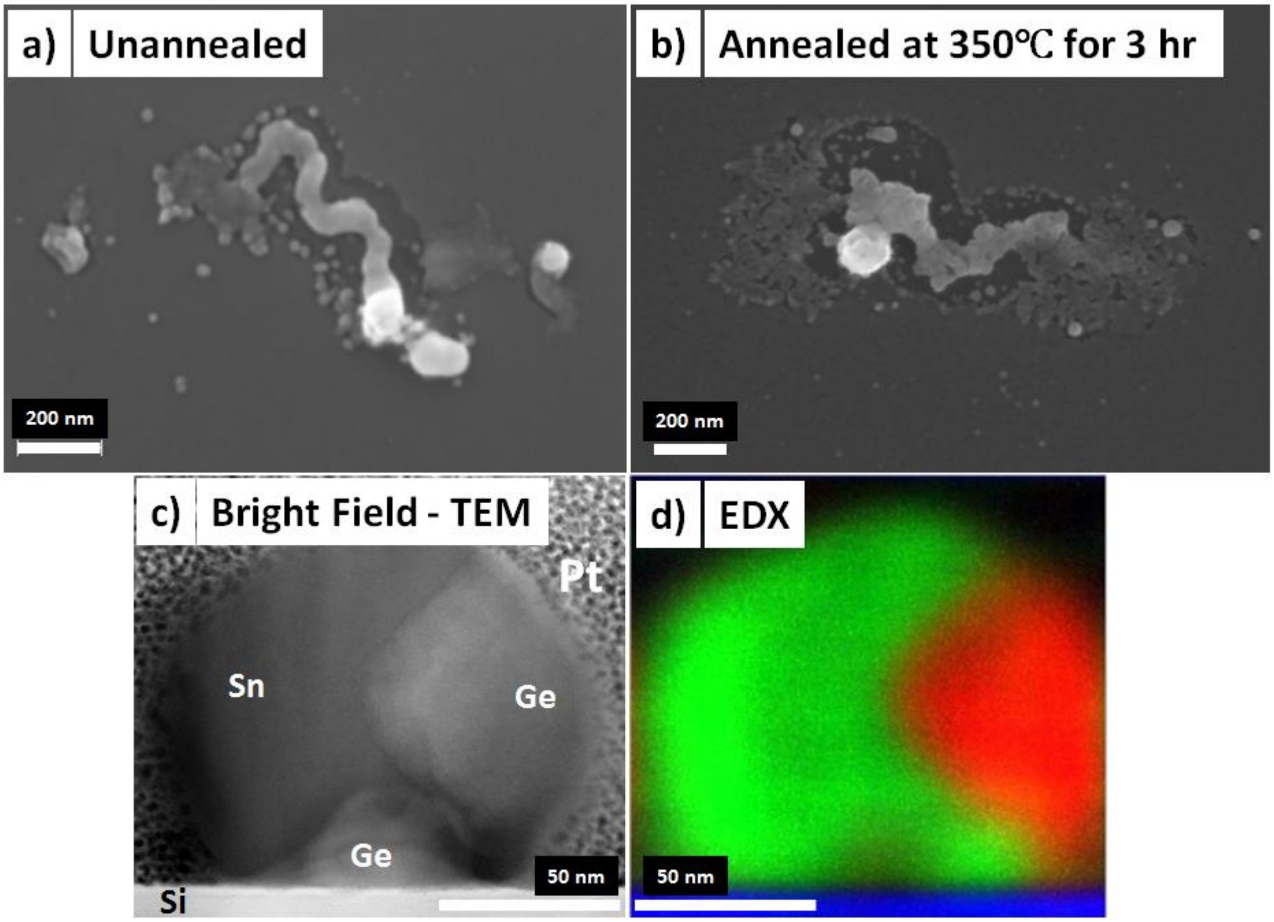

Fig.IV.15. Thermal stability of GeSn NWs. a) SEM image showing a $Ge_{0.78}Sn_{0.22}$ NW grown at 270℃. b) SEM image showing NWs of the same sample shown in (a) but annealed at 350℃ during 3 hours. c) STEM – bright field micrograph shows a Z-contrast, where Sn atoms (heavier than Ge) are darker than Ge atoms. Note that this NW is protected by a Pt layer during FIB preparation. d) The STEM-EDX map displays the spatial distribution of Ge in red, Sn in green, and Si in blue, explaining the inhomogeneous radial contrast. Thus the EDX presents a sharp evidence of a phase-separation into two phases: a Ge-rich region (< 1 at.% Sn) and a Sn-rich region (with at.% Ge smaller than the detectable threshold).

Upon the annealing step, the NWs appear rougher compared to the un-annealed ones, as shown be the SEM images in Fig.IV.15.a,b. For deeper structural and composition insights, TEM analyses are used. The phase separation starts at 350℃, which is lower than the separation temperature previously reported by Li et al (for ~ 8 at.% Sn). As shown in Fig.IV.15.c, two distinct regions (Ge and Sn) are obtained inside the nanowire. According to EDX measurements (Fig.IV.15.d), we identify a nearly pure Sn region (the Ge content here is below the detectable amount of 0.1 at.%), whereas Ge-rich regions contain a traceable amount of Sn (< 1 at.%). The bottom Ge region in Fig.IV.15.d does not appear well in the EDX map due to the superposition of Ge and Sn maps. As a conclusion, increasing the growth temperature leads to a Ge-Sn phase separation, such that the thermal window for a stable GeSn processing into devices is < 350℃.

IV.2.2.1.6 THE LAST STAGE OF GROWTH

As can be seen in Fig.IV.15.(a) and (b), a full wetting occurs at the end of the IPSLS - GeSn NWs growth. It was reported that $E_{Ge-Sn} < E_{Sn-Sn}$, with E_{a-b} bonding energy between atom a and atom b, thus, increasing the Ge composition in Sn NP alters the surface tension and the contact angle [36]. Therefore, possibly, the increment of Ge composition in the Sn catalyst might be the leading cause of the catalyst wetting at the end of the growth. Since the bonding energy of Ge-Sn is weaker than Sn-Sn and Ge-Ge as reported by Naidich et al. [36], the surface tension will be weaker upon the increment of the Ge concentration in the catalyst (number of Ge-Sn bonds is bigger than Sn-Sn or Ge-Ge bonds). This implies a decrease in the contact angle.

During growth, the only parameter changing is the diameter of the catalyst D_{NP} (hence D_{NW}) due to the incorporation of Sn. When the catalyst gets small enough, surface effects start to act. The classical thermodynamics will no longer predict the solubility of Ge in Sn. The phase-diagram shows that the solubility of Ge in Sn is ~ 0.5 at.% at 270℃ (that is the growth temperature) as shown in Fig.IV.16.

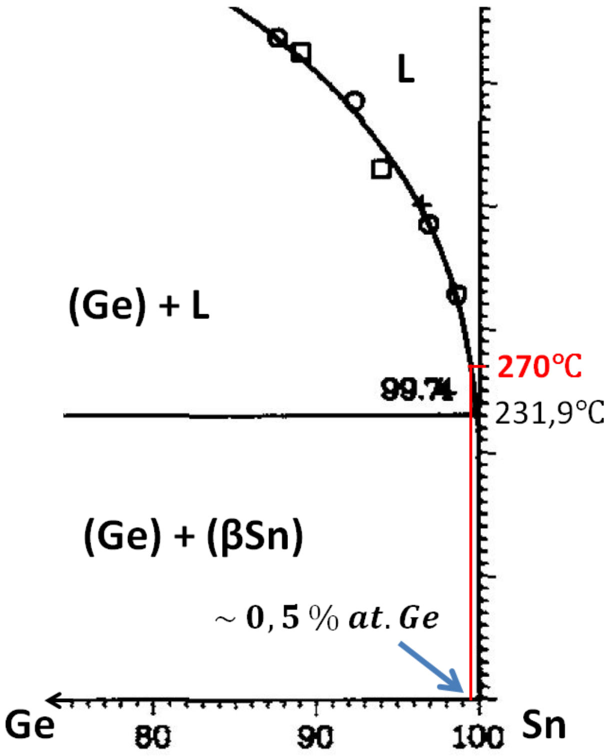

Fig.IV.16. Sn-rich region of Ge-Sn binary phase diagram, for a temperature of 270℃ Ge solubility in Sn NP is ~ 0.5 % at. Ge [37].

The Gibbs – Thomson effect shifts the solubility limit of Ge in Sn. As the particle gets smaller, Ge will be more soluble in Sn NPs. Thus a shift from the standard classical system having solubility limit of X_∞, towards a nano-thermodynamic system with a new solubility X (eq.1):

$$X = X_\infty exp\left(\frac{2\gamma v_m/R_P}{RT}\right) \qquad (1)$$

Where X is the new solubility limit, X_∞ is the solubility limit for a sufficiently big Sn NP (0.5 at.% Ge at 270℃), γ is the Sn surface tension (0.5 J/m^2 at 270℃), v_m is the molar volume of Sn (1.62×10^{-5} m^3/mol), R_P is the particle radius (m), R is the gas constant (8.314 J/K.mol), and T the temperature (543 K). In equation (1), the radius of the particle, R_P, is considered to be a radius of a sphere. However, in our case the liquid Sn NP shape is hard to determine. An adjustment of R_P is crucial to approach to the real volume. We propose the new volume to be ¼ spherical cap + ½ cone (smaller than a spherical volume) as shown in Fig.IV.17.

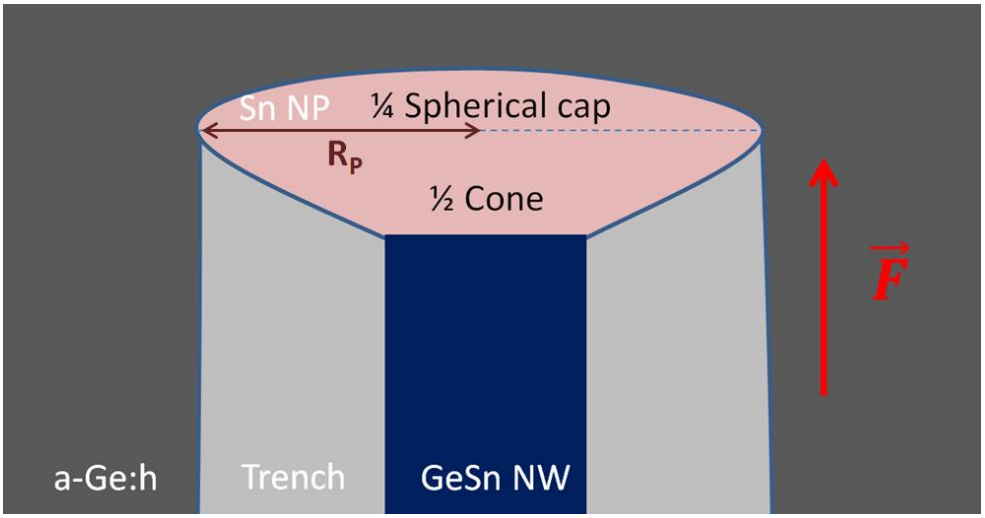

Fig.IV.17. Schema representing a second possible model to calculate the volume of Sn NP

A new radius, r_p, should be calculated (and inserted in eq.1). The Sn NP volume is considered to be:

$$V_{Sn\,NP} = V_{\frac{1}{4}cap} + V_{\frac{1}{2}cone} \qquad (2)$$

With:

$$V_{1/_4 cap} = \frac{\pi}{12} h^2 (3R_P - h) \qquad (3)$$

$$V_{1/_2 cone} = \frac{\pi}{3} {R_p}^2 . H_{cone} \qquad (4)$$

Where H_{cone} is the height of the cone, H_{cap} is the height of the spherical cap, and R_P is the measured radius. We assimilate the approximate volume of the Sn NP (V_{SnNP}) to a full-sphere volume with a new radius r_p instead of R_P (the measured one), because the Gibbs-Thomson formula does only account for spherical radiuses:

$$\frac{\pi}{12} h^2 (3R_P - h) + \frac{\pi}{3} {R_p}^2 . H_{cone} = \frac{4\pi}{3} r_p^3 \qquad (5)$$

After rearranging equation (5):

$$r_p = \sqrt[3]{\frac{1}{8}\left[R_p^2 . H_{cone} + h_{cap}^2\left(3R_p - h_{cap}\right)\right]} \qquad (6)$$

Where H_{cone} and h_{cap} are measured using SEM, and they are equal to 49 nm and 60 nm respectively. These geometrical parameters can be modified according to SEM images in regions prior to the wetting (last stage of growth). Equation (6) is the new value of Sn NP radius, r_p, assimilated to a sphere. To compute the variation of Ge solubility in the Sn NP ($X_{Ge/Sn}$) as a function of r_p, equation (6) is inserted into eq.(1). The plot is shown in Fig.IV.18.

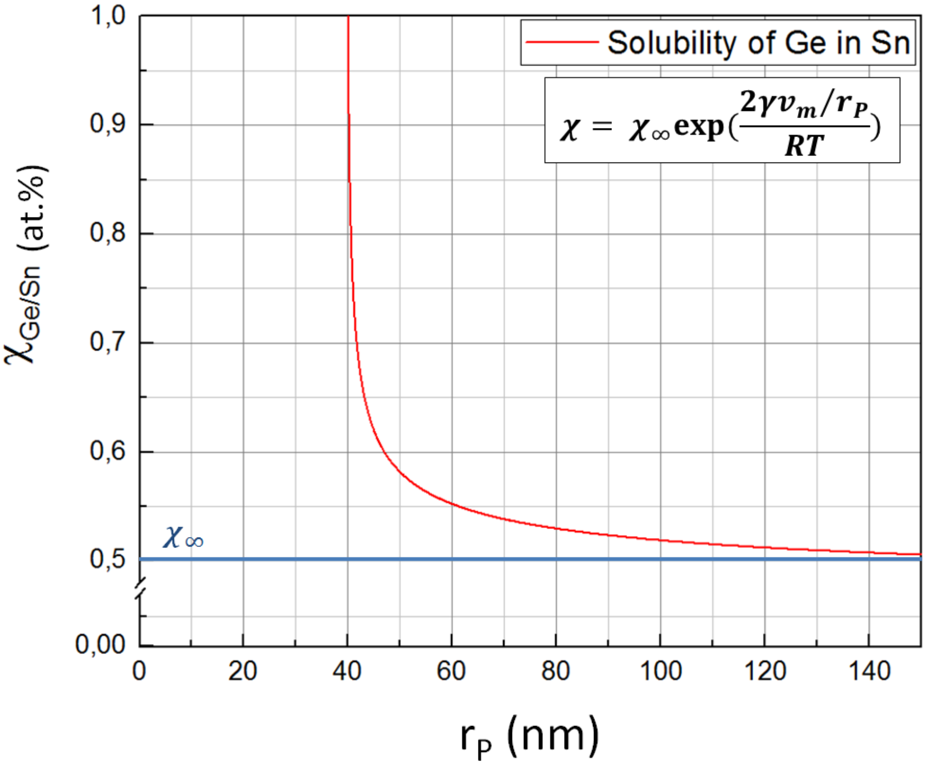

Fig.IV.18. The red curve represents the variation of the solubility of Ge in Sn NP ($X_{Ge/Sn}$) as a function of the approximated radius r_P. The blue line depicts the same solubility but for largely enough Sn NPs.

The Ge solubility in Sn starts to increase smoothly at nearly R_P = 140 nm and steeply rises at R_P ~ 50 nm. Therefore, according to Naidich et al. [36], Ge atoms start to bond with Sn atom inside the catalyst leading to a decrease in the surface tension of the Sn NP and possibly leading to the wetting at the end of the growth. Fig.IV.19 shows SEM images of the SLS GeSn NWs, the objective is to determine the trench size before wetting occurrence. Interestingly, whatever the catalyst size, the trench sizes before the wetting are almost the same (see Fig.IV.19) and averaged to be 160 nm. It is noteworthy that the measured trench size corresponds to $2R_P$ (not the real diameter of the catalyst). As previously mentioned, the diameter of the catalyst cannot be measured directly. We approximated the real radius to be: r_p which is a function of R_P. For instance, the trench size is equal to $2R_P = 160$ nm → $R_P = 80$ nm, the approximated radius is $r_p = 35$ nm which corresponds to the exponential increase of $X_{Ge/Sn}$ in the curve of Fig.IV.18.

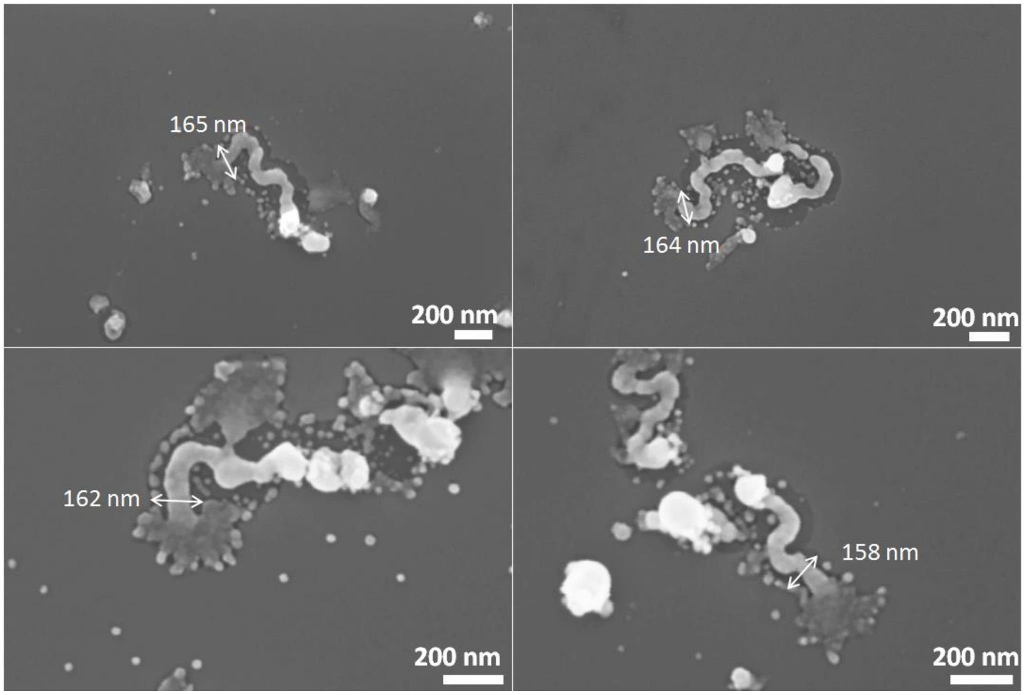

Fig.IV.19. SEM images of IPSLS GeSn NWs. The diameter of the catalyst before the wetting is averaged to be ~ 160 nm.

The difficulty is defining the shape of the catalyst before the wetting. As a perspective, an in-situ TEM or SEM measurements could help to reveal the shape of the catalyst, which can be used to improve the modelling of GeSn growth and termination.

After these investigations and analyses, Sn incorporation must also be achieved in the SiNWs shown in the first part of this chapter. For this reason, APT characterizations are done to quantify the Sn concentrations inside the SiNWs.

IV.3 ATOMIC 3D IMAGING AND CHEMICAL COMPOSITION

As it was shown in previous sections, Sn can be incorporated in large amounts inside IPSLS GeSn NWs due to the dimer incorporation. Therefore, we suspect that this kind of kinetic trapping occurs during the growth of Sn-catalyzed SiNWs, only if the growth rate is sufficient. For an atomic-scale investigation, high precision quantifications, and qualitative 3D mappings, the atom probe tomography is used for investigating the Sn-catalyzed IPSLS SiNWs. The objective is to compare SiNWs with different growth rates, to examine the concentration of Sn atoms in the NWs, and determine their spatial distribution. In Fig.IV.20, a SiNW is mounted on a W tip via an ex-situ micromanipulation process. In fact, a very sharp W-tip (needle-like) is attached to a micromanipulator system. Then, this tip is approached towards the SiNWs located on the substrate under an optical microscope. The micromanipulator system allows smooth and subtle movements (i.e. x,y,z). When the W-tip gets close to a SiNW, the electro-static force attaches the two together. Finally, the NW is lifted out, then inserted in FIB/SEM and welded by a Pt layer. It is noteworthy that SiNWs are much easier to lift-out since they are longer than GeSn NWs and not as adhered as GeSn NWs on the surface of the substrate. Afterwards the tip is inserted into the APT, and analyzed.

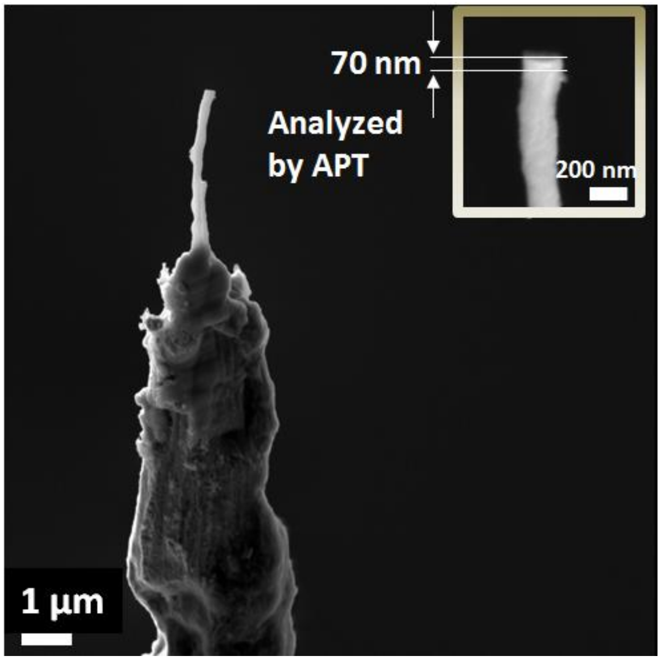

Fig.IV.20. SEM images of a SiNW mounted on a tungsten tip, and welded with Pt. The inset is a magnified view of the NW, approximately 70 nm are evaporated during the APT analysis.

Conditions for the APT analyses were chosen to be: 1) for the laser: an Ultra-Violet wavelength (λ = 343 nm), and a power of 2.22 mW corresponding to a laser energy of 22 nJ/ pulse, and 2) the temperature of the analysis was set to 80K. Those conditions are chosen first to avoid a high electric field, thus preventing preferential evaporation of atoms, and second to avoid a high laser power, thus preventing overheating the tip during analysis.

Two samples of Sn-catalyzed SiNWs have been analyzed using APT, one grown at 300°C and the other one at 400°C. In Fig.IV.21 the mass spectrum (MS) for SiNWs annealed at 400°C is shown, as an example, since MS for both cases are similar.

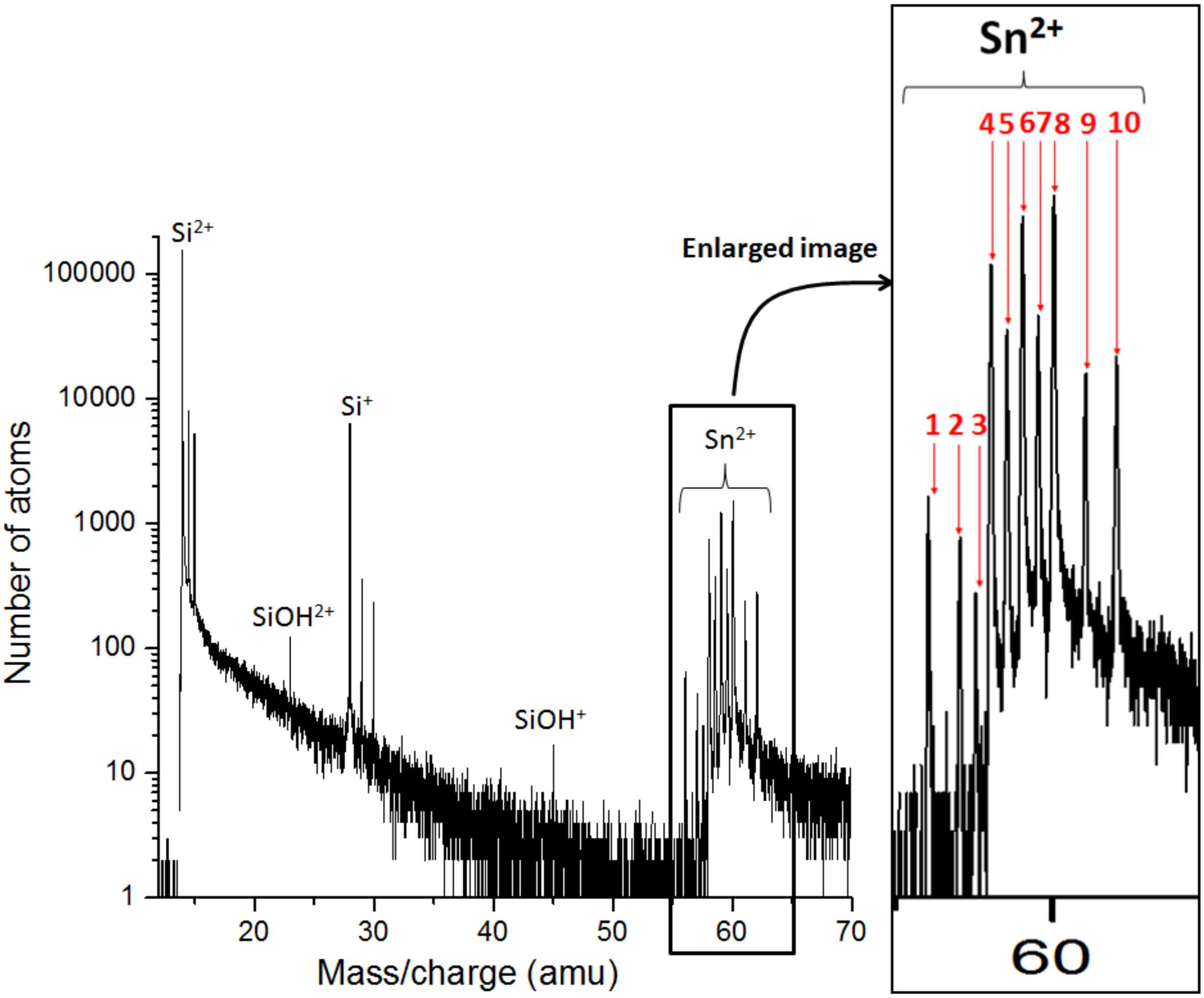

Fig.IV.21. Mass spectrum obtained using the time-of-flight measurements in APT.

The most abundant element is Si, which has three isotope peaks (for both single and double charged ions), whereas Sn has ten isotopes that are clearly visible in the MS of Fig.IV.21. Most of the detected Sn and Si atoms are doubly ionized. In fact, the state of ionization is firmly related to the electric field at the apex of the tip and to other APT parameters such as the laser power for a given detection rate. By using the charge to state ratio (CSR - number of Si^{2+} atoms over number of Si^{+} atoms) for both samples, Kingham curves [38] indicate that the electric field exerted on the tips is between 18 V/nm and 18.5 V/nm, for both Si and Sn elements. Note that both experiments presented here were done at the same CSR and hence same field of evaporation.

Quantifications were done for both samples and the overall concentration of Si and Sn throughout the analyzed NWs were given using the atomic percentage in Table.III.1. It is worth noting that the quantification in laser-assisted APT might be an issue, especially for binary compounds like GaAs or ZnO [39]. However, the quantification for Si is usually good, especially using detection systems with enhanced multi-hit detection capabilities [40].

Table.III.1 – Quantifications of Sn and Si in SiNWs for 300℃ and 400℃ growth temperatures.

Substrate Temperature	300℃	400℃
Tin	9.14 ± 0.04 at.%	10.01 ± 0.08 at.%
Silicon	90.86 ± 0.04 at.%	89.99 ± 0.08 at.%

Amazingly, highly out-of-equilibrium Sn concentrations were incorporated in those IPSLS SiNWs. Varying from ~ 9.1 at.% Sn to ~ 10 at.% Sn for 300℃ and 400℃ respectively, these NWs are rather SiSn alloy NWs. These concentrations are far beyond the predictions of the Si-Sn phase diagram. It is roughly 3 orders of magnitude the solubility of Sn in Si at the temperatures used for the growth. Using our previous analogy about the kinetic-based incorporation, large injection of Sn-based dimers (Si-Sn or Sn-Sn) into the Si crystalline matrix (i.e. NW) is suggested. The temperature is an essential parameter that influences the dynamics of the growth, namely the growth rate (GR) of the NWs. Therefore one would expect higher GR for higher temperatures. In the case of 300℃, the growth rate is ~ 2 nm/s, meanwhile it is ~ 6 nm/s in the case of 400℃. This difference between the GRs has resulted in a subtle change in Sn concentrations inside the SiSn NWs.

The 3D reconstructions associated to the analyses of both samples are presented in Fig.IV.22 a and b. Each point (red for Si and blue for Sn) represents an atom. Reconstructions are made with the home-made 3D GPM Software developed by G. Da Costa using a cone-angle protocol. As it can be seen in Fig.IV.22, one reconstruction is conical (a) while the other is cylindrical (b). For the latter, the SiSn NW was only welded to the tip by a Pt layer deposited via IBID (please refer to section II.3.1.2.1) with no further milling or cleaning. As a consequence, evaporation is made at constant voltage, what results in a 0-degree cone angle in the reconstruction protocol and the observed cylindrical shape. The other sample (in Fig.IV.22.a) was welded to a tungsten tip by Pt via IBID, but then milled annularly and cleaned using FIB to reduce its diameter, hence, inducing a conical shape. This conical shape in turns induces a voltage change during APT experiment to keep a constant detection rate. This voltage change results in a magnification change and then to a varying radius during the tip reconstruction. This was taken into account by choosing a 10 degree cone angle in the reconstruction protocol.

The 3D reconstructions show that Si atoms are homogeneously distributed in both samples, as shown by the associated elemental reconstructions in Fig.IV.22.

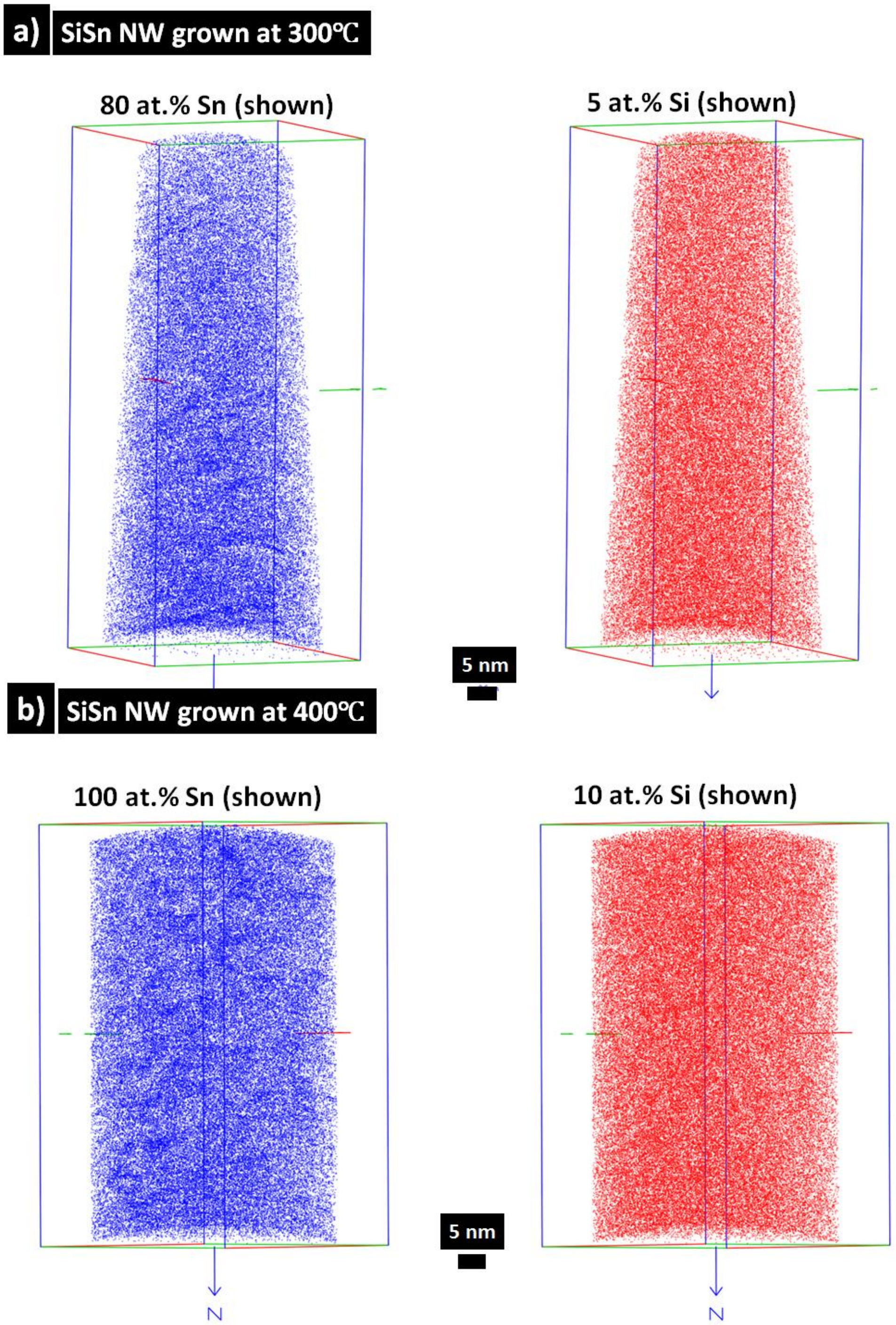

Fig.IV.22. 3D reconstructions of APT analyses of SiSn NWs grown at a) 300℃, and b) 400℃. The blue points are Sn atoms, and the red points are Si atoms. For clarity, in (a) only 80 at.% Sn and 5 at.% Si were represented in the holograms, and in (b) only 10 at.% Si was represented.

Concerning the Sn spatial distribution, most of the atoms are homogeneously distributed with small enrichments spread in the NWs. In the case of 300℃, the concentration as given by 3D selected regions (i.e. cubes of 3×3×3 nm^3) inside these enrichments can go up to 28 at.% ± 5 at.%, whereas in the case of 400℃, Fig.IV.22 (b), Sn can reach up to 17 at.% ± 2 at.%. These enrichments vary in size from 4 nm to 8 nm in both samples. To correlate these observations to the crystalline structure of SiSn NWs, TEM analysis is essentially required.

IV.4 SUMMARY

In the first part, the growth of SiSn NWs using Sn as catalyst is discussed. Sn NPs seem to be more stable during the growth of these NWs compared to GeSn NWs. No complete wetting behavior was encountered using Sn catalyst for SiSn NWs. Moreover, the solubility of Sn in Si is lower than in Ge, which leads to longer SiSn NWs compared to GeSn NWs.

In the second part, we studied the fabrication of GeSn NWs. In a first approach, pure metallic Sn was deposited using thermal evaporation. However, the resulting pure Sn NPs lead to an unsuccessful growth of NWs. Two reasons for this failure were presented: 1) the very high density of Sn NPs on the surface which is ~ 2×10^{11} NP/cm^2, 2) the strong wetting behavior caused by the contact of Sn with a-Ge:H layer. To understand the reason, a sample with Sn strips (with low density Sn NPs) is used to make room for the catalyst to travel on the substrate. Despite this strategy, Sn NPs still wet upon the contact with a-Ge:H layer. A second type of catalyst precursor was proposed: SnO_2 colloids. This time the SnO_2 NPs were partially reduced to pure Sn. The objective was to limit the wetting behavior of Sn by the pinning effect created using SnO_2 NPs. This design was successful and crystalline GeSn NWs were obtained with an amazing 22 at.% Sn incorporated homogeneously inside the NWs. Three kinetic models were presented to explain the high concentration of Sn in the GeSn NWs: step-wise flow, continuous growth, and dimer-based insertion. The first two models were not able to predict the high Sn percentage as function of the GR. The dimer-insertion model was developed for Sn catalyzed GeSn NWs. Based on this model, we predicted that for 22 at.% Sn concentration the GR should be 7 nm/s which is consistent with the estimated growth rate interval of IPSLS GeSn NWs grown at 270℃.

In the third part, atomic scale mappings and quantifications were done on IPSLS SiSn NWs. Interestingly; the quantifications have shown that SiSn NWs have far from equilibrium Sn concentrations varying from ~ 9 at.% to 10 at.% for 300℃ and 400℃ respectively. Unfortunately, the same APT analysis for GeSn NWs were not possible due to their short length (< 1.5μm), and their well adherence on the surface of the substrate.

IV.5 REFERENCES

1. Homewood Kevin, P., Lourenço Manon A., *The rise of the GeSn laser.* Nature Photonics, 2015. **9**: p. 78.
2. Cho, Y.J., Kim, Chang Hyun, Im, Hyung Soon, Myung, Yoon, Kim, Han Sung, Back, Seung Hyuk, Lim, Young Rok, Jung, Chan Su, Jang, Dong Myung, Park, Jeunghee, *Germanium–tin alloy nanocrystals for high-performance lithium ion batteries.* Physical Chemistry Chemical Physics, 2013. **15**(28): p. 11691-11695.
3. Dong, Y., Wang, Wei, Xu, Xin, Gong, Xiao, Lei, Dian, Zhou, Qian, Xu, Zhe, Loke, Wan Khai, Yoon, Soon-Fatt, Liang, Gengchiau, *Germanium-tin on Si avalanche photodiode: device design and technology demonstration.* IEEE Transactions on Electron Devices, 2015. **62**(1): p. 128-135.
4. Lei, D., Lee, Kwang Hong, Huang, Yi-Chiau, Bao, Shuyu, Wang, Wei, Masudy-Panah, Saeid, Yadav, Sachin, Kumar, Annie, Dong, Yuan, Kang, Yuye. *Enhanced Germanium-Tin P-Channel FinFET Performance using Post-Metal Anneal*. in *2018 IEEE 2nd Electron Devices Technology and Manufacturing Conference (EDTM)*. 2018. IEEE.
5. Han, G., Su, Shaojian, Zhan, Chunlei, Zhou, Qian, Yang, Yue, Wang, Lanxiang, Guo, Pengfei, Wei, Wang, Wong, Choun Pei, Shen, Ze Xiang. *High-mobility germanium-tin (GeSn) p-channel MOSFETs featuring metallic source/drain and sub-370 C process modules*. in *Electron Devices Meeting (IEDM), 2011 IEEE International*. 2011. IEEE.
6. Chen, W., Yu Linwei, Misra Soumyadeep, Fan Zheng, Pareige Philippe, Patriarche Gilles, Bouchoule Sophie, Cabarrocas Pere Roca i, *Incorporation and redistribution of impurities into silicon nanowires during metal-particle-assisted growth.* Nature Communications, 2014. **5**: p. 4134.
7. Linwei Yu, M.O., Oumkelthoum Moustapha, Franck Fortuna, Pere Roca i Cabarrocas, *Guided growth of in-plane silicon nanowires.* Applied Physics Letters, 2009. **95**(11): p. 113106.
8. Linwei Yu, W.C., Benedict O'Donnell, Gilles Patriarche, Sophie Bouchoule, Philippe Pareige, Regis Rogel, Anne Claire Salaun, Laurent Pichon, Pere Roca i Cabarrocas, *Growth-in-place deployment of in-plane silicon nanowires.* Applied Physics Letters, 2011. **99**(20): p. 203104.
9. Cui, Y., Zhong; Zhaohui, Wang; Deli, Wang; Wayne U.; Lieber, Charles M., *High Performance Silicon Nanowire Field Effect Transistors.* Nano Letters, 2003. **3**(2): p. 149-152.
10. Linwei, Y.B., O'Donnell; Martin, Foldyna; Pere Roca i, Cabarrocas, *Radial junction amorphous silicon solar cells on PECVD-grown silicon nanowires.* Nanotechnology, 2012. **23**(19): p. 194011.
11. Olesinski, R.A., GJ, *The Si− Sn (Silicon− Tin) system.* Bulletin of Alloy Phase Diagrams, 1984. **5**(3): p. 273-276.
12. Rasmus, V.S.J.T., G. Pedersen; Arne, N. Larsen, *Quasiparticle electronic and optical properties of the Si–Sn system.* Journal of Physics: Condensed Matter, 2011. **23**(34): p. 345501.
13. Lozac'h, M.Š., Vladimir; Askari, Sadegh; Mariotti, Davide; Ohashi, Noboru; Koganezawa, Tomoyuki; Miyadera, Tetsuhiko; Matsubara, Koji, *Semiconducting silicon-tin alloy nanocrystals with direct bandgap behavior for photovoltaic devices.* Materials Today Energy, 2018. **7**: p. 87-97.
14. Misra, S., et al., *Wetting Layer: The Key Player in Plasma-Assisted Silicon Nanowire Growth Mediated by Tin.* The Journal of Physical Chemistry C, 2013. **117**(34): p. 17786-17790.
15. Nebol'sin, V.A. and A.A. Shchetinin, *Role of Surface Energy in the Vapor–Liquid–Solid Growth of Silicon.* Inorganic Materials, 2003. **39**(9): p. 899-903.

16. Chambouleyron, I., et al., *Mössbauer study of hydrogenated amorphous germanium‐tin thin‐film alloys.* Journal of Applied Physics, 1989. **66**(5): p. 2083-2090.
17. I. Chambouleyron, F.C.M., *Use of hydrogenation in the study of the properties of amorphous germanium tin alloys.* Journal of Applied Physics, 1989. **65**(4): p. 1591-1597.
18. Kulikov, G.S. and K.K. Khodzhaev, *Diffusion doping of undoped hydrogenated amorphous silicon with tin.* Semiconductors, 1998. **32**(2): p. 123-123.
19. Yu, L., et al., *Guided growth of in-plane silicon nanowires.* Applied Physics Letters, 2009. **95**(11): p. 113106.
20. Dash, J.K., et al., *Metal-enhanced Ge1-xSnx alloy film growth on glass substrates using a biaxial CaF2 buffer layer.* CrystEngComm, 2014. **16**(37): p. 8794-8804.
21. Rojas-López, M., et al., *Raman scattering from fully strained Ge1−xSnx (x⩽0.22) alloys grown on Ge(001)2×1 by low-temperature molecular beam epitaxy.* Journal of Applied Physics, 1998. **84**(4): p. 2219-2223.
22. Downs Robert, T., Hall-Wallace Michelle, *The American Mineralogist crystal structure database.* American Mineralogist, 2003. **88**(1): p. 247-250.
23. Thompson, K., Gorman B, Larson D, van Leer Brandon, Hong Liang, *Minimization of Ga induced FIB damage using low energy clean-up.* Microscopy and Microanalysis, 2006. **12**(S02): p. 1736.
24. Alchagirov, B.B., Chochaeva A. M., *Temperature dependence of the density of liquid tin.* High Temperature, 2000. **38**(1): p. 44-48.
25. Moutanabbir, O., et al., *Colossal injection of catalyst atoms into silicon nanowires.* Nature, 2013. **496**(7443): p. 78-82.
26. Biswas, S., et al., *Non-equilibrium induction of tin in germanium: towards direct bandgap Ge1−xSnx nanowires.* 2016. **7**: p. 11405.
27. Reitano, R., P.M. Smith, and M.J. Aziz, *Solute trapping of group III, IV, and V elements in silicon by an aperiodic stepwise growth mechanism.* Journal of Applied Physics, 1994. **76**(3): p. 1518-1529.
28. Bruson, A., Gerl, M, *Diffusion coefficient of Sn 113, Sb 124, Ag 110 m, and Au 195 in liquid Sn.* Physical Review B, 1980. **21**(12): p. 5447.
29. Aziz, M.J., Tsao J. Y., Thompson M. O., Peercy P. S., White C. W., *Solute Trapping: Comparison of Theory with Experiment.* Physical Review Letters, 1986. **56**(23): p. 2489-2492.
30. Aziz, M.J., *Model for solute redistribution during rapid solidification.* Journal of Applied Physics, 1982. **53**(2): p. 1158-1168.
31. Goldman, L.M., Aziz M. J., *Aperiodic stepwise growth model for the velocity and orientation dependence of solute trapping.* Journal of Materials Research, 2011. **2**(4): p. 524-527.
32. Xue, Z., et al., *In‐Plane Self‐Turning and Twin Dynamics Renders Large Stretchability to Mono‐Like Zigzag Silicon Nanowire Springs.* Advanced Functional Materials, 2016. **26**(29): p. 5352-5359.
33. Olesinski, R.W., Abbaschian, G. J., *The Si−Sn (Silicon−Tin) system.* Bulletin of Alloy Phase Diagrams, 1984. **5**(3): p. 273-276.
34. Yu, L., Alet Pierre-Jean, Picardi Gennaro, Roca i Cabarrocas Pere, *An In-Plane Solid-Liquid-Solid Growth Mode for Self-Avoiding Lateral Silicon Nanowires.* Physical Review Letters, 2009. **102**(12): p. 125501.
35. Li, H., et al., *Strain relaxation and Sn segregation in GeSn epilayers under thermal treatment.* Applied Physics Letters, 2013. **102**(25): p. 251907.
36. Naidich, Y.V. and V.M. Perevertailo, *Surface and contact properties in the system composed of germanium and a tin-germanium melt.* Soviet Powder Metallurgy and Metal Ceramics, 1971. **10**(2): p. 142-147.
37. Olesinski, R., Abbaschian GJ, *The Ge− Sn (Germanium− Tin) system.* Bulletin of Alloy Phase Diagrams, 1984. **5**(3): p. 265-271.
38. Gault, B., Michael P, Cairney Julie M, Ringer Simon P, *Atom probe microscopy*. Vol. 160. 2012: Springer Science & Business Media.

39. Nooshin, A., Rodrigue Lardé, Etienne Talbot, Philippe Pareige, Lorenzo Rigutti, Lorenzo Mancini, Jonathan Houard, Celia Castro, Vincent Sallet, Emir Zehani, Said Hassani, Corine Sartel, Ahmed Ziani, Xavier Portier, *Quantitative analysis of doped/undoped ZnO nanomaterials using laser assisted atom probe tomography: Influence of the analysis parameters.* Journal of Applied Physics, 2015. **118**(21): p. 215703.
40. G. Da Costa, H.W., S. Duguay, A. Bostel, D. Blavette, B. Deconihout, *Advance in multi-hit detection and quantization in atom probe tomography.* Review of Scientific Instruments, 2012. **83**(12): p. 123709.

V NEW BOTTOM UP APPROACH: SOLID-SOLID-SOLID (SSS) MECHANISM

Metal catalysts are traditionally often used in their liquid phase during the catalytic growth of NWs, so that NWs can grow by the classical VLS [1] or SLS [2] mechanisms, in which the material is deposited onto the growing terrace of the NW via a liquid NP. In fact, the metal NP (e.g. In, Sn, Au, Fe, and Ti) forms an alloy with the semiconductor material (e.g. Si) at temperatures defined by their corresponding phase diagrams (i.e. Au-Si, Fe-Si, and Ti-Si). The eutectic temperature is in general lower than the melting point of pure metal catalyst (such as Au, Fe, or Ti-catalyzed SiNWs). It was thought that the temperature should be increased above the eutectic temperature of a given metal-semiconductor NP to activate the growth. Interestingly, the growth of vertical NWs has been achieved below the eutectic point for many systems; such as: Au-catalyzed Ge NWs, InAs and GaAs NWs, and Ti-catalyzed SiNWs [3-7]. These growth processes follow the VSS (vapor-solid-solid) mechanism which resembles the VLS but has relatively smaller growth rates, and produces out-of-plane NWs. However, there are no reports on the growth of in-plane NWs below a eutectic point. So the question is: is it possible to grow in-plane NWs using a solid catalyst? Can a solid catalyst move while it is buried (coated) under an a-Ge:H layer?

Amazingly, experimental proofs of the GeSn NWs growth below the eutectic point are presented. Hence, in this chapter, the growth of Sn-catalyzed GeSn NWs at temperatures below the melting point of Sn is studied. The thermal activation window for GeSn NWs is determined. Moreover, the differences between NWs produced at different temperatures are highlighted; which enables to distinguish two types of NW growth: the classical IPSLS [2] and the new IPSSS. Many possible explanations will be proposed about the driving force and the energy interplay underlying the IPSSS growth mode. At the end of this chapter, we will show that by changing the growth process steps, out-of-plane GeSn NWs can also be synthesized, and the possible mechanisms for the out-of-plane GeSn NWs growth are discussed.

V.1 SN-CATALYZED IN-PLANE SSS (IPSSS) GERMANIUM-TIN NANOWIRES

A gas precursor decomposes on the surface of a catalyst to form a metal-semiconductor alloy, and the eutectic temperature (T_E) of this alloy is lower than the melting temperature (T_M) of the metal catalyst itself. Considering Ti-catalyzed SiNWs for instance, Ti has T_M = 1668℃, meanwhile the newly formed $TiSi_2$ NP alloy has T_E = 1300℃. According to the Ti-Si phase diagram [8], Si is soluble in the Ti droplet. Hence, it can form the $TiSi_2$ alloy and, thereby, melt at temperatures below T_M. As mentioned in the introduction of this chapter, this is the case of many metal-semiconductor systems [3-7]. However, Sn-catalyzed GeNWs are a different case. The Ge-Sn phase diagram [9] shows that $T_M = T_E$ = 231.9℃, and that the Ge solubility in Sn at temperatures below T_M is close to 0.1 at.%. This means, that it is very unlikely that Ge forms an alloy with the Sn droplet. Therefore, in principle, the temperature should be equal to T_M = 231.9℃ or higher to activate the growth. The latter analogy is following the Ge-Sn phase diagram predictions. Nonetheless, we cannot ascertain theoretically the failure of the growth of in-plane NWs at temperatures below the eutectic point without an experimental attempt, because vertical VSS-NWs have been successfully produced by solid-phase catalysts. To reveal the plausibility of the SSS mechanism, growth trials are done in an attempt to grow in-plane GeNWs at temperatures below $T_E = T_M$. The IPSSS growth mode resembles the IPSLS mechanism, except that it leads to NW growth at temperatures below the melting point of Sn, as shown in Fig.V.1.

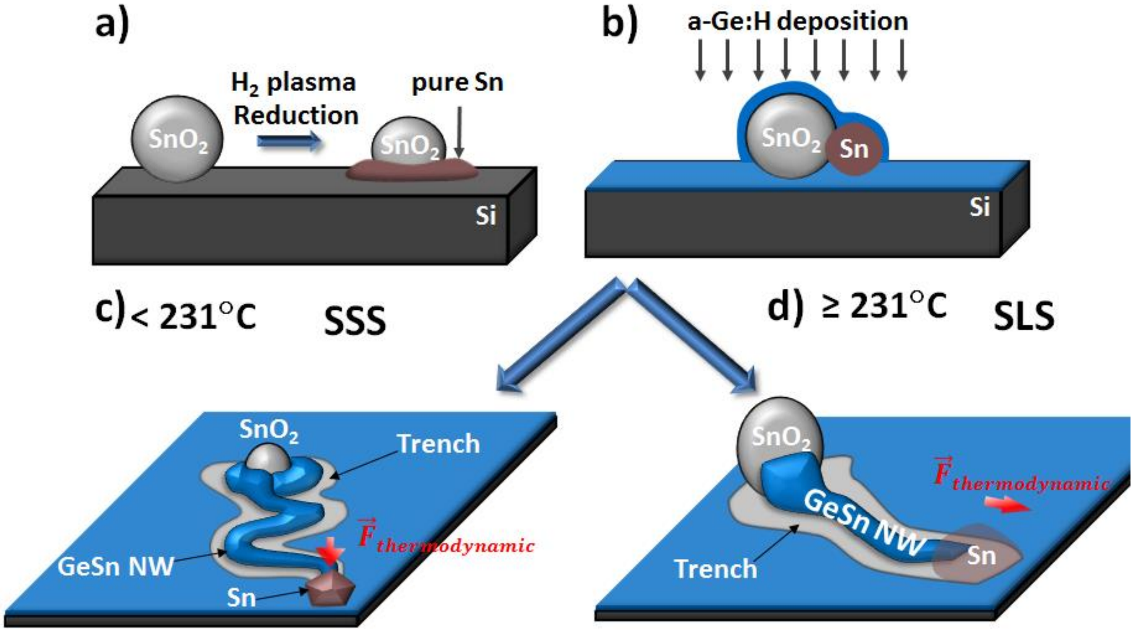

Figure.V.1- Growth of GeSn nanowires using SnO_2 as a precursor for the production of Sn catalyst. a) Partial reduction of SnO_2 NPs under hydrogen plasma. b) Deposition of a hydrogenated amorphous Ge layer (~17 nm) on the partially reduced SnO_2 NPs. c) Growth of Zig-Zag GeSn NWs at 180 °C. d) Growth of NWs following a random trajectory at 270 °C.

Briefly, the fabrication process consists of: i) deposition of SnO_2 colloidal NPs on a Si substrate, ii) partial reduction of SnO_2 to metallic Sn using a H_2 plasma (Fig.V.1.a), iii) deposition of an amorphous germanium layer (Fig.V.1.b), iv) annealing below the eutectic temperature of Sn to activate the SSS growth (Fig.V.1.c), or above for the SLS mode (Fig.V.1.d).

V.1.1 IPSSS THERMAL ACTIVATION WINDOW

Surprisingly, the NWs growth can be promoted at temperatures below the melting point of Sn ($T_M = T_E = 231.9$℃). The temperature below which no IPSSS-GeSn NWs could be grown is determined experimentally to be 140℃, whereas at higher temperatures 160℃ to 230℃, the IPSSS growth mechanism is activated. Increasing the temperature above the eutectic point of GeSn will result in the growth of IPSLS GeSn NWs. Further temperature increase (above 300℃) may lead to phase separation between Ge and Sn. The thermal activation window for each mechanism is shown in Table.V.1. In the case of in-plane NW growth, the catalyst should be in the liquid state, so it can be supersaturated by Si or Ge to promote the growth of in-plane NWs [2, 10, 11]. However, in the IPSSS growth mode, the catalyst is most probably in its solid state since the temperature can be as low as 160℃; i.e., 70℃ below the melting point. Reducing the size of a NP will increase the surface-to-volume ratio (i.e. the surface energy increases), which in turn modifies the properties of the NP, in particular its melting temperature [12]. To investigate the possibility that the catalysts are in their liquid state even below the melting point of the bulk material, the general expression of the variation of the transition temperature with the size of the structure is used [13]:

$$T = T_{m,\infty}\left(1 - \frac{b}{D_C}\right) \qquad (1)$$

Where $T_{m,\infty}$ is the bulk melting temperature, b is a coefficient depending on the material, and D_C is the diameter of the nanoparticle. Note that eq.(1) is only used for spherical particles.

Discrepancies exist concerning the experimental value of the coefficient “b” where b_{Sn} = 1.476 nm in ref. [14] or 1.57 nm in ref. [15]. Let us consider that D_C is equal to 80 nm, and knowing that $T_{m,\infty}$ is ~ 232°C, then the melting temperature for an 80 nm Sn NP would be T = 227°C. This means that the melting temperature is only decreased by ~ 5°C when D_C is 80 nm. However, in our case, the growth occurs for temperatures 30°C to 70°C below the melting point, and the activated NPs have larger diameters, up to 280 nm. By rearranging eq.(1), the variation of the NP’s size as a function of the melting temperature can be calculated:

$$D_C = \frac{b}{1 - \frac{T}{T_{m,\infty}}} \qquad (2)$$

Therefore, the size of a Sn NP to get melted at 160°C should be ~ 5 nm, which is unambiguously smaller than the observed sizes. These calculations let us consider that the growth takes place with a solid catalyst. Further experimental backup will be shown and discussed in section IV.1.2.

Growing NWs at different temperatures will result in different intrinsic parameters such as different: length of the NW (L_{NW}), diameter of the NW (D_{NW}), diameter of the catalyst (D_C), and the areal density of the NWs (NW/cm^2). As mentioned in chapter III – section III.2.2.1.2, increasing the temperature will increase the size of the activated catalyst. For this reason and based on SEM observations, the largest D_C measured from each sample will be considered for further investigations. Table.V.1 represents these intrinsic parameters for different growth temperatures.

Table.V.1. Influence of the substrate temperatures on the growth of GeSn NWs.

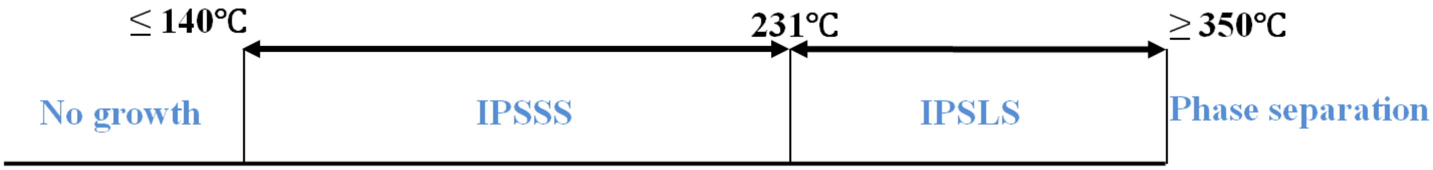

$T_{substrate}$	160°C	180°C	207°C	270°C	300°C
L_{NW} (nm)	860 ± 5	1555 ± 10	690 ± 10	840 ± 50	1000 ± 65
D_C (nm)	182 ± 5	220 ± 5	280 ± 3	410 ± 5	496 ± 10
D_{NW} (nm)	58 ± 2	65 ± 2	90 ± 2	120 ± 2	145 ± 2
Density (NW/cm²)	5.10^{6}	6.10^{6}	18.10^{6}	35.10^{6}	9.10^{7}

It is noteworthy that the error bars correspond to the uncertainty in the measurements using SEM observations done on each nanowire. Indeed, increasing the temperature will increase the activated catalyst size (D_C), i.e. from ~ 182 nm (at 160℃) to ~ 500 nm (at 300℃). The diameter of the nanowires, D_{NW}, is proportional to D_C, therefore upon the increase of the substrate temperature, the D_{NW} increase as well. L_{NW} is much harder to interpret, since it depends on the incorporation rate of Sn in the NWs (see Chap IV – section IV.2.2.1.5), and on D_C. If the incorporation rate of Sn is considered to be the same in all the samples (i.e. independent of the substrate temperature), larger catalysts do not necessarily mean longer NWs, because D_{NW} might also be large enough to produce NWs having the same lengths. The density of NWs increases with the increasing of the substrate temperature. This is the result of activating more catalysts of larger sizes alongside the smaller ones.

V.1.2 COMPARSION BETWEEN SSS- AND SLS-GROWN NANOWIRES

Many differences between the NWs produced via SSS and SLS approaches exist, for example: trajectories, morphologies, trenches, a-Ge:H consumption, structure and growth endings. These differences are highlighted in Fig.V.2.

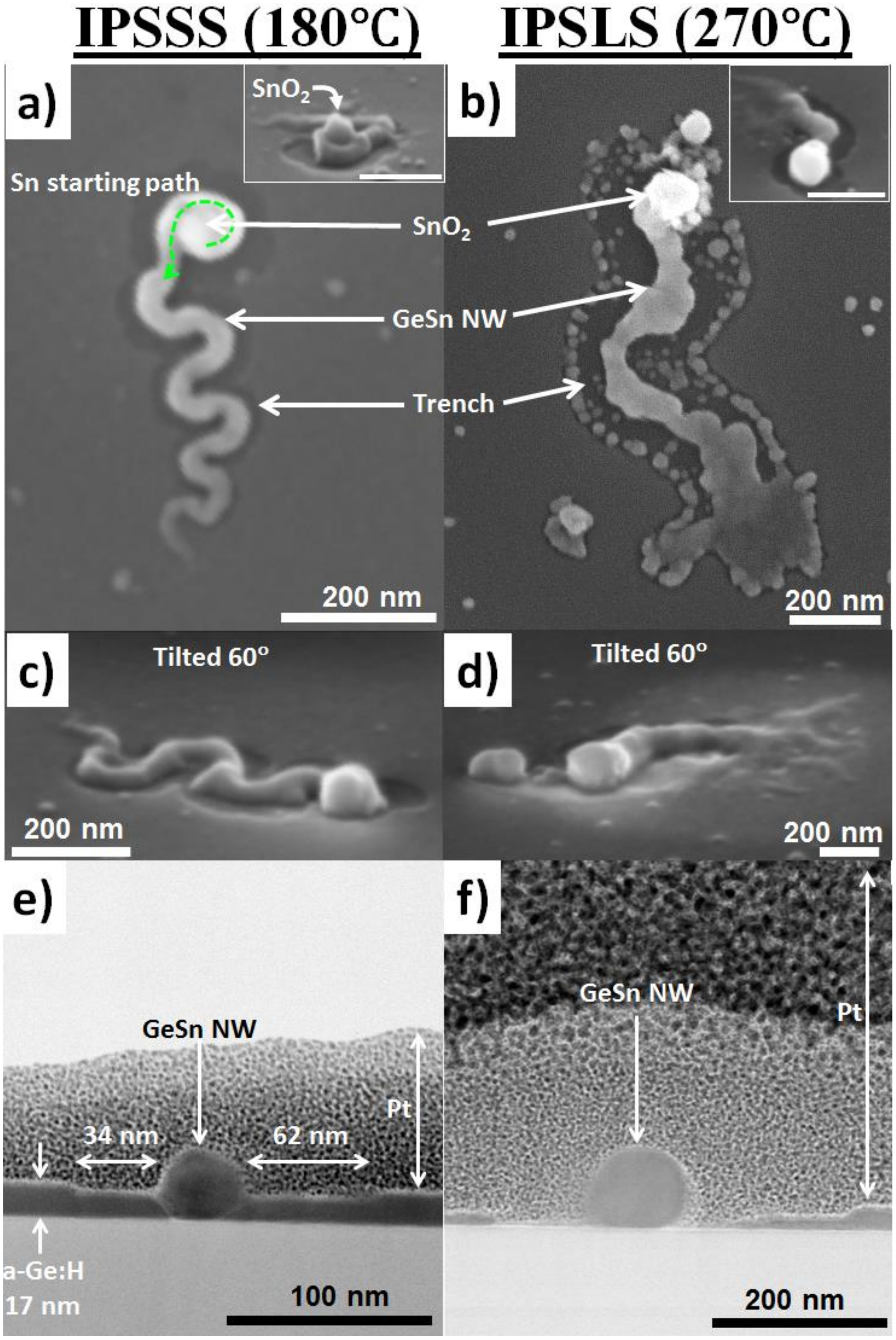

Figure.V.2- Main differences between SSS and SLS grown GeSn NWs. a) SEM image of an IPSSS GeSn NW grown at 180°C; the green arrow indexes the starting path of the catalyst. The inset is a tilted view showing that the NW has grown around the SnO_2 NP (scale bar 200 nm). b) SEM image of an IPSLS GeSn NW grown at 270°C, the inset is a tilted view showing the SnO_2 NP at the beginning which was not surrounded by the NW (scale bar 200 nm). c,d) SEM images tilted 60°, showing the entire

IPSSS and IPSLS grown NWs respectively. Cross-sectional TEM (bright-field) view with low magnification of GeSn NWs grown at e) 180℃ f) 270℃.

In Fig.V.2, the SEM images show the two types of NWs. The SSS-NW has a regular zig-zag shape with a smooth surface, whereas in the case of SLS mode, the NW trajectory is irregular and its surface is rougher compared to the previous one. In the case of SSS mode, the solid Sn NP turns around the SnO_2 NP while growing the GeSn NW (Fig.V.2.a), until it detaches from the SnO_2 NP (the reason for this turning and detachment from the SnO_2 NP will be explained in section IV.1.5). However for the SLS growth, the catalyst simply moves away from the SnO_2 NP as soon as the NW starts to grow (Fig.V.2.b.d). Tiny Sn nanoparticles (25 nm ± 5 nm) are pinned along the a-Ge:H trench in the SLS case (Fig.V.2.b), most probably due to the wetting of liquid Sn during the NW growth. Conversely, no such pinning effect is observed in the case of SSS (Fig.V.2.a,c), since the catalyst is most probably solid. At the last stage of the SLS growth, the catalysis is ended with a strong Sn-wetting (the case of liquid Sn), whereas, in the case of SSS growth this wetting does not exist, see for instance Fig.V.2.(c) and (d). Cross-sectional TEM images are shown in Fig.V.2.(e) and (f) for 180℃ and 270℃ samples, respectively. In the case of IPSSS, the thickness of the a-Ge:H film decreases near the GeSn NW growth region (more details in section V.1.4), whereas, a-Ge:H was completely consumed in IPSLS. These analyses were based on SEM and TEM observations; however for a more fundamental comprehension a chemical analysis is required.

V.1.3 STRUCTURE AND COMPOSITION OF IPSSS GESN NANOWIRES

The STEM-HAADF and STEM-EDS investigation of GeSn NW cross-sections prepared by FIB for samples grown at 180°C and 270°C are displayed in Fig.V.3. In Fig.V.3.a, the HAADF shows the faceted topology of the NW grown at 180°C (see the green indexed interface between Pt and NW) with the inset indicating its crystalline nature. The EDS mapping in Fig.V.3.b shows that the outer layers of the shell are made of pure c-Ge having a thickness of ~ 13.5 nm, and the core part of the NW made of GeSn has a diameter of ~ 23 nm. Therefore, the structure is unambiguously a core-shell, with a GeSn core and Ge-rich shell. The Sn concentration starts to increase from the outer part (Ge-rich region) to the core, eventually to reach its highest value (~ 35 at.%) at nearly the core part of the NW (as shown in Fig.V.3.c). Core-shell structures were observed on all the IPSSS GeSn NWs grown at temperatures below the eutectic one. For comparison, the NWs grown at higher temperature (270°C) are also shown (cross-sectional TEM in Fig.V.3.d), and their distribution of Sn according to the EDX in Fig.V.3.e-h is homogeneous. However, this homogeneity cannot be ascertained on an atomic scale, due to resolution limitations of the EDX (~ 1.5 nm), see chapter IV – section IV.2.2.1.2 for more details.

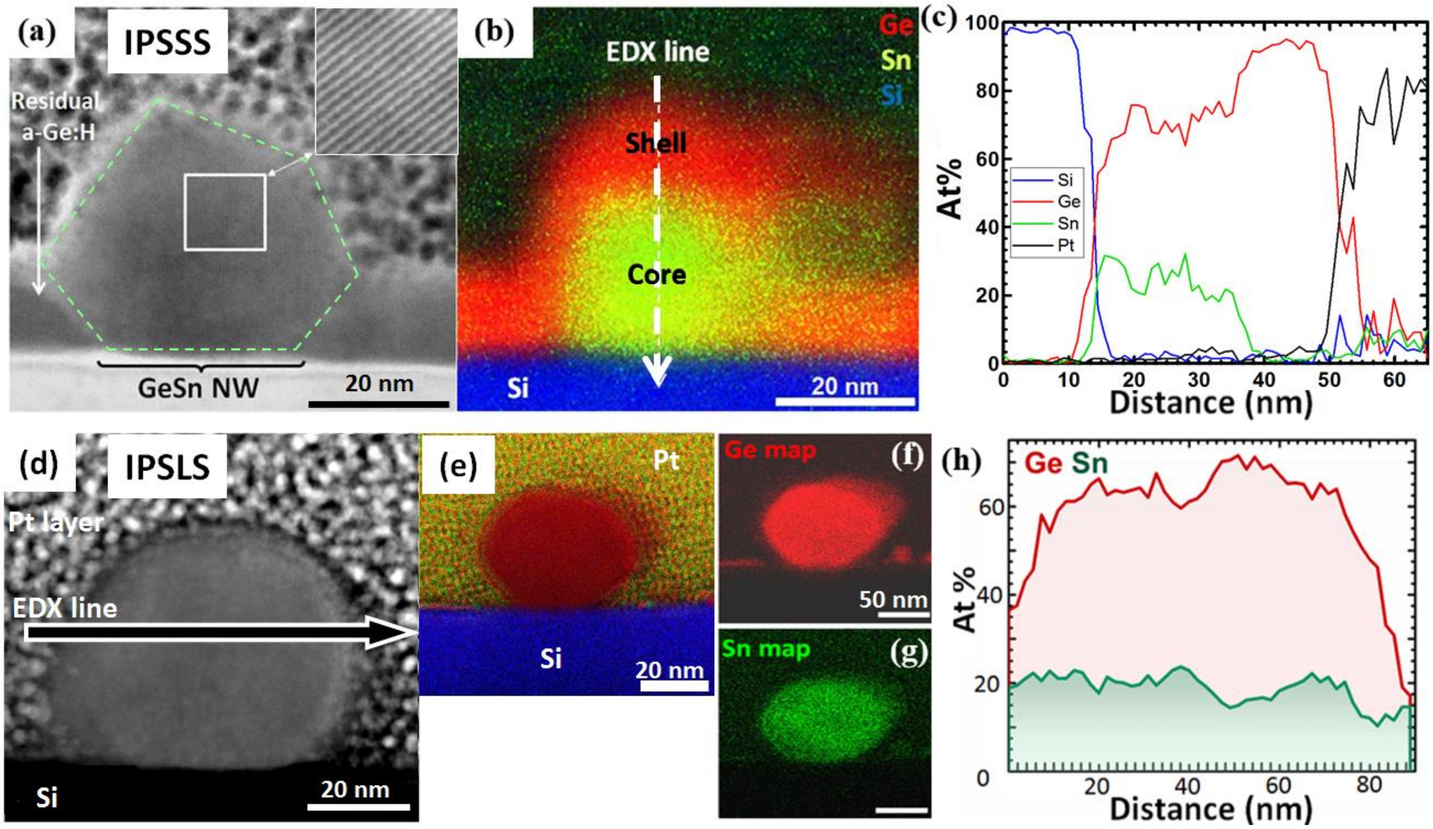

Figure.V.3- HRTEM and EDX mapping of GeSn NWs grown at 180 and 270°C. a) HAADF micrograph showing a radial cross-section of a GeSn NW grown on a Si substrate at 180°C. b) The corresponding EDX mapping of IPSSS GeSn NW showing a core-shell structure. c) Composition profile along the vertical white dashed line in (b). d) Cross-section TEM image of GeSn NWs grown at 270°C. e) The corresponding EDX mapping of the IPSLS GeSn NW in (d), showing a homogeneous distribution; Ge and Sn elemental spatial distributions are shown in (f) and (g) respectively. (h) Composition profile along the black arrow indicating the atomic percentage of Ge and Sn (the complement to 100% is due to presence of

Si, Ga, O, and Pt atoms incorporated at the surface of the sample during the ion beam preparation process). The EDX error is approximately ± 3 at.%.

Based on the previous observations a comparison is made between the SLS and SSS as shown in table.V.2.

Table.V.2. IPSSS and IPSLS GeSn NWs comparison

	Mechanism **Description**	SSS	SLS
SEM	**Starting point**	Sn NPs turn around the SnO_2 NPs while growing the nanowires	Sn NPs move away from SnO_2 NPs while growing the nanowire
	Trajectory	Zig-Zag	Random
	Morphology	Smooth	Rough
	Trench edge	No pinned Sn NPs	Sn NPs are pinned
	Ending point	No wetting	Wetting
TEM-EDX	**a-Ge:H layer**	Partially consumed	Largely consumed
	Element distribution	Sn-rich Core/Ge-rich shell	Homogeneous GeSn
	Structure	Polycrystalline	Polycrystalline

As previously described, many experimental observations support the hypothesis that the catalyst is solid during the growth, such as: no pinned NPs on the trench, no wetting at the end of the growth, and smooth morphology of the NWs. In fact, the morphology variations of SLS NWs are induced by the catalyst deformation during the growth [2]. However, if the catalyst is solid, these deformations will most probably not happen, thus, leading to a smoother NWs surface in IPSSS mode compared to IPSLS-NWs.

Another unique feature of the IPSSS growth mode is that some of the examined GeSn NWs are porous (specifically two IPSSS-NWs grown at 160℃ and 180℃ out of 18 examined), see Fig.V.4.

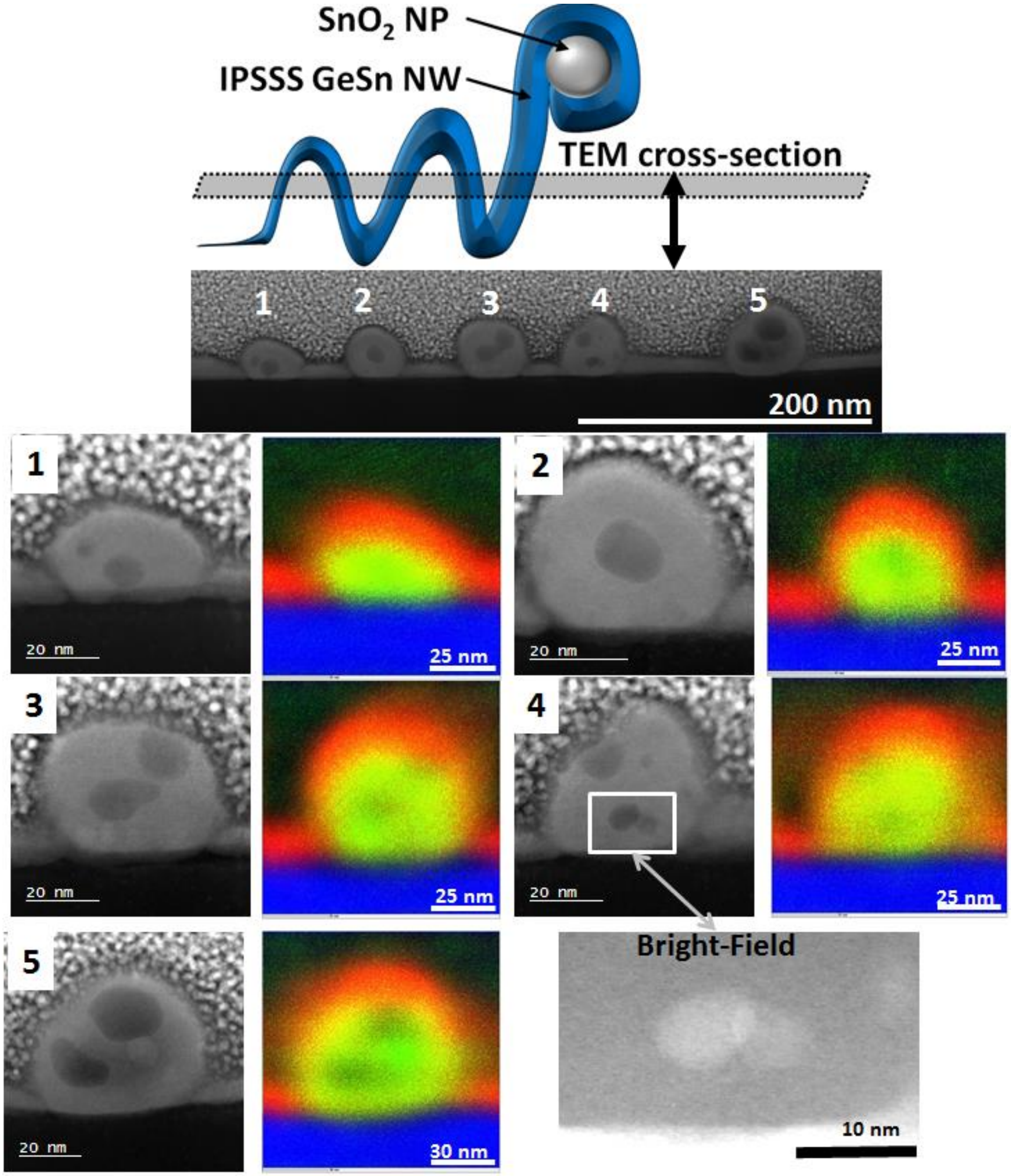

Figure.V.4- Cross-section STEM – HAADF and EDX mapping of different regions of a porous IPSSS GeSn NW grown at 180℃. The indexed (white rectangle) region in site 4 is shown in Bright-field view for more clarity.

The porosity is not related to the growth temperature, this has been proven by the observation of many IPSSS-NWs cross-sections analyzed in TEM from samples grown at different temperatures. The growth mechanism of the IPSSS might be responsible of this porosity which is believed to be formed during the growth. The voids are located in the core region (Sn-rich region) of the GeSn NW, as shown by the EDX maps of Fig.V.4. On the image 4 in Fig.V.4, the white rectangle contains two pores that are shown in the bright field micrograph. These two pores seem to be empty separate bubbles inside the NW, with no connection between them. Yet, a clear proof on the existence of a tubular void along the entire NW is not available (it would require a statistical study, i.e. hundreds of cross-sections are necessary).

V.1.4 GROWTH RATE ESTIMATION

The growth rate (GR) is obtained by dividing the length of a nanowire by the duration of its growth. In our case, the high incorporation of Sn results in a rapid consumption of the catalyst into the NW, therefore, no Sn NPs can be observed after the growth. Therefore, as it was mentioned in Chap.IV – section 2.2.1.3.2, because the real growth time is not known, a lower value of GR could be obtained. In order to determine a value of GR close to the real one, the growth should be stopped before the full incorporation of the catalyst in the NW. The growth steps are: 1) reduction of SnO_2 NPs, 2) deposition of a-Ge:H layer, and 3) annealing to activate the growth. Thus, many growth trials are needed to determine at which step the NWs are growing and for how long the growth lasts. Table.V.3 resumes a number of trials serving the investigation. The first three trials include an annealing process (at 270℃) to activate the growth. However, the catalysts were completely consumed even after decreasing the annealing time from 90 min to 10 min. The 4th trial proves that annealing is unnecessary because the growth is achieved during the deposition of a-Ge:H at 180 ℃ for 10 min, which means that the RF plasma is still ignited during the growth. This could be a reason why the Sn NPs pinned on the edges of the trench in the SLS case do not exist in the SSS case; the plasma may etch them leaving a smoother trench (compare for instance Fig.V.2.(a) and (b)). Another possibility is that the plasma modifies the surface energy of a-Ge:H (i.e. decreases it) and therefore reduces the wetting behavior. This has been observed in the case of VLS growth of SiNWs catalyzed by Au [16].

Table.V.3 – Different growth trials by decreasing the annealing and deposition times.

T°C	180°C	270°C	
Trial	Deposition time	Annealing time	Description
1	10 min	90 min	Sn consumed totally
2	10 min	60 min	Sn consumed totally
3	10 min	10 min	Sn consumed totally
4	10 min	-	Sn consumed totally
5	5 min	-	Sn consumed totally
6	3 min	-	Sn consumed totally
7	2 min	-	Discontinuous NWs
8	1 min	-	no NWs

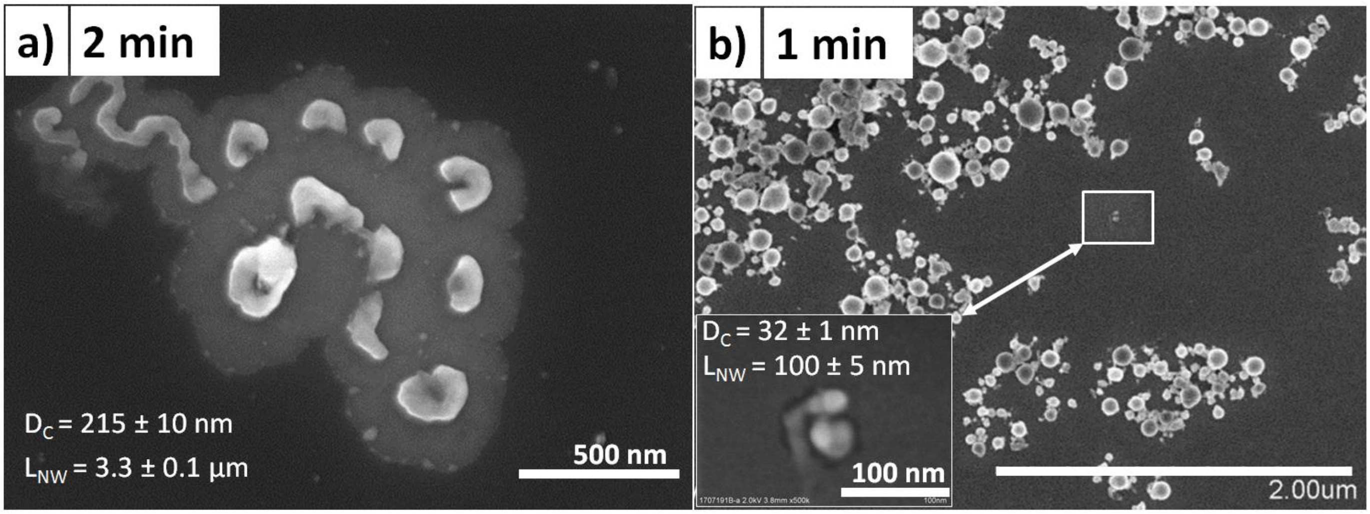

Figure.V.5- Top-view SEM image of IPSSS GeSn NWs grown during the deposition of a-Ge:H for a) 2 min, b) 1 min.

Decreasing the deposition time to 2 min leads to the growth of discontinuous GeSn NWs (Fig.V.5.a). In this case, the quantity of the a-Ge:H was not enough to build a continuous NW, but smaller catalysts build continuous ones (see inset Fig.V.5). This raises questions on the growth mechanism, especially if the catalyst is considered in its solid state. A discussion will be made in the next section about the possibility of supersaturating a solid catalyst by Ge, and the possible growth mechanisms of the IPSSS GeSn NWs.

Further decrease in the deposition time results in almost no growth of NWs. In fact, for the one minute deposition sample (at 180°C), only very tiny nanowires are activated, as the one shown in the inset Fig.V.5.b, which means that the a-Ge:H thickness is an important factor for starting the growth. There are two conditions to start the growth: i) if the small catalysts (e.g. with an average trench size at the starting position of ~ 25 nm) are liquid, then the amorphous thickness is enough to supersaturate them and precipitate c-Ge seeds which will create a Gibbs energy difference, thus, a driving force, and ii) if the catalysts are solid, than the Ge atoms will diffuse on their surface and form c-Ge seeds on one side of the catalyst, thereby, an energy difference and a driving force. In the latter case, Ge atoms will have to diffuse a short distance to reach a bottom edge region or the SnO_2/Sn interface; due to the small catalyst size, the c-Ge seed needed to create the driving force will have a smaller size as well. Despite the decrease of the deposition time down to 1 min, the activated (small) catalyst has been totally consumed which complicates even more the determination of the GR.

The TEM images (for instance Fig.V.2.e) show that the trench region, in the SSS mode, contains an a-Ge:H layer surrounding the IPSSS NWs. Normally these layers are totally consumed (or extremely thinned) by the liquid catalyst. The fact that the NWs are growing during the plasma deposition step means that the a-Ge:H layer is continuously deposited during or after the growth of the NWs. Based on this hypothesis, the growth rate of the NWs can be calculated using the thickness of the a-Ge:H deposited after the formation of the core part. Let us assume that W is the initial thickness of the a-Ge:H deposited when the catalyst just grew the NW at the moment $t = t_0$ (as shown in Fig.V.6.a) and W_{end} is the thickness of the a-Ge:H layer at the end of the deposition step, in other terms, it is the total thickness of the a-Ge:H layer at the end of the deposition (as shown in Fig.V.6.b).

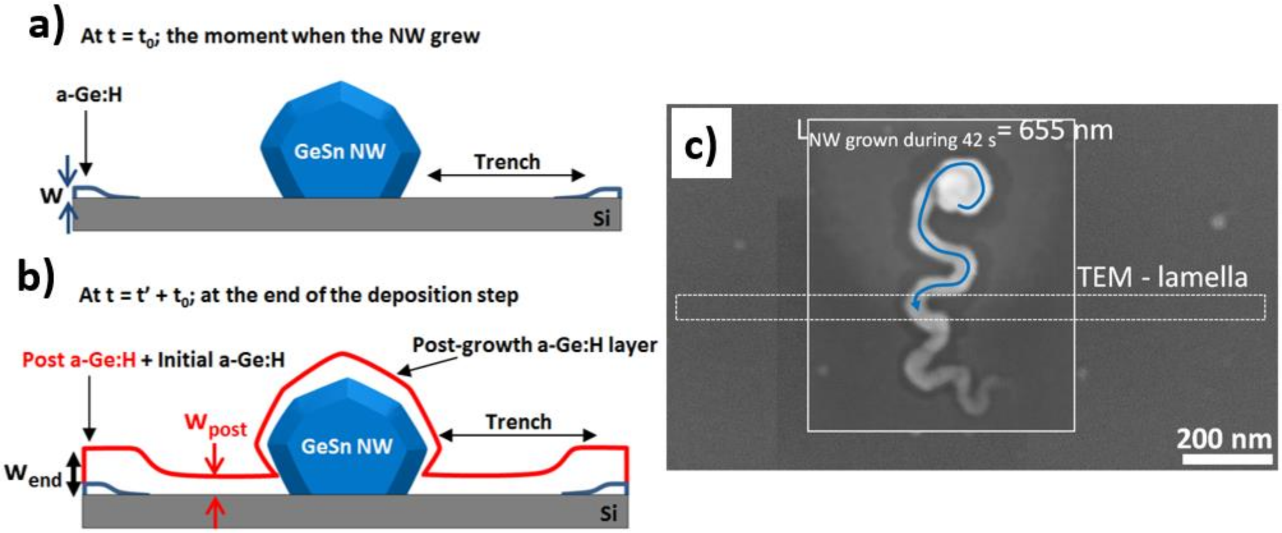

Figure.V.6- Determination of the growth rate a) GeSn NW cross-section schema showing the thickness (W) of the a-Ge:H at the moment when this region of the nanowire is grown, b) same as previous schema, except that a-Ge:H deposition has continued after the NWs growth, therefore more thickness of a-Ge:H is added. W_{end} denotes the total thickness of the a-Ge:H at the end of the deposition process, and W_{post}: the width of the a-Ge:H layer added after the growth of the nanowire to a certain length. c) SEM top-view of the NW used for the growth rate calculation. The TEM lamella obtained using FIB is indexed by the rectangle, the length of the nanowire starting from the initial position till the lamella is ~ 655 nm.

Thus, it can be written that $W_{end} = W + W_{post}$, where W_{post} is the thickness of the a-Ge:H deposited after the growth of the NW, and till the end of the deposition process (at $t = t_0 + t'$). Therefore to calculate the growth rate, it is necessary to calculate W (the initial thickness at the moment when the NW grew which is the one shown in Fig.V.6.a); $W = W_{end} - W_{post}$. The measurements using the TEM micrograph (Fig.V.2.e) gives: W_{end} ~ 17 nm and W_{post} ~ 15 nm; and therefore W = 2 nm. Under the deposition conditions used in the PECVD reactor (PLASFIL), every 6 min of GeH_4 plasma corresponds to ~ 17 nm thickness of a-Ge:H (i.e. growth rate of a-Ge:H is ~ 0.047 nm/s), then the W = 2 nm corresponds to ~ 42 s. The SEM top-view image corresponding to the NW cross-section of Fig.V.2.e, is shown in Fig.V.6.c. It indicates the region which was prepared by the FIB (the indexed rectangle in Fig.V.6.c), hence, the length of the NW grown during 42 s (= t_0) is ~ 655 nm therefore the growth rate of the NW is GR ~ 16nm/s. By referring to the DIM (dimer-insertion model) in chapter III – section 2.2.1.3.4, the GR of 16 nm/s corresponds to an incorporation of 35 at.% Sn into the NW, which is consistent with the experimental results.

The NW growth takes place during the deposition of a-Ge:H by PECVD, as it is shown in table.V.3. This means that the core region of the NW (Sn-rich) is fabricated by the catalyst, then, the Ge covers the core of the NW, resulting in a core-shell structure (schematically shown in Fig.V.6.b). Interestingly, the post deposition of a-Ge:H (after the formation of the core part of the GeSn NW) indicated in Fig.V.6.b is, under the used conditions, heteroepitaxially grown. As it was shown previously by the TEM in Fig.V.3.a, the Ge shell has a crystalline structure and it is faceted. The shell growth is a standard vapor-solid deposition at 180℃, however in the case of the core region, which is the NW catalyzed by Sn is more complicated. In the following part, various possibilities for the IPSSS growth mechanism will be discussed.

V.1.5 IPSSS GROWTH MECHANISM

There are two aspects to consider when trying to explain the SSS growth mechanism: first, the essential mechanism of Ge mass transport to form the NWs, and second, the detachment of Sn NPs from the SnO_2 NP at the beginning of the growth.

The mass transport mechanism of Ge to reach the NW is important to understand for an advanced growth control. Many hypotheses can be proposed to explain the growth mechanism.

i) As a first possibility, the Ge transport could be achieved by diffusion inside the solid catalyst [17], as shown in Fig.V.7.a. To assess this possibility, the duration of Ge diffusion should be calculated. Because, no data is available on the diffusion of Ge in Sn, we will consider the interdiffusion coefficient of Ge/Sn [18]. The diffusion coefficient of Ge in Sn is:

$$D = D_0 . e^{-\frac{E_A}{kT}} \, cm^2 . s^{-1}$$

With D_0 being the pre-exponential factor that equals to 2.9×10^{-7} $cm^2.s^{-1}$, the activation energy E_A that equals to 1.21 eV, k is the Boltzmann constant, and T is the temperature in Kelvin. The diffusion coefficients corresponding to 210℃, 180℃, and 160℃ are 6.8×10^{-20}, 1×10^{-20}, and 2.3×10^{-21} $cm^2.s^{-1}$ respectively. Here, we consider that the diffusion process occurs in one direction (according to the white arrow in Fig.V.7.a), which means that L = $\sqrt{2Dt}$. Supposing that the diameter of the catalyst has a typical value of 115 nm which is the distance to be travelled by Ge atoms (L) to reach the NW, therefore the time needed to travel from the front side of the catalyst to the rear side (that is the NW/catalyst interface) for 210℃, 180℃, and 160℃ are 16×10^{6} hours, 112×10^{6} hours, and 47×10^{7} hours respectively. Knowing that the growth is done in less than 5 min during the deposition phase, the calculations do not support the diffusion through the solid catalysts as being the dominant growth mechanism. The distance L can be lower than the diameter of the catalyst since the growth is proven to be done during the deposition stage. In other words, Ge atoms can be deposited on the surface of the catalyst then diffuse inside the catalyst towards the NW using a shorter distance than the latter case. However, even if the distance is divided by two, Ge atoms still need $\sim 4 \times 10^{6}$ hours to reach the NW at 210℃.

ii) Grain boundaries (GBs) can exist in catalysts having diameters around 100 nm, which can be considered as ultra-fine grained nanoparticles [19]. Since no TEM experiment is done to prove the GBs existence, and no data is available on the diffusion of Ge through them, this possibility remains a hypothesis. The activation energy for GB diffusion is, in general, lower than that of solid diffusion [20]. As a result, a faster mass transport can occur compared to the standard diffusion through the catalyst structure (Fig.V.7.b). In general, the melting process starts at GBs and defects in the crystalline structure, at temperatures that are around 80% of the melting point of the system [21]. In our case, the temperatures used for the growth vary between 70% and 90% of the melting temperature of bulk Sn (~ 232℃), therefore, the GBs can be premelted which can further enhance the diffusion of Ge atoms through them.

iii) The third possibility is the diffusion on the surface of the catalyst, as shown in Fig.V.7.c. Since the mass transport via volume diffusion requires an extremely long time to be achieved, perhaps the surface diffusion is a more favorable mechanism of mass transport. In the vapor-solid-solid mechanism, the diffusion occurs on the surface of the catalyst [22]. Briefly, the VSS uses a gas precursor that decomposes on the surface of the catalyst, and the feeding atoms migrate on the surface towards the triple-phase boundary (NW/catalyst/atmosphere) which is considered the main gate for the insertion of atoms. By analogy, we suggest that the same mechanism can occur for the SSS growth process. However, the sources of Ge atoms for the NWs growth are: the plasma, and the amorphous layer. The plasma decomposes the gas precursor, thus, providing Ge atoms to the Sn NPs, while the a-Ge:H layer is a very dense source of Ge atoms compared to the gas precursor. Therefore, a higher growth rate is expected for the

SSS compared to VSS. Moreover, the incubation time is considered to be lower for a solid catalyst compared to a liquid catalyst, which increases more the growth rate of the NWs.

iv) The last possibility is the diffusion through a premelted surface, as shown in Fig.V.7.d. As mentioned previously, the growth temperature varies between 160℃ and 210℃, and the liquid-solid phase transition occurs progressively but not spontaneously via the boundaries interface, surface, and structural defects of the catalyst [21]. The incoming Ge atoms (from the plasma and a-Ge:H thin-film) can diffuse inside the premelted surface of the catalyst towards the Ge NW. This diffusion process can be simply dictated by Fick’s law. This possibility can also explain the discontinuous NWs obtained at low temperatures (< 231℃). In fact, the Ge should supersaturate the molten surface of the catalyst in order to precipitate a crystalline NW. However, for the two minutes deposition case, the Ge atoms were insufficient to keep the molten surface supersaturated, which therefore created a discontinuous NW.

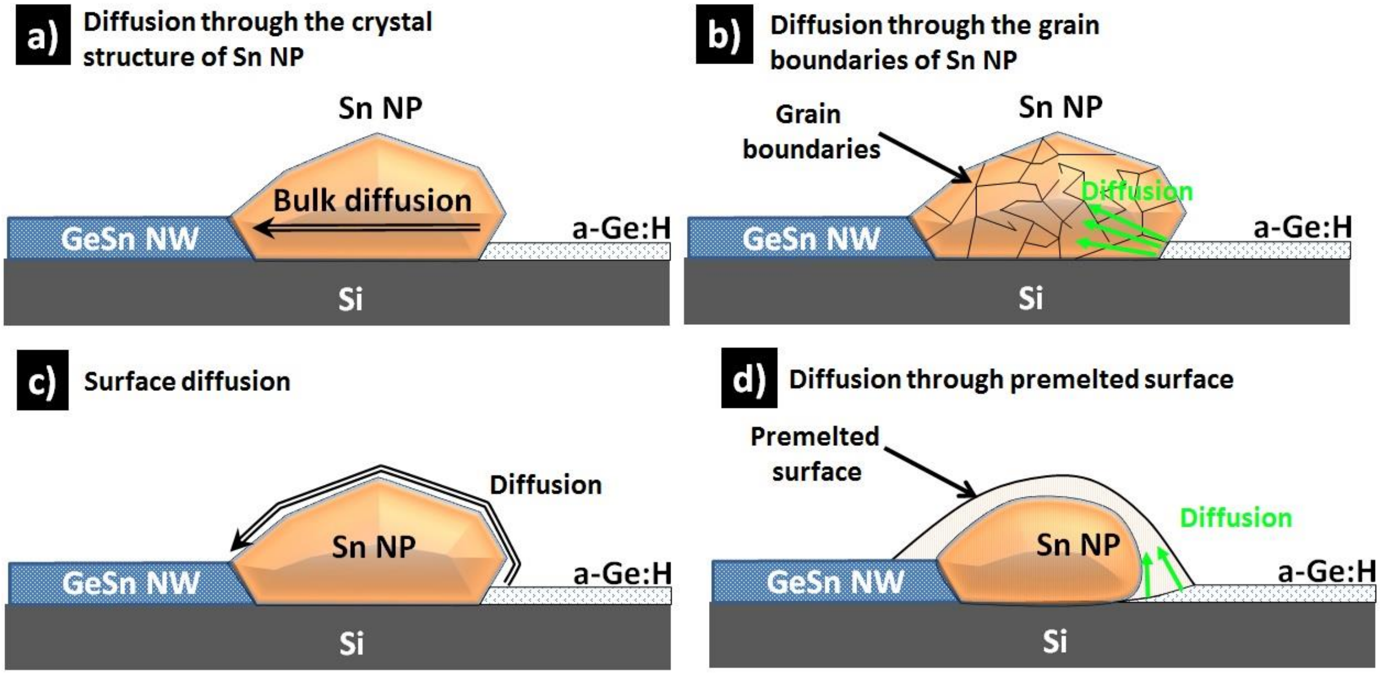

Figure.V.7- Proposed IPSSS mass transport mechanisms a) volume diffusion of Ge through the catalyst b) diffusion via the grain boundaries, c) diffusion on the surface of the catalyst, and d) diffusion inside the molten surface of the catalyst.

Since the GeSn NW growth takes place during the plasma deposition step, an experiment was done to investigate if it is possible to do the IPSSS growth without the plasma Fig.V.9.c. It is important to reveal whether IPSSS NWs are grown using GeH_x radicals coming from the plasma or from the amorphous layer or from both sources. Therefore, approximately 8 nm of a-Ge:H were deposited on top of the catalysts, and the deposition temperature was chosen to be 110℃, to avoid the growth during this step. Then, the plasma was turned off, and the temperature was raised to 180℃ for 1 hour to activate the growth in vacuum environment. The resulting nanostructures are shown in Fig.V.8. It is not straightforward to call these nanostructures as NWs. So the result is that the catalyst cannot rely only the a-Ge:H layer to achieve the growth. However, if the catalyst relies only on the radicals (GeH_x) that are coming from the plasma during the deposition step, then we shall see no "trench" after the growth (see Chap I section I.3 – Fig.I.11). After careful analysis of these data, we conclude two main points: 1) the catalyst uses both sources of Ge (GeH_x radicals, and a-Ge:H) for the growth, 2) since the Gibbs energy of plasma-produced radicals is relatively higher than that of the a-Ge:H, then a greater driving force is created compared to using only a-Ge:H as Ge source. For these reasons, the growth of IPSSS GeSn NWs is successful in the presence of plasma radicals.

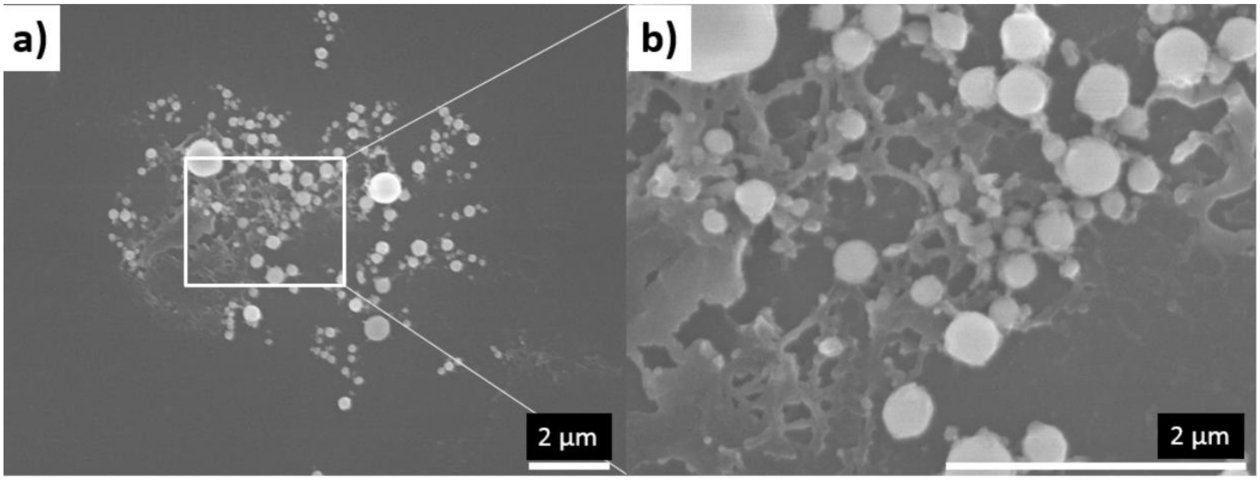

Fig.V.8 SEM images of a validation test of SSS mechanism. a) An aggregate of Sn catalyst topped with an a-Ge:H layer and activated at 180℃ for 55 min b) a magnified image of (a).

In the IPSSS mode, the Sn NP turns around the SnO_2 NP during the initial stages of the growth. It is energetically more favorable for the solid Sn NP to stay in contact with the SnO_2 NP, as shown in Fig.V.2.a and in Fig.V.9.a. This pinning effect remains until it reaches the NW already grown at the starting position. In fact, alongside the pinning effect, the catalyst is advancing circularly around the SnO_2 NP, and the driving force is created by the Gibb energy difference between the amorphous and crystalline Ge on its both sides (Fig.V.9.c). As soon as the SnNP reaches the already grown NW, after almost completing a circular turn, it gets detached from the SnO_2 NP.

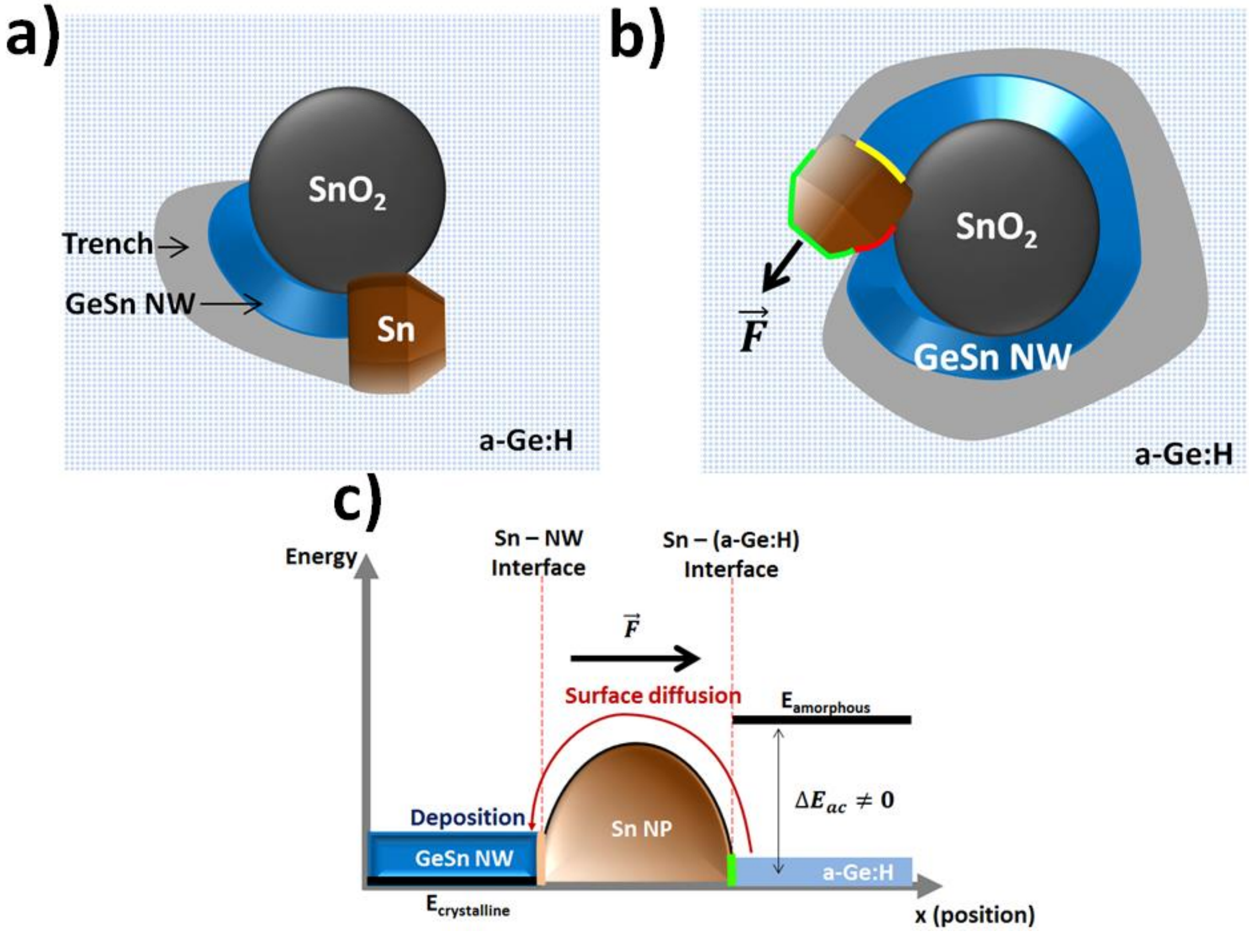

Figure.V.9- The detachment of the Sn NP from the SnO_2 NP. a) Initial stages of the turning process of Sn driven by the pinning effect of SnO_2 NPs, b) the detachment of the Sn NP due to the existence of the NW on its front and rear side. The green, red, and orange lines are respectively the catalyst/a-Ge:H, catalyst/NW, and NW/catalyst interfaces; and c) the driving force between the orange and the green lines is derived from the Gibbs energy difference of a-Ge:H and the c-GeNW.

In Fig.V.9.b, there are two interfaces: catalyst/a-Ge:H (green) and catalyst/NW (orange, and red). When the catalyst meets the NW grown earlier, the circular advancement of the catalyst will stop due to the existence of a crystalline Ge on both sides of the catalyst (orange and red interfaces in Fig.V.9.b). As a result, there is no Gibbs energy difference between these two interfaces, thus, no driving force. However, the catalyst is still in contact with a-Ge:H, as indicated by the green interface in Fig.V.9.b, where the thermodynamic force drags the catalyst away from the SnO_2 NP. As a conclusion, four possible mechanisms of Ge transport to the NW were considered: i) bulk diffusion, ii) grain boundary diffusion, iii) surface diffusion, and iv) diffusion through the premelted surface of the catalyst. We concluded that the last two possibilities are the most probable, because the diffusion process is easier on the surface of the catalyst or through its premelted surface compared to the other two cases. The IPSSS GeSn NWs are synthesized during the deposition, where the plasma helps achieving the growth. Moreover, it was shown that the detachment of Sn NP from the SnO_2 NP is a consequence of the Gibbs free energy. In the following section, we will present growth experiments that are designed to improve the crystalline quality of the GeSn NWs.

V.2 OUT-OF-PLANE GERMANIUM-TIN NANOWIRES

In all the previous experiments, the NWs were grown on native silicon oxide layers (SiO_x) topping the c-Si substrate. In fact, crystalline Si wafers were used for the growth, but since they are exposed to the atmosphere, a typical ~ 2 nm SiO_x layer is formed. To improve the crystallinity of the in-plane NWs, the idea was to remove the native SiO_x and grow the NWs directly on a c-Si surface. To remove the SiOx from the surface of the c-Si substrate a HF dip was used. The experimental procedure is shown in Fig.V.10.

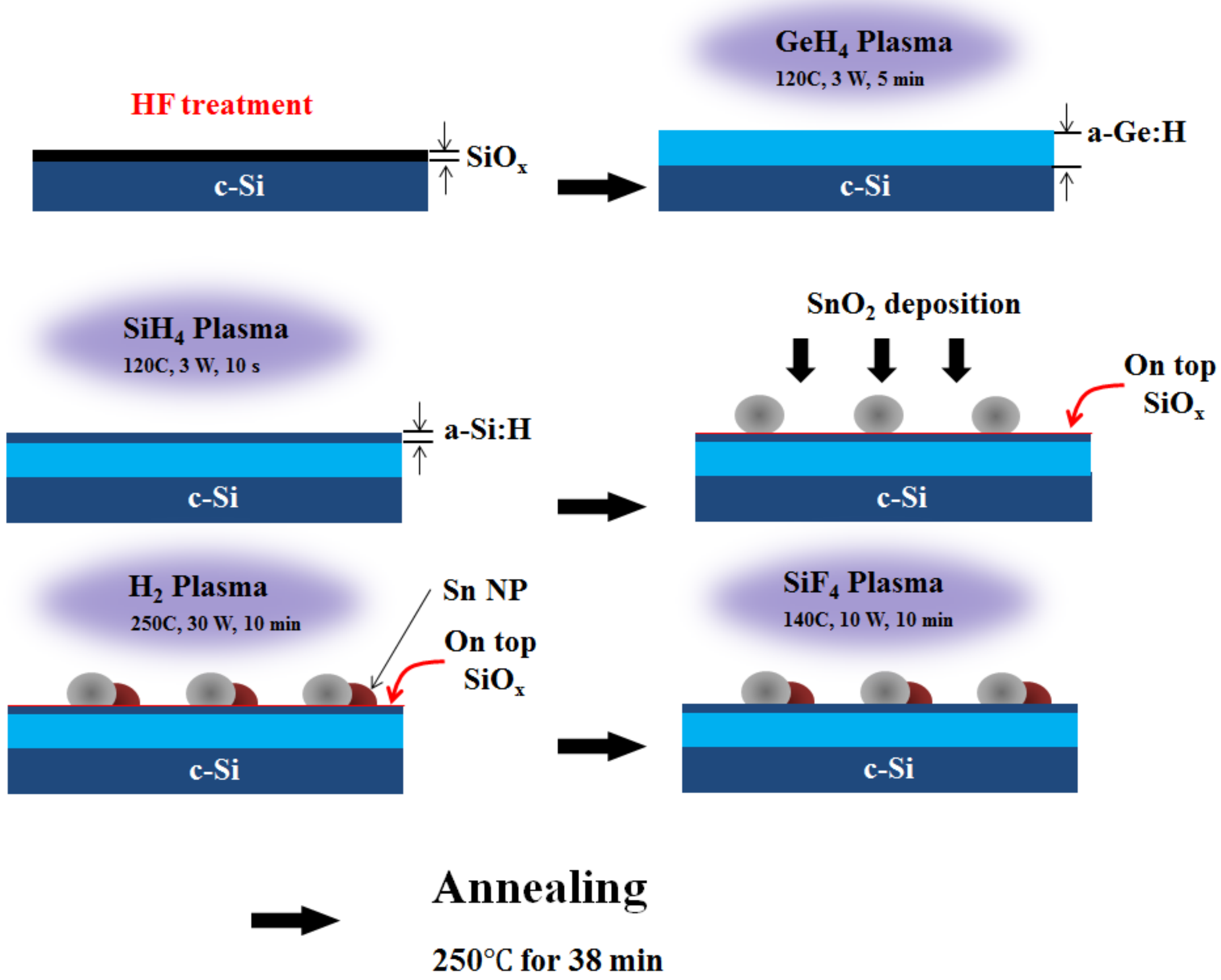

Figure.V.10- Schematic illustration showing the growth process where the native oxide on the c-Si wafer was removed via HF dip. The crystalline surface of the substrate was protected from oxidation using a 7 nm a-Ge:H and 1 nm of a-Si:H. SnO_2 NPs were deposited and partially reduced to Sn using a hydrogen plasma. Then a SiF_4 plasma was ignited for 10 min to remove the silicon native oxide. The temperature was raised from 140°C to 250°C in 38 min (under hydrogen flow), and then the sample was left to cool-down to 180°C. The sample was kept in the PECVD reactor for 14 hours at 180°C (under high-vacuum).

Directly after dipping the substrate in HF for 30 seconds, the substrate was rinsed with deionized water and dried with Nitrogen gas. Afterwards, the substrate is introduced in the PECVD reactor where a-Ge:H and a-Si:H layers of 7 nm and 1 nm respectively were deposited to protect the c-Si surface from oxidation. Then, the SnO_2 colloids were deposited on top of the amorphous layers, and partially reduced using a H_2 plasma (30 W) at 250°C for 10 min. Finally, the native oxide layer formed on top of the a-Si:H was treated by SiF_4 plasma (10 W) at 140℃ for 10 min. To activate the SLS growth, the temperature was raised from 140℃ to 250℃ in 38 min, and the sample was left for 14 hours under vacuum at 180℃.

We expected that Sn NPs would dissolve the amorphous layers beneath, get supersaturated, and precipitate NWs on the crystalline surface of the Si substrate. However, unexpectedly, out-of-plane NWs have been grown, as can be seen in Fig.V.11. The Sn NPs have catalyzed NWs that have different lengths and diameters. For instance, the length can vary from 500 nm to 1 μm, whereas the diameter ($\emptyset_{top}$ and $\emptyset_{bottom}$ represents the top and the bottom diameters respectively) can vary for the same NW, which might be due to the consumption of Sn catalyst (see Fig.V.11). The surface of the sample is roughened by the SiF_4 or H_2 plasma treatment, as shown in Fig.V.11.a. Moreover, the regions around the grown NWs seem to be thinner (Fig.V.11.a,b), and the regions that are more close to the growth are possibly wetted by the liquid Sn (Fig.V.11.c,d,e).

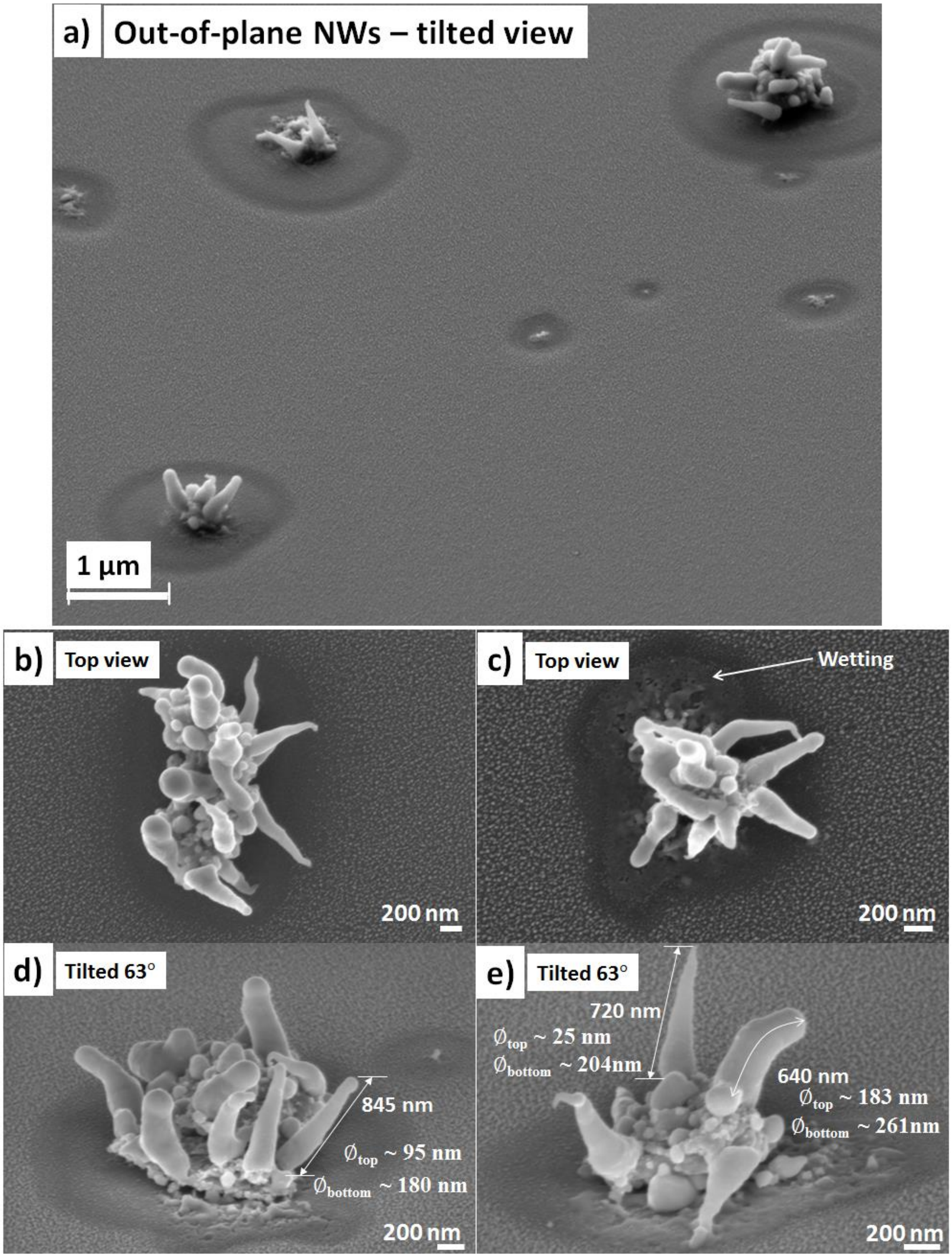

Figure.V.11- SEM images showing the out-of-plane NWs. a) Low magnification showing the NWs and the topology of the surface of the substrate near and away from the growth regions. b) Top view of a NWs region where there is no visible wetting. c) Top view of NWs region where the Sn wetting is visible. (d) and (e) tilted view of two NWs regions.

In order to further analyze the process, a region of NWs was selected for TEM characterizations, see Fig.V.12. Using FIB/SEM, a cross-sectional TEM lamella was obtained containing the indexed NWs (NW1, and NW2) in Fig.V.12.a. The axial cross-sections (Fig.V.12.b,c) show that each NW has two NPs, one located on its top and the other one on its bottom. Most probably the NP sitting on the top of the NW is Sn, whereas the bottom one is most probably SnO_2. The diffraction pattern obtained using TEM shows the crystalline nature of NW2 (inset of Fig.V.12.c). In the next section, an EDX measurement is used to reveal the spatial distributions and the composition of these NWs.

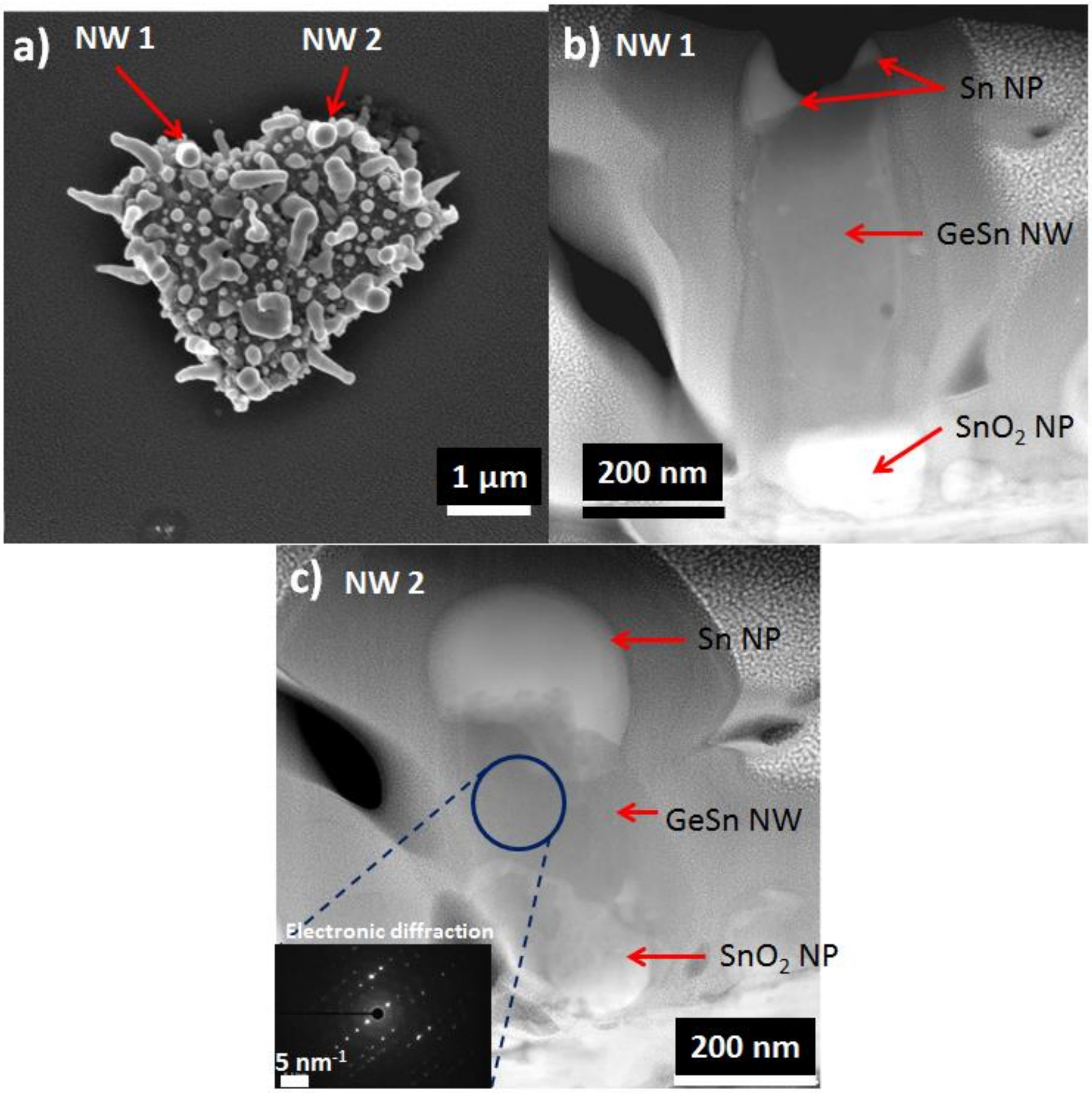

Figure.V.12- Out-of-plane nanowire micrographs. a) SEM image showing a heart-shaped catalyst pad with vertical NWs on top. NW1, and NW2 were analyzed using TEM and EDX. b) An axial cross-section of NW1. Two catalysts can be observed in this micrograph, the top one was partially destroyed during FIB operation. c) Axial cross-section of NW2. This image shows the catalyst on top of the NW as well as a catalyst on its bottom. The inset is an electronic diffraction pattern proving the crystallinity of this NW.

V.2.1 COMPOSITION OF GE-SN NANOWIRES

For further composition investigations, STEM-EDX measurements were performed. The EDX cartography done on NW2, is shown in Fig.V.13.a, and the cartography of its composition (Fig.V.13.b) proves that it is a GeNW with a Sn NP on its top. To quantify the NW composition, a region depicted “spectre” is chosen. The quantification results are shown in the table of Fig.V.13.c, ~ 5 at.% Sn is incorporated inside such kind of NWs which is higher than the equilibrium solubility (< 0.5 at.% of Sn in Ge).

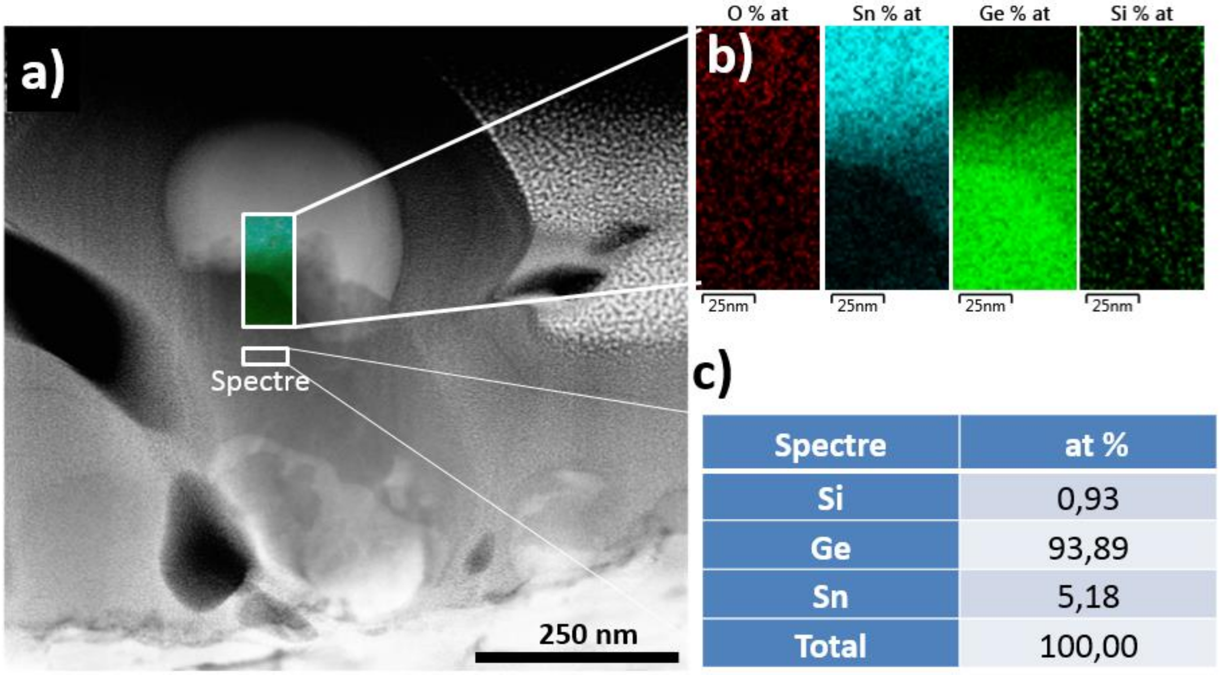

Spectre	at %
Si	0,93
Ge	93,89
Sn	5,18
Total	100,00

Figure.V.13- EDX measurements on the upper part of NW3. a) A NW micrograph showing the 2D EDX cartography at the top NW/catalyst interface. b) EDX measurement on the interface, showing the 2D spatial distribution of the elements (atomic percentage). c) A quantification of the NW composition showing the atomic concentration in the NW’s body (far from the catalyst).

It is also important to determine the nature of the remaining part of the catalyst precursor on the bottom part of the NW in order to understand the growth mechanism. It is expected to be SnO_2 since it is standing still on the bottom side of the NW (Fig.V.14.a,b), and the EDX quantification confirmed our expectation. Therefore, when raising the temperature only the molten part of the catalyst (Sn) will catalyze the growth while the SnO_2 NP will remain inactive.

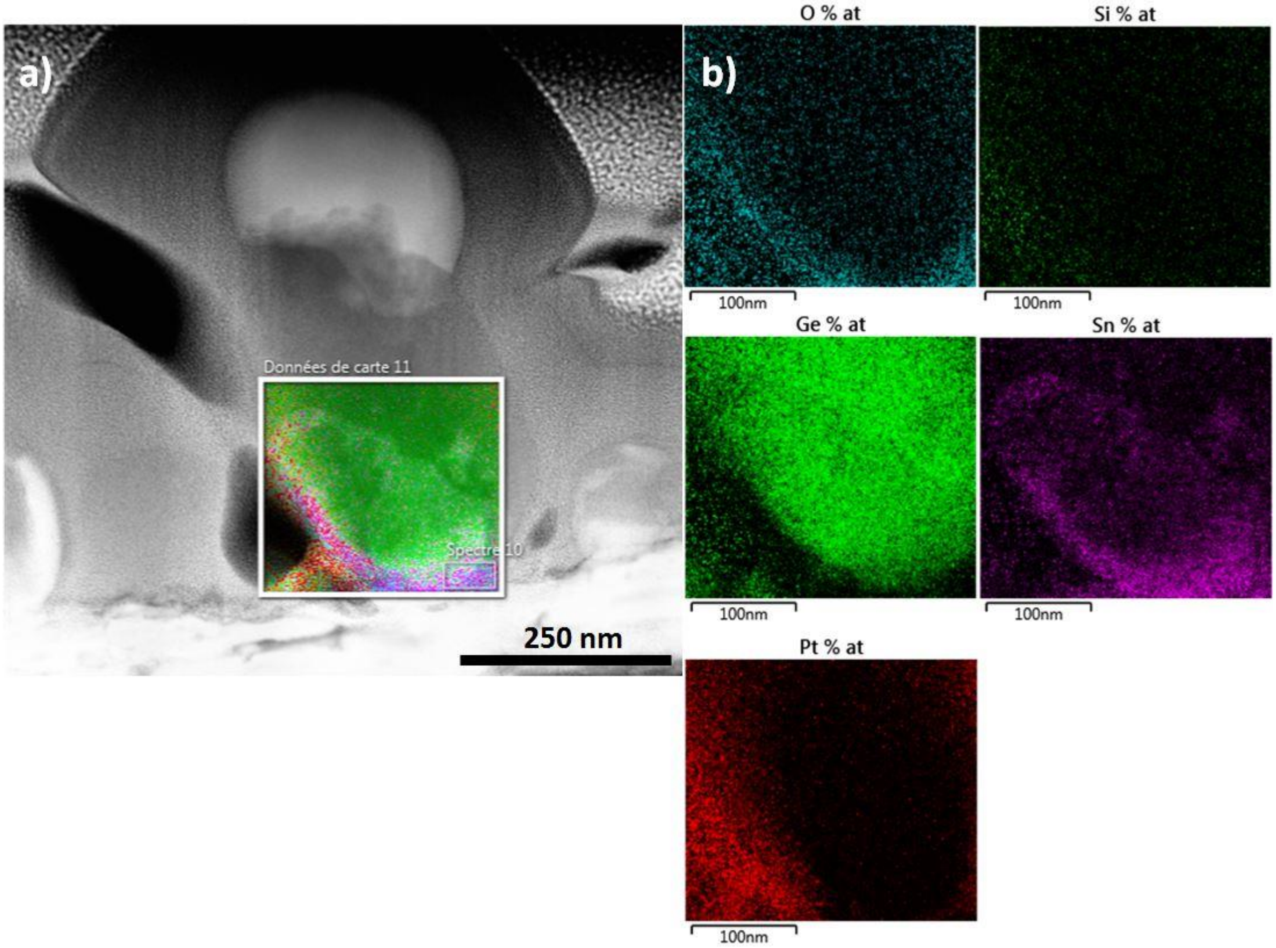

Figure.V.14- EDX measurements on the bottom part of NW2 a) A NW micrograph showing the 2D EDX cartography at the bottom NW/catalyst interface. b) EDX elemental mapping, showing the 2D spatial distribution of elements (atomic percentage).

The SEM, TEM, and EDX analysis are important to reveal the nature, and structure quality of the obtained NWs. They are equally important to help the determination of the growth mechanism. Four hypotheses are proposed and discussed in the following section based on the characterization results.

V.2.2 PROPOSED GROWTH MECHANISM

Three samples were successfully fabricated containing out-of-plane NWs, each having the same process conditions, except that the amorphous Ge thickness was increased from 3 nm to 5 nm. This means that this kind of NWs is reproducible. Four scenarios are proposed to explain this growth:

1- Ge atoms are transported by the plasma from the reactor inner walls (which are coated by a-Ge:H) and from the a-Ge:H layer on the substrate. This mass transport can be done during the H_2 or SiF_4 plasma. In the case of H_2 plasma, the catalysts are in their liquid state (the temperature during this process is 250℃) leading to the standard VLS mechanism.

2- Ge atoms might be provided during the SiF_4 plasma treatment. Note that the SiF_4 plasma duration is 10 min with a flow of 30 sccm at 140℃, therefore the growth should proceed via VSS mechanism (solid catalyst).

3- Ge atoms can be provided during the annealing step; when the temperature is raised from 140℃ to 250℃ during 38 min. Since there is no plasma during this step, then there is no Ge transport via H_2 or SiF_4 plasma. Therefore, the only way the Ge can reach the liquid catalyst is by surface diffusion.

4- As the previous analysis, but this time during the last step, which is the annealing at 180℃ during 14 hours. These atoms may nucleate under the bottom part of the solid catalyst to grow a NW, or between the SnO_2 and the Sn NPs. The superficial diffusion process is only allowed when the native oxide of the amorphous layer is treated by SiF_4 plasma, because the SiO_x plays the role of a barrier preventing the diffusion of Ge atoms. Note that these samples have been kept in the reactor for 14 hours at 180℃ after raising the temperature to 250℃ during 38 min. An approximate calculation to estimate the surface diffusion length is made using 1.63 eV [23] as an activation energy for surface diffusion of Ge, and 5.10^2 cm^2/s as a pre-exponential factor [24]. During 14 hours, Ge atoms can diffuse approximately ~ 42 nm on the surface of the substrate. This diffusion length is enough for the Ge to migrate towards the catalyst, nucleate and grow a NW.

Since it is proved using EDX that these are GeSn NWs, the second possibility is dismissed. The GeH_4 gas was not used after the deposition of SnO_2 and the subsequent treatments (but only before the SnO_2 colloidal deposition). To restrain the number of possibilities, two experiments were designed to reveal the step at which the vertical nanowires are grown.

In the first experiment, the same fabrication procedure is repeated with the same conditions except that we stopped after the H_2 plasma treatment step which is done at 250℃ for 10 min. No further SiF_4 plasma treatment or annealing in this case. Then, the sample is taken out for SEM inspection. The growth was unsuccessful; no NWs are produced at this step. It means the H_2 plasma did not etch the a-Ge:H layer (that have a superficial native oxide) to transport Ge atoms to the liquid catalyst.

In the second experiment, the same procedure as the previous one is repeated, but this time the SiF_4 plasma treatment is added alongside the H_2 plasma. The duration of the treatment is 10 mins, and the temperature used is 140℃, which means that the catalyst NPs stay in their solid state. The growth is unsuccessful, no NWs are produced. Same analogy as the previous condition, the SiF_4 plasma did not etch the amorphous layer to provide Ge atoms for the catalysts, despite removing the native oxide of the amorphous layer. Leaving the last two mechanisms as the most probable, unfortunately it was not possible to perform further experiments. This leaves the underlying mechanisms of these NWs as perspective for future studies.

V.3 SUMMARY

As a conclusion, a new mechanism was proposed for the growth of GeSn NWs using Sn NPs at substrate temperatures below the melting point of Sn. It was shown that Sn NPs are small in size but not enough to shift their melting point towards lower temperature. Therefore, Sn NPs are expected to be in their solid state during the growth of NWs. An activation window is defined for the growth of GeSn NWs, with a lower limit at 160℃, which is 70℃ below the eutectic temperature. The IPSSS NWs have different morphologies than IPSLS NWs. Moreover, at the region where the NW ends, wetting is not observed for the IPSSS mechanism, which is considered as additional evidence that the catalysts are solid. The IPSSS NWs are shown to have a core-shell structure (Sn-rich core and Ge-rich shell) compared to a homogeneous (at a nanoscale) distribution for the IPSLS GeSn NWs. The Sn concentration in the IPSSS GeSn NWs can reach up to 35 at.% at the core part, while in the shell it is nearly pure Ge. Four mechanisms were suggested for the IPSSS GeSn NWs growth: bulk diffusion, grain boundary diffusion, surface diffusion, and premelted surface diffusion. We concluded that the last two possibilities are the most probable.

Unexpectedly, out-of-plane GeSn NWs were obtained using a modified growth process, where an amorphous Ge layer is deposited at the first place, then, SnO_2 colloids and their subsequent plasma treatments. The EDX quantifications have shown that the Sn concentration can be ~ 5 at.% in the NWs. Various growth mechanisms are proposed for this kind of vertical NWs. After many experiments, their reproducibility is proven. Many trials are done with different conditions proving that the growth is neither a VLS nor a VSS mechanism. The most probable mechanisms for the growth are SLS or SSS out-of-plane. As perspective work, its suggested to repeat the same growth process of the out-of-plane including the 14 hours annealing at 180℃, in order to verify that the growth is done in the last step.

V.4 REFERENCES

1. Dubrovskii, V., Sibirev NV, Cirlin GE, Harmand JC, Ustinov VM, *Theoretical analysis of the vapor-liquid-solid mechanism of nanowire growth during molecular beam epitaxy.* Physical Review E, 2006. **73**(2): p. 021603.
2. Yu, L., i Cabarrocas Pere Roca, *Growth mechanism and dynamics of in-plane solid-liquid-solid silicon nanowires.* Physical Review B, 2010. **81**(8): p. 085323.
3. Kodambaka, S., Tersoff J, Reuter MC, Ross FM, *Germanium nanowire growth below the eutectic temperature.* Science, 2007. **316**(5825): p. 729-732.
4. Hiruma, K., Yazawa M, Katsuyama T, Ogawa K, Haraguchi K, Koguchi M, Kakibayashi H, *Growth and optical properties of nanometer‐scale GaAs and InAs whiskers.* Journal of Applied Physics, 1995. **77**(2): p. 447-462.
5. Kamins, T., Stanley Williams R, Basile DP, Hesjedal T, Harris JS, *Ti-catalyzed Si nanowires by chemical vapor deposition: Microscopy and growth mechanisms.* Journal of Applied Physics, 2001. **89**(2): p. 1008-1016.
6. Ohlsson, B., Björk MT, Persson AI, Thelander Claes, Wallenberg LR, Magnusson MH, Deppert Knut, Samuelson Lars, *Growth and characterization of GaAs and InAs nano-whiskers and InAs/GaAs heterostructures.* Physica E: Low-dimensional Systems and Nanostructures, 2002. **13**(2-4): p. 1126-1130.
7. Persson, A.I., Larsson Magnus W, Stenström Stig, Ohlsson B Jonas, Samuelson Lars, Wallenberg L Reine, *Solid-phase diffusion mechanism for GaAs nanowire growth.* Nature materials, 2004. **3**(10): p. 677.
8. Bandyopadhyay, D., *The Ti-Si-C system (titanium-silicon-carbon).* Journal of phase equilibria and diffusion, 2004. **25**(5): p. 415-420.
9. Olesinski, R., Abbaschian GJ, *The Ge− Sn (Germanium− Tin) system.* Bulletin of Alloy Phase Diagrams, 1984. **5**(3): p. 265-271.

10. Yu, L., Alet Pierre-Jean, Picardi Gennaro, Roca i Cabarrocas Pere, *An In-Plane Solid-Liquid-Solid Growth Mode for Self-Avoiding Lateral Silicon Nanowires.* Physical Review Letters, 2009. **102**(12): p. 125501.
11. Linwei Yu, M.O., Oumkelthoum Moustapha, Franck Fortuna, Pere Roca i Cabarrocas, *Guided growth of in-plane silicon nanowires.* Applied Physics Letters, 2009. **95**(11): p. 113106.
12. Liu Minglu, W., Robert Y., *Size-Dependent Melting Behavior of Colloidal In, Sn, and Bi Nanocrystals.* Scientific Reports, 2015. **5**: p. 16353.
13. Wautelet, M., *Effects of size, shape and environment on the phase diagrams of small structures.* Nanotechnology, 1992. **3**(1): p. 42.
14. Allen G. L., B.R.A., Gile W. W., Jesser W. A., *Small particle melting of pure metals.* Thin Solid Films, 1986. **144**(2): p. 297-308.
15. Wautelet, M., *Estimation of the variation of the melting temperature with the size of small particles, on the basis of a surface-phonon instability model.* Journal of Physics D: Applied Physics, 1991. **24**(3): p. 343.
16. Chen, W., Pareige Philippe, Castro Celia, Xu Tao, Grandidier Bruno, Stiévenard Didier, Roca i Cabarrocas Pere, *Atomic characterization of Au clusters in vapor-liquid-solid grown silicon nanowires.* Journal of Applied Physics, 2015. **118**(10): p. 104301.
17. Wen, C.-Y., Reuter MC, Tersoff J, Stach EA, Ross FM, *Structure, growth kinetics, and ledge flow during vapor− solid− solid growth of copper-catalyzed silicon nanowires.* Nano letters, 2009. **10**(2): p. 514-519.
18. Wei Wang, Y.D., Qian Zhou, Eng Soon Tok, Yee-Chia Yeo, *Germanium–tin interdiffusion in strained Ge/GeSn multiple-quantum-well structure.* Journal of Physics D: Applied Physics, 2016. **49**(22): p. 225102.
19. Sauvage, X., Wilde Gerhard, Divinski SV, Horita Zenji, Valiev RZ, *Grain boundaries in ultrafine grained materials processed by severe plastic deformation and related phenomena.* Materials Science and Engineering: A, 2012. **540**: p. 1-12.
20. Mishin, Y., Herzig Chr, *Grain boundary diffusion: recent progress and future research.* Materials Science and Engineering: A, 1999. **260**(1-2): p. 55-71.
21. Alsayed Ahmed M, I.M.F., Zhang Jian, Collings Peter J, Yodh Arjun G, *Premelting at defects within bulk colloidal crystals.* Science, 2005. **309**(5738): p. 1207-1210.
22. Kolasinski, K.W., *Catalytic growth of nanowires: vapor–liquid–solid, vapor–solid–solid, solution–liquid–solid and solid–liquid–solid growth.* Current Opinion in Solid State and Materials Science, 2006. **10**(3-4): p. 182-191.
23. Fukatsu, S., et al., *Self-limitation in the surface segregation of Ge atoms during Si molecular beam epitaxial growth.* Applied Physics Letters, 1991. **59**(17): p. 2103-2105.
24. Allen, C.E., R. Ditchfield, and E.G. Seebauer, *Surface diffusion of Ge on Si(111): Experiment and simulation.* Physical Review B, 1997. **55**(19): p. 13304-13313.

CONCLUSION & PERSPECTIVES

This thesis is a pioneering work on GeSn nanowires, backed up by atomic scale characterization techniques such as APT and TEM. The objective is to fabricate crystalline GeSn NWs with a high Sn incorporation, while maintaining the crystallinity and avoiding phase separation of Sn and Ge. Among several growth mechanisms, the bottom-up in-plane SLS was chosen for the growth of GeSn NWs, since it helps achieving high growth rates, which are necessary for a non-equilibrium kinetically driven incorporation of Sn.

Chap I presented a literature review about the state-of-the-art methods of growing nanowires. The main focus was on the bottom up approaches VLS and SLS. Since the SLS allows achieving higher growth rates, and SLS nanowires can be controlled and guided to assemble a certain circuitry design, therefore, the SLS mechanism was chosen to fabricate the GeSn NWs. The $Ge_{1-x}Sn_x$ alloy is an interesting material for electronics and optoelectronics due its better properties compared to Si. The carrier mobility is improved by the increment of Sn concentration in Ge, and an indirect-to-direct transition of the energy band-gap occurs for a sufficient amount of Sn (between 6 at.% and 11 at.%).

Chap II described the fabrication and characterization machines used in this thesis. In the first part, the fabrication techniques were discussed. For the fabrication of catalysts, magnetron sputtering coater, and thermal evaporator were used. The PECVD reactor was used for surface treatments, depositions, and growth of NWs. In the second part, different characterization techniques were used for investigations of the obtained NWs. The FIB/SEM dual beam was used to fabricate specially-designed specimens for TEM and APT characterizations. The TEM allowed having a deep insight on the NWs atomic structure, and the EDX allowed the quantification of the components constituting the NWs. APT is an ultra-fine characterization tool, with abilities to reconstruct in 3D real-space the atom-by-atom evaporated NWs. The mass-spectrometry, equipped in the atom probe, gives the ability of identifying the detected evaporated atoms with single atom precision.

In Chap III, In-catalyzed Ge NCs and NWs were studied. Indium catalysts are obtained using the reduction of an ITO thin film which was deposited by magnetron sputtering. The feeding layer (a-Ge:H) is then deposited on top of the whole system at a temperature below the eutectic point of Ge-In (< 156 ℃). The temperature was raised above the latter temperature to activate the growth. The analysis showed that the size of the catalyst influences the length of the NWs. Large catalysts drops (700 nm to 1.5 μm in diameter) can grow shorter NWs compared to smaller catalysts (60 nm to 200 nm), which were able to grow Ge NWs up to 15 μm long under the same conditions. As a perspective, further characterization are needed for the GeNWs produced by the In NPs (i.e. 60 nm – 200 nm) in APT, in order to see if the In is incorporated in the NWs. The incorporation of In in Ge NWs might produce p-type NWs, which might be useful in nanoelectronics.

In the first part of Chap IV, the growth of IPSLS SiSn NWs is described. Two temperatures were used for the growth 300℃ and 400℃. In the second part of this chapter, the fabrication of GeSn NWs was studied. The evaporated metallic Sn lead to unsuccessful GeSn NWs growth attempts. The reason for this failure is the strong wetting behavior caused by the contact of Sn with a-Ge:H layer. Another catalyst precursor was used: the SnO_2 NPs. These NPs were partially reduced to pure Sn in PECVD. The objective was to limit the wetting behavior of Sn by the pinning effect created by SnO_2 NPs. This strategy was successful and crystalline GeSn NWs were grown with an amazing 22 at.% Sn incorporated homogeneously inside the NWs. Four kinetic models were presented to explain the high concentration of Sn in the GeSn NWs: Ge-Sn complementarity, step-wise flow, continuous growth, and dimer-based insertion. The first three models were not able to account for the high Sn percentage, even by using the atomic line formation velocity, which is more than 9000 times higher than the interface velocity. The dimer-insertion model was developed for Sn catalyzed GeSn NWs. Based on this model, we predicted that in order to obtain 22 at.% Sn concentration, the growth rate should be 7 nm/s which is consistent with the estimated growth rate interval of IPSLS GeSn NWs grown at 270℃. In the third part, atomic scale mappings and quantifications were done on IPSLS SiSn NWs. These quantifications show that these NWs have far from equilibrium Sn concentrations varying from ~ 9 at.% to 10 at.% for 300℃ and 400℃ respectively. Although, Sn seemed homogeneously distributed throughout the NWs Sn enrichments existed at both temperatures. As perspective, the density of GeSn NWs should be increased by optimizing the density of the catalyst NPs, and should be passivated. This will allows investigating the indirect-to-direct bandgap transition by micro-photoluminescence.

In the last chapter, we have presented a new in-plane Solid-Solid-Solid mechanism for the growth of GeSn NWs using Sn NPs at substrate temperatures below the melting point of Sn. It was shown that the size of Sn NPs is not small enough to melt at the growth temperatures. An activation window is defined for the growth of GeSn NWs, with a lower limit at 160℃ (i.e. 70℃ below melting point). The IPSSS NWs have different morphologies than IPSLS NWs. Moreover, at the region where the NW ends, wetting is not observed for the IPSSS mechanism, which is considered as additional evidence that the catalysts are solid. The IPSSS NWs are shown to have a core-shell structure (Sn-rich core and Ge-rich shell) compared to a homogeneous (at a nanoscale) distribution for the IPSLS GeSn NWs. The Sn concentration in the IPSSS GeSn NWs can reach up to 35 at.% at the core part, while in the shell it is nearly pure Ge. Four mechanisms were suggested for the IPSSS GeSn NWs growth: bulk diffusion, grain boundary diffusion, surface diffusion, and premelted surface diffusion. We concluded that the last two possibilities are the most probable. Finally, unexpected out-of-plane GeSn NWs were obtained using a modified growth process. The amorphous Ge layer is deposited at the first place, then, SnO_2 colloids were deposited thereafter, and then comes the subsequent plasma treatments. The EDX quantifications have shown that the Sn concentration can be ~ 5 at.% in the NWs. Various growth mechanisms are proposed for this kind of vertical NWs. Many trials were done with different conditions proving that the growth is neither a VLS nor a VSS mechanism. The most probable mechanisms for the growth are SLS or SSS out-of-plane. As perspectives, first, IPSSS mechanism should be utilized to grow other types of NWs, such as IPSSS SiNWs catalyzed by Sn, which can result in a sufficient concentration of Sn transforming the bandgap of Si into a direct one. Second, an in-situ TEM can provide an invaluable insight on the catalyst state (i.e. solid or liquid) during an IPSSS growth, and on the mass transport mechanism of these IPSSS NWs. Third, the dimer-insertion model for GeSn NWs should be validated by investigating more NWs cross-section in TEM.